



Thèse présentée pour obtenir le grade de  
**Docteur de l'Université de Strasbourg**  
Discipline: Chimie-Physique

Par  
**Gabriela Popa**

# **Spray-on hybrid nanoscale coatings**

Soutenue publiquement le 26 novembre 2010

## **Membres du jury:**

*Directeur de Thèse:* M. Gero Decher, Professeur, Strasbourg, France

*Rapporteur:* M. Wolfgang Knoll, Professor, Vienna, Austria

*Rapporteur:* M. Jean-Francois Gerard, Professor, Lyon, France

*Examineur:* Mme. Sylvie Begin-Collin, Professeur, Strasbourg, France

*Examineur:* M. Jean-Claude Voegel, Directeur de recherche, Strasbourg, France

*Examineur:* M. Clement Sanchez, Directeur de recherche, Paris, France



# Fabrication de couches minces hybrides par pulverization

Résumé de Thèse en Français (PhD resume in French)

Les films minces et les surfaces fonctionnelles constituent un domaine important en science et technologie avec des applications dans divers domaines tels que les biomatériaux, les recouvrements optiques, l'ingénierie de dispositifs, etc.

Ces applications résultent du développement de méthodes de préparation de films organiques, inorganiques et hybrides. Au cours de cette thèse, la préparation de films multicomposites a été envisagée dans le cadre de différents projets par la technique couche-par-couche (LbL).

Cette méthode, développée dans les années 90, permet de construire des films multimatériaux nano-organisés sur une multitude de surfaces (métaux, verre, polymères, ...) avec un grand nombre de matériaux (polymères, colloïdes, protéines, cellules, ...). La préparation de films multicouches est réalisée par dépôts consécutifs de composés cationiques et anioniques en solution, en particulier des polyélectrolytes, sur un substrat par trempage et pulvérisation (Figure 1).

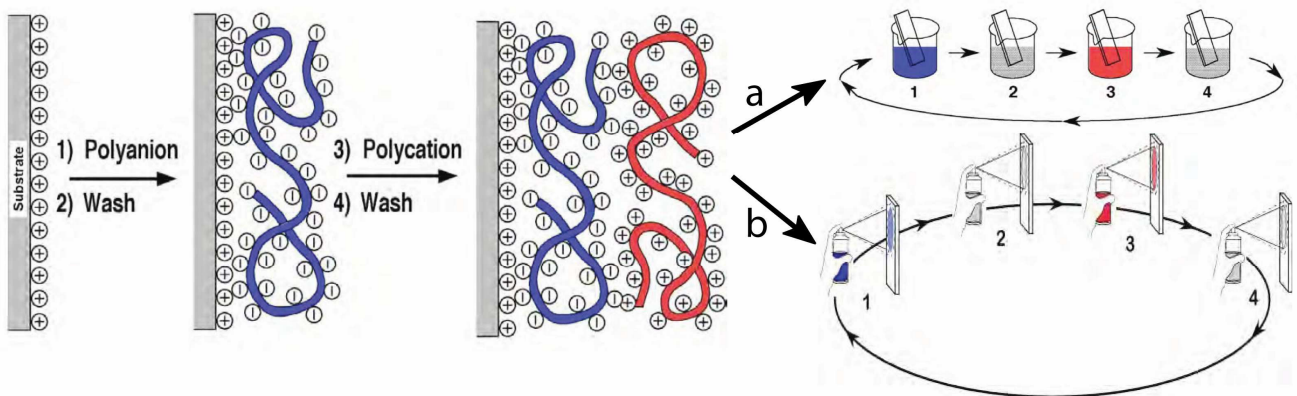


**Figure 1. Représentation schématique simplifiée des deux premières étapes d'adsorption illustrant le dépôt d'un film de polyélectrolytes sur un support chargé positivement par trempage (a) et par pulvérisation (b). Les contre ions ont été omis pour des raisons de clarté. La conformation des polyélectrolytes est hautement idéalisée et l'interpénétration des couches est montrée afin de mieux représenter l'inversion de la charge de surface après chaque étape d'adsorption. La nomenclature (A/B) $n$  est utilisée pour décrire la construction d'un film à partir de deux polyélectrolytes (A et B) où  $n$  correspond au nombre de cycles de trempage/pulvérisation ou au nombre de paires de couches.**

Chaque étape d'adsorption d'un composé est suivie d'une étape de rinçage nécessaire pour évacuer l'excédant non-adsorbé ou faiblement adsorbé. La répulsion électrostatique entre la dernière couche déposée et l'excès de matériel en solution conduit à la formation d'une couche unique de quelques nanomètres à chaque étape de dépôt. Cette technique s'applique également à des composés interagissant par d'autres interactions non covalentes (liaisons hydrogènes, liaisons de coordination, ...) et par des liaisons covalentes.

Mon premier projet de recherche, intégré à l'ANR Cartilspray, a consisté à participer à l'élaboration d'un cartilage articulaire artificiel où la technique LbL a été utilisée pour

construire un film collagène-hydroxyapatite. Ce travail a été réalisé à l'Institut Charles Sadron (ICS) en collaboration avec l'équipe de Pierre Schaaf (ICS) et avec l'unité INSERM UMR 595 dirigée par Jean-Claude Voegel.

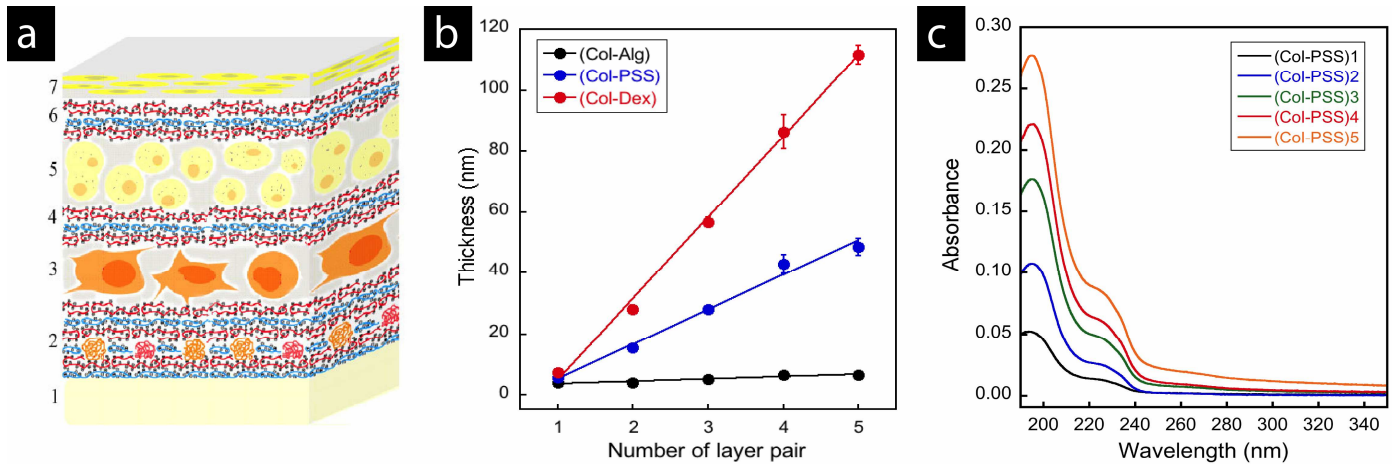


**Figure 2. a) Représentation schématique de la section verticale du modèle de cartilage proposé. (1) Couche collagène-hydroxyapatite comme matrice ostéo-chondrale ; (2)-(4)-(6) film de multicouche comme compartiment actif ; (3)-(5)-(7) Gel d'alginate contenant des cellules souches à différencier en chondrocytes. b) Variation de l'épaisseur de films (Col/Alg)<sub>n</sub>, (Col/PSS)<sub>n</sub> et (Col/Dex)<sub>n</sub> en fonction du nombre de paires de couches mesurée par ellipsométrie. c) Variation de l'absorbance du film (Col-PSS)<sub>n</sub> en fonction de nombre de paires de couches déposées. Chaque spectre d'absorption comporte deux pics : le pic du Collagène qui absorbe vers 190 nm et le pic du PSS qui absorbe vers 220 nm.**

Le cartilage est un tissu possédant une parfaite organisation spatiale où les cellules (chondrocytes) et les autres constituants matriciels sont distribués de façon à permettre à chaque domaine de remplir son ou ses rôle(s) spécifique(s). On distingue ainsi une couche superficielle (dédiée au glissement), une partie intermédiaire (amortissement des chocs) et une couche profonde (ancrée à l'os sous-jacent). Malgré les progrès de la chirurgie, les méthodes de remplacement, de régénération ou de réparation du cartilage endommagé ne permettent pas actuellement de récupérer une fonction de 100%. L'ingénierie tissulaire constitue une des approches prometteuses pour remplacer, régénérer ou réparer un cartilage défectueux. Dans le cadre de ce projet ANR, il a été envisagé de construire un cartilage artificiel possédant une structure et des propriétés proches du tissu original pour assurer une implantation avec un minimum d'effets secondaires (rejet, réactions inflammatoires, ...). Ainsi, un modèle de cartilage articulaire par empilement de plusieurs strates, inspiré de la composition et de la structure du cartilage articulaire chez l'homme, a été proposé (**Figure 2**, à gauche). Ce modèle comporte essentiellement trois types de couches : (i) des films polymères agissant comme compartiment actif, (ii) un gel d'alginate de calcium contenant les cellules, (iii) un film collagène-hydroxyapatite assurant la bonne adhésion du cartilage à l'os. Dans le cadre de ma thèse, la construction de ce dernier film a été envisagée en deux étapes par la technique LbL. Dans un premier temps, la fabrication de films multicouches à base de collagène a été validée pour permettre ensuite le dépôt d'un film d'hydroxyapatite.

Le collagène est une protéine chargée positivement qui est présente dans le cartilage articulaire à une teneur pouvant atteindre 20%. Sa nature biologique favorise l'implantation d'un biomatériau en limitant les réactions secondaires (problèmes de cytotoxicité, inflammation, faible irrigation de l'implant, etc...). Cependant, sa faible solubilité à pH neutre a nécessité de construire les films multicouches à un pH acide de 4. La croissance de films multicouches de collagène (Col) avec différents polyanions (poly (styrène) sulfonate (PSS), dextrane sulfate (Dex) et alginate (Alg)) a été caractérisée par différentes méthodes (ellipsométrie, microbalance à cristal de quartz, spectroscopie UV-visible et IR). La **Figure 2** (à droite) montre clairement que la croissance du film (augmentation de l'épaisseur en fonction du nombre de paires de couche) dépend fortement de la nature du polyanion utilisé. La topographie de films minces à base de Collagène a été étudiée par la technique de microscopie à force atomique (AFM). Une structure fibrillaire est observée pour le film mince à base de Collagène – Alginate et Collagène- PSS dans la **Figure 3**. Pour le cas Collagène- Alginate : le diamètre de fibres formées est plus important que pour le cas Col/PSS. De plus, on observe l'apparition de certaines fibrilles ayant de longueur et diamètre supérieures à la majorité de fibres. La rugosité de films augmente avec le nombre de couche de paire de polyelectrolytes déposés pour les deux cas présentés.

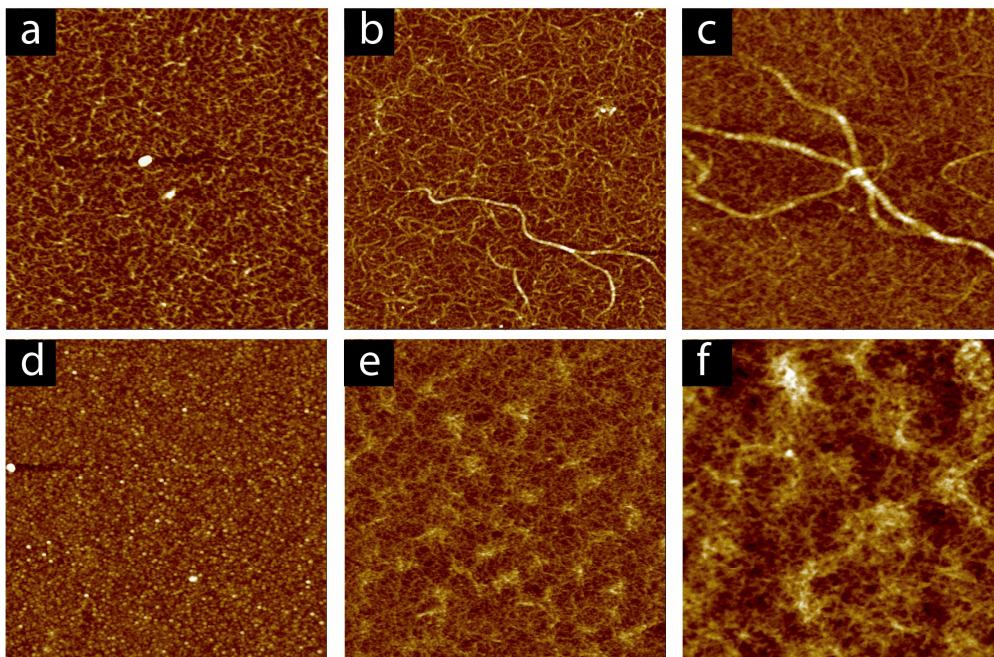


**Figure 3. Images de microscopie AFM de films de (Col/Alg) (a-c) et (Col/PSS) (d-f) en fonction de nombre de cycles de pulvérisation : a) (Col/Alg)<sub>1</sub>, b) (Col/Alg)<sub>5</sub>, c) (Col/Alg)<sub>30</sub>, d) (Col/PSS)<sub>1</sub>, e) (Col/PSS)<sub>5</sub>, (Col/PSS)<sub>15</sub>. La barre d'échelle est de 15 nm pour les films de (Col/Alg) (a-c), 25 nm pour les films (Col/PSS) (d-e) et 45 nm pour le film (Col/PSS)<sub>15</sub> (f). La zone imagée par AFM est de 5  $\mu\text{m}$   $\times$  5  $\mu\text{m}$  pour toutes les images.**

Ensuite, nous nous sommes intéressés au dépôt d'une couche inorganique d'hydroxyapatite sur les films multicouches préparés précédemment. La synthèse d'hydroxyapatite est en

général réalisée par co-précipitation à partir d'une solution de sel de calcium et d'une solution de sel de phosphate préparées toutes les 2 à un pH basique de 10. Ce milieu basique assure l'obtention d'hydroxyapatite sous sa forme cristalline. La difficulté de cette étape provient de la dissolution partielle du film multicouche à base de collagène, construit à pH acide, en milieu basique lors de la construction du film d'hydroxyapatite. L'inversion des 2 étapes de fabrication d'un film collagène-hydroxyapatite ne permet pas de résoudre le problème de dissolution.

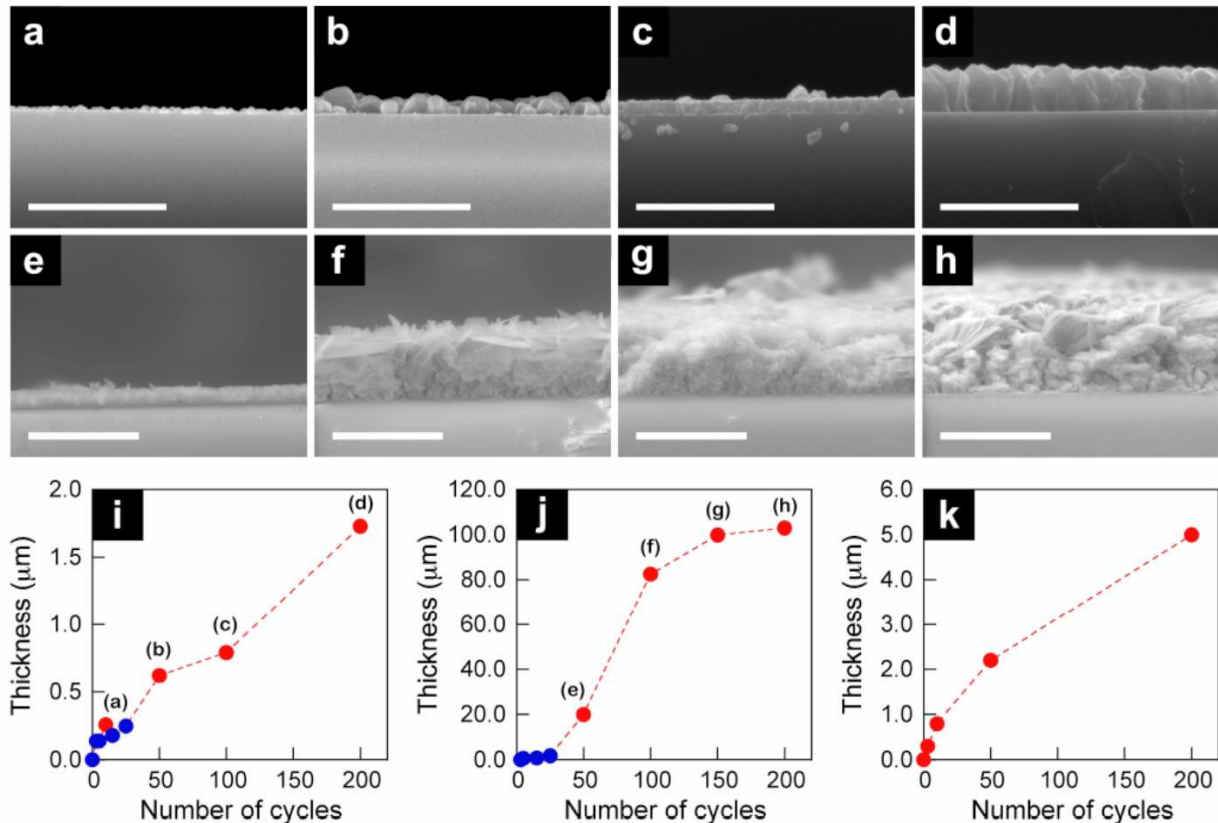


**Figure 4. Images de microscopie électronique à balayage de coupes en Z de films inorganiques de CaF<sub>2</sub> (a-d) et CaHPO<sub>4</sub> (e-h). Evolution de l'épaisseur des films de CaF<sub>2</sub> (i), CaHPO<sub>4</sub> (j) et CaC<sub>2</sub>O<sub>4</sub> (k) en fonction du nombre de cycles de pulvérisation. L'épaisseur est calculée à partir de mesures de grattage des films par AFM (cercles bleus) et des coupes en Z obtenues par MEB (cercles rouges). Le nombre de cycles de pulvérisation est égal à : 10 (a), 50 (b,e), 100 (c,f), 150 (g) et 200 (d,g). La barre d'échelle est de 5 μm pour (a-d) et 100 μm (e-h). Les lignes pointillées ont été ajoutées uniquement pour guider l'œil.**

Le dépôt du film de phosphate de calcium a été réalisé par pulvérisation consécutive de sel de calcium et de phosphate (**Figure 4** e-h et i). Le succès de cette approche s'explique par le contact très court des solutions avec la surface lors de la construction. Contrairement à la pulvérisation de polyélectrolytes, il n'y a pas d'étape de rinçage entre le dépôt de chaque sel. Les avantages de cette technique par rapport à la méthode de trempage classique appelée

SILAR (Successive Ionic Layer Adsorption and Reaction) sont la diminution du temps de déposition et une meilleure homogénéité des films obtenus.

L'utilisation de cette approche a non seulement permis d'atteindre les objectifs fixés dans le cadre de l'ANR Cartilspray mais a également initié le deuxième projet de recherche de ma thèse, à savoir la fabrication de couches minces inorganiques et hybrides par pulvérisation alternées. Ainsi, la méthode de construction de couches inorganiques par pulvérisation alternée a été validée pour d'autres types de cristaux (**Figure 4**) : fluorure de calcium, oxalate de calcium, phosphate de fer, chlorure d'argent, hexacyanoferrate de fer (III) (bleu de Prusse). L'épaisseur de la couche inorganique déposée est contrôlée par le nombre de cycle de pulvérisation des deux sels, de la nature du cristal inorganique formé et du temps de pulvérisation de la solution de chaque cycle (**Figure 4** et **Figure 5**).

La **Figure 5** montre que le mécanisme de croissance des films inorganiques est différent en fonction de type de cristal déposé. Pour le fluorure de calcium et l'oxalate de calcium, l'augmentation de l'épaisseur des films (proportionnelle à l'absorbance) est indépendante du temps de pulvérisation pour un temps de pulvérisation supérieur à 1-2 secondes. Dans le cas du phosphate de calcium, on observe une épaisseur maximale pour un temps de pulvérisation de 2 secondes. Au delà de ce maximum, la dissolution des cristaux inorganiques est plus rapide que leur réaction de formation.

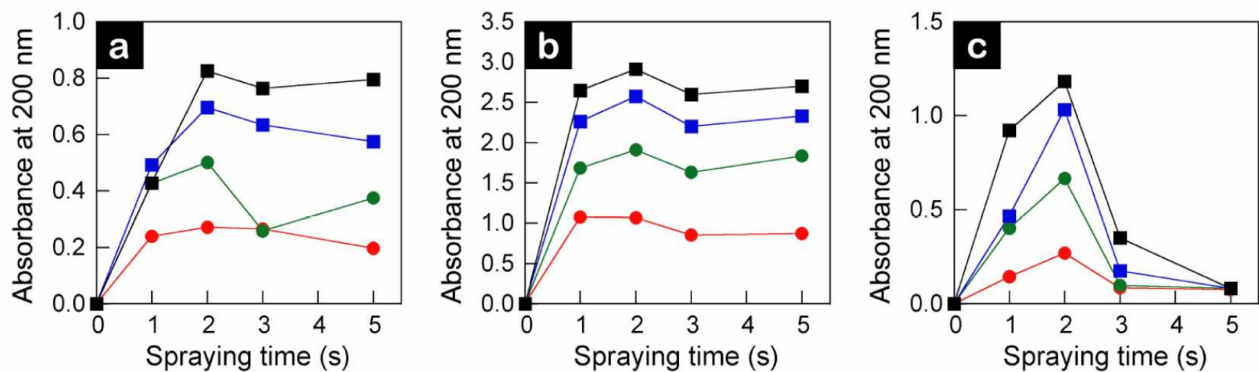


**Figure 5. Variation de l'absorbance mesurée par spectroscopie UV-VIS à 200 nm en fonction de temps de pulvérisation pour le dépôt de CaF<sub>2</sub> (a), CaC<sub>2</sub>O<sub>4</sub> (b) et CaHPO<sub>4</sub> (c) après 5 (●), 10 (●), 15 (■), 20 (■) cycles de pulvérisation. Les lignes pleines connectant les points ont été ajoutées uniquement pour guider l'œil.**

Ensuite, nous avons montré que cette approche est compatible avec l'assemblage LbL de polyélectrolytes et qu'elle peut être utilisée pour la construction de films multimatériaux de type "sandwich". La Figure 6 montre la structure de film de oxalate de calcium (CaC<sub>2</sub>O<sub>4</sub>)<sub>10</sub> (a) et la structure de films hybrides de oxalate de calcium – fluorure de calcium : (CaC<sub>2</sub>O<sub>4</sub>)<sub>10</sub>-(CaF<sub>2</sub>)<sub>20</sub> (b) et (CaC<sub>2</sub>O<sub>4</sub>)<sub>10</sub>-(CaF<sub>2</sub>)<sub>40</sub> (c) observées par microscopie à force atomique. Un changement de la structure morphologique de films multimatériaux est visible à partir de couches inorganiques de fluorure de calcium (**Figure 6** b-c) déposées sur le film inorganique d'oxalate de calcium (**Figure 6** a). La rugosité de film multimatériaux est plus élevée que la rugosité de film inorganique formé d'un seul cristal (**Figure 6** a).

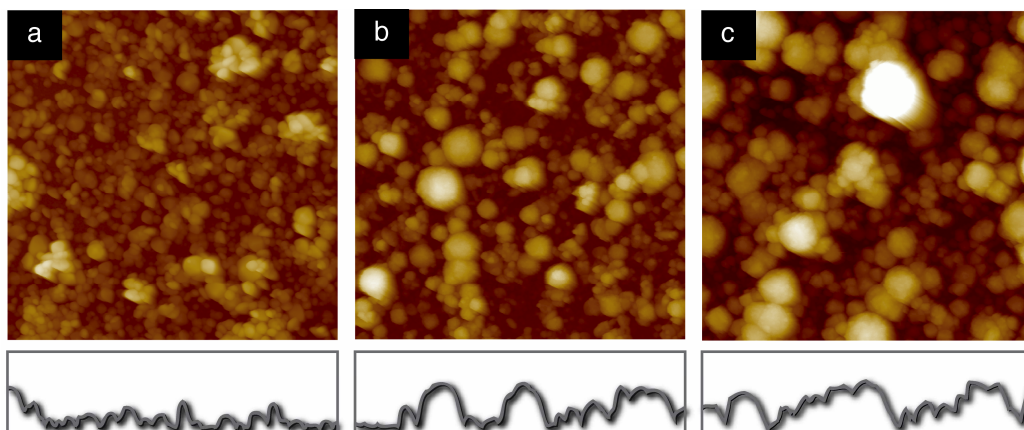


**Figure 6.** En haut : Image AFM de films inorganiques de seulement oxalate de calcium ( $\text{CaC}_2\text{O}_4$ )<sub>10</sub> (a), oxalate de calcium sur lequel on a déposé de fluorure de calcium ( $\text{CaC}_2\text{O}_4$ )<sub>10</sub>-( $\text{CaF}_2$ )<sub>20</sub> (b) et ( $\text{CaC}_2\text{O}_4$ )<sub>10</sub>-( $\text{CaF}_2$ )<sub>40</sub> (c). La taille d'images est  $5\ \mu\text{m} \times 5\ \mu\text{m}$ . La barre d'échelle est de  $800\ \text{nm}$ . En bas : la Z- section d'image AFM réalisée au milieu de cette image. La barre d'échelle pour Y-axis de la section est  $1.2\ \mu\text{m}$ .

La **Figure 7** montre la structure d'un film hybride  $\text{PEI}-(\text{CaC}_2\text{O}_4)_{100}-(\text{PSS}/\text{PAH})_5-(\text{CaF}_2)_{100}$  observée par microscopie confocale Raman. Malgré une résolution spatiale limitée, il est évident que le film est riche en oxalate de calcium en bas et riche en fluorure de calcium en haut. Cette étude a démontré la simplicité et l'adaptation de cette technique pour construire des films inorganiques et hybrides. Cependant, à l'heure d'aujourd'hui, nous n'avons pas encore optimisé les propriétés "matériaux" de ces films en fonction de leurs applications potentielles dans des dispositifs. Ce travail a également soulevé la complexité du processus de fabrication de ces films, en particulier l'influence de l'espace interstitiel entre les cristaux (porosité) sur la vitesse de nucléation et de croissance du processus.

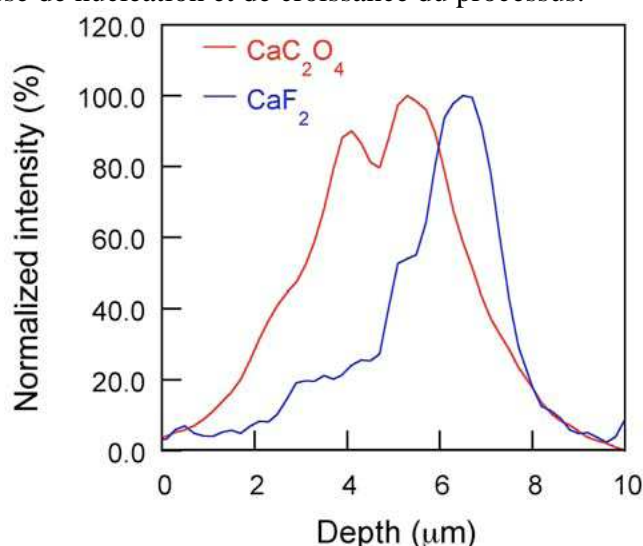


**Figure 7.** Profil de profondeur du film hybride  $\text{PEI}-(\text{CaC}_2\text{O}_4)_{100}-(\text{PSS}/\text{PAH})_5-(\text{CaF}_2)_{100}$  visualisée par l'intensité des bandes Raman de l'oxalate de calcium (rouge) et de fluorure de calcium (bleu) obtenu par microspectroscopie confocale Raman.



Finalement, j'ai récemment participé au développement d'une nouvelle méthode de dépôt de couches minces : la pulvérisation simultanée (**Figure 8**, à droite). Elle repose sur la pulvérisation simultanée de 2 composés interagissant au plus sur une surface réceptrice. Ainsi, la réaction rapide entre les composés complémentaires conduit à la croissance continue et graduelle du film dont l'épaisseur est contrôlée par le temps de pulvérisation. Cette approche a pu être généralisée à différents systèmes : polyélectrolytes/polyélectrolytes, polyélectrolytes/petits oligo-ions, polymères interagissant par liaisons hydrogènes, polyélectrolytes/nanoparticules et des sels inorganiques complémentaires.

Dans le cadre de ce développement, j'ai construit les films inorganiques décrits précédemment via pulvérisation alternée par pulvérisation simultanée. L'avantage de cette technique est une réduction significative du temps de dépôt par rapport à la pulvérisation alternée. Dans la **Figure 8** (à gauche), on peut voir l'influence de temps de pulvérisation sur l'épaisseur et la morphologie de film de fluorure de calcium.

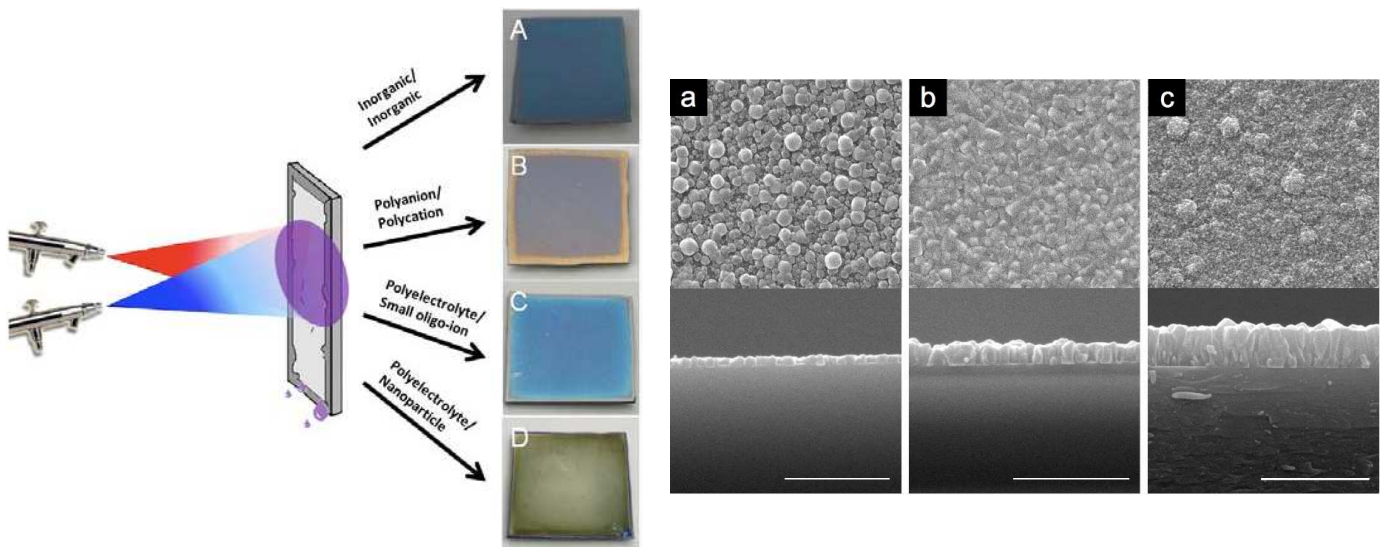


**Figure 8.** A droite : Représentation schématique du système de pulvérisation simultanée (à gauche) et exemples de systèmes étudiés (à droite). Au cours de cette thèse, seule la réaction inorganique/inorganique (exemple A) a été étudiée. A gauche : Images de microscopie électronique à balayage d'un films de  $\text{CaF}_2$  vue de dessus (en haut) et vue latérale (en bas) en fonction du temps de pulvérisation : 1 minute (a), 5 minutes (b) et 10 minutes (c). La barre d'échelle est de  $5 \mu\text{m}$  (a-c).

Un autre exemple de couche inorganique qui a été étudié au cours de ma thèse est le bleu de Prusse ou en anglais, Prussian blue (PB),  $(\text{Fe}_4[\text{Fe}(\text{CN})_6]_3)$ . Films minces à base de PB sont utilisés dans le domaine de bio-détection de Glucose, électrochromisme (changement de la longueur d'onde d'absorption en fonction de valence de complexe/courant électrique appliqué), etc. La même technique de pulvérisation simultanée a été utilisée pour la préparation de couches minces homogènes pour de temps de pulvérisation très courts (**Figure 9**).

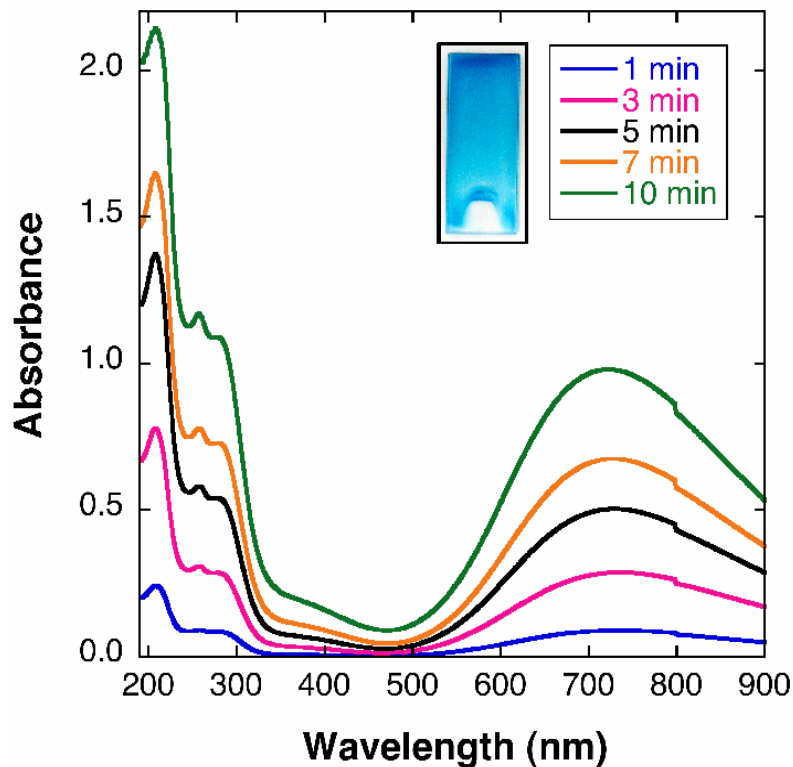


**Figure 9. Spectre UV-VIS pour un film de PB obtenu par la pulvérisation d'un sel de chlorure de fer (II) ( $3 \cdot 10^{-3}M$ ) et hexacyanoferrate (III) de potassium ( $3 \cdot 10^{-3}M$ ) en fonction de temps de pulvérisation simultanée des deux solutions de sel. La discontinuité de spectre vers 790 nm est due au changement automatique de filtres dans le spectrophotomètre. Image insérée dans le spectre: image optique de film obtenu pour une durée de 5 minutes de pulvérisation. En bas du substrat, l'inhomogénéité du film est due à la pince qui tient le substrat (une plaque de quartz).**

Nous nous sommes rapidement aperçus de la puissance de l'approche par pulvérisation simultanée. De ce fait, nous avons décidé d'explorer l'étendue de cette méthode plutôt que d'étudier un seul exemple en détail. Ainsi, nous avons d'abord étudié la croissance des différents films et leur morphologie et dans le cas de  $CaF_2$ , nous avons démontré la composition chimique des films par diffraction électronique en TEM. Ce choix stratégique a conduit à ce que beaucoup d'autres aspects importants de cette approche tels que la nucléation et la croissance de cristaux, le rôle de l'espace interstitiel en tant que réservoir et la diffusion des espèces chimiques dans le liquide du l'espace interstitiel n'ont pas encore pu être étudiés. De plus, les questions suivantes restent complètement ouvertes : si et comment la composition des films inorganiques peut être contrôlée, en particulier si elle peut être différente de la composition du précipité cristallin dans les réactions de précipitation classiques. Ceci est également valable pour d'autres aspects comme l'obtention de phases cristallines spécifiques induites par cette méthode de préparation.

Au cours de ma thèse, j'ai été impliqué dans différents projets impliquant la fabrication de couches minces organiques, inorganiques et hybrides à l'aide de diverses techniques de pulvérisation pour des applications potentielles en science des matériaux et en science de la vie. Les résultats obtenus lors de ces travaux ont également soulevé de nombreuses questions qui devront être étudiées pour mieux comprendre les mécanismes de formations de ces couches (paramètres expérimentaux) et optimiser les propriétés de ces matériaux en fonction de leurs applications potentielles.

## **Acknowledgements**

This thesis work was conducted at the Institut Charles Sadron (ICS) located in Strasbourg, France. The ICS provided the necessary environment, but it was especially the people working there, who made, with their help in various ways, this thesis possible.

I would like to express my sincere gratitude to my advisor Professor Gero Decher for the continuous support during my doctoral studies and research, for his patience, enthusiasm, and help in science.

I would like to express my gratitude to Dr. Jean-Claude Voegel, Prof. Sylvie Begin-Collin, Prof. Wolfgang Knoll, Prof. Clément Sanchez, Prof. Jean-Francois Gérard, for having accepted to act as jury members for my thesis work.

I am grateful for the abundant and invaluable help from Dr. Fouzia Boulmedais and Dr. Olivier Félix, without whose extraordinary support my research project would not have been possible.

I would like to express my gratitude to Professor Pierre Schaaf, Mr. Joseph Hemmerle for collaboration and discussions.

Special thanks to all my colleges, Rebecca, Yulia, Dasha, Rita, Diana, Johanna, Ying, Emek, Mathias, Gauthier, Ivan, Alexandru, Loic, Ali, Patricia...., in one word: all ICS institute, for all the joyful moments that we have shared in the past three years.

Thanks to French ministry of Higher Education and Research (Ministère de l'enseignement supérieur et de la recherche) for providing me with financial support.

<b>1</b>	<b>INTRODUCTION.....</b>	<b>16</b>
<b>2</b>	<b>LITERATURE – STATE OF THE ART.....</b>	<b>21</b>
<b>2.1</b>	<b>Cartilage.....</b>	<b>21</b>
2.1.1	Cartilage: Basic notions.....	21
2.1.2	Tissue engineering.....	22
2.1.3	Our approach of cartilage tissue repairing.....	26
<b>2.2</b>	<b>Collagen.....</b>	<b>29</b>
2.2.1	Collagen. Structure, type, applications.....	30
<b>2.3</b>	<b>Hydroxyapatite.....</b>	<b>36</b>
<b>2.4</b>	<b>Film deposition techniques.....</b>	<b>40</b>
2.4.1	Thin-Film Applications.....	41
2.4.2	Classifications of deposition process.....	43
2.4.3	SILAR method. A dipping method.....	51
2.4.4	An example of new deposition technologies. Sol-gel deposition.....	52
<b>2.5</b>	<b>The layer-by-layer deposition technique.....</b>	<b>52</b>
2.5.1	Preparation of PEM films.....	54
2.5.2	Mechanism of formation and general properties of polyelectrolyte multilayers.....	55
2.5.3	Preparation of Collagen PEM films.....	60
2.5.4	The advantages of consecutive and simultaneous spray deposition methods.....	62
<b>2.6</b>	<b>Bibliography.....</b>	<b>65</b>
<b>3</b>	<b>MATERIALS AND METHODS.....</b>	<b>70</b>
<b>3.1</b>	<b>Polyelectrolyte multilayers.....</b>	<b>70</b>
<b>3.2</b>	<b>Inorganic coatings.....</b>	<b>70</b>
<b>3.3</b>	<b>Spraying. Equipment and implementation.....</b>	<b>74</b>
3.3.1	General considerations on atomization.....	74
3.3.2	Atomizers, airbrushes.....	77
3.3.3	Spray parameters.....	80
<b>3.4</b>	<b>Thin film characterization.....</b>	<b>81</b>
3.4.1	Atomic Force Microscopy.....	81
3.4.2	Electron microscopy.....	88
3.4.3	UV-Visible Spectroscopy.....	93
3.4.4	Infrared (IR) Spectroscopy.....	97
3.4.5	Ellipsometry.....	101
<b>3.5</b>	<b>Bibliography.....</b>	<b>108</b>

<b>4</b>	<b>RESULTS AND DISSCUSION.....</b>	<b>111</b>
<b>4.1</b>	<b>Collagen based LbL multilayers .....</b>	<b>111</b>
4.1.1	Multilayer growth .....	111
4.1.2	The Collagen LbL film topography by AFM microscopy .....	117
4.1.3	The use of Collagen non-aqueous solutions for the LbL multilayer film formation ....	120
<b>4.2</b>	<b>Consecutive spraying method .....</b>	<b>124</b>
4.2.1	Calcium phosphate (CaP) coatings .....	124
4.2.2	Biomaterial fabrication based on Collagen-CaP coatings.....	131
4.2.3	Use of (PAH-PSS) <sub>n</sub> films as barrier for preventing dissolution of CaP crystals .....	135
4.2.4	Combination of barrier layers with Collagen and CaP coatings .....	139
4.2.5	Consecutive spraying method applied to other inorganic coatings .....	144
4.2.6	Inorganic “sandwich” structure fabrication by alternating spraying .....	148
<b>4.3</b>	<b>Simultaneous spraying: deposition method for thin films .....</b>	<b>150</b>
4.3.1	Manually simultaneous spraying deposition .....	150
4.3.2	Calcium phosphate coatings prepared by the method automatic simultaneous spray (ASS) method .....	155
<b>4.4</b>	<b>Prussian Blue film preparation by AS/SSC method .....</b>	<b>170</b>
<b>4.5</b>	<b>Thin film preparation based on polyelectrolyte-small molecule interaction.....</b>	<b>175</b>
<b>4.6</b>	<b>Bibliography.....</b>	<b>180</b>
<b>4.7</b>	<b>Article 1 .....</b>	<b>182</b>
<b>4.8</b>	<b>Article 2 .....</b>	<b>190</b>
<b>5</b>	<b>CONCLUSIONS AND PERSPECTIVES.....</b>	<b>197</b>



## 1 Introduction

Cartilage has a spontaneous repair for a full thickness defect (usually caused by the osteoarthritis) but limited in terms of form and function. In order to improve the disadvantages of most painful surgical cartilage repairs and slow cartilage regeneration rates, new tissue engineering applications need to be developed.

Consequently, the fabrication of cartilage scaffolds is an ambitious project. Layer-by-layer assembly is a powerful tool for preparing hybrid materials for new applications. Various scaffold materials have been tested, including both naturally derived and synthetic polymers.

The natural polymer that has received the most attention is the collagen. In 1983, it was reported that chondrocytes maintain differentiated phenotype and glycosaminoglycan chains (GAG) production for six weeks in collagen gels. The main advantage of collagen is the remodeling and the degradation to provide space for the growing tissue. Collagen matrices are also found to stimulate the new collagen production by transplanted cells as compared with other scaffold types. Our challenge was to have Collagen and hydroxyapatite (calcium phosphate mainly found in bone) in a hybrid film using the Layer-by-Layer (LbL) technique.

The natural articular cartilage has a stratified structure based on differences in matrix morphology and biochemistry. Our cartilage model mimics this property and the biomaterial structure is divided into four different regions: superficial, transitional, middle and calcified. We focused the present work on the calcified zone fabrication. The calcified cartilage zone is closest to the bone tissue and it allows the transition from soft (transitional and middle zone of cartilage) to hard regions (bone matrix).

The very attracting layer-by-layer assembly of polyelectrolyte multilayers is introduced at the beginning of the 1990s. Its advantages are the possibility to coat practically any



surface whatever its nature and geometry, the easy coating procedure (mainly by dipping and spraying method), the high level of control over composition and structure of deposited films as well as the large range of possibilities for further functionalization. Due to these versatile possibilities for functionalization, polyelectrolyte multilayers have high potential for applications in the nano-biotechnology field.

The Layer-by-Layer deposition technique, mostly used for the polyelectrolyte deposition, needed to be extended for the deposition of inorganic coatings. Various inorganic crystalline deposits were prepared by consecutive spraying such as calcium phosphate, calcium fluoride, calcium oxalate, Prussian Blue, etc. The coating thickness increases with the number of deposition steps. In addition, a new deposition method was explored based on the simultaneous spray of the reactive species solutions.

The third chapter describes the fabrication steps made for the hybrid film preparation containing collagen fibers and the calcium phosphate (hydroxyapatite). In order to prepare these hybrid films, the incorporation of the barrier films (e.g. Poly (allylamine) - Poly (styrene sulfonate) or (PAH-PSS)) was needed. It also provides more details on the Collagen LbL films preparation and the solvent influence on the film rate construction, as well as on calcium phosphate coatings rate growth depending on various deposition parameters (time, concentration, deposition method).

The first chapter of this thesis provides a more detailed review on the state of the art in the cartilage repair and especially in coating techniques and strategies to obtain cartilage scaffolds as well as on the current understanding of the underlying mechanisms, being the background of this study. It is followed by the second chapter on the materials and methods employed in this study.



# Literature - State of the Art



## **2 Literature – State of the Art**

### **2.1 Cartilage**

With an aging population and a growing problem of obesity, the number of osteoarthritis patients is estimated to grow in the coming years. In 2007, more than 250 000 knee and hip replacements were performed in the United States because of two major cartilage defects: severe cartilage damage or end-stage disease joint failure (1). With a more active population, cartilage damage due to sport injuries can often result in premature cartilage degeneration.

#### **2.1.1 Cartilage: Basic notions**

Cartilage is present in different places of the body: skeleton (articular surfaces of synovial joints, intervertebral discs), ears, respiratory tract, and nose. The extracellular matrix (ECM) is the predominant component of cartilage into which cells are embedded (chondrocytes). Chondrocytes maintain cartilage matrix structure by continued remodeling.

Cartilage, connective tissue, can be classified into three main types of cartilage:

- Hyaline cartilage
- Fibrocartilage
- Elastic cartilage

Each type differs in its biochemical composition, number and morphology of chondrocytes.

Chondrocytes are specialized mesenchymal cells that are differentiated from other cells such as fibroblasts by the nature of molecules produced. Chondrocytes secrete large quantities of different types collagen and proteoglycan (2). Different phenotypic chondrocytes can be found in different parts of the cartilage. Interactions between chondrocytes and the extracellular matrix are important to cell anchorage, matrix biosynthesis and matrix degradation.

Extracellular matrix (cartilage matrix, ECM) is composed of water (65-80%), collagen (15-25%), proteoglycans (3) and non-collagenous proteins (10%).

### 2.1.2 Tissue engineering

Rapid developments in cellular and molecular biology and in material scaffold engineering facilitated the development of tissue engineering that turned out to be a budding field in modern biomedical sciences (1, 4).

	1 <sup>st</sup> Generation (2002)	2 <sup>nd</sup> Generation (emerged after 2002)	3 <sup>rd</sup> Generation (present day)
Principal approach	Autologous cell transplants	Performed tissue flaps, 3D scaffolds and osteochondral transplants	In vivo regeneration and guided tissue repair
Important component	Periosteal flap	Delivery substances and scaffold	Growth factors and biomaterials

**Table 1. Trends in developing procedures used in cartilage tissue engineering from 2002 (4)**

Two approaches are possible for the reconstruction process of mammalian tissues: entirely in vitro or partially in vitro which is then completed in vivo, in situ.

Since 1987, autologous chondrocyte transplantation (ACT) has been used clinically to treat cartilage defect in more than 12 000 patients worldwide (5). This approach involves an in vitro reconstruction coupled with an in vivo phenomenon. Chondrocytes cells are isolated from donor tissue/cartilage defect then they are expanded in vitro. The next step is the delivery of expanded chondrocyte cells to the cartilage defect site to produce new cartilage tissue. One limitation of this technique is the low density of cells obtained by biopsy of the mature cartilage tissue.

Three important constituents need to be optimized in tissue engineering: a matrix scaffold, cells and signaling molecules (such as growth factors).

### 2.1.2.1 Cell source

Different types of cells (chondrocytes, fibroblasts, stem cells, and genetically modified cells) have been explored for their potential as a viable cell source for cartilage repair(1).

Chondrocytes are most explored for producing, maintaining and remodeling the cartilage ECM since they are found in native cartilage (1, 6-8). They are characterized by a round morphology and the production of ECM molecules (type II Collagen, sulfated glycosaminoglycans (GAGs)). Chondrocytes are limited in number, comprising only 5 to 10% of cartilage tissue (7).

Fibroblasts are relatively abundant cells present in the skin. They are used in the cartilage engineering and can be redirected towards a chondrocytic phenotype under appropriate conditions. An example is the PLA meshes with fibroblasts already used for cartilage defects repairing causing fibrous tissue fabrication (9).

Stem cells have been recently investigated as an alternative to autologous chondrocytes for cartilage tissue engineering (6). They are pluripotent cells that can be differentiated down multiple cell lineages given the appropriate cues. Stem cells can be extracted from different sources: bone marrow, adipose tissue, synovium, periosteum, muscle.

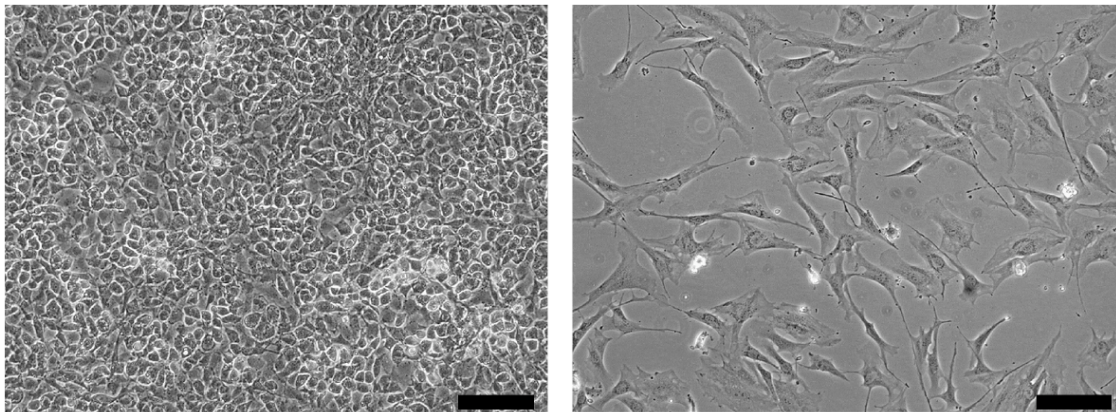


**Figure 10. Primary bovine chondrocytes (left) and bone marrow-derived bovine mesenchymal stem cells (right) morphology. The scale bar is 10 mm (6).**

### 2.1.2.2 Protein-based matrices

Matrices can be classified according to their chemical nature into protein based polymers, carbohydrate based polymers, artificial polymers and a mix of those (see Table 2). There are some matrix properties necessary in order to use these matrices biologically as tissues (see Figure 11).

<b>Protein based polymers</b>	Fibrin
	Collagen
	Gelatin
<b>Carbohydrate based polymers</b>	Polylactic acid
	Polyglycolic acid
	Hyaluronan
	Agarose
	Chitosan
<b>Artificial polymers/inorganic products</b>	Dacron (Polyethylene terephthalates)
	Teflon (Polytetrafluoroethylene)
	Carbon fibers
	Polyesterurethane
	Polybutyric acid
	Polyethylmethacrylate
	Hydroxyapatite
<b>Others</b>	Crosslinkage
	Chemical modifications
	Matrix combinations
	Material modification (foams, gels, fiber)

**Table 2. Types of biomaterials used in cartilage tissue engineering.**

There are different parameters that should be optimized in the same time for a good biological response of the artificial matrix (6, 7, 10). Porosity is an important parameter for matrix. Survival and proliferation of cells in biologic liquid medium close to implant is important for matrix implantation. A matrix should promote good adhesion of cells by the coating of some molecules onto the matrix or by their incorporation inside the matrix (6). The integration of a matrix in biological medium followed by small adverse immunological reactions indicates biocompatibility properties of the matrix. Integration



of some drugs can help in reducing adverse reactions. In some cases, the matrix should be biodegradable, destroyed by physiological fluids and replaced by natural tissue constructed in time. In other cases, the scale time of biodegradation is designed for months or years, depending on the implantation site of the matrix and the patient's age. A matrix should be biodegraded in non-toxic and non-cumulative smaller molecules, which can be easily eliminated from the human body.

Such matrices should have not only good biological properties, but also mechanical stable properties. Some matrices are needed to be more elastic; others are designed for bigger pressure and load.

Layer-by-layer technique (described below in chapter 2.5) allows constructing scaffolds which already contain layers of cells that are assembled by this technique (11-13).

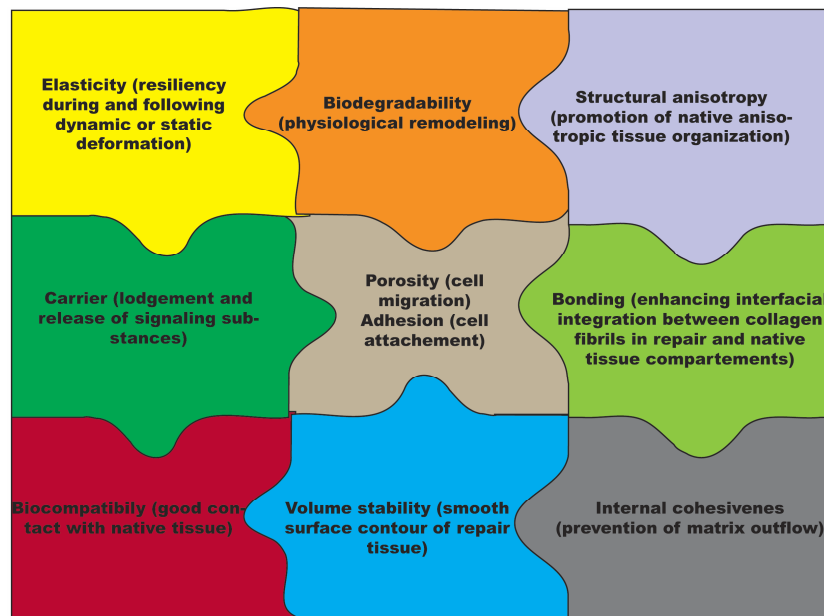


**Figure 11. Matrix requirements for the cartilage repair**

Surgery experiences on articular cartilage showed that some naked matrices (without cells or growth factors) promote spontaneous repair response in a complete and reproducible manner. After implantation of a naked porous matrix, blood penetrates inside the pores of the matrix and forms a hematoma. Spontaneous healing occurs and the volume of the matrix increases because of the hematoma formation. Cells and signaling molecules from the blood migrate in the matrix providing a good incorporation of this

matrix in damaged articular cartilage. They provide nutrients for new cartilage formation. This process of blood irrigation is stopped after a while and hematoma changes into a “dry” state. The matrix volume is decreased and its detachment from the walls of lesion should be minimized (14).

This makes it clear that the preparation of synthetic scaffolds is a very difficult and complex task without practical solution. We will take here the first step to assemble two key elements of cartilage scaffolds: Collagen and calcium phosphate.

#### **2.1.2.2.1 Collagen matrices**

Collagen matrices are usually used as carriers for allogeneic chondrocytes or mesenchymal stem or in combination with growth factors in rabbits and embryonic chondrocytes in chicken (1). Collagen matrices haven't been employed in human cartilage repair except in cosmetic facial surgery. Collagen matrix enhances the spontaneous healing response, because of cells originating from the blood and bone-marrow spaces represent a big population compared to cells originating from matrix-bone. A few studies about biocompatibility of collagen scaffolds are found in literature, however collagen is a natural polymer. The degradation of collagen produces non-toxic products.

#### **2.1.2.2.2 Gelatin matrices**

Gelatin matrices have been used just as carriers for mesenchymal stem cells but never as scaffold for enhancing the spontaneous repair in cartilage (1). Gelatin can be used as support for chondrocyte growth in vitro or in vivo.

### **2.1.3 Our approach of cartilage tissue repairing**

Articular cartilage can be divided into four zones: superficial, transitional, middle and calcified based on differences in matrix morphology and biochemistry. Each zone is divided into three distinct regions: pericellular, territorial and inter-territorial zone.

The superficial zone is the thinnest zone; it is made of two distinct layers. The deep layer is composed of flattened chondrocytes with their long axes parallel to the articular surface. The exterior layer contains mostly the collagen fibers aligned parallel to the

surface. The extracellular matrix (ECM) in this zone contains more collagen and less proteoglycan; and large amounts of Fibronectin and water.

The transitional zone contains spherical chondrocytes. The ECM analyzed shows larger collagen fibrils, more proteoglycans, less collagen and water.

The middle (or radial) zone has the largest diameter collagen fibrils, the most proteoglycans, the least water and it occupies the biggest volume of cartilage. The cells are round but stacked in a different way that in the transitional zone.

The calcified cartilage zone is closet to bone tissue and allows the transition from soft to hard regions. The cells are smaller in this region. The ECM is calcified.

Our model takes into account the stratification of natural cartilage. We proposed a model based on multilayers units construction. There are units that contain polymer multilayers impregnated with various growth factors, alginate gels embedded with chondrocytes or inorganic layers.

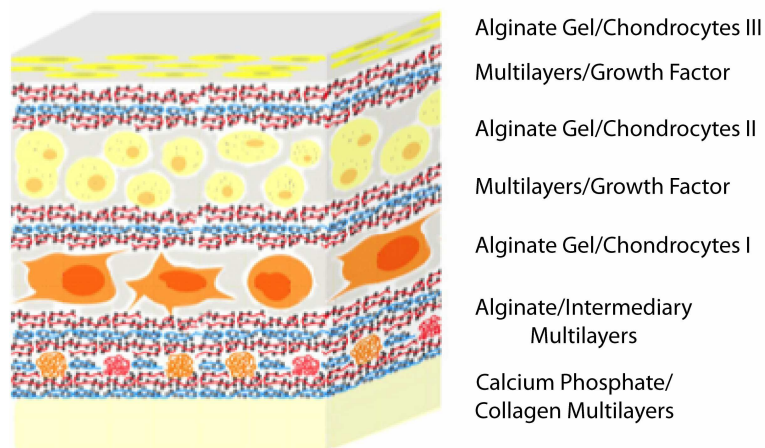


**Figure 12. Our cartilage scaffold model**

The main project was divided into two secondary projects:

- Project A that incorporates the upper part of artificial cartilage fabrication with alginate gels and chondrocytes and natural polymers multilayer construction
- Project B that contains the bottom part of tissue that “sticks” to the bone. It explores the inorganic layers and collagen multilayers.

### 2.1.3.1 The project A

The project A was realized in the group of Jean-Claude Voegel by PhD. Hajare Mjehed. They reported the construction of micro-stratified 3D scaffolds constituted of alternating strata of alginate gels (AGLs) and polymeric multilayer films based on poly (L-lysine) (PLL) and hyaluronic acid (HA) (15).

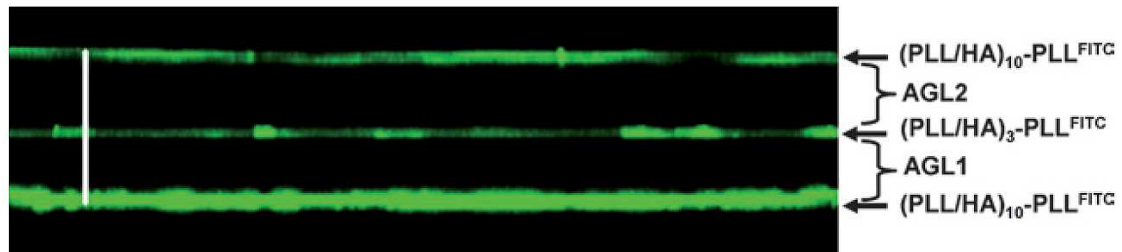


**Figure 13.** Vertical section image observed by Confocal Laser Scanning Microscope (CLSM) of  $(\text{PLL-HA})_{10}\text{-PLL}^{\text{FITC}}\text{-AGL1-(PLL-HA)}_3\text{-PLL}^{\text{FITC}}\text{-AGL2-(PLL-HA)}_{10}\text{-PLL}^{\text{FITC}}$  architecture. AGL1 and AGL2 were obtained by spraying (10 s) and by dipping of the architecture in a 0.05 M  $\text{CaCl}_2$  solution (2 h).  $(\text{PLL-HA})_{10}\text{-PLL}^{\text{FITC}}$  precursor film was built in 0.15 M NaCl solution.  $(\text{PLL-HA})_3\text{-PLL}^{\text{FITC}}$  intermediary film and  $(\text{PLL-HA})_{10}\text{-PLL}^{\text{FITC}}$  final film were built in a 0.05 M  $\text{CaCl}_2$  solution The scale bar represents 60  $\mu\text{m}$ .

AGLs are obtained by complexation of alginate by  $\text{Ca}^{2+}$  ions. After alginate solutions are sprayed, a  $\text{CaCl}_2$  solution is then either sprayed onto the substrate or the substrate is dipped into a  $\text{CaCl}_2$  solution. They observed a micro-porosity of AGLs by spraying the  $\text{CaCl}_2$ , whereas the dipping in a  $\text{CaCl}_2$  aqueous solution leads to a more homogeneous gel layer. The dipping process also allows the formation of AGLs with a controlled thickness.

The next steps for the scaffold design fabrication are the incorporation of chondrocytes in the AGL (3D scaffold) and the filling of the PLL-HA multilayers (should act as reservoirs) with biologically active molecules.

During this project an interesting phenomenon of hole formation was discovered in the exponentially growing multilayer films (PLL-HA). An increase of ionic strength induces the hole formation inside the polyelectrolyte multilayered films (16).

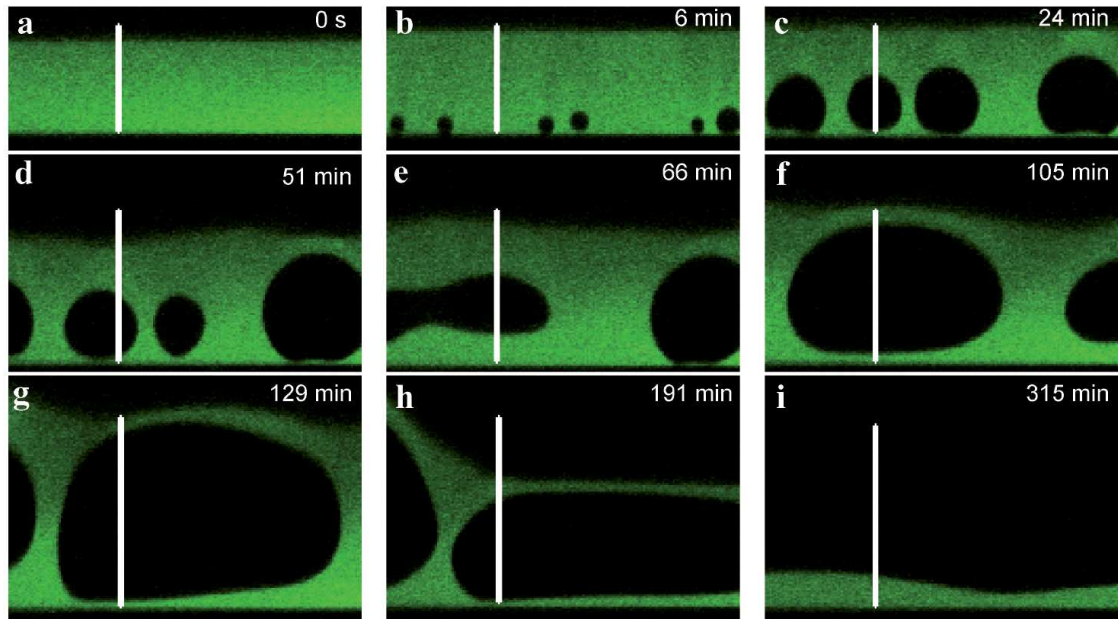


**Figure 14.** Vertical section images observed by CLSM of a  $(\text{PLL}/\text{HA})_{50}\text{-PLL}^{\text{FITC}}$  film built in 0.15 M NaCl and progressively swelled by contact with solutions of increasing NaCl concentrations up to 0.48 M, followed as a function of time. The scale bars represent 50  $\mu\text{m}$  for images a, b and c, 60  $\mu\text{m}$  for images d, e and f, and 80  $\mu\text{m}$  for images g, h and i.

### 2.1.3.2 The project B

The part B of the project is this PhD work. The main goal of this work is the fabrication of hybrid films containing Collagen and hydroxyapatite (calcium phosphate) (for more details, see the results presented in the chapter 4).

## 2.2 Collagen

In both tissues: cartilage and bone, a major constituent is the fibril-forming collagen. A major component presented only in cartilage is the proteoglycan that has an important role in distributing loads, flexibility and low friction surface in joints. Most cartilage never calcifies, whereas bone contains a predominant component that is the mineral matrix, which allows the tissue to be rigid.

### **2.2.1 Collagen. Structure, type, applications**

Collagen represents the main structural protein accounting for approximately 30% of all vertebrate body protein. The Collagen content in extracellular protein in tendon and bone is more than 90% and more than 50% in the skin (17, 18). Currently at least 20 distinct human collagens are known, the most abundant being found in fibrils with an axial 67 nm periodicity (8). The Collagen molecule consists of a unique triple- helix configuration of three polypeptide chains known as  $\alpha$ -chains.

Type I collagen is predominant especially in the skin, tendon and bone where extreme forces are transmitted. It is composed of three chains, two of them are identical ( $\alpha 1(I)$ ) and one that has a different amino-acid composition ( $\alpha 2(I)$ ). Rarely, all three chains are similar representing a trimer ( $\alpha 1(I)_3$ ). Type II collagen is particularly found in hyaline cartilage and the structure of the amino-acid chain  $\alpha 1(II)$  is similar to  $\alpha 1(I)$ . Limited quantities (10%) of type III collagen are associated with type I collagen and it is mainly located in blood vessels. It is possible to find impurities of collagen III in the collagen I produced from the skin (18, 19).

Collagen type	Chain composition	Tissue distribution
I	$(\alpha 1(I))_2\alpha 2(I)$ , trimer $(\alpha 1(I))_3$	Skin, tendon, bone, cornea, dentin, fibrocartilage, large vessels, intestine, uterus, dentin, dermis, tendon
II	$(\alpha 1(II))_3$	Hyaline cartilage, vitreous, nucleus pulposus, notochord
III	$(\alpha 1(III))_3$	Large vessels, uterine wall, dermis, intestine, heart valve, gingival (usually coexists with type I except in bone, tendon, cornea)
IV	$(\alpha 1(IV))_2\alpha 2(IV)$	Basement membranes
V	$\alpha 1(V)\alpha 2(V)(3(V))$ or $(\alpha 1(V))_2\alpha 2(V)$ or $(\alpha 1(V))_3$	Cornea, placental membranes, bone, large vessels, hyaline cartilage, gingiva
VI	$\alpha 1(VI)\alpha 2(VI)\alpha 3(VI)$	Descemet's membrane, skin, nucleus pulposus, heart muscle
VII	$(\alpha 1(VII))_3$	Skin, placenta, lung, cartilage, cornea
VIII	$\alpha 1(VIII)\alpha 2(VIII)$ chain organization of helix unknown	Produced by endothelial cells, Descemet's membrane
IX	$\alpha 1(IX)\alpha 2(IX)\alpha 3(IX)$	Cartilage
X	$(\alpha 1(X))_3$	Hypertrophic and mineralizing cartilage
XI	$\alpha 1\alpha 2\alpha 3$ or $\alpha 1(XI)\alpha 2(XI)\alpha 3(XI)$	Cartilage, intervertebral disc, vitreous humour
XII	$(\alpha 1(XII))_3$	Chicken embryo tendon, bovine periodontal ligament
XIII	Unknown	Cetal skin, bone, intestinal mucosa

Figure 15. Chain composition and body distribution of collagen types (18, 20).

Type I, II, III, V and IX are built up of three chains that form a triple-helix structure. Type I, II, III and V are called fibril forming collagens and have large sections of homologous sequences independent of species (21). Type IV collagen (membrane basement) has triple-helical conformational regions interrupted by short non-helical conformational regions.

The molecular structure of collagen has been established from earlier studies, such as amino-acid composition analysis, X-ray diffraction analysis, electron microscopy and physicochemical characterization of solutions (22-24). The basic collagen molecule contains the three  $\alpha$ -chains of polypeptide with more than 1000 amino acids each. There are only minor differences between the collagen from different vertebrate species (18, 25).

The repetitive Gly-X-Y triplet, where X can be another amino acid but is generally a proline and Y is usually hydroxyproline, allows the tight triple helix configuration (20, 22, 26). Glycine has the smallest side group that can occupy the limited space in the center of the triple helix. The three main amino acids (glycine, proline, hydroxyproline) account for more than 50% of the total amino acids content (8, 17, 20, 21). The various levels of order observed in collagen are illustrated in Figure 16. The  $\alpha$ -chains combine to form left-handed helices with 3.3 residues per turn and a pitch of 0.87 nm as identified by X-ray analysis (Figure 16b).



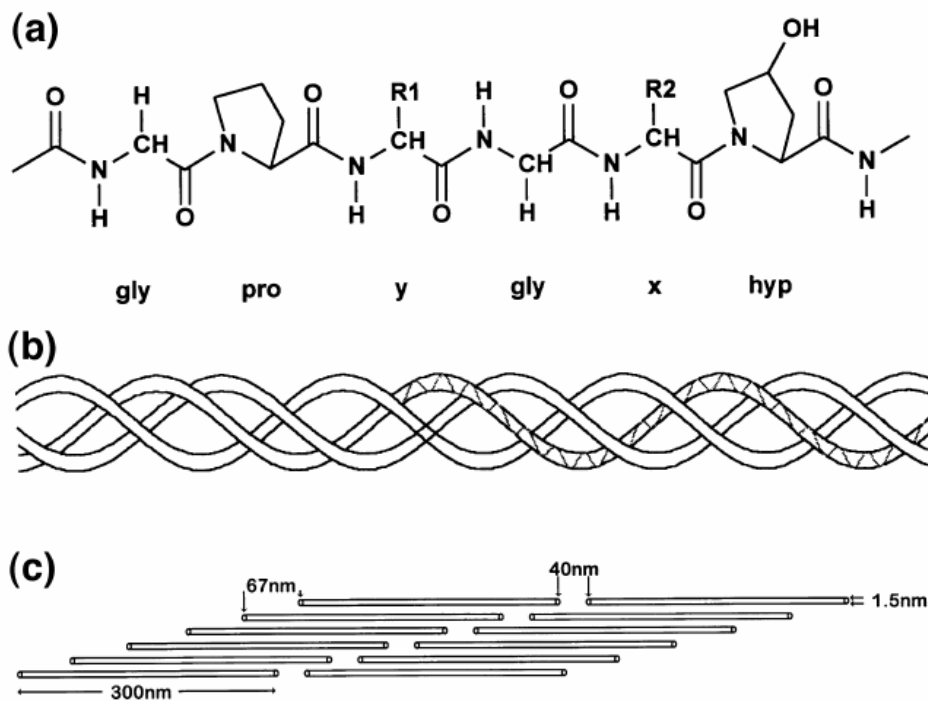


**Figure 16. The chemical structure of collagen type I. (a) Primary amino acid sequence, (b) secondary left handed helix and tertiary right handed triple- helix structure and (c) staggered quaternary structure.**

The tertiary structure refers to the fundamental unit also known as tropocollagen: three polypeptide chains intertwined to form a right-handed triple-helix with a pitch of approximately 8.6 nm. The rod-shaped triple helix has an average molecular weight of approximately 300 kDa, a length of 300 nm with a diameter of 1.5 nm (Figure 16c)(18). There are non-helical regions denoted as telopeptides formed of 9–26 amino acids at the terminal chain ends of the molecule that are not incorporated into the helical structure.

The collagen fibrils reach from 10 to 500 nm in diameter depending on the tissue type and the stage of development. The triple-helices are staggered by 67 nm with an additional gap of 40 nm between succeeding molecules. These collagen fibrils organize into fibers, which on their part can form even larger fiber bundles.

In 1982, Privalov underlined the important role of enthalpy and hydrogen bonding in the stabilization of the collagen triple helix (20).

Water molecules may bond two carbonyl groups or they may link one carbonyl group with a hydroxyl group of hydroxyproline (Figure 17). The number of waters involved in bridging two groups appears to vary along the molecule, such that two, three, four, or even five water molecules may form a chain linking the two groups.

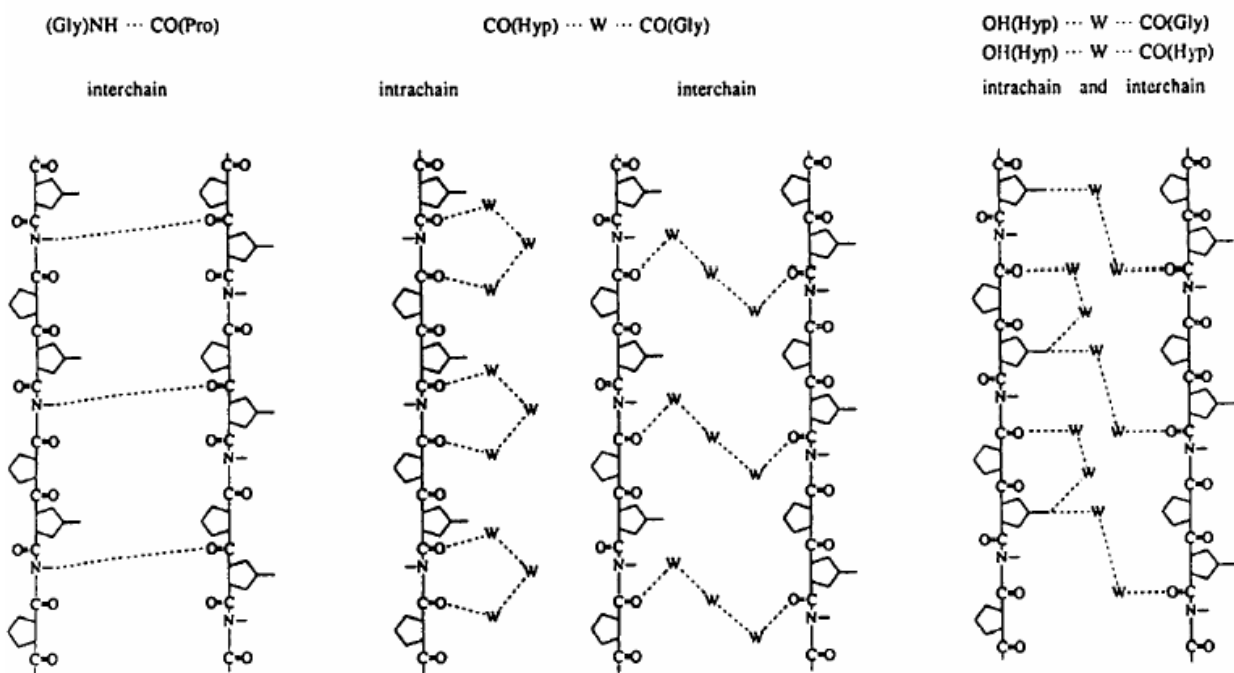


**Figure 17.** A schematic drawing illustrating the types of hydrogen bonding patterns found in the triple-helix: (a) direct peptide group hydrogen bonding; (b) water mediated hydrogen bonding linking carbonyl groups; and (c) water mediated hydrogen bonding linking hydroxyproline OH groups and carbonyl groups. Variations in the number of water molecules linking the groups shown in (b) and (c) are seen in the crystal structure, and the water-mediated hydrogen bonds shown are not fully occupied (27).

Collagen, a natural polymer, is largely used as a biomaterial with a low immunogenicity and is therefore seen by the body as a normal constituent rather than foreign matter. In the Table 3, major characteristics (advantages and drawbacks) (19, 28) are summarized:

Advantages	Disadvantages
<ul style="list-style-type: none"> <li>• Available in abundance and easily purified from living organisms (constitutes more than 30% of vertebrate tissues);</li> <li>• Non-antigenic;</li> <li>• Biodegradable and bioreabsorbable;</li> <li>• Non-toxic and biocompatible;</li> <li>• Synergic with bioactive components;</li> <li>• Biological plastic due to high tensile strength and minimal expressibility;</li> <li>• Hemostatic — promotes blood coagulation;</li> <li>• Formulated in a number of different forms;</li> <li>• Biodegradability can be regulated by cross-linking;</li> <li>• Easily modifiable to produce materials as desired by using its functional groups;</li> <li>• Compatible with synthetic polymers;</li> </ul>	<ul style="list-style-type: none"> <li>• High cost of pure type I collagen;</li> <li>• Variability of isolated collagen (e.g. crosslink density, fiber size, trace impurities, etc.);</li> <li>• Hydrophilicity which leads to swelling and more rapid release;</li> <li>• Variability in enzymatic degradation rate as compared with hydrolytic degradation;</li> <li>• Complex handling properties;</li> <li>• Side effects, such as bovine spongiform encephalopathy (BSF) and mineralization</li> </ul>

**Table 3. Collagen (advantages and disadvantages) (18, 29, 30).**

The nonhelical telopeptides can be removed from the collagen molecule by using pepsin, atelocollagen is produced. The source of antigenicity (caused by telopeptides) is eliminated. And the atelocollagen has demonstrated potential application as drug delivering agent, especially for gene delivery (28, 31, 32).

Collagen can be processed into a number of forms such as sheets, tubes, sponges, powders, fleeces, injectable solutions and dispersions, all of which have found use in medical practice. The collagen biomaterials are applied as numerous systems for drug

delivery in a variety of applications such as ophthalmology (form: insert, shield, particle, gel, solution), wound and burn dressing, tumor treatment, and tissue engineering.

### **2.3 Hydroxyapatite**

Calcium phosphate crystallizes in various crystal structures (polymorphs) with different mechanical, thermal and chemical properties. Important parameters are the molar Ca/P ratio and the solubility (Table 4). Generally, the lower the Ca/P ratio is, the more acidic and soluble in water the calcium phosphate is.

The chemical composition of hydroxyapatite is roughly equivalent to that of the inorganic matrix of the human bone and is extensively used in the bone tissue engineering (33). The main component found in bone is hydroxyapatite (HAP,  $\text{Ca}_{10}(\text{PO}_4)_6(\text{OH})_2$ ), but there are some other common phases explored as well: octacalcium phosphate (OCP), tricalcium phosphate (TCP), dicalcium phosphate dihydrate (DCPD) and dicalcium phosphate (DCP).

Polymorph <sup>a)</sup> (Common name)	Chemical formula (Crystal system)	Synthesis from aq. solution at ambient cond.	pH of formation	Precursor for	Typical shape	Solubility product	Ca/P ratio
ACP <sup>b)</sup>	Ca <sub>3</sub> (PO <sub>4</sub> ) <sub>2</sub> · nH <sub>2</sub> O (N/A)	yes	all	all crystalline phases	beads		1.5
DCPD <sup>c)</sup> (brushite)	CaHPO <sub>4</sub> · 2H <sub>2</sub> O (monoclinic, C2/c)	yes	acidic (<4–5)	HAP monetite	large plates	1.87 × 10 <sup>-7</sup> (mol · L <sup>-1</sup> ) <sup>2</sup>	1
DCPA (monetite)	CaHPO <sub>4</sub> (triclinic, P1)	yes	acidic (<4–5)	brushite apatite	plates	9.2 × 10 <sup>-7</sup> (mol · L <sup>-1</sup> ) <sup>2</sup>	1
α-TCP <sup>d)</sup> (whitlockite)	Ca <sub>3</sub> (PO <sub>4</sub> ) <sub>2</sub>	no <sup>n)</sup>	basic				1.5
β-TCP <sup>e)</sup>	Ca <sub>3</sub> (PO <sub>4</sub> ) <sub>2</sub>	no <sup>n)</sup>	basic			2.8 × 10 <sup>-29</sup> (mol · L <sup>-1</sup> ) <sup>5</sup>	1.5
OCP <sup>f)</sup>	Ca <sub>8</sub> H <sub>2</sub> (PO <sub>4</sub> ) <sub>6</sub> · 5H <sub>2</sub> O (triclinic, P1)	yes	acidic (<5–6)	HAP		2.5 × 10 <sup>-99</sup> (mol · L <sup>-1</sup> ) <sup>8</sup>	1.33
HAP <sup>g)</sup> (hydroxyapatite)	Ca <sub>5</sub> (OH)(PO <sub>4</sub> ) <sub>3</sub> (hexagonal, P63/m) <sup>l)</sup> (monoclinic) <sup>m)</sup>	yes	basic (>7)	OXA	needles	5.5 × 10 <sup>-118</sup> (mol · L <sup>-1</sup> ) <sup>9</sup>	1.7
CIAP (chloroapatite)	Ca <sub>5</sub> (Cl)(PO <sub>4</sub> ) <sub>3</sub> (hexagonal, P63/m)	yes	basic (>7)		needles		1.7
FAP <sup>h)</sup> (fluoroapatite)	Ca <sub>5</sub> (F)(PO <sub>4</sub> ) <sub>3</sub> (hexagonal, P63/m)	yes	basic (>7)		needles	5.0 × 10 <sup>-123</sup> (mol · L <sup>-1</sup> ) <sup>9</sup>	1.7
TTCP (hilgenstockite)	Ca <sub>4</sub> O(PO <sub>4</sub> ) <sub>2</sub>		basic	HAP			2
OXA <sup>i)</sup>	Ca <sub>10</sub> O(PO <sub>4</sub> ) <sub>6</sub>	no <sup>n)</sup>	basic				1.7
MCP <sup>j)</sup>	CaH <sub>4</sub> (PO <sub>4</sub> ) <sub>2</sub>	no <sup>o)</sup>	acidic				0.5
MCPM <sup>k)</sup>	CaH <sub>4</sub> (PO <sub>4</sub> ) <sub>2</sub> · H <sub>2</sub> O		acidic				0.5

**Table 4. Calcium phosphate polymorphs properties.** a) ACP: amorphous CaP; DCPD: dicalcium phosphate dihydrate; DCPA: dicalcium phosphate anhydrous; TCP: tricalcium phosphate; OCP: octacalcium phosphate; HAP: hydroxyapatite; CIAP: Chloroapatite; FAP: Fluoroapatite; TTCP: tetracalcium phosphate; OXA: oxyapatite; MCP: monocalcium phosphate; MCPM: monocalcium phosphate monohydrate; b) Two discrete forms ACP1 and ACP2; c) Large crystal face is 010; d) Widely used as bone substitute; e) Stabilized by magnesium ions; f) Layered structure (apatitic and hydrated layers); g) Major inorganic component in bone and teeth; h) Highly stable in acid, favored over HAP at pH<6; i) Decomposition product of HAP, water soluble; j) Highly water soluble; k) Water soluble; l) Biological form; m) More stable than the biological form; n) High temperature synthesis; o) High-temperature synthesis (>500 °C).

DCPD (the mineral name brushite) can be easily synthesized from aqueous solutions. It can be transformed into an anhydrous state (DCP) at temperatures above 80°C. Brushite is a compound of biological importance because it is often found in pathological calcifications (dental calculi, crystalluria, urinary stones) (34, 35). DCPD has been

proposed as an intermediate in the process of bone mineralization and the dissolution of enamel in acids (dental caries) (36, 37). DCPD is used in the field of clinical surgeries in the composition of calcium phosphate cements. It is a constituent of toothpaste in dentistry and in combination with fluoride-containing compounds (e.g. NaF) for the protection against caries. Other applications are in calcium supplements in food, mineral supplements in cereals, fertilizers, glass production (36).

Hydroxyapatite (HA) is the main mineral constituent of teeth and bones and it is forming together with collagen molecules mineralized collagen fibrils. They are forming the mineralized building blocks of 80-100 nm thickness and a few tens of microns in length (Figure 18). Contrary to metals or bio-inert ceramics, where an encapsulation takes place, HA is not only biocompatible but it is also bioactive. HAP ceramics does not exhibit any cytotoxic effects.

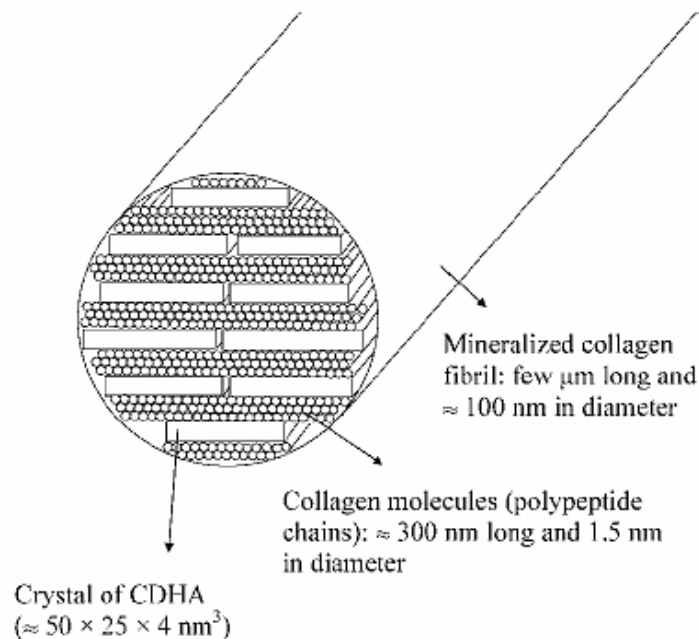


**Figure 18.** Schematic drawing of the mineralized collagen fibrils (10, 26, 38) that are the basic constituents of bone. Platelet-shaped nanocrystals of CDHA (calcium deficient hydroxyapatite that is characterized by substitutions of calcium, hydroxide and phosphate ions with others species (substitution of  $\text{Ca}^{2+}$  with  $\text{Na}^+$ ,  $\text{K}^+$ ,  $\text{Mg}^{2+}$ ,  $\text{Sr}^{2+}$ ; substitution of phosphate with carbonate; substitution of hydroxide ions with fluoride, chloride, carbonate) are incorporated in a parallel way between collagen molecules, with the crystallographic c axis parallel to the fiber axis.

The incorporation of impurities in the HAP structure as partial substitution of hydroxide by fluoride or chloride ions stabilizes the HAP hexagonal structure at room temperature. Multiple techniques have been used for HAP synthesis, they can be divided into two main ways: wet methods and solid-state techniques. The wet methods can be classified in three classes: precipitation, hydrothermal technique and hydrolysis of other calcium phosphates. Depending on the HAP preparation method applied, it is possible to change the morphology, the stoichiometry or the level of crystallinity. Solid state reactions usually give a stoichiometric and well-crystallized product, but with drawbacks like relative high temperature and long calcinations time needed for fabrication.

The temperature of precipitation is usually not higher than 100°C and nanometric size crystals can be obtained. Aqueous solutions at pH>9 (Calcium containing and Phosphate containing) with stoichiometric Ca/P ratio are heated for several days under a CO<sub>2</sub> free atmosphere, then filtered and dried. They can have various shapes particles, needles, rods or blades. Their crystallinity and Ca/P ratio depend strongly upon preparation parameters, but generally are lower than those for well-crystallized stoichiometric HAP.

The hydrothermal methods are usually used for the synthesis of HAP ceramics with higher degree of crystallinity and a Ca/P ratio close to the stoichiometric value. The size range for crystals prepared by hydrothermal technique is large from nanometers to micrometers.

The HAP fabrication by hydrolysis of other calcium phosphates (tricalcium phosphate, monetite, brushite, or octacalcium phosphate) requires low temperatures and results in HAP needles or blades having the size of microns. However, in most cases, the hydrolysis product is highly non stoichiometric (33, 39).

Pure HAP never occurs in biological systems. However, because of the chemical similarities to bone and teeth, HAP is used as coating for orthopedic, dental implants, cements in surgery or in liquid chromatography of proteins and other biological compounds.

## ***2.4 Film deposition techniques***

Since the mid-1990s the number of film products has increased, including applications as photovoltaic, energy conversion, energy efficiency, biomedical, pharmaceutical, and flat panel displays. Furthermore, coatings are no longer limited to the traditional applications associated with wear and corrosion. The demand for advanced optical thin film coatings including optical components, telecommunications, windows glazing, large area and decorative applications, laser mirrors, ophthalmic applications, and aircraft windows has also increased. The global market for solar cells will increase due to the increased renewable energy demands, increased efficiency of organic and transparent solar cells, and low-cost solar concentrator systems. Additional energy applications for thin films like photocatalytic coatings, thin film fuel cells, thin film lithium batteries, electrochromic and thermochromic coatings, and solar control coatings have also increased. Nowadays, the production of advanced wear- and corrosion-resistant materials allows the development of new medical implants or combustion and gas turbine engines (40).

Another main cause for the rapid growth of deposition technology is the improved knowledge of the physics and chemistry of films, surfaces, interfaces, and microstructures realized by the amazing advances in analytical instrumentation during the past thirty years.

For example the semiconductor industry is totally dependent on the preparation of thin solid films that can be deposited from the gas, vapor, liquid, or solid phase. The semiconductor device technology is frequently very complex. There are different deposition techniques involved like molecular beam epitaxy, chemical vapor deposition, spin-on deposition and others in the alternate film deposition of materials.



### 2.4.1 Thin-Film Applications

The main coating applications may be classified into the following generic categories:

**Electronic Components.** The fabrications of electronic components have found the widest and most demanding applications for thin film depositions. Semiconductor materials, dielectric and insulating materials, metal or refractory metal silicide conductors are crucial coatings found in the electronic device composition.

**Electronic Displays.** Different components and device structures are produced, such as: liquid-crystal displays, light-emitting diodes (LEDs), electroluminescent displays, plasma and fluorescent displays, electrochromic displays.

These displays are based on thin films such as conductive films, transparent and conductive films, small organic molecule doping materials, luminescent or fluorescent films, dielectric and insulating layers.

**Optical Coatings.** Interference filters on solar panels, infrared solar reflectors and for laser optics are a few of the optical antireflection coating applications. The fabrication of these optical coatings requires thin films with refractive index gradients, dielectric materials with precisely defined indices of refraction and absorption coefficients, metal reflective coatings or infrared reflecting coatings.

**Magnetic and Optical Films for Data Storage.** The substrates of magnetic films can be metal, glass or plastic polymeric materials. The thin optical films for optical data storage devices in compact disks and computer memory applications market is increasing since the personal computer appearance.

**Antistatic Coatings.** Thin films of conductive or semiconductive materials are deposited to provide protection from electrostatic discharges.

**Hard Surface Coatings.** The fabrication of cutting tools, automotive engine requires thin films of carbides, silicides, nitrides, and borides, which improve the wear characteristics of metal surfaces. The diamond-like carbon films have found wide industrial applications due to high heat dissipation properties, electrical insulation, hardness, and resistance to high-temperature and high-energy radiation.

	Electro-plating	CVD, PECVD ALD	Vapor phase MBE	Anodization	Thermal	Evaporation	Sputtering	VPD
Conductors resistors	Orange	Green	Orange			Green	Orange	
Insulators Capacitors		Green	Orange	Green	Orange	Green	Green	
Active devices		Green	Green			Orange	Orange	
Magnetic materials	Green					Orange	Green	
Super-conductors		Green	Orange			Green	Orange	
Encapsulation		Orange					Orange	Green

**Figure 19. Applicability of preparation methods to microelectronics. Orange color indicates that the component can be prepared by the method; green color indicates that the method is widely used (41).**

The selection of a particular deposition process depends on several factors, such as: material to be deposited, limitations imposed by the substrate (e.g. material, size), temperature stability, specific application, deposition rate, adhesion of film to substrate, throwing power, purity of source material, apparatus required and availability of these apparatus, cost, safety considerations, e.g. toxicity, process stability, manufacturing considerations, (e.g. batch size, throughput, process controls), abundance of source materials.

Usually one deposition technique cannot meet all of the requirements and more than one technique can be used to deposit a given material. As a result, many thin film materials are currently prepared using hybrid processes (41).

## **2.4.2 Classifications of deposition process**

There are many deposition techniques for material formation. There are several classifications of deposition process. One classification is based on the type of interactions which create the thin film deposition process. Principally, the thin-film deposition technologies are either purely physical (e.g. evaporative process) or purely chemical, (e.g. gas- and liquid-phase chemical processes). There are a considerable number of processes that are based on both physical and chemical reactions (e.g. glow discharges and reactive sputtering).

A classification scheme is presented in Table 5. The thin-film deposition techniques are classified into four categories: evaporative glow discharge, glow discharges, gas-phase chemical and liquid-phase chemical processes.

Evaporative methods	Glow discharge methods	Gas-phase chemical methods	Liquid-phase chemical methods
<ul style="list-style-type: none"> <li>• <b>Vacuum Evaporation</b></li> <li>○ Conventional vacuum evaporation</li> <li>○ Electron-beam evaporation</li> <li>○ Molecular-beam epitaxy (MBE)</li> <li>○ Reactive evaporation</li> </ul>	<ul style="list-style-type: none"> <li>• <b>Sputtering</b></li> <li>○ Diode sputtering</li> <li>○ Reactive sputtering</li> <li>○ Bias sputtering (ion plating)</li> <li>○ Magnetron sputtering</li> <li>○ Ion beam deposition</li> <li>○ Ion beam sputter deposition</li> <li>○ Reactive ion plating</li> <li>○ Cluster beam deposition (CBD)</li> <li>• <b>Plasma Processes</b></li> <li>○ Plasma-enhanced CVD</li> <li>○ Plasma oxidation</li> <li>○ Plasma anodization</li> <li>○ Plasma polymerization</li> <li>○ Plasma nitridation</li> <li>○ Plasma reduction</li> <li>○ Microwave ECR plasma CVD</li> <li>○ Cathodic arc deposition</li> </ul>	<ul style="list-style-type: none"> <li>• <b>Chemical Vapor Deposition (CVD)</b></li> <li>○ CVD epitaxy</li> <li>○ Atmospheric-pressure CVD (APCVD)</li> <li>○ Low-pressure CVD (LPCVD)</li> <li>○ Photo-enhanced CVD (PHCVD)</li> <li>○ Laser-induced CVD (PCVD)</li> <li>○ Electron-enhanced CVD</li> <li>○ Metalorganic CVD (MOCVD)</li> <li>○ Atomic layer deposition (ALD)</li> <li>• <b>Thermal Forming Processes</b></li> <li>○ Thermal oxidation</li> <li>○ Thermal nitridation</li> <li>○ Thermal polymerization</li> <li>○ Ion implantation</li> </ul>	<ul style="list-style-type: none"> <li>• <b>Electro Processes</b></li> <li>○ Electroplating</li> <li>○ Electroless plating</li> <li>○ Electrolytic anodization</li> <li>○ Chemical reduction plating</li> <li>○ Chemical displacement plating</li> <li>○ Electrophoretic deposition</li> <li>• <b>Mechanical Techniques</b></li> <li>○ Spray pyrolysis</li> <li>○ Spray-on techniques</li> <li>○ Spin-on techniques</li> <li>○ Liquid phase epitaxy</li> </ul>

**Table 5. Classification of thin film deposition technologies**

### 2.4.2.1 Evaporative Methods

**Thermal evaporation** or **vacuum evaporation**, one of the oldest techniques used for depositing thin films, requires a vapor that is generated by boiling or subliming a source material. The vapor is then transported from the source to the substrate, where it is condensed into a solid film on the substrate surface. Resistance-heated filaments, electron beams, conduction, radiation, RF-induction, arcs, exploding wires, and lasers cause the boiling of materials.

**Molecular Beam Epitaxy (MBE)** is a sophisticated controlled method for growing single-crystal epitaxial (extreme regular) films under high vacuum ( $10^{-11}$  torr).

**Reactive Evaporation** is a process in which a reactive gas is added to the vacuum chamber so that the gas reacts chemically with the evaporating material for the deposition of a film onto the substrate.

### 2.4.2.2 Glow Discharge Methods

Glow Discharge Evaporation and Sputtering are processes performed under soft vacuum ( $10^{-2} - 10^{-1}$  torr), in precise pressure range and precise source–substrate distance.

**Sputtering** is the most well-known glow discharge process. Bombarding with reactive species ejects the surface atoms. The sputtering method is used in the microelectronic devices industry as an etching process such as for the surface cleaning and the pattern delineation. It is more frequently used as a method of film deposition like the evaporative deposition method.

**Diode sputtering** uses the cathode electrode as target material to be deposited in a glow discharge. The material can thus be transported from the target to a substrate to form a film. The films that can be deposited using noble gas discharges (usually Argon) with metal targets are pure metals or alloys.

**Ion Plating** is a coating process in which the film deposition is continuously or periodically bombarded by energetic atomic-sized inert or reactive particles that can

affect the growth and properties of the film. The source of depositing atoms may be from sputtering, vacuum evaporation, or chemical vapor precursor.

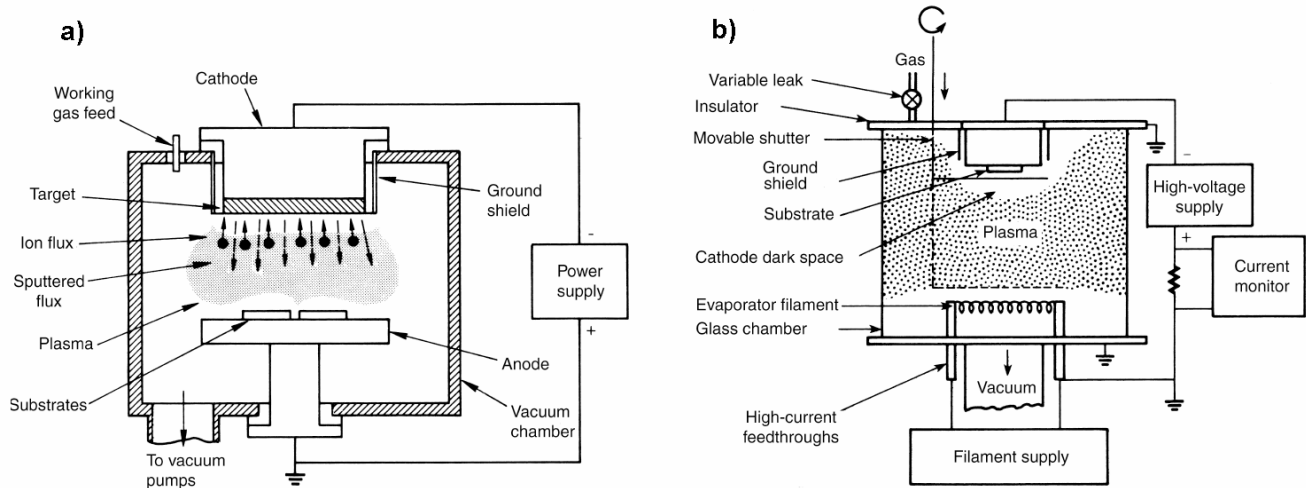


Figure 20. a) Typical sputter coating process, b) Schematic representation of an ion plating process

**Reactive Ion Plating** happens when partial pressure of a reactive gas reacts with the sputtered material to form a compound surface coating.

**Plasma deposition** is a combination of a glow-discharge process and low-pressure chemical vapor deposition. It can be classified into both categories. Typical plasma contains a number of electrons with sufficient energy to dissociate a molecule. The probability of dissociation is 10 to 100 times larger than the probability of ionization. The plasma produces even for a modest fractional ionization a large supply of excited and dissociated molecules and thus reactive radicals.

The complete and detailed plasma deposition process is extremely complex since the detailed interactions of plasma chemistry, plasma physics, and possible synergistic effects are still largely unexplained. But once the fundamentals and engineering technology are fully understood, the plasma deposition process offers great possibilities for film formation.

### 2.4.2.3 Gas-Phase Chemical Methods

**Chemical Vapor Deposition (CVD)** is a process in which the substrate is exposed to one or more volatile precursors, which react chemically near or on the substrate surface to form a thin film. The basic chemical reactions that take place in a CVD process include pyrolysis (thermal decomposition), oxidation, reduction, hydrolysis, nitride and carbide formation, and synthesis reactions. Most CVD processes are chosen to be heterogeneous reactions. The deposition rate and the properties of the deposited film can be tuned by the variation of parameters such as temperature, pressure, input concentrations, gas flow rates, reactor geometry or operating principle.

**Plasma-Enhanced Chemical Vapor Deposition (PECVD)** is a form of CVD that involves creation of the reacting gases by plasma and then depositing them onto the substrate.

**Atomic Layer Deposition (ALD)** is a sequential surface chemistry that deposits conformal thin films of materials onto substrates of varying compositions. ALD film growth is self-limited and based on surface reactions. Atomic scale deposition control can be achieved. ALD is similar in chemistry to CVD.

### 2.4.2.4 Liquid-Phase Chemical Methods

The growth of inorganic thin films from liquid phases by chemical reactions is realized primarily by electrochemical processes (which include anodization, electrophoretic deposition and electroplating), and by chemical deposition processes (which include reduction plating, chemical reduction plating, electroless plating, conversion coating, and displacement deposition). Other liquid phase chemical deposition techniques are accomplished by mechanical techniques that include spray pyrolysis, spray-on and spin-on techniques and liquid phase epitaxy.

**Electrostatic (or electro spraying) deposition** technique is a deposition technique in which the liquid material is atomized and charged, then directly deposited onto the substrate using an electrostatic field.

**Electrolytic deposition (electroplating)** is primarily concerned with the deposition of ions rather than colloidal particles (as electrophoretic deposition). Two electrodes are immersed in an electrolyte containing an ionic salt, which dissociates in aqueous solution into its constituent ions. The deposition of the positive ions takes place onto the cathode. The coating deposition control can be realized by the variation of important electroplating variables including current efficiency, current density, current distribution, pH, temperature, agitation, and solution composition.

Wetting processes are typically pure physical processes in which material is applied in liquid form and then becomes solid by solvent evaporation, spinning, curing, baking, or cooling.

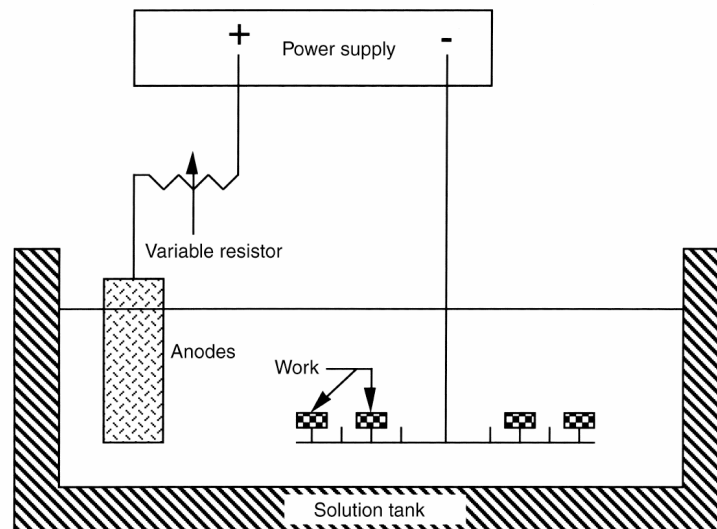


**Figure 21. Schematic of a typical electroplating process**

Conventional **dip coating** is a wetting processes in which the substrate to be coated is dipped into the liquid under controlled conditions of deposition (such as withdrawal rate, temperature).

**Spin coating** is a process used to apply uniform coating to flat substrates in which the substrate is then rotated at high speed in order to spread the fluid by centrifugal forces. The applied solvent is usually volatile, and simultaneously evaporates. The higher the angular speed of spinning is the thinner the film will be.



**Liquid spray coating** is probably the most versatile mechanical coating technique of the deposition techniques noted, and it is particularly well suited for high-speed automated mass production. The spraying processes are presented in more details in chapter 2.

**Ink Jet Printing** (a form of spray) is a process that operates by controlling the production of variable sized (nanometer to micrometer size) droplets of liquid or molten material (ink) onto almost any medium.

**Thermal spray** is a common deposition technique for the metallic or nonmetallic coatings. It can be grouped into three major categories: flame spray, electric arc spray, and plasma arc spray. These energy sources are used to heat the coating material (in powder, wire, or rod form) to a molten or semi-molten state (Table 6).

Vacuum methods well developed but solution based methods see rapid recent development. One of these powerful techniques is the Layer-by-layer (see chapter 2.5).

**Table 6. Criteria for deposition process (41)**

	<b>Evaporation</b>	<b>Ion plating</b>	<b>Sputtering</b>	<b>Cathodic arc deposition</b>	<b>Chemical vapor deposition</b>	<b>Polymer deposition</b>	<b>Electro-deposition</b>	<b>Thermal spraying</b>
Mechanism of production of depositing species	Thermal energy	Thermal energy	Momentum transfer	Thermal energy	Chemical reaction	Thermal energy	Solution	Flames or plasmas
Deposition rate	Can be very high (up to 750000 Å/min)	Can be very high (up to 250000 Å/min)	Low except for pure metals and dual magnetron	Can be very high	Moderate (200–2500 Å/min)	Very high (up to 100000 Å/s)	Low to high	Very high
Deposition species	Atoms & ions	Atoms & ions	Atoms & ions	Ions	Atoms	Monomers/polymers	Ions	Droplets
Throwing power for: Complex shaped objects	Poor, line of sight coverage except by gas scattering	Good, but non uniform thickness distribution	Good, non uniform, and uniform thickness distributions	Good, but non uniform thickness distribution	Good	Good	Good	No
Into small blind holes	Poor	Poor	Poor	Poor	Limited	Poor	Limited	Very limited
Metal deposition	Yes	Yes	Yes	Yes	Yes	No	Yes, limited	Yes
Alloy deposition	Yes	Yes	Yes	Yes	Yes	No, but molecular doping possible	Quite limited	Yes
Refractory compound deposition	Yes	Yes	Yes	Yes	Yes	No	Limited	Yes
Energy of deposited species	Low (0.1–0.5 eV)	Can be high (1–100 eV)	Can be high (1–100 eV)	Can be high	Can be high with plasma assisted CVD	Low	Can be high	Can be high
Bombardment of substrate/ deposit by inert gas ions	Generally no	Yes	Yes or no, depending on geometry	Yes	Possible with PECVD	No	No	Yes
Growth interface perturbation	Not normally	Yes	Yes	Yes	Yes (by rubbing)	No	No	No
Substrate heating (by external means)	Yes, normally	Yes or no	Yes or no	Yes or no	Yes	No, cooling generally required	No	Not normally

### 2.4.3 SILAR method. A dipping method

One of the solution methods for the deposition of thin film, similar to consecutive and simultaneously spray technique, is the successive ionic layer adsorption and reaction (SILAR) method. The SILAR method can be used to prepare metal chalcogenide films (metal sulphide, metal selenide, metal telluride, metal oxide films) (42). In the chemical bath deposition (CBD) method, the deposition of metal semiconducting thin films occurs because the substrate is maintained in contact with dilute chemical bath containing both metal cations and anions. The film formation on substrate takes place when the ionic product exceeds the solubility product. The disadvantage of single bath deposition methods is the precipitate formation that takes place in the bulk of the solution and which cannot be eliminated. In order to avoid such precipitation, a sequential deposition method CBD is used and known as SILAR method. Thin films are obtained by immersing a substrate into separately placed cationic and anionic precursors and water rinsing between every immersion. The rinsing time is critical for ionic layer formation.

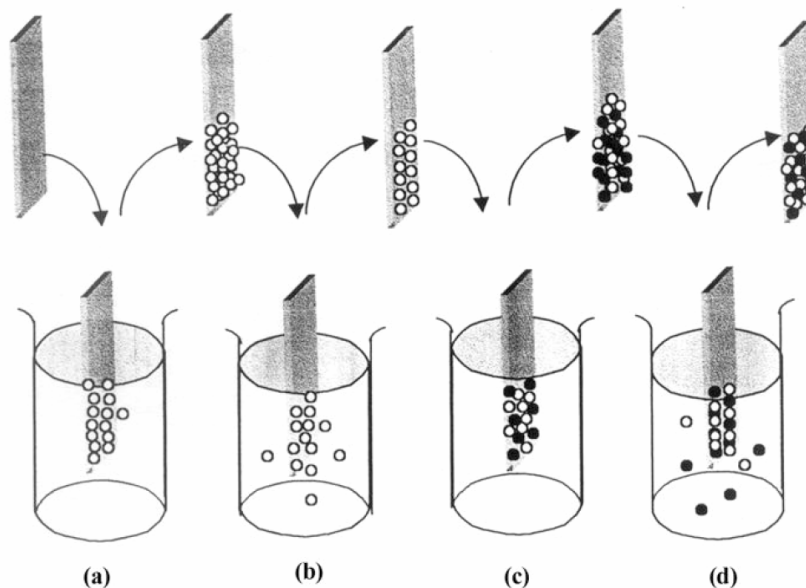


Figure 22. The scheme of SILAR method for the deposition of CdS thin films (empty dots: Cd<sup>2+</sup> ions, filled dots: S<sup>2-</sup> ions) (a) cationic precursor - adsorption, (b) ion exchange water - rinsing, (c) anionic precursor - adsorption and (d) ion exchange water - rinsing.

The same sequential adsorption process is used for the SILAR method and the consecutive spray deposition. The advantages of using the new spraying method are the better thickness control, the increase in homogeneity of the sprayed film and the reduced time of deposition.

#### **2.4.4 An example of new deposition technologies. Sol-gel deposition**

Several new or advanced deposition technologies have emerged and become important since more advanced thin film applications and structures are demanded.

The sol-gel process is one of the newly emerged technologies for functional hybrid organic-inorganic nanocomposite synthesis. The conventional sol-gel process involves the hydrolysis and condensation of metal alkoxide to form metal oxide molecules. Numerous commercial applications of sol-gel technology are found in various domains such as photoactive coatings, photochromic coatings, encapsulation of active organic components in the cosmetics industry, in the field of biotechnology as biosensors, bioreactors, biomaterials, antifouling or hydrophobic coatings, protective and decorative coatings and much more (43, 44). The smart hybrid materials fabrication is possible by tailoring the sol-gel synthesis. ORMOCER®s hybrids are an examples of smart hybrid class which gather different properties in only one material, such as tuning the refractive index and mechanical properties, transparency, as well as good adhesion and corrosion protection, etc.

### ***2.5 The layer-by-layer deposition technique***

Various techniques have been developed to coat solid substrates by thin organic films from liquid solutions or dispersions. The oldest method is the Langmuir-Blodgett deposition that allows depositing molecular layers and multilayers of amphiphilic molecules on solid substrates with high control of the spatial arrangement (45-47). A layer of amphiphilic molecules is formed at the air-water interface and it can be

transferred to a substrate. The process can be repeated several times, which allows obtaining multilayer films (see Figure 23).

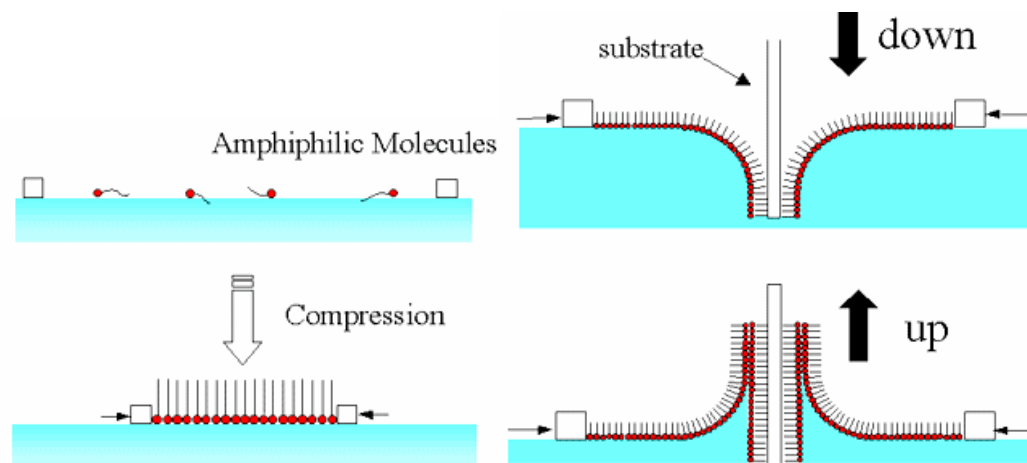


**Figure 23. Assembly of Langmuir-Blodgett films. Amphiphilic molecules are assembled at a liquid-air interface and compressed in order to form a relatively dense monolayer. The molecules are brought onto the substrate by movement of the substrate across the liquid-air interface (48).**

The disadvantages of the LB technique are rather the small set of molecules (amphiphilic nature), small surfaces that can be employed, very impractical for industrial applications and the limited stability due to the weak interactions involved in layer deposition.

The layer-by-layer (LbL) technique is a rather general deposition method for the fabrication of complex surface coatings. Decher and coworkers have introduced the LbL technique in the early 1990s (49). It is mostly based on the alternating physicosorption of oppositely charged polyelectrolytes. Beside polyelectrolytes, LbL technique can be applied for a wide range of materials (organic or inorganic reagents): biomacromolecules (proteins (50-55), DNA (11, 56)), inorganic nano-objects (nanorods (57, 58), nanoparticles (59-62), nanopatelllets (63, 64)) or polymeric colloids, liposomes (65), small molecules, complex ions (66). Compared with other deposition methods, LbL films can be deposited on various substrates, from classical silica wafers, to other polymeric substrates, metallic surfaces, flexible substrates or cells. Beside the various nature of substrates, LbL technique deposition is available from large substrates to nanometric size

objects, from glass slide to nanoparticles. The main driving force for the multilayer build-up is the electrostatic force, but there are many other interactions that had been used for LbL film deposition such as donor/acceptor interactions, hydrogen bonding (67), covalent bonds (68), stereocomplex formation or specific recognition. LbL build-up deposition is a low-cost, environmentally friendly, wet-bench technique that allows the fabrication of ordered nanocomposites easily.

### 2.5.1 Preparation of PEM films

Polyelectrolyte multilayer assembly is realized by bringing a charged substrate in contact with a solution of the oppositely charged polyelectrolyte, followed by a rinsing step to remove weakly adhering polyelectrolyte chains (49, 69). The adsorption of polyelectrolytes leads to overcompensation of the original surface charge. Then, the substrate is brought in contact with a solution of an oppositely charged polyelectrolyte, followed again by rinsing. These steps are then repeated until the desired film thickness is obtained (see Figure 24). The material adsorbed during one adsorption step is usually referred to as a layer and that adsorbed during two consecutive adsorption steps as a layer pair.

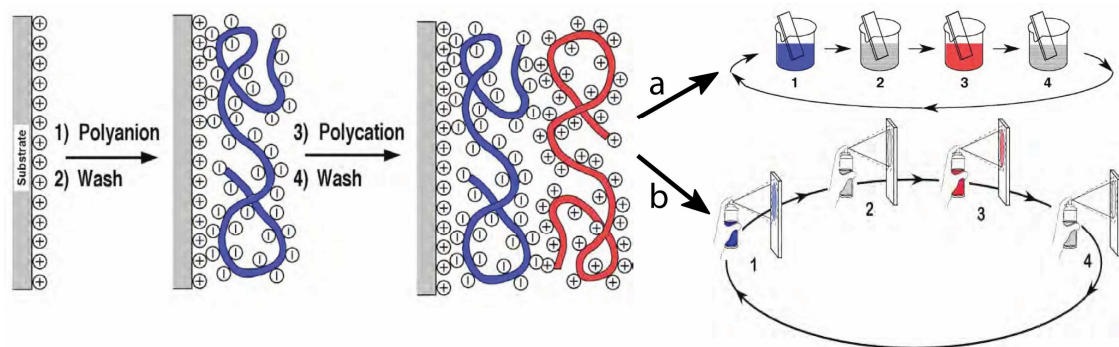


**Figure 24.** Assembly of polyelectrolyte multilayer films by dipping (a) or by spraying (b). A charged substrate is brought in contact with a solution of a polyelectrolyte of opposite charge, followed by rinsing. The substrate is then brought in contact with a solution of the second polyelectrolyte and followed again by a rinsing step. This cycle of deposition can be made more times until a desired number of layer pairs is obtained.

Aqueous solutions of polyelectrolytes are used in most cases. The simplest version of the method is dipping of the substrate into the solutions for a given time. Other techniques were introduced after the dipping technique. First, the spray -assembly method was introduced by Winterton (70) and then by Schlenoff (71). The spin assisted spraying LbL deposition was reported firstly by Hong (72, 73) and Wang (74). The spray and spin techniques present some advantages compared to the dipping method. First, the amounts of solutions required are reduced for bigger deposited surface areas; then, the time of adsorption is considerably reduced (e.g. for classical PAH-PSS LbL film deposition, typical adsorption times are approximately 15 minutes by dipping and 10 seconds by spraying). X-ray reflectometry and AFM analysis showed that in general sprayed polyelectrolyte multilayer films are thinner and smoother than dipped ones (75). Changing the deposition conditions make it possible to tune the polyelectrolyte multilayer film properties. The list of possible changeable parameters is long: solvent composition, concentration of adsorbing species, adsorption time, temperature, ionic strength, nature and concentration of added salt, rinsing time, air humidity, air drying, agitation during adsorption or rinsing, pH and so on and so forth. For spraying deposition technique, the list becomes longer by adding controllable parameters: spray distance, spray volume, concentrations of polyelectrolyte, droplet size, droplet speed and speed distribution during spraying process, concentrations of polyelectrolyte in droplets.

### **2.5.2 Mechanism of formation and general properties of polyelectrolyte multilayers**

The adsorption of a given polyelectrolyte to an oppositely charged surface leads not only to a compensation of the surface charge, but also to an overcompensation (see Figure 25). For example, the elaboration of polyelectrolyte multilayers to a silica substrate starts with the adsorption of PEI, a branched polymer that promotes the adhesion on different type of substrates. The next step is the adsorption of a polyanion, the surface charge changes

from positive to negative. An important step in the PEM construction is the rinsing step after each polyelectrolyte adsorption. It allows the weakly attached polyelectrolytes to be removed from the substrate. In most cases, the duration of rinsing is a key parameter for LbL film construction. The adsorption leads thus to a reversal charge of the surface that allows adsorbing an opposite charge polyelectrolyte and thus continuing the growth process.

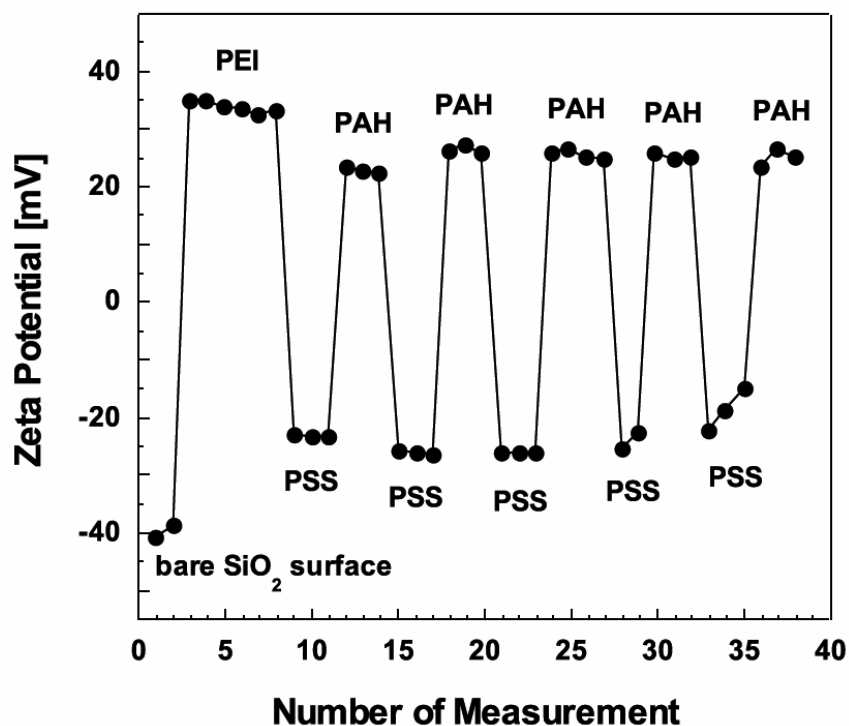


Figure 25. Zeta potential measurement showing the surface charge reversal during multilayer build-up. PEI was the first layer followed by the deposition of 5 layer pairs of PSS/PAH (76).

Polyelectrolyte multilayers are closely related to polyelectrolyte complexes in solution. However, the film properties prepared by polyelectrolyte multilayers deposition technique are superior to those prepared from polyelectrolyte complexes deposition (76). PEM films are thinner than cast PEC films because of the high control of film growth obtained by using LbL deposition. Other film properties such as homogeneity, smoothness and applicability to rough substrates or 3D objects are often achieved by PEM deposition method. Complexation of polyelectrolytes can be exothermic, athermal and even endothermic. The overall Gibbs free energy change is mainly due to the release



of counterions, originally associated with the charges of the polyelectrolytes, leading to an increase in entropy. The small free energy changes per segment are additive, leading to a strong association on a per-molecule basis due to the cooperative nature of polyelectrolyte complexation. As ions are strongly hydrated, the transition from free, solvated polyelectrolytes to the complex leads to the liberation of hydration water. The driving forces of polyelectrolyte complexation as well as multilayer formation can thus be considered to be in great part due to the release of counterions and hydration water (76).

Based on these considerations, the key equilibrium of complex formation can be expressed for two positively and negatively charged polyelectrolyte repeat units as presented in Figure 26.

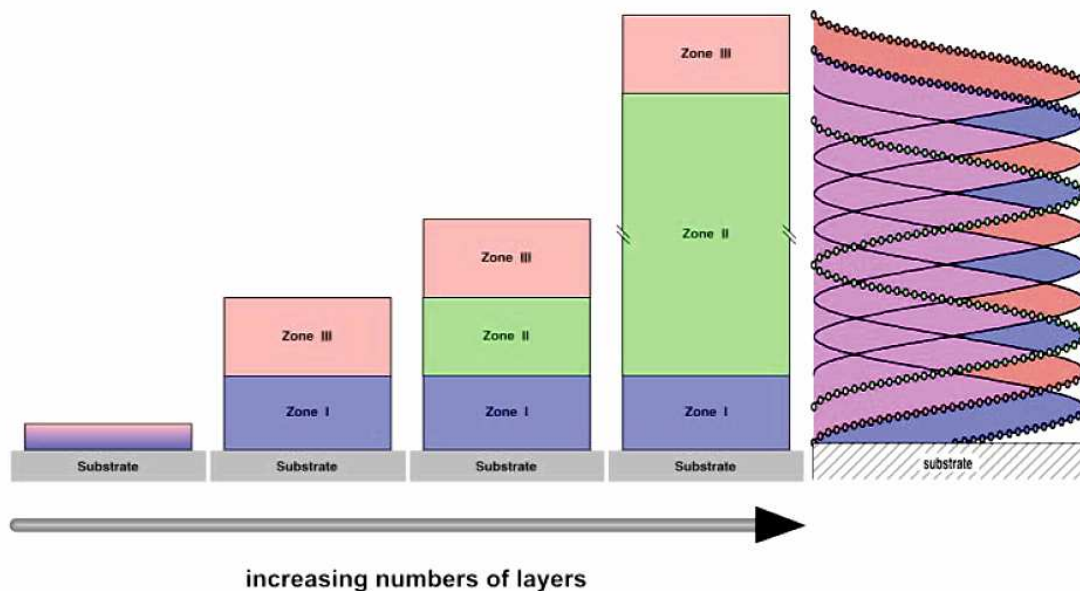


**Figure 26. The first zone model for polyelectrolyte multilayer formation. It describes how one can have charged surfaces and internal charge stoichiometry (1:1) at the same time (76).**

A polyelectrolyte multilayer can be separated into three different zones: zone I close to the substrate, zone II comprising the bulk of the multilayer and zone III close to the surface of the multilayer film. All zones have different properties (chemical composition, structure, charge). The borders between zones are not sharp but gradual. Zone I is typically only a few layers thick and influenced by the nature and charge of the substrate.

The bulk, zone II, is made up of homogeneous complexes of the two polyelectrolytes and it is a neutral zone. The neutrality is maintained by a combination of two charge compensations. The charge compensation between a positively charged polymer and a negatively charged polymer is called intrinsic compensation. The charge is also compensated by salt counterions available in the polymer solution or in the rinsing solution (extrinsic compensation). A continuum of intermediate compositions of compensations is possible, though in the completely extrinsic case, no multilayer would form as this corresponds basically to the equilibrium in Figure 27 shifted completely to the left.

The salt concentration of the solution in contact with the multilayer has a great influence on the equilibrium in Figure 27 and thus the structure and properties of the bulk of the multilayer.

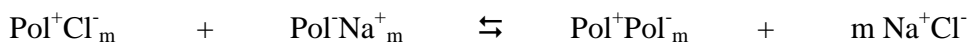
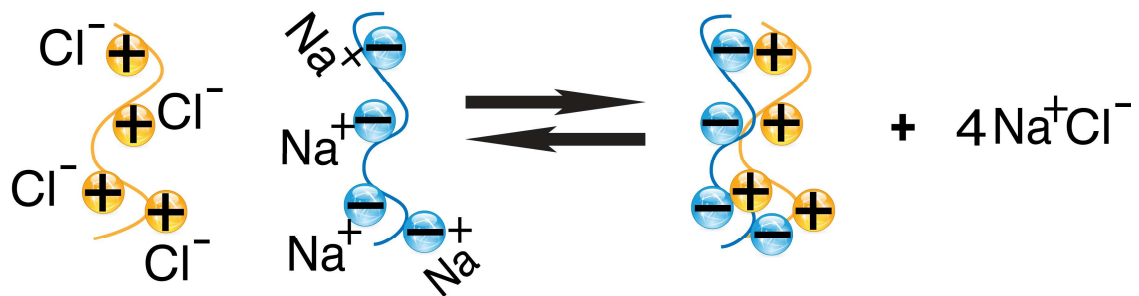


**Figure 27. Complexation between polyanion and polycation segment and release of counterions and the corresponding equilibrium. Pol+ and Pol- represent respectively a positively and a negatively charged polyelectrolyte segment. The index m refers to groups in the multilayer.**

Salt allows the “lubrication” of polymer chains. Higher salt concentrations enhance the mobility of “fixed-frozen” segments by changing the position of equilibrium from right to left. At critical high salt concentration, the extrinsic compensation increases and the number of polymer-polymer ion pairs is reduced a lot so that the polymers are no longer capable of forming a PEM film. Salt added to the external rinsing bath increases the swelling of film and the hydrophobicity index (relative water content in PEM film).

Zone II is formed only when both Zone I and Zone III have reached their final chemical composition and thickness. More polyelectrolyte deposition will not change the thickness of Zone I and III, only the thickness of Zone II will increase.

The zone III at the interface multilayer-air concentrates the excess polyelectrolyte charge responsible for the growth of the multilayer (at least in the case of linearly growing multilayers). The outer part of this zone is probably formed by loops of the last adsorbed polyelectrolyte “dangling” out from the film into the solution (77-76), which would result in a region where only chains of this polyelectrolyte are present. Adding salt after the PEM construction accelerates the conformational changes in the last layers of adsorbed polyelectrolytes and the film roughness often decreases. The excess polyelectrolyte charge is distributed over several layer thicknesses, of the order of 2.5 nominal layers (71).

Two types of growth regimes are observed for polyelectrolyte multilayers, generally termed linear and exponential growth. The exponential growth becomes linear after a certain number of deposition steps, even if the diffusion of polyelectrolytes during the deposition cycle still takes place. This process is linked to the strength of interaction between the polyelectrolytes. The negative complexation enthalpies and hence an enthalpic contribution to the free energy of complexation is characteristic of the linear growth, like PSS and PAH. For an exponential growth, complexation enthalpy is positive and the complexation is entirely entropy driven, like PGA and PLL (78).

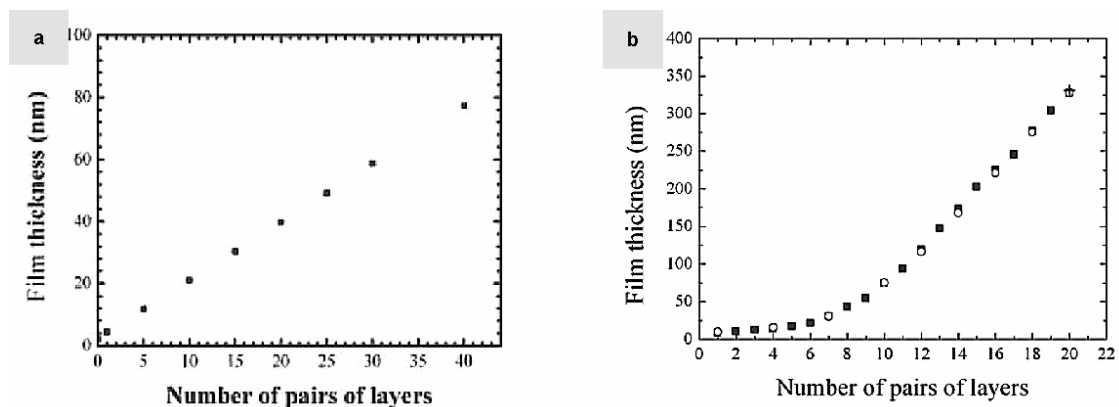


**Figure 28. Linear versus exponential growth of polyelectrolyte multilayers. The comparison of the growth of (PSS/PAH)<sub>40</sub> (a) (HA/PLL)<sub>20</sub> (b) multilayer measured by ellipsometry in the dry state (79).**

### 2.5.3 Preparation of Collagen PEM films

In order to develop new medical applications for PEM films, it was required to combine the Collagen biological properties and the advantages of LbL technique. A few studies based on Collagen LbL films are presented in the next examples.

A first example is described by J.L. Chen et al. They explored the heparin–collagen multilayer films fabrication on titanium using the LBL technique (80).

The Collagen multilayer film improved the anticoagulant potency of titanium cardiovascular implants.

A second example is the work of Kotov and col. Group, one of the pioneer groups that studied the Collagen LbL films for biomedical applications. The biocompatibility improvement of uncoated CdTe nanoparticles, which are otherwise strongly cytotoxic is achieved by the deposition of a Collagen LbL film (81). The CdTe/PDDA multilayers formation is the first step toward the study of interactions between nanoparticles /polymer composites and living tissues.

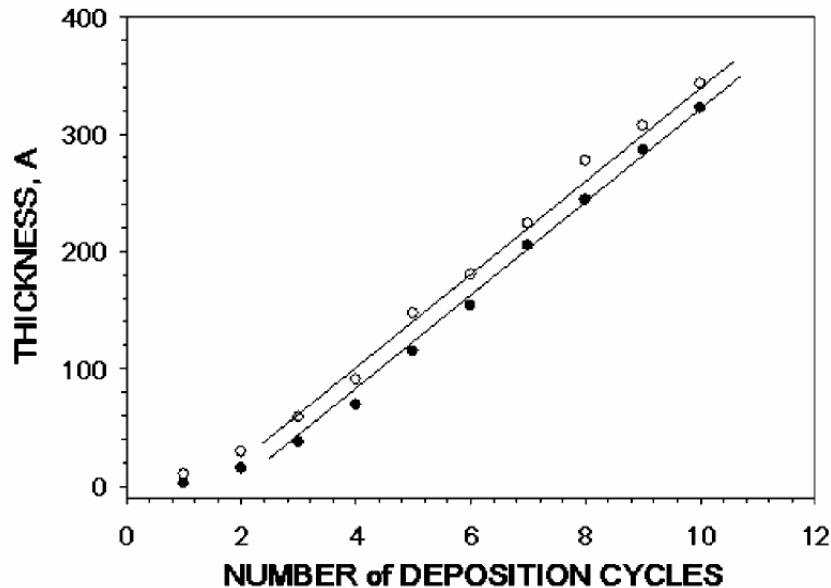
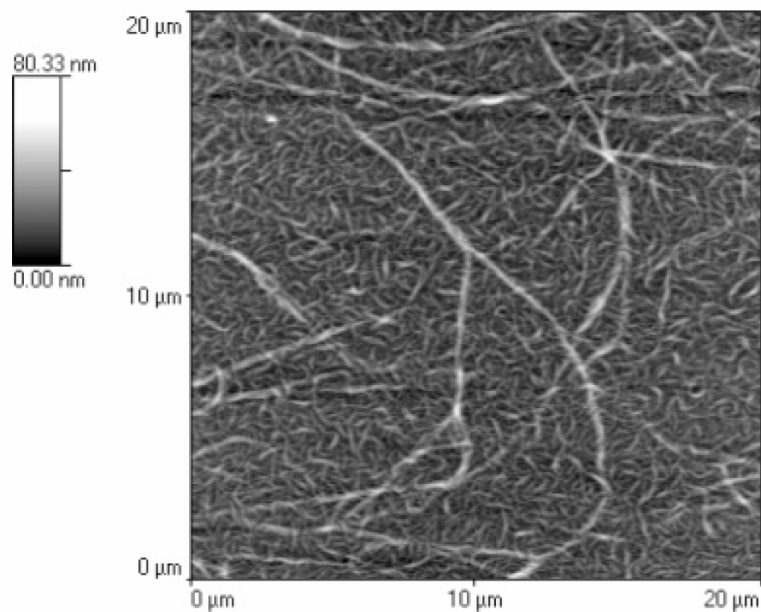


Figure 29. Ellipsometric measurements of the thickness of PDDA(PAA/collagen)<sub>n</sub> multilayers, n= 1-10, for collagen (closed circles) and PAA (open circles) layers vs. the number of adsorption cycles, n.

Multilayer assemblies containing cell-adhesive macromolecules, such as ECM proteins (collagens, laminin and fibronectin) were prepared for the adhesion and growth of mouse embryonic stem cells line D3 by the Dvorak group (82). Two important effects are reported: the laminin immobilized on top of the surfaces prevented the protein adsorption and the surfaces coated with gelatin and collagen assemblies are most suitable for cell growth.

Another example is that of the Swedish Hilborn group that worked for the preparation of an extracellular mimetic coating consisting of ECM components (Collagen and hyaluronic acid) having the capability of binding regulatory molecules (83). Collagen provides the necessary environment for cell attachment, while hyaluronic acid offer conditions for cell migration. The LbL film role is in most case used as scaffold for the cell anchoring and for storing the present soluble regulatory molecules (e.g. growth factors, drugs).



**Figure 30. AFM image of collagen and hyaluronic acid polyelectrolyte multilayers with eight layer pairs (83).**

#### **2.5.4 The advantages of consecutive and simultaneous spray deposition methods**

Table 7 summarizes the characteristics of four major coating methods (electro/electroless plating, chemical vapor deposition (CVD), physical vapor deposition (PVD) and thermal spray) and our methods (consecutive and simultaneously spray). Both the initial equipment costs and the operating costs for electro/electroless plating coatings and consecutive and simultaneously spray are relatively low. The operating costs are very much dependent on the cost of consumables such as raw materials, gases used, the automatization degree of deposition system, the degree of surface cleanliness necessary for coating adhesion, the facility of cleaning the equipment, as well as the target costs.

The consecutive and simultaneously spray technology is a very convenient method compared to PVD coating equipment which has high operating costs due to the need to maintain high vacuums in the deposition chambers. Both spray methods invented in our laboratory are described in the chapter 2 and in the articles attached.

Characteristics	Electro/electroless plating	Thermal spray	Chemical vapor deposition	Physical vapor deposition	Consecutive/simultaneously spray deposition
Equipment cost	Low	Low to moderate	Moderate	Moderate to high	Low
Operating cost	Low	Low to moderate	Low to moderate	Moderate to high	Low
Process environment	Aqueous solution	Atmospheric to soft vacuum	Atmospheric to soft vacuum	Hard vacuum	Atmospheric
Coating geometry	Omnidirectional	Line of sight	Omnidirectional	Line of sight	Line of sight
Coating thickness	Moderate to thick (10 um- mm)	Thick (50 um- cm)	Thin to thick (0.1 um- mm)	Very thin to moderate	Very thin to thick (10 nm- mm)
Substrate temperature	Low	Low to moderate	Moderate to high	Low	Low
Adherence	Moderate mechanical bond to very good chemical bond	Good chemical bond	Very good chemical bond to excellent diffusion bond	Moderate mechanical bond to very good chemical bond	Moderate mechanical bond to very good chemical bond
Surface finish	Moderately coarse to glossy	Coarse to smooth	Smooth to glossy	Smooth to high glossy	Smooth to glossy
Coating materials	Metals	Powder/wire, polymers, metals/ceramics	Metals, ceramics, polymers	Metals, ceramics, polymers	Ceramics, polymers

**Table 7. General characteristics of major coating methods (40)**

One of the advantages of consecutive and simultaneous spray technology is the range of substrates that can be used for film deposition. The main criteria for selecting a substrate are the ability to attach a growing film to the substrate and the insolubility of the substrate in the spray solution (solvent, pH, airflow rate). The low value processing of temperatures and the possibility for large-scale deposition are other advantages of our spray technique.

Investigations on the mechanism of the sprayed thin films growth have not been made yet, but two growth mechanisms could be identified (similar to CBD mechanism (84)):

- Ion by ion growth

Ion by ion growth is characterized by the formation of crystal nuclei on the surface of the substrate followed by the growth of those nuclei.

- Cluster by cluster growth

Cluster by cluster growth is defined by the formation of colloids (or crystal agglomerates) in droplets before they reach the substrate, which then adsorb onto the substrate and coalesce to form a film. There are also stable aggregates or clusters formed in droplets that do not deposit onto the substrate.

The growth mechanism is dependent on the crystal structure and the reaction steps leading to the formation of inorganic film. A combination of both growth mechanisms can also be proposed for explaining certain film deposition behaviors. The porosity of deposited films may be related to the type of film growth mechanism. Dense and compact films can be formed by ion by ion growth mechanism and more porous films are possibly formed by cluster by cluster mechanism.



## 2.6 Bibliography

1. C. Chung, J. A. Burdick, *Advanced Drug Delivery Reviews* **60**, 243 (2008).
2. D. M. Salter, *Current Orthopaedics* **12**, 251 (1998).
3. D. Heinegard, A. Oldberg, *Faseb Journal* **3**, 2042 (1989).
4. M. Endres *et al.*, *Tissue & Cell* **39**, 293 (2007).
5. S. Marlovits, P. Zeller, P. Singer, C. Resinger, V. Vecsei, *European Journal of Radiology* **57**, 24 (2006).
6. C. K. Kuo, W. J. Li, R. L. Mauck, R. S. Tuan, *Current Opinion in Rheumatology* **18**, 64 (2006).
7. J. Riesle, A. P. Hollander, R. Langer, L. E. Freed, G. Vunjak-Novakovic, *Journal of Cellular Biochemistry* **71**, 313 (1998).
8. F. Z. Cui, Y. Li, J. Ge, *Materials Science & Engineering R-Reports* **57**, 1 (2007).
9. H. Yan, C. L. Yu, *Arthroscopy-the Journal of Arthroscopic and Related Surgery* **23**, 178 (2007).
10. M. A. Meyers, P. Y. Chen, A. Y. M. Lin, Y. Seki, *Progress in Materials Science* **53**, 1 (2008).
11. N. Jessel *et al.*, *Proc. Natl. Acad. Sci. U. S. A.* **103**, 8618 (Jun, 2006).
12. Z. Z. Lu *et al.*, *Biomaterials* **29**, 733 (Feb, 2008).
13. C. M. Jewell, J. T. Zhang, N. J. Fredin, D. M. Lynn, *J. Control. Release* **106**, 214 (Aug, 2005).
14. E. B. Hunziker, *Osteoarthritis and Cartilage* **10**, 432 (2002).
15. H. Mjahed *et al.*, *Soft Matter* **4**, 1422 (2008).
16. H. Mjahed *et al.*, *Soft Matter* **5**, 2269 (2009).
17. A. J. Bailey, R. G. Paul, *Journal of the Society of Leather Technologists and Chemists* **82**, 104 (1998).
18. W. Friess, *European Journal of Pharmaceutics and Biopharmaceutics* **45**, 113 (1998).
19. D. R. Eyre, M. A. Paz, P. M. Gallop, *Annual Review of Biochemistry* **53**, 717 (1984).
20. B. Brodsky, J. A. M. Ramshaw, *Matrix Biology* **15**, 545 (1997).
21. K. Kuhn, R. Timpl, *Prog Clin Biol Res* **154**, 45 (1984).
22. M. Vanderrest, R. Garrone, *Faseb Journal* **5**, 2814 (1991).
23. R. E. Burge, *Journal of Molecular Biology* **7**, 213 (1963).
24. J. Gross, *Biochimica Et Biophysica Acta* **71**, 250 (1963).
25. A. G. Cole, B. K. Hall, *Acta Zoologica* **85**, 69 (2004).
26. S. Viguet-Carrin, P. Garnero, P. D. Delmas, *Osteoporosis International* **17**, 319 (2006).
27. J. Bella, B. Brodsky, H. M. Berman, *Structure* **3**, 893 (1995).
28. C. H. Lee, A. Singla, Y. Lee, *International Journal of Pharmaceutics* **221**, 1 (2001).
29. K. P. Rao, *Journal of Biomaterials Science-Polymer Edition* **7**, 623 (1995).
30. K. Fujioka, M. Maeda, T. Hojo, A. Sano, *Advanced Drug Delivery Reviews* **31**, 247 (1998).
31. E. Kohmura *et al.*, *Brain Research* **849**, 235 (1999).

32. T. Ochiya *et al.*, *Nature Medicine* **5**, 707 (1999).
33. W. Suchanek, M. Yoshimura, *Journal of Materials Research* **13**, 94 (1998).
34. S. V. Dorozhkin, M. Epple, *Angewandte Chemie-International Edition* **41**, 3130 (2002).
35. A. Hesse, D. Heimbach, *World Journal of Urology* **17**, 308 (1999).
36. R. Z. LeGeros, *Clinical Orthopaedics and Related Research*, 81 (2002).
37. R. Z. Legeros, S. Lin, R. Rohanzadeh, D. Mijares, J. P. Legeros, *Journal of Materials Science-Materials in Medicine* **14**, 201 (2003).
38. L. Knott, A. J. Bailey, *Bone* **22**, 181 (1998).
39. I. Mobasherpour, M. S. Heshajin, A. Kazemzadeh, M. Zakeri, *Journal of Alloys and Compounds* **430**, 330 (2007).
40. K. Seshan, *HANDBOOK OF THIN-FILM DEPOSITION PROCESSES AND TECHNIQUES Principles, Methods, Equipment and Applications (Second Edition)*
41. P. Martin, *Handbook of Deposition Technologies for Films and Coatings, Third Edition: Science, Applications and Technology*.
42. H. M. Pathan, C. D. Lokhande, *Bulletin of Materials Science* **27**, 85 (2004).
43. C. Sanchez, B. Julian, P. Belleville, M. Popall, *Journal of Materials Chemistry* **15**, 3559 (2005).
44. P. Judeinstein, C. Sanchez, *Journal of Materials Chemistry* **6**, 511 (1996).
45. Y. F. Dufrene, W. R. Barger, J. B. D. Green, G. U. Lee, *Langmuir* **13**, 4779 (1997).
46. P. Dynarowicz-Latka, A. Dhanabalan, O. N. Oliveira, *Advances in Colloid and Interface Science* **91**, 221 (2001).
47. D. K. Schwartz, *Surface Science Reports* **27**, 245 (1997).
48. A. Reich, *Universite de Strasbourg*, (2009).
49. G. Decher, *Science* **277**, 1232 (1997).
50. Y. Lvov, K. Ariga, I. Ichinose, T. Kunitake, *J. Am. Chem. Soc.* **117**, 6117 (Jun, 1995).
51. F. Caruso, H. Mohwald, *J. Am. Chem. Soc.* **121**, 6039 (Jun, 1999).
52. D. V. Volodkin, N. I. Larionova, G. B. Sukhorukov, *Biomacromolecules* **5**, 1962 (Sep-Oct, 2004).
53. K. Y. Cai, A. Rechtenbach, J. Y. Hao, J. Bossert, K. D. Jandt, *Biomaterials* **26**, 5960 (Oct, 2005).
54. C. Picart *et al.*, *Langmuir* **17**, 7414 (Nov, 2001).
55. L. Richert *et al.*, *Langmuir* **20**, 448 (Jan, 2004).
56. F. Meyer, V. Ball, P. Schaaf, J. C. Voegel, J. Ogier, *Biochim. Biophys. Acta-Biomembr.* **1758**, 419 (Mar, 2006).
57. A. Gole, C. J. Murphy, *Chem. Mat.* **17**, 1325 (Mar, 2005).
58. P. C. Wu *et al.*, *Chem.-Eur. J.* **13**, 3878 (2007).
59. R. A. Caruso, A. Susha, F. Caruso, *Chem. Mat.* **13**, 400 (Feb, 2001).
60. L. Y. Wang *et al.*, *Angew. Chem.-Int. Edit.* **44**, 6054 (2005).
61. J. Schmitt *et al.*, *Adv. Mater.* **9**, 61 (Jan, 1997).
62. G. Schneider, G. Decher, *Nano Lett.* **4**, 1833 (Oct, 2004).
63. P. Podsiadlo *et al.*, *Science* **318**, 80 (2007).
64. P. Podsiadlo *et al.*, *Nano Lett.* **8**, 1762 (2008).

65. M. Malcher *et al.*, *Langmuir* **24**, 10209 (Sep, 2008).
66. D. Grieshaber *et al.*, *Langmuir* **24**, 13668 (Dec, 2008).
67. B. S. Kim, S. W. Park, P. T. Hammond, *ACS Nano* **2**, 386 (Feb, 2008).
68. W. W. Yang, J. X. Wang, S. Zhao, Y. Y. Sun, C. Q. Sun, *Electrochem. Commun.* **8**, 665 (Apr, 2006).
69. G. Decher, J. D. Hong, J. Schmitt, *Thin Solid Films* **210**, 831 (1992).
70. A. Gilliard, L. C. Winterton, R. V. Andino, J. Lally, (2004).
71. J. B. Schlenoff, S. T. Dubas, T. Farhat, *Langmuir* **16**, 9968 (Dec, 2000).
72. S. S. Lee *et al.*, *Macromolecules* **34**, 5358 (2001).
73. J. Cho, K. Char, J. D. Hong, K. B. Lee, *Advanced Materials* **13**, 1076 (2001).
74. P. A. Chiarelli *et al.*, *Advanced Materials* **13**, 1167 (2001).
75. A. Izquierdo, S. S. Ono, J. C. Voegel, P. Schaaf, G. Decher, *Langmuir* **21**, 7558 (2005).
76. G. Decher, J. B. Schlenoff, *Ed. G. Decher, J. B. Schlenoff, Wiley-VCH*, (2003).
77. M. Castelnovo, J. F. Joanny, *Langmuir* **16**, 7524 (2000).
78. N. Laugel *et al.*, *Journal of Physical Chemistry B* **110**, 19443 (2006).
79. C. Porcel *et al.*, *Langmuir* **22**, 4376 (2006).
80. J. L. Chen, Q. L. Li, J. Y. Chen, C. Chen, N. Huang, *Appl. Surf. Sci.* **255**, 6894 (May, 2009).
81. V. A. Sinani *et al.*, *Nano Lett.* **3**, 1177 (Sep, 2003).
82. E. Brynda, J. Pachernik, M. Houska, Z. Pientka, P. Dvorak, *Langmuir* **21**, 7877 (Aug, 2005).
83. J. A. Johansson *et al.*, *Biomacromolecules* **6**, 1353 (May-Jun, 2005).
84. M. Froment, H. Cachet, H. Essaïdi, G. Maurin, R. Cortes, *Pure and Applied Chemistry* **69**, 77 (1997).

# Materials and Methods



## **3 Materials and methods**

### ***3.1 Polyelectrolyte multilayers***

Different polyelectrolytes have been used in multilayer construction (see Table 8). Conventional LbL multilayer films based on PEI (poly (ethylene imine)), PSS (poly (styrene sulfonate)), PAH (poly (allylamine)) or biopolymers such as Collagen, Dextran Sulfate and Alginate were used as precursor films for the deposition of inorganic coating. Generally, the polyelectrolyte concentrations are 1 mg/ml and the ionic strength of solutions is 0.15 M sodium chloride. Collagen is a natural protein dispensable only in acidic solutions (pH=4). For buffer preparation, acetic acid (8.1 mM), sodium acetate solution (1.8 mM) and sodium chloride (154 mM) are used. The buffer solution was prepared by weighting. For all solutions, ultra pure water (Milli-Q Gradient System, Millipore) with a resistivity of 18.2 M $\Omega$ cm was used.

Collagen (COL, batch: 07CBPE2040) was purchased from SYMATESE Biomatériaux (Grenoble, France). It is a type I bovine Collagen, medical grade purified. Collagen was stirred for one night to obtain clear suspensions (0.2 mg/ml). Medical grade sodium Alginate was bought from Nova Matrix (Alginate Pronova UPLVG). No pH adjustment is needed and overnight stirring is necessary because of slow Alginate dissolution rate.

### ***3.2 Inorganic coatings***

In this study, various inorganic salts were used for the preparation of inorganic coatings. Table 8 presents all inorganic coatings prepared (final product) and the corresponding complementary salts required for coating deposition (reactants).

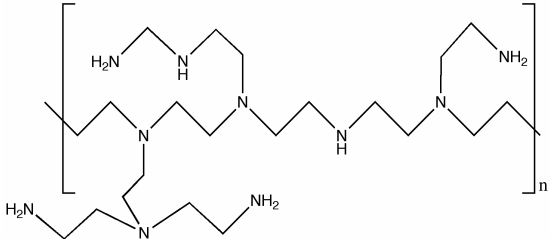
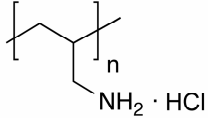
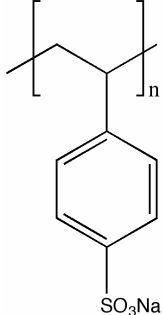
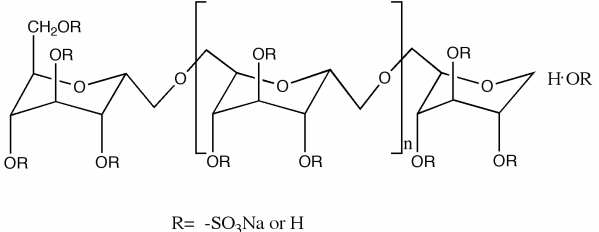
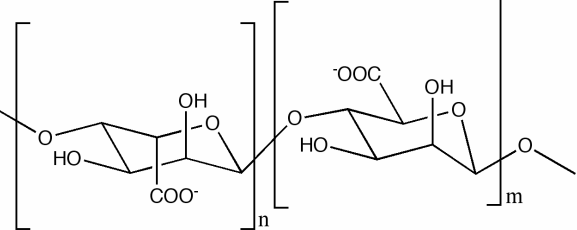
Reactants /Supplier	Final product
<ul style="list-style-type: none"> <li>• Calcium nitrate tetrahydrate (<math>\text{Ca}(\text{NO}_3)_2 \cdot 4\text{H}_2\text{O}</math>) / Sigma-Aldrich</li> <li>• Diammonium hydrogen phosphate (<math>(\text{NH}_4)_2(\text{HPO}_4)</math>) / Fluka</li> </ul>	Calcium phosphate (Dicalcium dihydrogen phosphate or brushite) ( $\text{Ca}(\text{HPO}_4) \cdot 2\text{H}_2\text{O}$ )
<ul style="list-style-type: none"> <li>• Calcium chloride (<math>\text{CaCl}_2 \cdot 2\text{H}_2\text{O}</math>) / Carlo Erba Reagents</li> <li>• Sodium fluoride (<math>\text{NaF}</math>) / Fluka</li> </ul>	Calcium fluoride (Fluorspar) ( $\text{CaF}_2$ )
<ul style="list-style-type: none"> <li>• Calcium chloride (<math>\text{CaCl}_2 \cdot 2\text{H}_2\text{O}</math>) / Carlo Erba Reagents</li> <li>• Sodium oxalate (<math>\text{Na}_2\text{C}_2\text{O}_4</math>) / Fluka</li> </ul>	Calcium oxalate ( $\text{CaC}_2\text{O}_4$ )
<ul style="list-style-type: none"> <li>• Iron chloride (<math>\text{FeCl}_3</math>) / Sigma-Aldrich</li> <li>• Diammonium hydrogen phosphate (<math>(\text{NH}_4)_2\text{HPO}_4</math>) / Fluka</li> </ul>	Iron phosphate ( $\text{Fe}_2(\text{HPO}_4)_3 \cdot n\text{H}_2\text{O}$ )
<ul style="list-style-type: none"> <li>• Silver nitrate (<math>\text{AgNO}_3</math>) / Sigma-Aldrich</li> <li>• Sodium chloride (<math>\text{NaCl}</math>) / Sigma-Aldrich</li> </ul>	Silver Chloride ( $\text{AgCl}$ )
<ul style="list-style-type: none"> <li>• Iron chloride (<math>\text{FeCl}_3</math>) / Sigma-Aldrich</li> <li>• Potassium ferrocyanide (<math>\text{K}_3[\text{Fe}(\text{CN})_6]</math>) / Sigma-Aldrich</li> </ul>	Prussian Blue (PB) (ferric ferrocyanide or iron(III) hexacyanoferrate(II)) ( $\text{Fe}_4[\text{Fe}(\text{CN})_6]_3$ )

**Table 8. Inorganic coating: from reactants to final coating**

Other chemicals used include Trizma hydrochloride (T32253) purchased from Sigma-Aldrich, Sodium acetate ( $\text{CH}_3\text{COONa}$ , 3 M solution) purchased from Fluka, acetic acid ( $\text{CH}_3\text{COOH}$ ) purchased from VWR Prolabo, Sodium phytate from Sigma-Aldrich, Potassium ferricyanide ( $\text{K}_4[\text{Fe}(\text{CN})_6]_3$ ) / Sigma-Aldrich. Calcium nitrate tetrahydrated

and diammonium hydrogen phosphate solution are prepared in a basic buffer (Trizma buffer, pH= 10). All the products were used without further purification. The salt solutions were prepared in ultrapure water (Milli-Q Gradient System, Millipore) with a resistivity of 18.2 M $\Omega$  cm.



Polyelectrolyte	Structure	Molecular weight (Mw, g/mol)	Isoelectric point (pKa)	Supplier
Poly (ethylene imine) - PEI		25,000	-	BASF
Poly (allylamine) hydrochloride - PAH		56,000	10	Sigma-Aldrich
Poly (styrene sulfonate) sodium salt - PSS		70,000	1	Sigma-Aldrich
Dextran Sulfate sodium salt - Dex	 <p style="text-align: center;">R= -SO<sub>3</sub>Na or H</p>	500,000		Sigma-Aldrich
Alginate - Alg			3.5	Nova Matrix

### 3.3 Spraying. Equipment and implementation

#### 3.3.1 General considerations on atomization

##### 3.3.1.1 Drop size distribution of sprays

Most atomizers generate drops in the size range of micrometers to 500  $\mu\text{m}$ .

Generally, natural sprays (rain, drizzle, fog, waterfall) or practical atomizers do not have a uniform drop size distribution, only under certain special conditions the spray droplets are homogeneous.



Figure 31. Airbrush system from 1880 (Liberty Walkup Air Brush Mfg. Co.) (1)

Spray nozzles are designed to break a liquid jet into droplets. Most frequently used spray nozzles are hydraulic nozzles, gas nozzles (in gas nozzle a stream of e.g. air is used to break up liquid), ultrasound nozzles and electrospray nozzles (2).

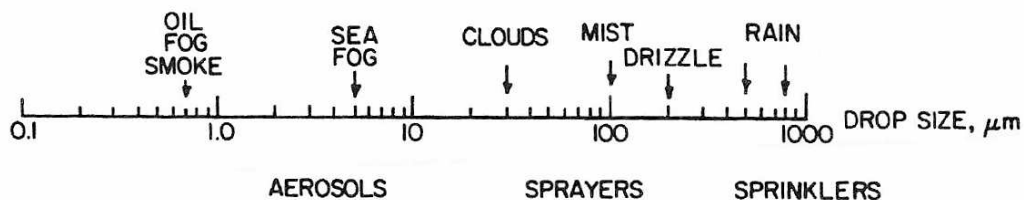


Figure 32. Spectrum of drop size

The most used graphical representations of drop size distribution are frequency distribution curves (Figure 33).

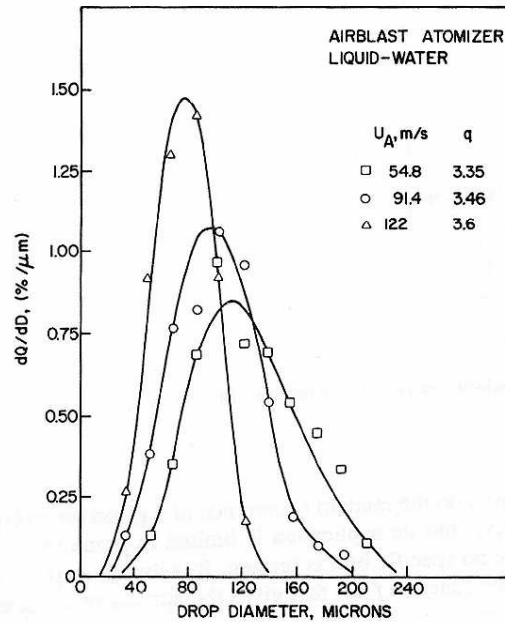


Figure 33. Effect of atomizing air velocity on drop size distribution (a) and cumulative volume distribution (b). Where  $D$  is the drop diameter,  $Q$  is the fraction of the total volume contained in drops of diameter less than  $D$ ,  $U_A$  is the air flow and  $q$  is a drop size parameter that provides information about spread of drop size (higher is the value, more uniform is the spray) (3).

Several empirical distribution functions have been developed to characterize the distribution of drop size in a spray: Nukiyama-Tanasawa, Rosin-Rammler, modified Rosin-Rammler, upper-limit function (4). There is no universal correlation between representative diameters and drop size distribution.

### 3.3.1.2 Drop size measuring methods

We can classify drop-sizing techniques in three main categories: mechanical, electrical and optical methods (Table 9). Two parameters have been measured: number density (size distribution) and drop velocity, both or only one parameter can be measured on the same instrument. No single method is completely satisfactory: mechanical techniques are simple and low cost but extraction and collection of typical sprays take place with difficulty; electrical hot wire technique is applicable only for low drop velocity (<10m/s); optical methods are very sensitive to instrument alignment (lens, beam, detector), detector characteristics.

Special problems arise in drop size measuring such as:

1. Very high number of drops in a spray
2. Velocity of drops in a spray is high and varies
3. Drops in a spray can evaporate and coalesce

Mechanical methods	Electrical methods	Optical methods
<ul style="list-style-type: none"> <li>• Drop collection on slides or in cells</li> <li>• Molten-wax and frozen-drop techniques</li> <li>• Cascade impactors</li> </ul>	<ul style="list-style-type: none"> <li>• Charged wire</li> <li>• Hot wire</li> </ul>	<ul style="list-style-type: none"> <li>• Imaging (photography, holography)</li> <li>• Non-imaging (single particle counters, light scattering, Malvern particle analyzer)</li> </ul>

Table 9. Numerous drop size measuring techniques (5)

Malvern particle sizer (Spraytec) was used for the characterization of our atomizers (blue bottles, Aztek, Parker air gun). The principle of Fraunhofer diffraction (parallel beam of monochromatic light diffracting a spray drop) is applied for the Malvern instrument (Figure 34). Interaction between the beam (laser) and the drop produces a Fraunhofer diffraction pattern. Different spacing patterns (alternate light/dark concentric rings) are obtained for each drop diameter size. The overlapping diffraction rings focused by Fourier Transformer Lens on a multielement photodetector provides a large range of drop size measurement.

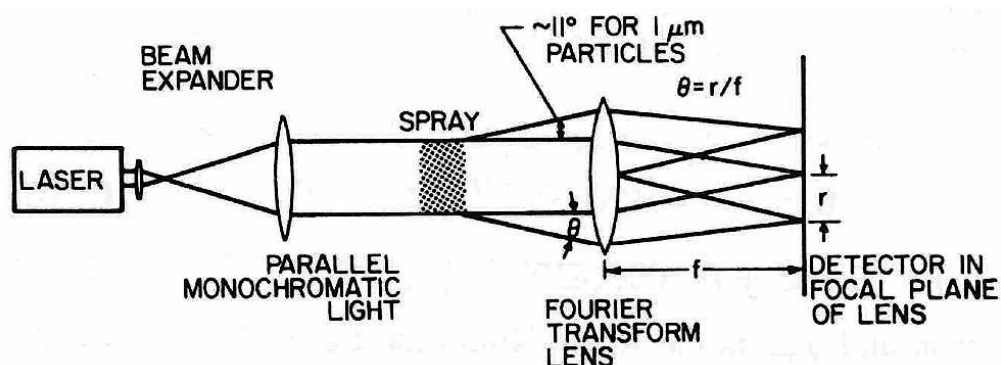


Figure 34. Schematic drawing of Malvern Particle Sizer (5)

### 3.3.2 Atomizers, airbrushes

Since the nineteenth century, atomizers are used in different applications. Different types of atomizers have been developed toward our days: pressure atomizers (plain orifice atomizer, simplex or pressure-swirl atomizer, duplex atomizer, fan spray) rotary atomizers, air-assisted atomizers, airblast atomizers, effervescent atomizers, electrostatic atomizers, ultrasonic atomizers and whistle atomizers. Each type of atomizer represents a different way to transform liquid jet into drops:

- Pressure atomizers: high-pressure allow to obtain relative high velocity between gas and liquid
- Rotary atomizers: centrifugal force creates uniform films that are broken into homogeneous drops
- Air-assisted, airblast, effervescent atomizers: high flow of air stream transforms jets, sheets of liquid into drop.
- Electrostatic atomizers: electrical field applied for liquid jet between an anode and a cathode transforms the jet of liquid into drop.
- Ultrasonic atomizers: powerful ultrasound is used as energy source for breaking up the liquid jet.

Airboys (or spray can or spray bottle) from Carl Roth GmH Germany (see Figure 36) made from polyethylene and poly (propylene) are pressure atomizers with a mono-component nozzle. They were used for rinsing, polyelectrolyte spraying or salts spraying. They are characterized by nozzle diameter of 0.40 mm, maximal pressure of 13 bar, thermally stable and chemical stability until + 40°C and a big capacity of liquid filling (max. 190 ml).



**Figure 35. Carl Roth Airboy (Air bottle)**

A second system that has been tested for spraying is an internal mixing airbrush, dual action, siphon feeding, connected with an air compressor. Airbrush model HS-28P (HSENG, China) has a smaller fluid cup capacity. The nozzle diameter is 0.35 mm. This allows a spray with smaller drop diameters than that obtained with manual spray bottles. Liquid consumption for this system is smaller than that of spray bottles such airbrushes are well suited for spraying expansion components.



**Figure 36. Airbrush model HS-28P**

Generally, this type of airbrush is used in art paintings, photo retouching, clothing, spray murals, graphics. Various airbrushes can be found on the market nowadays (old version of airbrush, Figure 31), in our case, we used an internal mixing airbrush (air flow and liquid are mixed before being sprayed). With the internal-mixing airbrush, the spray cone is minimum for a maximum airflow, furthermore with the external mixing system; the spray cone is constant, not depending on the value of airflow. One advantage of air-

assisted atomizers (HS-28P Airbrush, see Figure 36) compared with pressure atomizers is the good atomization at low liquid flow rate. Airflow is controlled by an Airbrush compressor (piston type) model AS196 that has a maximal pressure of 6 bars.

The last airbrush system used for spraying is an Aztek airbrush model A470 (see Figure 37). Made from steel and plastic only, the Aztek airbrush provides chemical stability for aerosol formation. The contamination with ions is therefore reduced. Various nozzle diameters are available for this model starting from 10 mm to 60 mm for a better control of drop size diameter range.

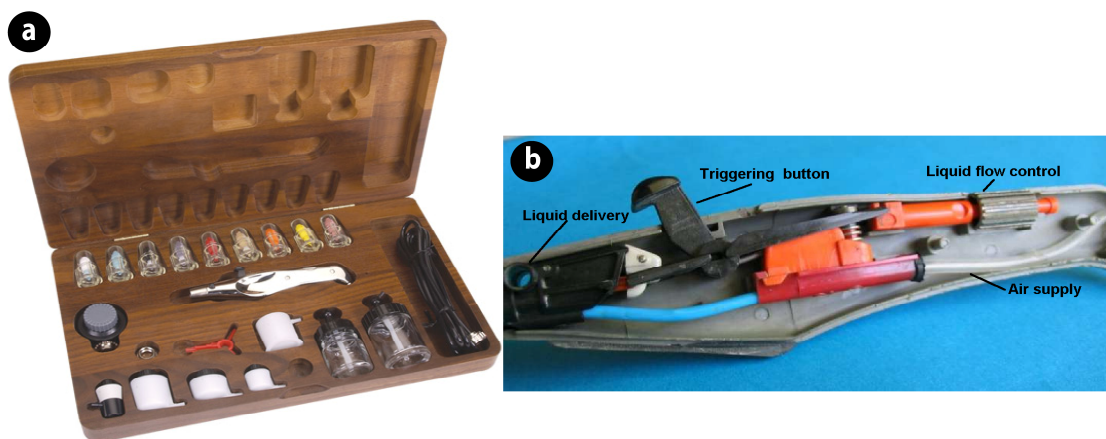


**Figure 37. a) Aztek airbrush A470 and accessories (nozzles, liquid can), b) Inside an Aztek airbrush**

Like the first airbrush used (HS- 28P), Aztek Airbrush is an internal mixing atomizer, dual action: pushing triggering button for air pressurized and liquid feed (first step), then moving triggering button for mix air and liquid to be sprayed. The feeding system is the same as the first airbrush system: siphon feed. However, the compressor is replaced by air tube supply from our laboratory. The air quality is good since the air before being sended in the airbrush is passing through two filters. The airflow delivered by the compressed air system is restricted at a maximum pressure of 8 bars.

The Aztek airbrush can be automated by replacing trigger action by pumps delivering liquids and gas flows. A computerized system replaces manual spraying for a more efficient spraying procedure and eliminates the manipulation errors.

In a spraying system, various parameters can be optimized for a desired result. Some of the parameters play a bigger role than others, but controlling each of them allows the preparation of a controlled coating-spray.

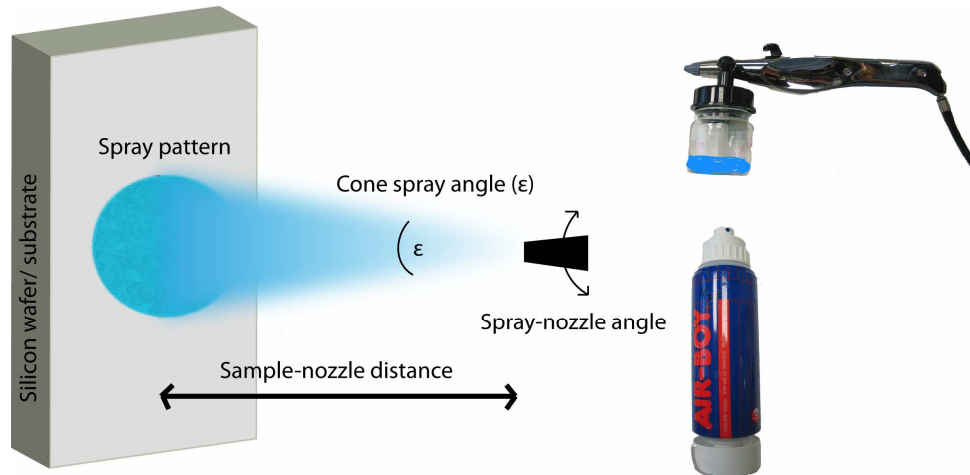


**Figure 38.** Schematic illustration of spraying and some physical parameters involved in spraying such as the spraying system (Airboy bottle or Aztek airbrush), the spraying distance or geometry.

### 3.3.3 Spray parameters

There are four main parameters that can influence spray characteristics and coatings: solution (liquid) that should be sprayed, substrate, gas and set-up. Playing with different values of these parameters will influence and thus allow controlling the deposition of coatings.

Parameter	Properties
Solution	Flow rate, concentration of solution, solvent properties, surface tension, density, viscosity, temperature, solubility
Substrate	Surface structure, surface geometry, surface energy, solubility
Set-up	Nozzle geometry, spray distance, number of nozzles, alignment of nozzles
Gas portent	Flow rate, gas properties, temperature



Each of the characteristic parameters has an influence on spray droplets, jet formation, film formation at liquid-surface interface and finally on coatings properties (porosity, morphology, thickness, etc.).

For our coatings preparation method it is necessary to have at least two nozzles. Our spraying system becomes more difficult than spraying only one solution as electro spraying or dry spraying. The spraying system is generally placed in atmospheric air but can also be placed in a controlled atmosphere in the case of oxidizing molecules or inflammable solvents.

### ***3.4 Thin film characterization***

#### **3.4.1 Atomic Force Microscopy**

Invented in 1981 by Binnig, Rohrer, Gerber, Weibel (1982) in IBM Zurich laboratory, scanning tunneling microscopy (STM) is the predecessor of atomic force microscopy (AFM). Park Scientific (company founded by Stanford researchers) introduced the first AFM microscope on the market in 1988. Invented for imaging individual atoms, atomic bonding investigation, the STM development was awarded with the Nobel Prize in Physics in 1986. Despite the enormous popularity of STM, it has some disadvantages. It requires conductive samples because it uses the tunneling current that is transferred between the tip and the sample (6). Working in air, adsorption and desorption of atoms and molecules onto the surface are very probable. An ultra high vacuum for imaging of conductor and semi-conductors is needed. AFM has one major advantage that no conductive surface is needed for imaging. However, a drawback of the AFM is its reduced resolution in comparison with STM.

The AFM range of surface mapping is very large, from molecular scale (a few nanometers) to large-scale size (>125  $\mu\text{m}$ ). An AFM can examine various rough surfaces from nano-scale to 8-10  $\mu\text{m}$  keeping a good resolution in the x-y plan. Large samples can be fitted directly into the AFM microscope without cutting them (7).

Compared with the scanning electron microscope (SEM), the AFM provides superior topographic contrast and 3D mapping images instead of 2D SEM images. No metallic coating is necessary for AFM microscope compared to SEM sample preparation.

Consequently, no dehydration, therefore no shrinkage of coating/substrate needs to be realized for AFM utilization. The sample is analyzed directly after basic sample preparation. Images by AFM in liquid mode have better resolution than SEM images in environmental mode. In some cases low contrast of polymeric substances makes AFM the only technique for surface “looking”.

A schematic diagram of an AFM microscope is shown in Figure 39. The important parts of an AFM microscope are the tip, the cantilever, the deflection sensor and the microscope scanner.

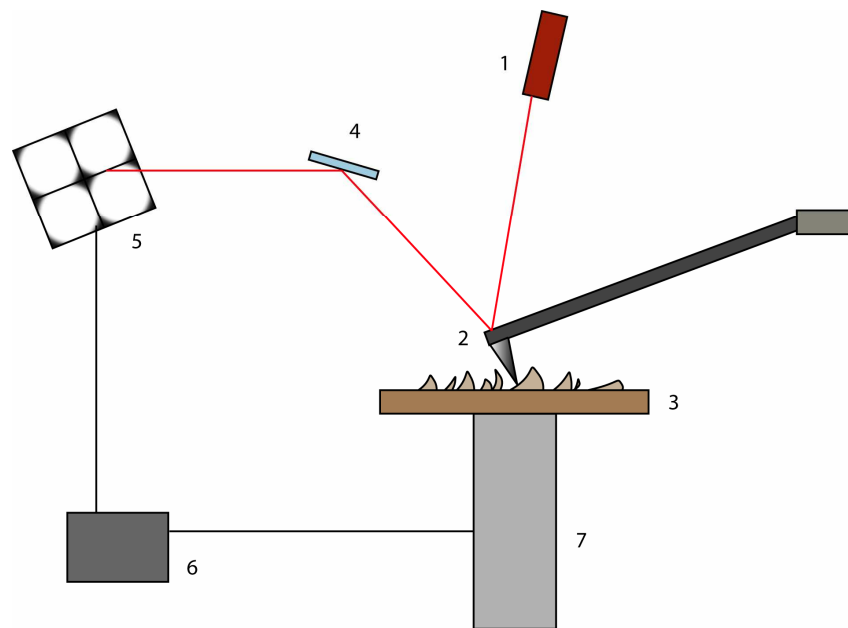


**Figure 39. Schematic illustration of an AFM microscope: 1.) Laser diode, 2.) Cantilever and tip, 3.) Substrate/coating, 4.) Mirror, 5.) Photodetector, 6.) Electronic controller, 7.) Scanner.**

The tip mounted on a cantilever is brought closest to the sample surface. A laser beam is reflected from the backside of the cantilever in the mirror and then to the photodetector. A small deflection of the cantilever will change the position of the laser beam on the detector. A feedback electronic circuit easily controls recording the images under the effect of interaction forces tip-surface as the cantilever scans the sample.

Different interactions can be involved in this approach tip-surface: electrostatic forces, capillary forces, Van der Waals forces, mechanical contact forces, magnetic forces, chemical bonding, solvation forces (8), etc.

The tip-cantilever assembly properties influence contrast images, proximity forces or surface properties. The sharper is the tip the more details for a rough surface are revealed. Various geometries and metal/coating combinations are available for tip fabrication. A large palette of commercial tip-cantilever tries to respond to different surface-sample studies.

Budget Sensor AFM tips are been used for characterizations of ours samples. Made only of Silicon without coating, these tips have special properties (see Table 10) and a pyramidal shape (see Figure 40).

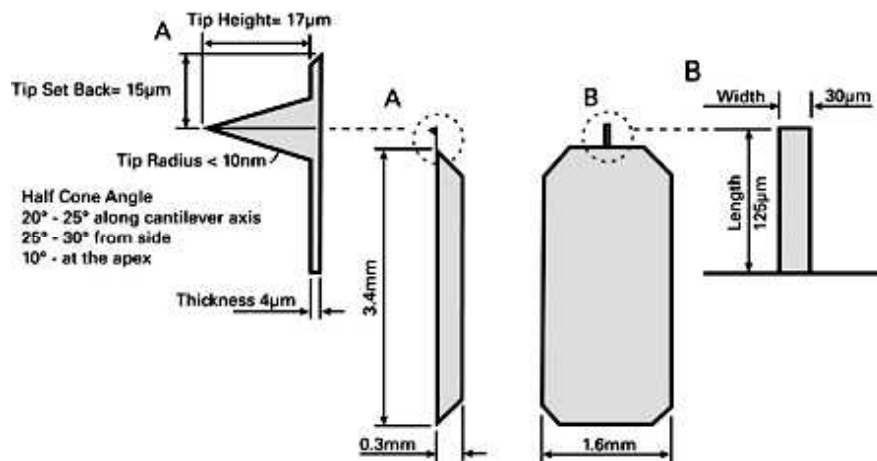


Figure 40. Tip-cantilever (model Tap300-G) schematic dimensions (9).

	Value	Range
<b>Resonance Frequency</b>	300 kHz	+/-100 kHz
<b>Force Constant</b>	40 N/m	20 - 75 N/m
<b>Length</b>	125 μm	+/-10 μm
<b>Mean Width</b>	30 μm	+/-5 μm
<b>Thickness</b>	4 μm	+/-1 μm
<b>Tip Height</b>	17 μm	+/-2 μm
<b>Tip Set Back</b>	15 μm	+/-5 μm
<b>Tip Radius</b>	<10 nm	
<b>Half Cone Angle</b>	20°-25° along cantilever axis 25°-30° from side 10°-at the apex	

Table 10. Tip-cantilever AFM probe (model Tap300-G) properties (9)

AFM microscopes can be classified into two classes: scanned-sample (see Figure 40) and scanned-tip microscopes. For scanned-samples microscopes, the sample is attached to the scanner and both are moved together under the tip.

The maximum scan size and the image resolution depend on the scanner piezo properties. Piezoelectric element (scanner) produces precise movement along the three major axes when an AC voltage is applied to the scanner. Longer scanners yield to larger scan sizes, however shorter scanners provide better resolution for smaller scan size images down to atomic scale (10).

The second type of AFM setup microscope is scanned-tip. The sample is fixed and the piezo-scanner is attached to the cantilever-tip that is moving. Often the noise level is higher in scanned-tip microscope than in scanned-sample microscopes, but they are more easily equipped with temperature-controllers, liquid cells, electrochemistry cells and atmosphere chambers.

Imaging in liquid is one reason for which AFM is very useful in biomedical investigations; imaging cells in physiological condition is a common example.

Only two types of setup AFM microscopes are possible, but different operation modes of AFM microscopes are possible (see Figure 41).

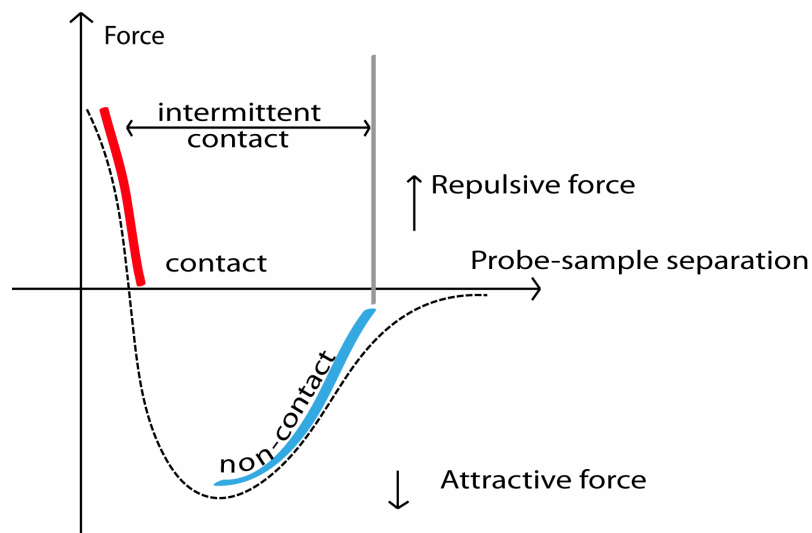


**Figure 41. A schematic plot with forces between tip and sample-surface; operating modes for AFM (non-contact, contact, intermittent-contact modes).**

Depending on whether the cantilever is oscillating close to its resonance frequency or not, two different modes can be operated: dynamic mode (AC mode) or static mode (DC mode).

In the static mode, the contact mode is very popular for larger scan areas. The tip is brought in contact with the sample (see Figure 42) and the cantilever deflection is kept constant while scanning the surface by the feedback loop. For softer samples, softer cantilevers should be used for reducing the number of surface-sample damages. Other DC modes are: deflection or error mode (the feedback loop is turned off) and lateral force microscopy (measuring the torsion of the cantilever exerted by lateral forces on the scanning probe. It is a relative measurement of surface friction).

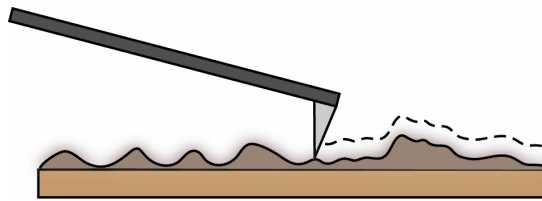


**Figure 42. The tip follows the sample's topography in contact mode.**

All dynamic modes are based on the cantilever oscillation close to its resonance frequency. A piezoelectric motor produces the oscillation or external coils if the cantilever is coated with a magnetic layer. In the same way as static modes, various dynamic modes are available for AFM microscopes: non-contact mode, intermittent contact mode, phase imaging mode, force modulation mode.

In non-contact AC mode, an oscillating probe is brought close to the sample-surface (10). Van der Waals forces are induced between the tip and the surface. During scanning a small variation in interaction forces produces a shift in the resonance frequency. The cantilever frequency is kept constant; only the probe amplitude variations are monitored while scanning the sample (see Figure 43). Non-contact mode is unpractical in liquid mode because of high capillary forces.

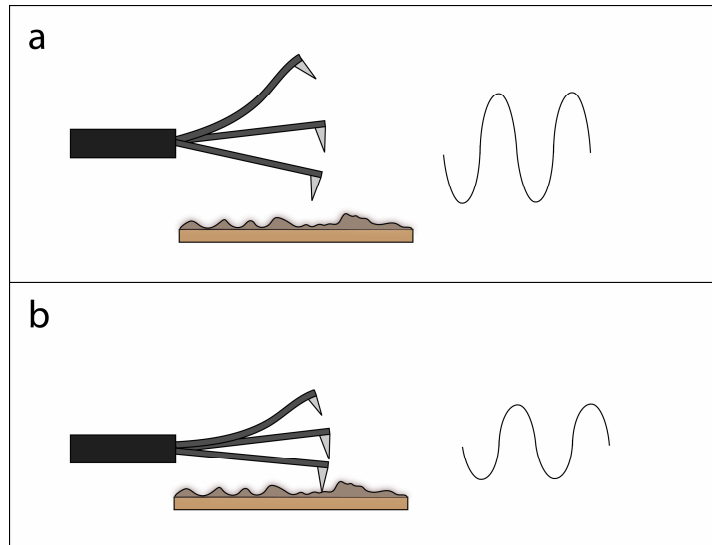


**Figure 43. In tapping mode, the free oscillation of the vibrating cantilever is decreased when the tip is touching the surface while scanning. The image is recorded at constant resonance frequency and variable amplitude.**

Intermittent contact mode (tapping mode) is similar to non-contact mode, but in this case the tip is touching the scanning surface while it oscillates. Repulsive forces that are present in contact mode induce a dampening of cantilever amplitude in intermittent contact mode. The lateral and the vertical resolutions are very good compared with other modes. It is used also in liquid mode.

The phase imaging mode represents a continuous monitoring of cantilever phase modifications during scanning. It is recorded at the same time as amplitude deviations in the intermittent contact mode. It is a helpful technique for obtaining information about physical properties: viscosity, stiffness, adhesion, etc.

The AFM can provide much more information than just imaging the surface of a sample. Recording the cantilever-surface forces (attractive or repulsive), it is possible to study local chemical/ mechanical properties as adhesion, elasticity, bonding forces, etc. Beyond topographical information AFM microscope can be useful for scanning force-vs-volume maps.

AFM is a powerful tool for imaging/scanning in various applications (11) (microelectronic, biotechnology, thin film, etc.) and for printing different molecules at atomic scale as “dip-pen” nanolithography (DPN) (12).

In our studies, we worked in tapping mode of a Nanoscope III (Santa Barbara, California, USA). Different polyelectrolyte multilayer film structures and inorganic coatings were imaged with Tap300-G microscope probes.

## 3.4.2 Electron microscopy

### 3.4.2.1 Introduction

Electron microscopy comprises a wide range of microscopes: Transmission Electronic Microscope (TEM), Scanning Electronic Microscope (SEM), and Scanning Transmission Electronic Microscope (STEM). A schematic illustration (Figure 44) shows the difference between TEM and SEM.

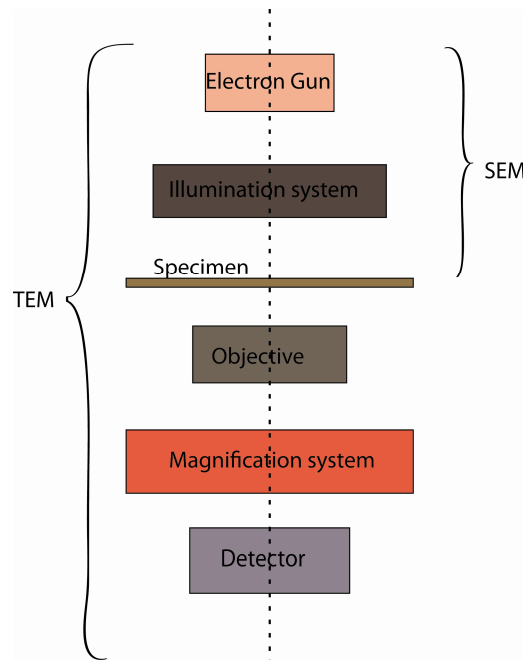


**Figure 44. Schematic difference between TEM and SEM (13)**

Electron Microscopy is frequently used for structure studies (High-Resolution TEM (HRTEM), TEM, STEM), composition studies (TEM, STEM), morphology studies (SEM, STEM) and elemental mapping studies (STEM, SEM).



### 3.4.2.2 Electron – sample interactions

Electrons can interact with the sample by two types of interactions: elastic and inelastic interactions (see Figure 45). For the elastic interaction, the electrons have the same energy after and before interaction with the sample. In the case of inelastic interaction, the electrons had lost some of their initial energy due to contact with the sample.

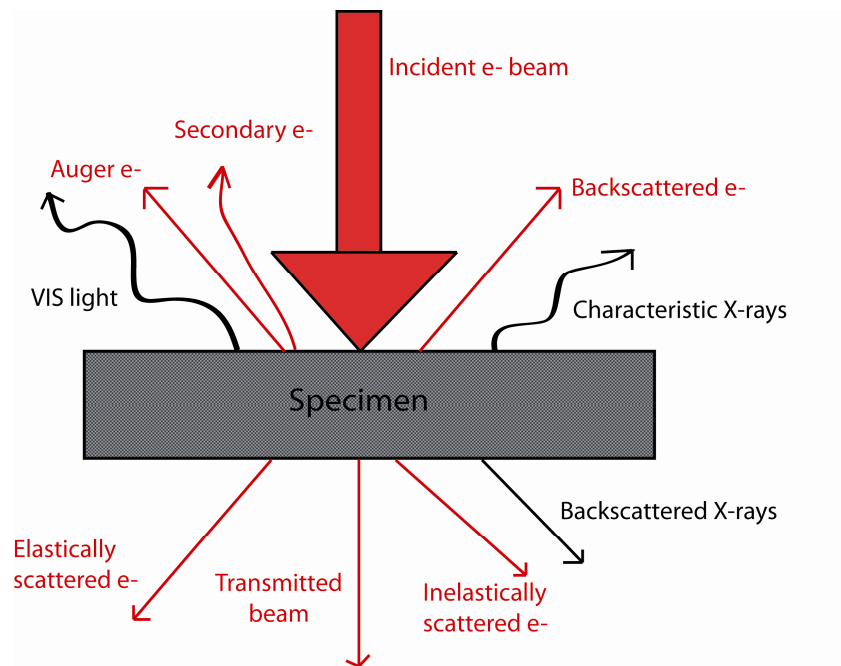


**Figure 45. Various species scattered and backscattered from incident electron beam – specimen interactions (13).**

Beam electrons are scattered at nuclei (elastic scattering) or at electronic shells (inelastic scattering). If the elastic scattering is applied in imaging in TEM and SEM, the inelastic scattering is used for analysis (ionization states, excitation of plasmons, phonons, secondary electron emission, etc.).

In Electron Microscopy, there are a high number of electrons in the incident beam and in the specimen. The high probability of interaction between species (electron – electron, electron – nuclei, etc) makes this technique complex. After interaction different particles can be detected (see Table 11). Each type of detected particle gives different information about the specimen.

<b>Particle</b>	<b>Applications</b>
Transmitted beam	No specimen information, used for TEM alignment
Elastically scattered electron	Electron Energy Loss Spectroscopy (EELS)
Backscattered electron (BSE)	Imaging in SEM uses the material contrast
Secondary electron (SE)	Imaging in SEM uses the topography contrast
Auger electron (AE)	Information about chemistry, composition of the specimen in SEM, not widely used
Characteristic X-ray	Elemental composition in TEM, SEM applied in Energy Dispersive X-ray Spectroscopy (EDXS) technique
Visible light (VIS light)	Information about electron states in specimen (excited states), cathodoluminescence in SEM (CL)

**Table 11. Classification of detected particles and their applications for specimen characterization (14)**

### **3.4.2.3 Working principle of TEM/SEM**

A setup of TEM is represented in Figure 46. In TEM microscopes, signals that are used for detection are elastically scattered electrons (direct and diffracted).

An electron beam is accelerated between the cathode (electron gun) and the anode. The electron beam is produced by different electron sources:

- Thermal emission source of Tungsten wire or LaB<sub>6</sub> crystal require high temperature of filament and high vacuum,
- Field emission source where high voltage is used and an ultra high vacuum is required.

Condenser lenses (CL 1, CL 2) and sometimes a condense aperture are forming the illumination system. The specimen (sample) has to be very thin (10-100 nm) for an easy penetration of the electron beam. The electron beam goes through the specimen. The

objective lens (OL) produces the image by focusing the electron beam in the object plane. For a high-resolution image, the intermediate lens (IL), the intermediate aperture (IA) and the projective lens (PL) are necessary for the microscope magnification. At the end of TEM microscope, a screen detector or camera is needed for “seeing” the image produced by the interaction electron beam – specimen. Electron speed is measured by installing an electron spectrometer before the screen detector.

TEM microscope allows “to look” inside the material by making a projection of the interior of the specimen.

A main advantage of TEM is the possibility to obtain information from imaging mode and diffraction mode almost simultaneously.

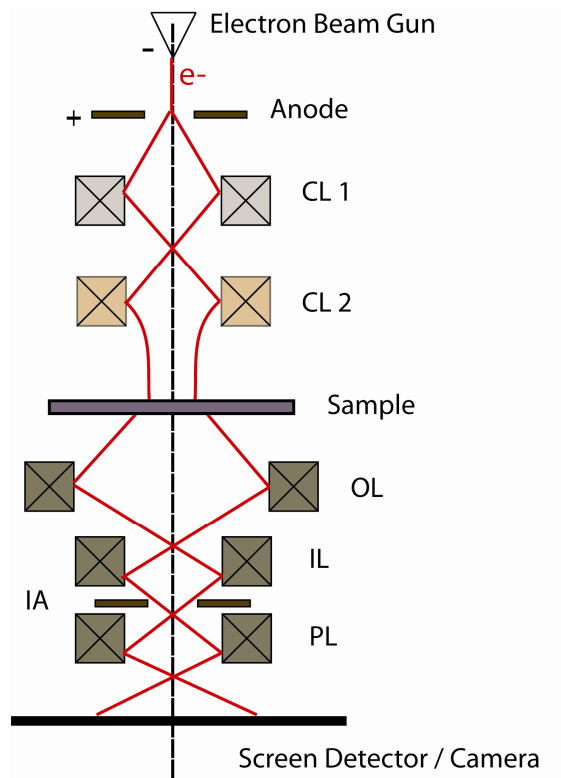


**Figure 46. Schematic Setup of a Transmission Electron Microscope (TEM) (13)**

SEM setup is similar to TEM setup (see Figure 47). A SEM microscope “looks” at the surface of materials (specimen). An accelerated electron beam as in the TEM setup is focused using the condenser lenses system (CL 1, CL 2) and the aperture. The electronic spot is scanned onto the surface using scan coils (SC) and condenser lens (CL 3). The electron detector is placed close to the specimen for a better measure of scattered species (electrons, light, etc.). There is a direct correlation between the signal from the detector and the intensity on the TV screen. Analyzed TV screen allows visualization of SEM images.

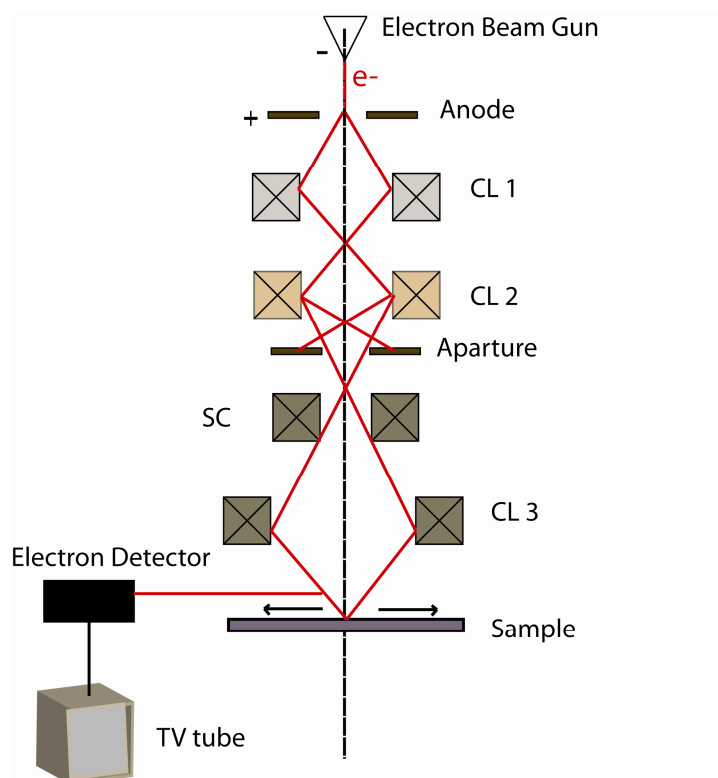


Figure 47. Schematic Setup of a Scanning Electron Microscope (SEM) (13)

#### 3.4.2.4 Our experiments using electron microscopy

A Transmission Electron microscope (TEM, Philips CM200) provided information about particle size and shape of inorganic crystals in Transmission mode and crystalline structure in Electron Diffraction mode (low dose mode at 200 kV accelerating voltage.). Images were taken with a numerical camera (Gatan, Orius 1000). The resolution of this set-up is about 0.2 nm.

For homogeneity of films and thickness measurements, SEM images were recorded using an Environmental Scanning Electron Microscopy (ESEM, FEI Quanta 400).

### 3.4.3 UV-Visible Spectroscopy

#### 3.4.3.1 Basic theory and concepts

UV-Vis spectroscopy is used for measuring the optical absorbance of films (our case) which is often proportional to quantity of a given component (active molecule in UV-Vis domain). It is used for identification of molecules and for determination of molecule concentration. It can be used to determinate small quantities of a drug from body fluids, metal traces from alloys, the study of enzymes (speed of enzymatic reaction, relative proportions of different enzymes) and different chemical transformations.

The absorption of visible light is what makes things colored. A close relation exists between the color of a substance and its electronic structure.

The wavelength range of UV-Vis light (see Figure 48) is between 10 nm (far UV) and 200 nm (near UV) to 750 nm.

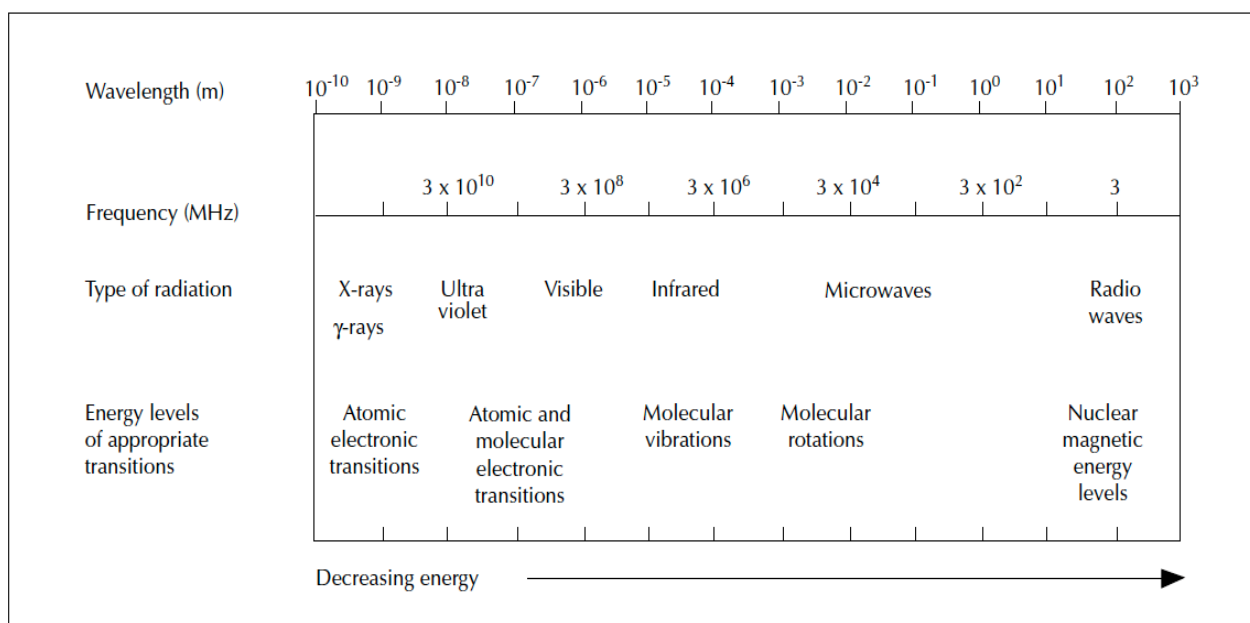
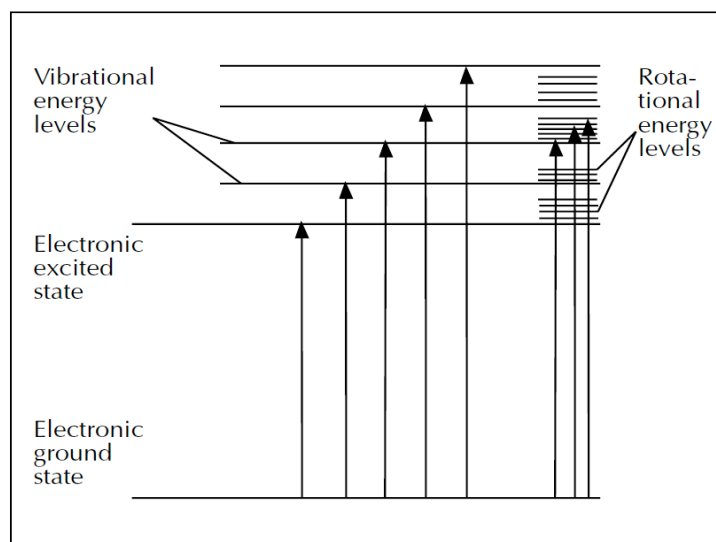


Figure 48. Electromagnetic spectrum

Absorbed radiation (in ultraviolet or visible region) produces electron transitions between electronic ground states to electronic excited states of a molecule.

Electronic energy level (electronic state) of a molecule has precise values (see Figure 49). In the case of a simple molecule, energy levels are widely separated and the absorption of a high-energy photon can produce the excitation from ground to excited state.



**Figure 49. Absorption in the electronic levels of a molecule**

In complex molecules, energy levels are more closely spaced and the absorption of a lower energy photon (longer wavelength) can produce vibrational changes. In contrast to single atoms, electronic transitions in molecules appear as broad adsorption bands due to the presence of vibrational states and rotational states. The absorption of photons is accompanied by changes between numerous vibrational and rotational levels.

Potentially three types of ground state orbitals may be involved: single bonding orbital ( $\sigma$ ), double or triple bonding orbital ( $\pi$ ), non-bonding orbital ( $n$ ). Absorbing the right photon (certain value of wavelength) produces the electronic transition to an unoccupied orbital (anti-bonding orbital). There are two types of anti-bonding orbitals:  $\sigma^*$  orbital and  $\pi^*$  orbital. Not every transition is possible, not every transition is seen in UV-Vis spectra (see Figure 50). Rules as LaPorte's rule, spin selection rule are applied for calculating the possible electronic transitions in UV-Vis domain (see Figure 50).

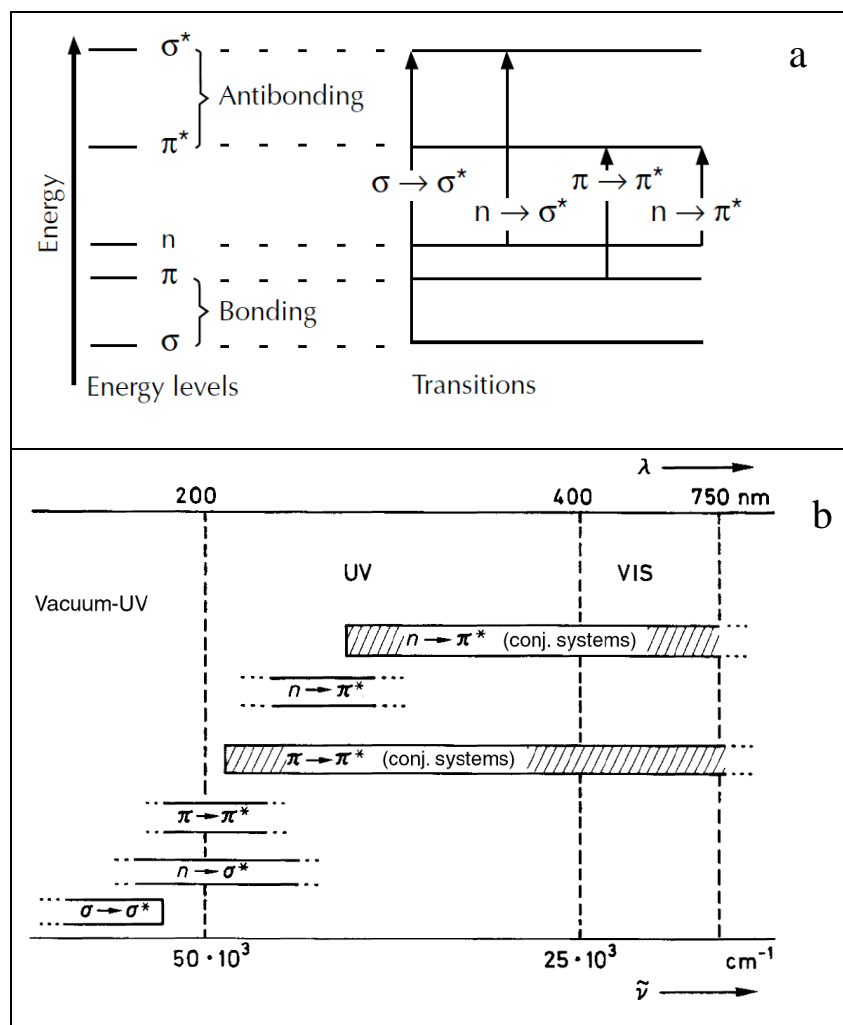


**Figure 50. Electronic transitions in UV-Vis spectroscopy (15)**

The Beer-Lambert law is used in UV-Vis spectroscopy (Equation 1). It states that the concentration of a substance in solution is directly proportional to the absorbance (A) of the solution.

$$A = \log_{10} \left( \frac{I_0}{I} \right) = \epsilon \cdot l \cdot c \quad \text{Equation 1}$$

$I_0$  = the intensity of incident light

$I$  = the intensity of transmitted light

$\epsilon$  = the molar absorption coefficient

$l$  = the path length of absorbing solution (cm)

$c$  = the concentration of absorbing molecules in solution (mole/dm<sup>3</sup>)

It is possible to calculate using this law: the extinction coefficient ( $\epsilon$ ) and the wavelength at maximum absorbance ( $\lambda_{\max}$ ) if the solution concentration and cell dimensions are known. In industry, this law is most applied for concentration calculations of different solutions when the extinction coefficient of the substance is known.

### 3.4.3.2 The spectrometer

Two types of spectrometers are available: single beam instruments and two beam instruments. In our study, we used a double beam instrument (see Figure 51): one beam passes through the reference cell (only solvent) and a second beam passes simultaneously through the sample cell (solvent + active molecule in UV-Vis spectra).

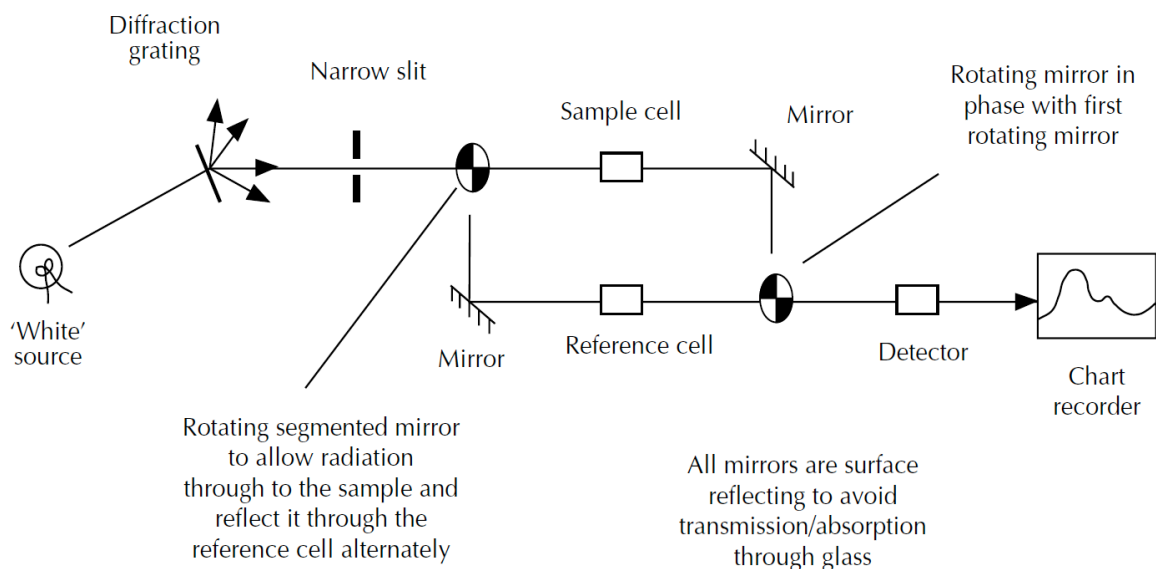


**Figure 51. Schematic diagram of a UV-Vis spectrometer (15)**

The spectrometer is equipped with two lamps: one emits in the UV domain (hydrogen/deuterium lamp) and the tungsten/halogen lamp for visible region. The spectrometer compares the light passing through the sample with the light passing



through reference cell. UV-Vis spectroscopy is a method suitable for liquids or gases but unsuitable for solids.

A Varian CARY 500 Scan UV-Vis-NIR spectrometer with the same construction concept is used in our studies.

### **3.4.4 Infrared (IR) Spectroscopy**

#### **3.4.4.1 Basic theory and concepts**

Infrared spectroscopy is one of the most important analytical techniques. It has the advantage that all material states can be studied: gases, liquids, fibers, paste, surfaces and solids. An improvement of IR spectroscopy was made in the early 1950s when dispersive instruments were replaced by FTIR (Fourier Transformer Infrared) spectrometers. FTIR spectrometers have dramatically improved the spectra quality and the acquisition time for IR spectra (16, 17).

IR spectroscopy as other spectroscopy methods is based on the interactions between the electromagnetic radiation and the matter. It implies radiations from the infrared region of electromagnetic spectrum (see Figure 48). If UV-Vis radiations produce changes in electron distribution of molecules, the IR radiations (less energetic radiations) produce changes in the molecule's configuration.

As UV-Vis spectra, IR spectra have broad peaks. There are a few factors that influence the broadening of peaks such as collisions between molecules, finite lifetime of states involved in transitions and indistinct values of energy states.

Infrared spectroscopy is a technique based on the vibrations of the atoms of a molecule. As UV-Vis spectroscopy, IR spectroscopy has its own rules (17). A molecule is active in IR spectroscopy if it has an electric dipole momentum during the molecular vibration. This is the main rule for IR spectroscopy. Dipole momentum of a molecular bond changes when a bond can expand or contract in time. Atoms are moving in a molecule, there are  $3N$  degrees of freedom in a polyatomic molecule (translation, rotation, vibration), where  $N$  is the number of atoms. An example of a "non-active" molecule in IR is a homonuclear diatomic molecule that has the dipole momentum constantly equal to zero.

Generally, symmetrical molecules have fewer “infrared active” vibrations.

There are different types of vibrations in a molecule: stretching (changes in bond length), bending (changes in angle bond). They can be symmetrical (in phase) or asymmetrical (out-a-phase), in the sample plan (in-plane) or out-of-plane (see Figure 52).

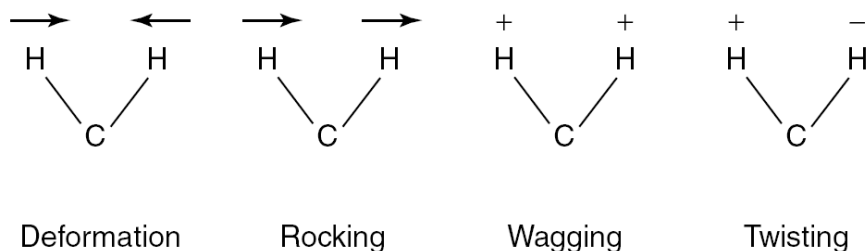


**Figure 52. Different types of bending vibrations**

The broadening and complexity of an IR spectrum come from the coupling of vibrations from a bond to neighbors bonds of a molecule. The coupling of dipole moment creates skeletal vibrations in a part of the molecule or in the molecule entirely. Database for special bands as carbonyl (C=O), double bond (C=C) or (N=N), carbon-nitrogen bond (C-N) exists for different organic/inorganic molecules.

#### 3.4.4.2 FTIR spectrometer

The idea of a FTIR spectrometer is the interference of two beams to obtain an interferogram. The interferogram is converted by the mathematical Fourier Transformer to wavelength. There are three main parts in a FTIR spectrometer: the beam source, the interferometer and the detector.



**Figure 53. Schematic illustration of FTIR spectrometer parts**

The monochromator from the dispersive spectrometer is replaced with an interferometer in the FTIR spectrometer. The problem of the monochromator is that is limited in wavelength range, response time and sensitivity. One advantage of the interferometer is that it acquires spectra with accuracy better than 0.01 cm<sup>-1</sup> using helium/neon laser as an internal reference.

The most used interferometer is the Michelson interferometer (see Figure 54), which consists of a beamsplitter and two mirrors: one fixed and the second mobile. The two mirrors are perpendicular to each other. The beamsplitter is a germanium or iron oxide coated infrared transparent support.

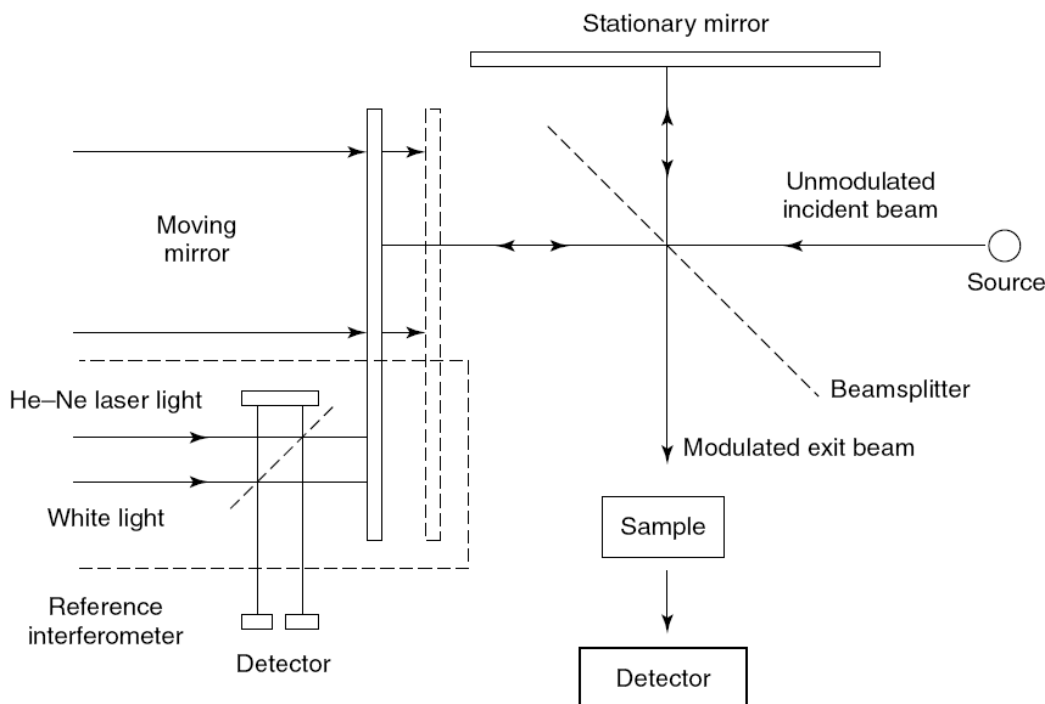


**Figure 54. Schematic of a Michelson interferometer (17)**

The radiation from the source encounters the beamsplitter of the interferometer and is split into two equal parts. 50% of the beam reaches the fixed mirror and the other 50% of the beam is transmitted to the mobile mirror. Beams transmitted from the two mirrors are recombined on the beamsplitter and the resultant beam is transmitted to the sample and then to the detector. Initially, both beams have the same optical path length (same phase), but varying the position of the moving mirror relative to the fixed mirror creates differences in the optical paths between the two split beams. The interference is constructive when the beams are in phase and which gives a maximum response in the detector. The interference signal from the sample contains the IR absorption pattern. It is recorded as a function of time and moving mirror position. The maximum interferogram (interference signal) is decreasing when the active molecule is absorbing in infrared region.

Usually, the IR spectrometer is equipped with two types of detectors: deuterated triglycine sulfate (DTGS) and mercury cadmium telluride (MCT). The DTGS detector is a pyroelectric detector that delivers rapid responses because it measures the changes in temperature rather than the value of temperature. The MCT detector is a photon (or quantum) detector that depends on the quantum nature of radiation and also exhibits very fast responses. Whereas DTGS detectors operate at room temperature, MCT detectors must be maintained at liquid nitrogen temperature (77 K) to be effective.

### 3.4.4.3 Attenuated Total Reflectance (ATR) Spectroscopy

ATR spectroscopy is a helpful method when the conventional transmittance mode is not suitable for materials such as thick or highly absorbing solid and liquid materials, films, coatings, powders, threads, adhesives, polymers, and aqueous samples (17). It has the advantage that sample preparation is easily in most cases.

ATR spectroscopy uses the phenomenon of total internal reflection (see Figure 55). The total reflection of radiation beam is produced at the interface between a higher refractive index medium (crystal) and a lower refractive index medium (sample). The entering beam angle at the interface should be greater than the critical angle of reflection for a total reflection. The beam penetration depth is a function of wavelength radiation, refractive index of the sample and crystal, and angle penetration. At the interface crystal/sample, the IR beam is absorbed by the sample. The beam loses a part of its initial energy but it is continuously reflected by the reflecting interface. The detector measures the resultant attenuated radiation.

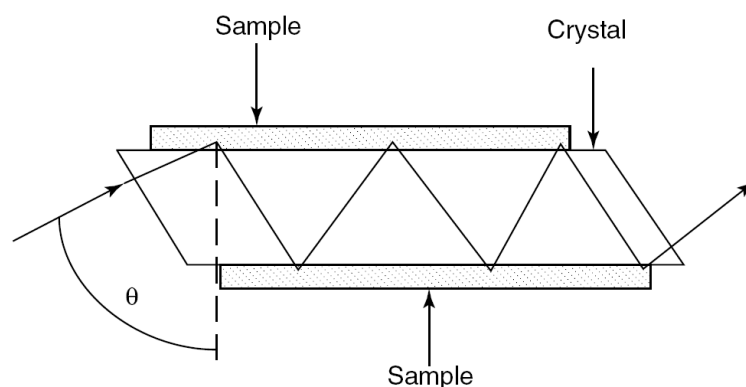


Figure 55. Scheme of a typical attenuated total reflectance set-up (17)

#### **3.4.4.4 Monitoring layer-by-layer technique by ATR spectroscopy**

Fourier transformation infrared (FTIR) spectra were recorded on a Bruker Vertex 70 spectrometer, using the ATR cell (Graseby-Specac, U.K.) equipped with a top plate (110  $\mu\text{L}$  cell volume) and a ZnSe crystal (6 reflections, dimensions of 72x10x6 mm). Measurements of multilayers were realized by injecting the different solutions in the cell using a peristaltic pump or in a dry state (construction of LbL layer was done outside the cell). A liquid-nitrogen-cooled MCT detector was employed in the liquid state and a DGTS detector in the dry state. Solutions used in the multilayer construction were prepared with  $\text{D}_2\text{O}$  to decrease  $\text{H}_2\text{O}$  signal from FTIR spectra.

#### **3.4.5 Ellipsometry**

##### **3.4.5.1 Basic theory and concepts**

Ellipsometry is an optical technique that measures changes in polarized light upon reflection and transmission on the sample. Paul Drude (1900), one of ellipsometry pioneers, carried out the first experimental studies.

Ellipsometry is a powerful tool for measuring thin film thickness, morphology interface (liquid-solid, solid-solid, liquid-vapor, liquid-liquid) or chemical composition of a sample. It is successfully used for very accurate studies of optical dielectric constants of thin films. It can be helpful in measurements of depth-profiles of interfaces, micro-roughness and composition of film layers (18).

Light is an electromagnetic wave composed by an electric field vector perpendicular to a magnetic field vector, and both vectors are perpendicular to the propagation direction. When the electric field vectors of an electromagnetic wave are all oriented in one plane, light is called polarized light. In Figure 56, a linearly polarized light is represented; the combination of two polarized beams in phase composes the linearly polarized light.

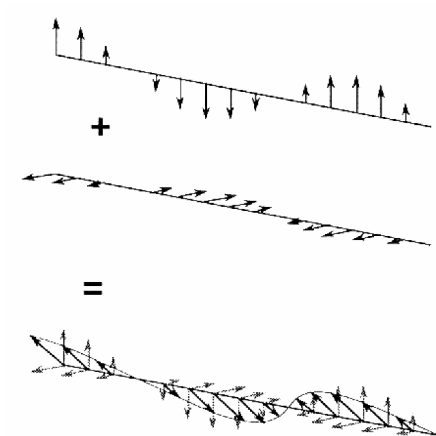


**Figure 56. Representation of a linearly polarized light (18)**

Another state of polarization of light used in ellipsometry is the elliptically polarized light. It is defined as the resultant light of two polarized beams out of phase (see Figure 56). It can be obtained from two different procedures: the linearly polarized light passes through a retarder or the light is reflected from a substrate.

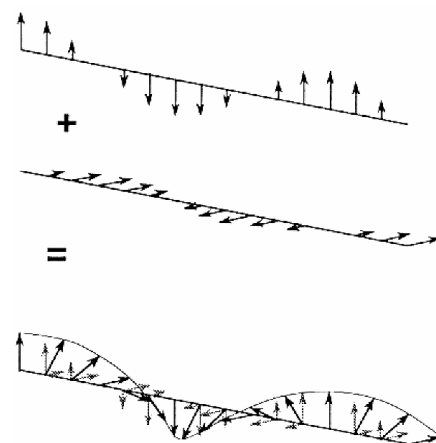


**Figure 57. Representation of an elliptically polarized light (18)**

### **3.4.5.2 Basic equation of ellipsometry**

Ellipsometry is based on physical phenomenon of reflection and refraction of light. During the ellipsometry experience, the initial polarization light state is changed after the beam reflection from the sample surface (see Figure 58). There is a shift of the phases of both components (parallel and perpendicular to the plane of incidence) of the incident

polarized light. The two directions of a polarized light are named: p-wave (p-light) when the electric field vector is oscillating in the plane of incidence and s-wave (s-light) when it is perpendicular to the plane of incidence.

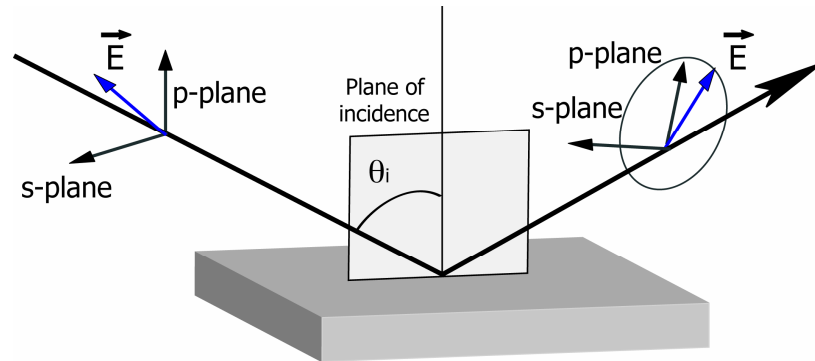


**Figure 58. Polarization state changing after reflection**

The Fresnel reflection coefficients are used to describe the ratio of wave amplitude (s-wave and p-wave) before and after the reflection. Figure 59 represents reflection/refraction phenomenon between two mediums (1 and 2) described by the Fresnel coefficients in Equation 2.

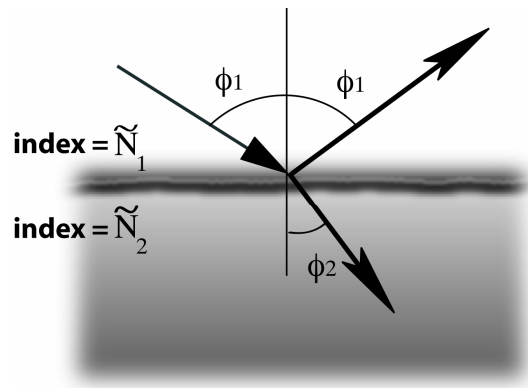


**Figure 59. Reflection and transmission of an incident beam onto a surface**

$$r_{12}^p = \frac{\tilde{N}_2 \cos \phi_1 - \tilde{N}_1 \cos \phi_2}{\tilde{N}_2 \cos \phi_1 + \tilde{N}_1 \cos \phi_2} \quad r_{12}^s = \frac{\tilde{N}_1 \cos \phi_1 - \tilde{N}_2 \cos \phi_2}{\tilde{N}_1 \cos \phi_1 + \tilde{N}_2 \cos \phi_2} \quad \text{Equation 2}$$

The reflectance is defined as the intensity ratio for both s-light and p-light. Equation 3 describes mathematically the reflectance.

$$\mathfrak{R}^p = |r_{12}^p|^2 \quad \mathfrak{R}^s = |r_{12}^s|^2 \quad \text{Equation 3}$$

What are recorded during the ellipsometry measurement of a thin film thickness are the amplitude and the phase of both s and p components. The Fresnel coefficients (or total reflection coefficients) have the form of a complex number in this case (see Equation 4). The reflectance is therefore calculated from the Equation 6.

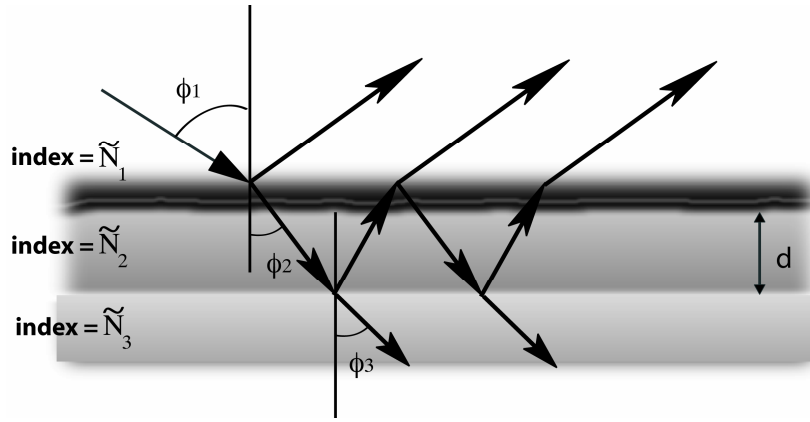


**Figure 60. Reflection and transmission with multiple interfaces (such as a multilayer film)**

$$R^p = \frac{r_{12}^p + r_{23}^p \cdot e^{-2i\beta}}{1 + r_{12}^p \cdot r_{23}^p \cdot e^{-2i\beta}} \quad R^s = \frac{r_{12}^s + r_{23}^s \cdot e^{-2i\beta}}{1 + r_{12}^s \cdot r_{23}^s \cdot e^{-2i\beta}} \quad \text{Equation 4}$$

Equation 5 defines  $\beta$  coefficient that describes the phase change from the top to the bottom of the film. Equation 6 links the Fresnel coefficients with the reflectance.

$$\beta = 2\pi \left( \frac{d}{\lambda} \right) \tilde{N}_2 \cos \phi_2 \quad \text{Equation 5}$$

$$\mathfrak{R}^p = |R^p|^2 \quad \mathfrak{R}^s = |R^s|^2 \quad \text{Equation 6}$$

The fundamental equation of ellipsometry (Equation 8) is defined as a relation between the phase difference induced by reflection ( $\Delta$  defined in Equation 7) and the ratio of the amplitude before and after reflection ( $\Psi$ ).



$$\Delta = \delta_1 - \delta_2 \quad \text{Equation 7}$$

$$\frac{R^p}{R^s} = \tan \psi \cdot e^{i\Delta} \quad \text{Equation 8}$$

$\Delta$  and  $\Psi$  are the two parameters given without any mathematical treatment by the ellipsometer. Physical properties such as thickness and refractive index are calculated after a mathematical model. There are some hypothesis that should be verified for calculation model close to real phenomenon: uniformity of film (difficult approximation for graded and anisotropic layers), plane parallel interfaces (the roughness is a problem in precise ellipsometric measurements), optical constants values known for multilayers.

### 3.4.5.3 Design of an ellipsometer

We can classify the ellipsometers into three main categories: null ellipsometer, photometric ellipsometer and spectroscopic ellipsometer (18). In Figure 61, more possibilities for ellipsometer configuration are presented.

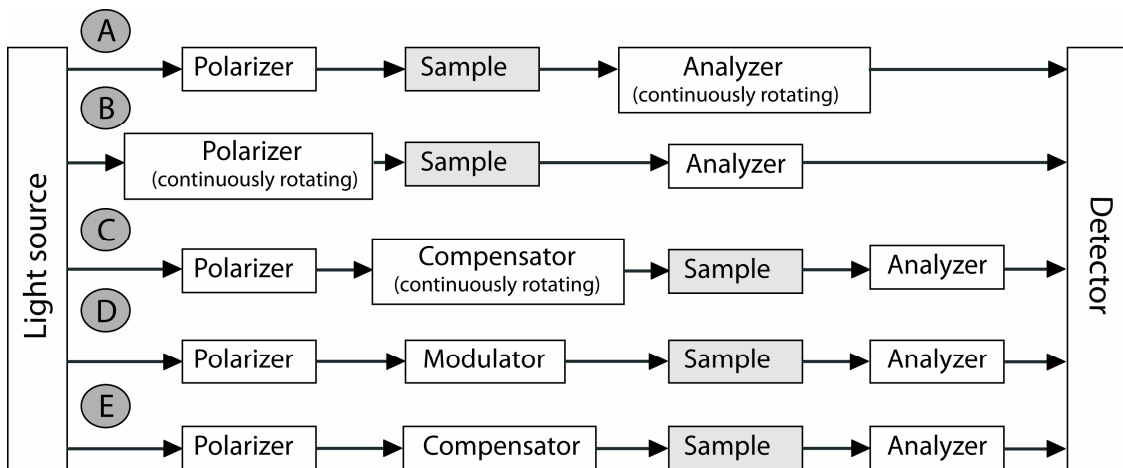


**Figure 61. Different types of ellipsometer configurations. (A) Rotating Analyzer Ellipsometer (RAE), (B) Rotating Polarizer Ellipsometer (RPE), (C) Rotating Compensator Ellipsometer (RCE), (D) Phase Modulation Ellipsometer (PME), (E) Null Ellipsometer (NE)**

The main components of a Null Ellipsometer (Figure 62) are a light source, a polarizer which produces linearly polarized light, a compensator which introduces a defined retardation of one field component with respect to orthogonal one (elliptically polarized light), an analyzer for reflected linearly polarized light and a detector.

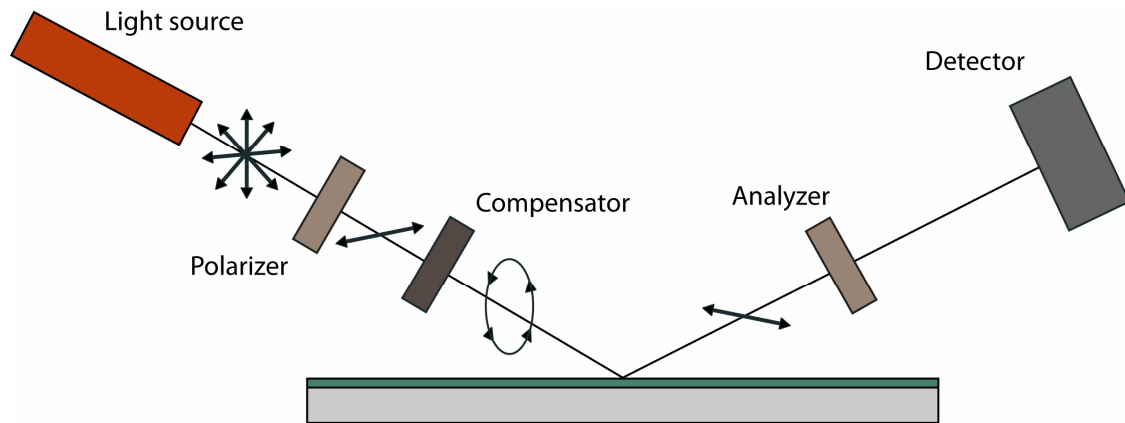


**Figure 62. The configuration of a Null Ellipsometer (NE)**

The Null Ellipsometer is characterized by automatically changing analyzer position for a minimum signal for detection.

The Phase Modulated Ellipsometer is more suited for modern-day since a faster response is recorded. The polarizer is usually fixed at 45°C, only the analyzer is rotated (Figure 63). It measures the intensity of reflected light as a function of time during analyzer rotation.

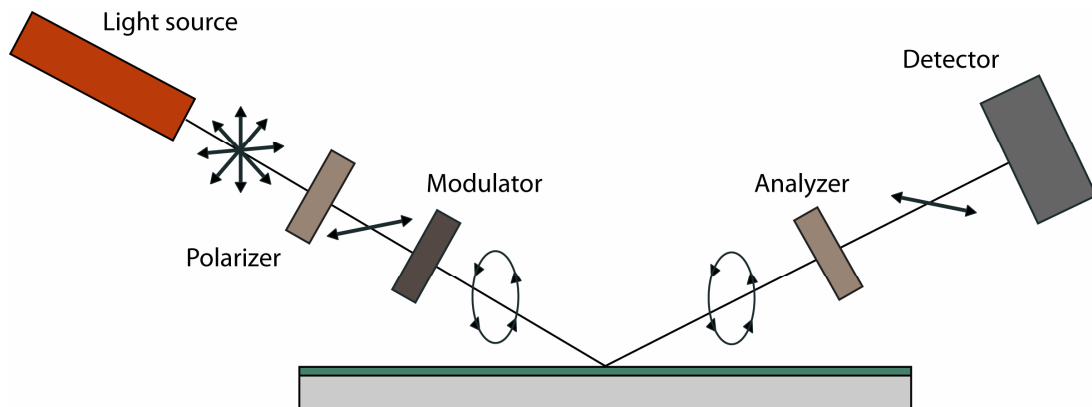


**Figure 63. The configuration of a Phase Modulation Ellipsometer (PME)**

#### **3.4.5.4 Ellipsometers in our laboratory**

PLASMOS SD2300 ellipsometer (Horiba Jobin Yvon, France) and a Multiskop ellipsometer (Optrel GbR, Kleinmachnow, Germany) are used for measuring film thickness. In the case of PLASMOS SD2300 ellipsometer (Rotating Analyzer ellipsometer), it works at a fixed incident angle of  $70^\circ$  and a single wavelength of 632.8 nm (He/Ne laser source). It is used for quick routine measurements (10 measurements for one scan). The calculating model behind the thickness measurement approximates the refractive index of the film with the refractive of silicon dioxide 1.465.

Multiskop ellipsometer (Null ellipsometer) is a more sophisticated ellipsometer with more measurement options (ellipsometry, surface plasmons, contact angle etc.). The incident angle can vary from  $0^\circ$  to  $90^\circ$ , adjustable refractive index and robust mathematical model. It is used for more accurate thickness measurements.

### 3.5 Bibliography

1. <http://www.airbrushmuseum.com>.
2. J. Eggers, E. Villermaux, *Reports on Progress in Physics* **71**, (2008).
3. N. K. Rizk, A. H. Lefebvre, *Journal of Energy* **6**, 323 (1982).
4. J. Bellan, *Progress in Energy and Combustion Science* **26**, 329 (2000).
5. A. Lefebvre, (1989).
6. F. J. Giessibl, *Reviews of Modern Physics* **75**, 949 (2003).
7. D. Ricci, P. C. Braga, *Methods Mol Biol* **242**, 13 (2004).
8. A. L. Weisenhorn, P. K. Hansma, T. R. Albrecht, C. F. Quate, *Applied Physics Letters* **54**, 2651 (1989).
9. [www.tedpella.com/probes\\_html/budgetsensors-1.htm#TAP300](http://www.tedpella.com/probes_html/budgetsensors-1.htm#TAP300).
10. V. I. Inc., (2004).
11. R. Garcia, R. Perez, *Surface Science Reports* **47**, 197 (2002).
12. R. D. Piner, J. Zhu, F. Xu, S. H. Hong, C. A. Mirkin, *Science* **283**, 661 (1999).
13. F. Banhardt, (2008).
14. D. v. D. S. Amelinckx, J. van Landuyt, G. v. Tendeloo, (1997).
15. *Royal Society Chemistry*.
16. S. Hsu, *Handbook of Instrumental Techniques for Analytical Chemistry*.
17. B. Stuart, *John Wiley & Sons, Ltd*, (2004).
18. I. Harland G. Tompkins.

# Results and Discussions



## 4 Results and discussion

### 4.1 Collagen based LbL multilayers

#### 4.1.1 Multilayer growth

##### 4.1.1.1 Ellipsometry and UV-Vis spectroscopy results

Collagen is a major structural protein in tissues, widely used in medical applications (1). It exists in different forms with type I being the most common. Its tertiary structure forms triple helices, and this entity is physico-chemically stable in solution (2-4). Collagen provides the necessary environment for cell attachment (5).

The major impediment to dissolution of collagen type I from tissue is the presence of covalent crosslinking between molecules. Collagen is insoluble in the majority of organic solvents. It is reported that water-soluble collagen represents only a small fraction of total collagen and the amount depends on the age of the animal and type of tissue extracted (6). Furthermore, collagen molecules present within fibrillar aggregates can be dissociated and brought into aqueous solution.

There is no consensus in the literature regarding the isoelectric point (iep) value of collagen. Experimental values of isoelectric point 5.5 (7) and 9 (8) were reported. The isoelectric point may be strongly affected by the way the collagen sample was produced (9). The net charge of type-I collagen, once dissolved in a solution at pH 4, is positive due to its isoelectric point value. The use of Collagen for the LbL film construction is already reported in the literature (5, 10, 11).

We chose different negatively charged polyelectrolytes as partners for the Collagen to prepare the LbL film: PSS, Alginate (Alg) or Dextran Sulfate (Dex). Both dipping and spraying were used for the deposition films (Figure 64a). The dipping method is more time consuming than the spraying method. Each polyelectrolyte adsorption takes 20 min and followed by the rinsing step which takes 2 min. In total, 44 min are needed for the deposition of one single layer pair. On the other hand, for the spray-coating process the

adsorption and rearrangement of adsorbed chains on the surface and the elimination of weakly bound polymer chains from the substrate are achieved almost simultaneously at a high rate of liquid drainage over a short time period. During spraying, the concentration of the polyelectrolyte solution is significantly increased when the sprayed solution reaches the substrate because of the rapid solvent evaporation. This spray preparation method can accelerate polymers adsorption time from 25 to 150 times depending on the chemical nature of the compounds and the experimental parameters. Preparing one layer pair took roughly 1 min for the spraying deposition. Generally, confirmed by X-ray reflectometry and AFM analysis, a sprayed polyelectrolyte multilayer is thinner but smoother one prepared by dipping (12). The sprayed Collagen films show the same behaviors as reported in the literature: the thickness and the roughness of sprayed films are lower than the dipped ones (Figure 64a).

This fact can be attributed to the fact that the newly absorbing layers do not necessarily reach their equilibrium thickness at a short contact time (13).

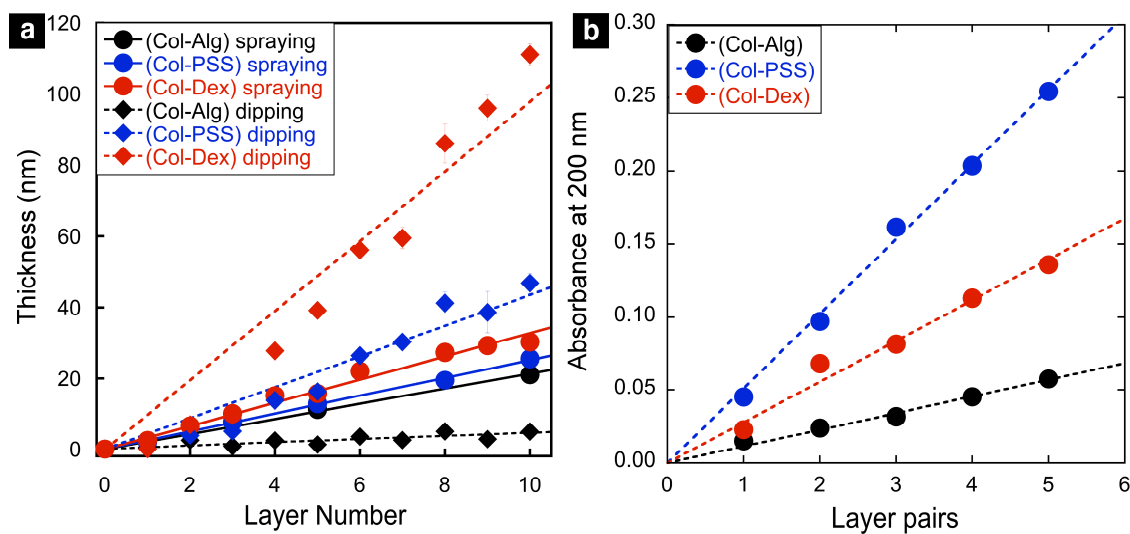


**Figure 64. Collagen LbL films deposition: thickness and UV-Vis absorbance measurements. The UV-Vis measurements were realized for sprayed LbL films. The dipping deposition parameters are: the dipping time per polyelectrolyte (20 min), the rinsing time (1 min per bath) using 2 consecutive baths. The spraying parameters for film deposition are: the spraying time per polyelectrolyte (5 sec), the polyelectrolyte adsorption time (15 sec), the rinsing time (5 sec).**



Oppositely to thickness values the (Col-PSS) film absorbance was higher than the (Col-Dex) film absorbance since the PSS absorbs around 220-225 nm and the Dex doesn't absorb in the UV-Vis region. For the other film, (Col-Alg), the Collagen absorbance is observed around 250-280 nm and the Alginate doesn't absorb in the UV-Vis domain. We calculated the thickness/absorbance values per layer pair (see Table 12) from the film thickness curve (ellipsometry) and the film absorbance slopes (UV-Vis) film (Figure 64).

<b>LbL film</b>	<b>Thickness per layer pair (nm)</b>	<b>Absorbance per layer pair (a.u.)</b>
<b>(Col-PSS)</b>	2.52	0.051
<b>(Col-Dex)</b>	3.27	0.028
<b>(Col-Alg)</b>	2.14	0.011

**Table 12.** Values calculated from Figure 64 corresponds to thickness/ absorbance increment per layer pair

#### **4.1.1.2 FTIR-ATR spectroscopy**

With the aim to obtain information about the Collagen LbL film structure and organization, we used the FTIR-ATR spectroscopy in the dry state. We followed the (Col-PSS) LbL film construction of 10 layer pairs (see Figure 65).

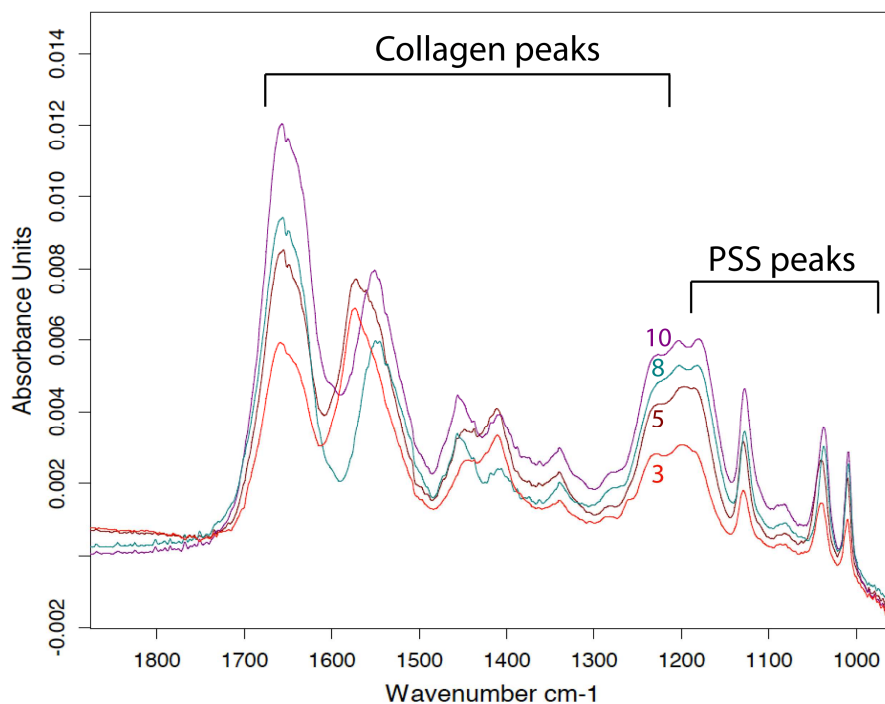


**Figure 65.** The FTIR-ATR spectra for the (Col-PSS) film prepared by LbL technique. The spectra are represented for different layer pairs 3, 5, 8 and 10, of the sprayed film.

The (Col-PSS) film growth was previously studied by ellipsometry and UV-Vis spectroscopy (Figure 64). The FTIR results confirm the linear growth of the LbL film (see Figure 65). The absorbance increase of the characteristic PSS peaks (around 1010 and 1040  $\text{cm}^{-1}$ ) characterizes the (Col-PSS) film deposition rate. The slight difference in deposition rate observed from the two PSS characteristic peaks may be due to the errors coming from the baseline correction.

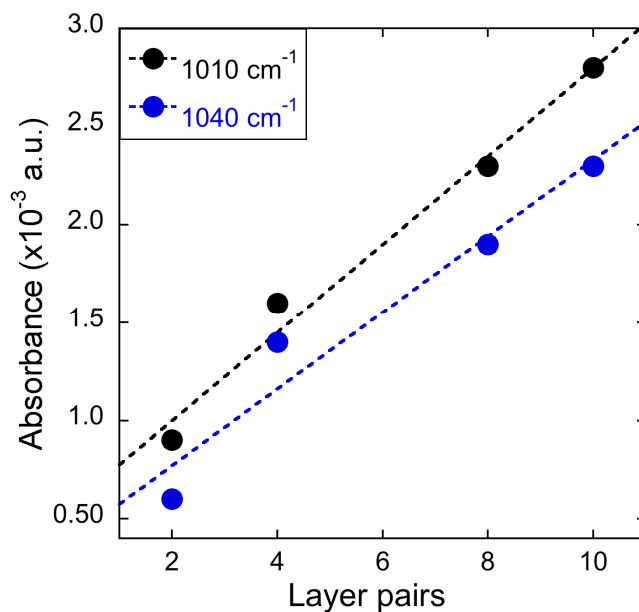


**Figure 66.** The linear growth of the (Col-PSS) LbL film absorbance (corresponding to PSS peaks: 1010 and 1040  $\text{cm}^{-1}$ ).

The Table 13 presents the characteristic peaks of the FTIR-ATR spectra for the sprayed LbL (Col-PSS)10 film.

Polyelectrolyte	Peak wave number $\text{cm}^{-1}$ from FTIR spectra
Collagen	1204, 1230, 1338, 1408, 1455, 1551, 1650, 1656 (1573, 1654)
PSS	1008, 1035, 1126, 1179

**Table 13.** Peak assignment for the (PSS-Col) film prepared by the LbL spraying technique

The PSS absorbs in the IR domain (see Table 13). The LbL (PAH-PSS) film formation was previously followed by FTIR spectroscopy which showed that the PSS characteristic peaks do not overlap with the PAH peaks (PAH gives a low signal in IR).

Frequency (cm <sup>-1</sup> )	Assignment
1008, 1126	Benzene ring: in plane skeleton vibration and in plane bending vibration
1035, 1179	SO <sup>3-</sup> group: antisymmetric and symmetric vibrations

**Table 14. PSS characteristic peaks and their assignment**

Fourier transform infrared (FTIR) spectroscopy is used to study the changes of the Collagen structure (primary to secondary structure), the crosslinking of collagen, the denaturation or the thermal self-assembly of Collagen. The Collagen's peaks position are assigned to various characteristic Collagen vibration bonds (bending, wagging, stretching).

There is a frequency shift of the absorption bands for amide II of Collagen. The shift is visible between the 6<sup>th</sup> and the 8<sup>th</sup> layer pairs of the (Collagen-PSS) multilayer film.

The intensity of absorption bands increases with the number of layer pairs (see Figure 65). It should be noted that the FTIR spectra of the 4<sup>th</sup> and the 6<sup>th</sup> layer pairs are similar. A change in intensity of the different amide bands (I, II, III) can be observed at the transition between the 6<sup>th</sup> to the 8<sup>th</sup> layer pairs. The intensities of amide I peak band and the peak at 1455 cm<sup>-1</sup> are increased. The intensities of amide II peak and the peak at 1408 cm<sup>-1</sup> are decreased.

Frequency (cm <sup>-1</sup> )	Assignment
1020-1130	C-O stretch
1230-1250	Amide III (N-H bend)
1420-1460	CH <sub>2</sub> bend, CH <sub>2</sub> wagging of proline (amino acid about 9% of collagen)
1540-1570	Amide II (N-H bend coupled with C-N stretch)
1640-1670	Amide I (C=O bend, Hydrogen bonding coupled with COO <sup>-</sup> )
2350-2930	CH <sub>2</sub> asymmetrical and symmetrical stretch
3070-3080	Amide B (N-H stretch)
3310-3630	Amide A (N-H stretch coupled with Hydrogen bonding)

**Table 15. The Collagen (Col) characteristic peaks and their assignment**

The same behavior (high shift in Amide II and amide III peaks combined with an increase in the Amide I peak intensity) has been observed in literature (14) for a study where the value of relative humidity (RH) of a Collagen film was changed from 0% to 76%. The interaction of water molecules with Gly-X-Y chain of Collagen stabilizes the Collagen triple helix. The lowly hydrated triple helix can be reversibly converted to a highly hydrated triple helix by simple addition of water. The water molecules can bind to C=O and C-N polar groups of the collagen.

The two peaks (1408 and 1455  $\text{cm}^{-1}$ ) are assigned to aliphatic side groups of various amino acids residues (15). The peak at 1408  $\text{cm}^{-1}$  is assigned to  $\text{CH}_2$  wagging from Proline (Collagen).

Our FTIR results for the LBL film construction showed the same tendency as increasing the RH of pure collagen films. The LBL films are dried for each FTIR measurement. In order to understand the water excess in the film with the increase in the number of layer pairs, we suppose that the film thickness increases significantly so that it becomes so eliminate all the water molecules from the film by air-drying. In conclusion, we noticed using FTIR spectroscopy that the water molecules can change the polyelectrolyte conformation inside the film.

#### **4.1.2 The Collagen Lbl film topography by AFM microscopy**

The fibrillar structure of the Collagen LBL films, already reported in the literature, was observed by the tapping mode AFM in the air (16-18). The film roughness increases with the number of deposited layer pairs (see Figure 67). The Collagen fibers adsorb as random single fibrils or multistrands fibrils in an inter-twisted form. In this case, the Collagen is deposited directly on the clean silica surface (negatively charged).

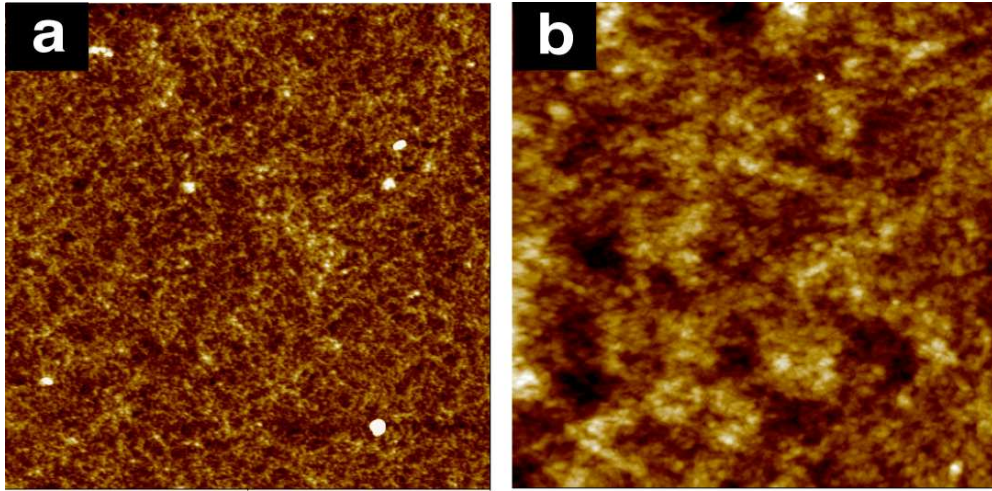


**Figure 67.** The AFM image of the  $(\text{Col-PSS})_5$  film (a) and the  $(\text{Col-PSS})_{25}$  film (b) sprayed directly on the silica wafers. The scale image (a, b) is  $5 \times 5 \mu\text{m}$ .

In order to have a better adhesion of the LbL film on the surface and a better homogeneity of the deposited film, a first layer of PEI was absorbed on the substrate. The film prepared with PEI as the first layer has similar to the LbL film without PEI layer. The fibrillar structure is not revealed from the first Collagen layer adsorbed on PEI. This could be due to the fact that the quantity of Collagen adsorbed is low and the PSS layer homogeneously “covers” the Collagen fibers (see Figure 68a). The collagen fibrils become more twisted and more Collagen bundles are observed when the number of layer pairs adsorbed increases. The PEI(LbL film) roughness increases when more deposition cycles are realized.

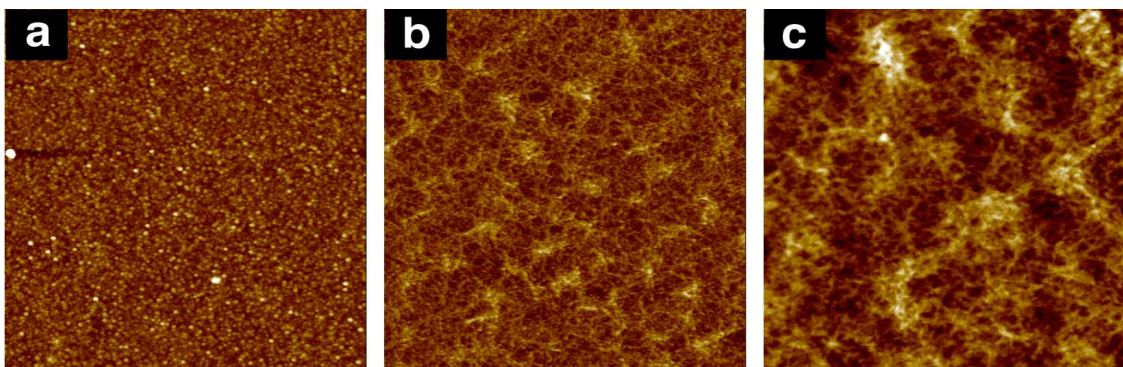


**Figure 68.** The AFM image of the sprayed  $\text{PEI}(\text{Col-PSS})_n$  films where  $n$  is the layer pair number.  $n=1$  (a),  $n= 5$  (b) and  $n= 15$  (c). The scale image (a, b, c) is  $5 \times 5 \mu\text{m}$ .

Another LbL multilayer film that was investigated for morphology studies by AFM is the (Col-Alg) film. Compared to PSS, the Collagen-Alginate film presents larger diameter of the Collagen fibers (Figure 69). The (Col-Alg)<sub>n</sub> fibrillar structure is more accentuated than the (Col-PSS)<sub>n</sub> structure, where n (number of layer pairs) can be 1, 3 or more. The single fibrils diameter and the increasing number of multistrands fibrils are observed when the film thickness (number of layer pairs) increases (see Figure 69).

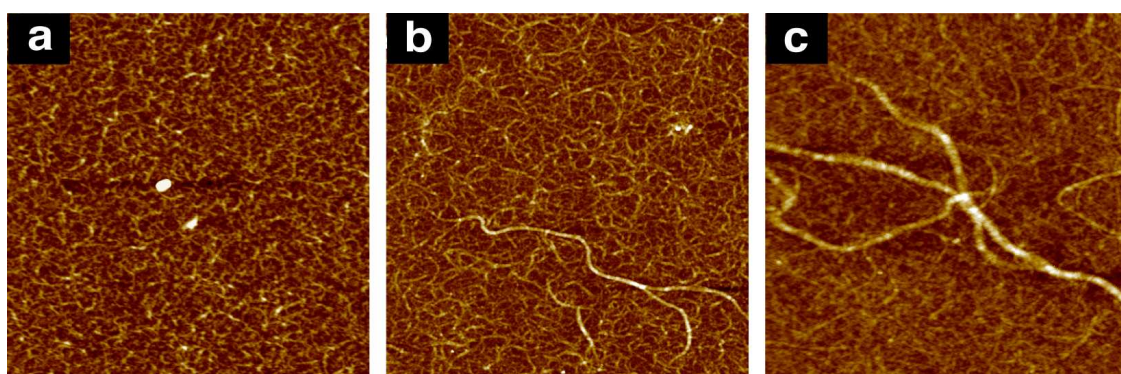


**Figure 69. Morphology study of the sprayed (Col-Alg)<sub>n</sub> films where n is the number of sprayed layer pairs. n=1 (a), n= 5 (b) and n= 30 (c). The scale image (a, b, c) is 5x5  $\mu$ m.**

One way to precisely measure the film thickness is using the scratch film analysis by AFM. The LbL film can be scratched using a sharp pen/needle for removing the deposited film. The thickness difference between the film and the substrate is recorded from the AFM image. This AFM scratch was realized for the (Col-PSS) and (Col-Alg) films (Figure 70). The (Col-PSS) film has different mechanical properties than (Col-Alg) film. The mechanical properties are linked to the electrostatic interaction forces. Since there are strong electrostatic interactions between the (Col-PSS) polyelectrolytes, the film is hard and it is easily imaged in the AFM tapping mode (Figure 70a). On the other hand, the (Col-Alg) electrostatic interaction is weaker and the film is softer which makes the recording of accurate AFM more difficult (Figure 70b).

The AFM scratch values are in agreement with the thickness values obtained from ellipsometry measurements. The (Col-PSS)<sub>5</sub> and the (Col-Alg)<sub>5</sub> film thickness are  $9.8\pm 0.9$  nm and  $2.4\pm 0.8$  nm, respectively.

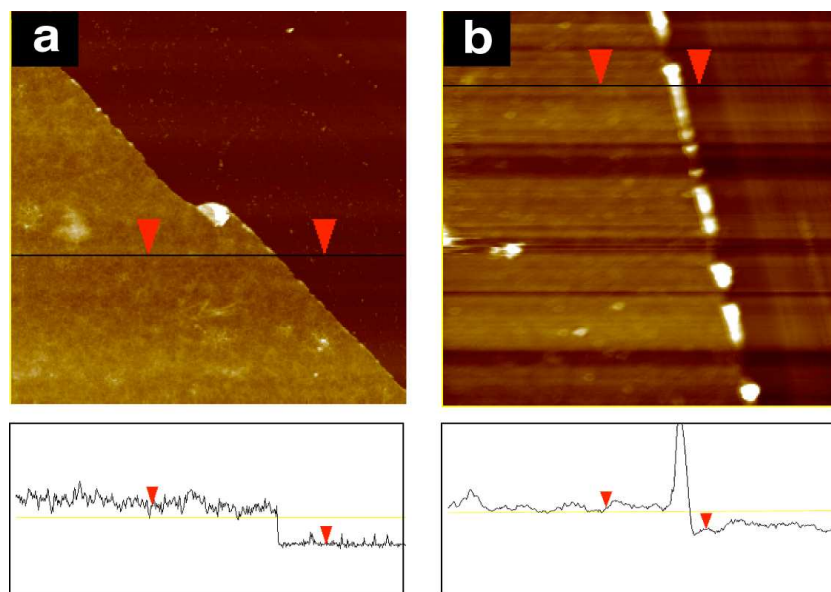


**Figure 70.** Up: Thickness measurements by the AFM scratch method for the (Col-PSS)<sub>5</sub> (a) and the (Col-Alg)<sub>5</sub> (b) films. The films are prepared directly on clean silica substrates. Bottom: Z section corresponding to the line position from the AFM image (up). The scale image (a, b) is 15x15  $\mu\text{m}$ .

#### 4.1.3 The use of Collagen non-aqueous solutions for the LbL multilayer film formation

Among the factors controlling the multilayer film structure, the charge density and the ionic strength of the adsorbed polyelectrolytes are considered to be important. These factors determine the strength of intramolecular and intermolecular electrostatic interactions and hence influence the polyelectrolyte conformation and the adsorbed amount per layer.

Another factors controlling the multilayer film structure is the quality of the solvent itself (19).

Theoretical studies suggested that the polyelectrolyte chains in poor solvents form “necklace-like” structures consisting of highly collapsed globules separated by stretched segments or strings. A few studies are reported in literature on the influence of solvent quality on the growth and structure of LbL multilayer films. The poly(styrenesulfonate sodium salt) (PSS)/poly(diallyldimethylammonium chloride) (PDADMAC) films thickness prepared from ethanol-water mixtures increases with the increasing ethanol



content in the adsorption solution (20). Carusso and al. have studied the decreasing solvent quality (the ethanol/water mixture) on the progressive (PAH-PSS) film thickness increase (19). The films exhibit an exponential-like growth and a high thickness increase close to the precipitation point of polyelectrolyte in the poor solvent.

In order to fabricate Collagen-CaP hybrid films without the CaP dissolution by the acidic pH of Collagen, we need to prepare the Collagen non-aqueous solutions. Among the non-aqueous solvents used to solubilize the Collagen fibers, the water/ethanol (or water/ethanol/ iso-propanol) mixture (3) and the HFP (1,1,1,3,3,3 hexafluoro-2-propanol) (21) are chosen for our study of LbL film formation. The LbL films prepared using the non-aqueous Collagen solvent are realized by the dipping method (previously presented).

0.1 mg/ml concentrated Collagen solutions prepared in different solvents (buffer solution pH=4, ethanol/water mixture, HFP) were used for the dipped (Col-PSS) LbL film formation. The strength of the Collagen and PSS electrostatic interaction is stronger in a good solvent as for example a buffer pH=4; it decreases for the ethanol/water mixture (50/50 %vol) and it is very low in the case of HFP.

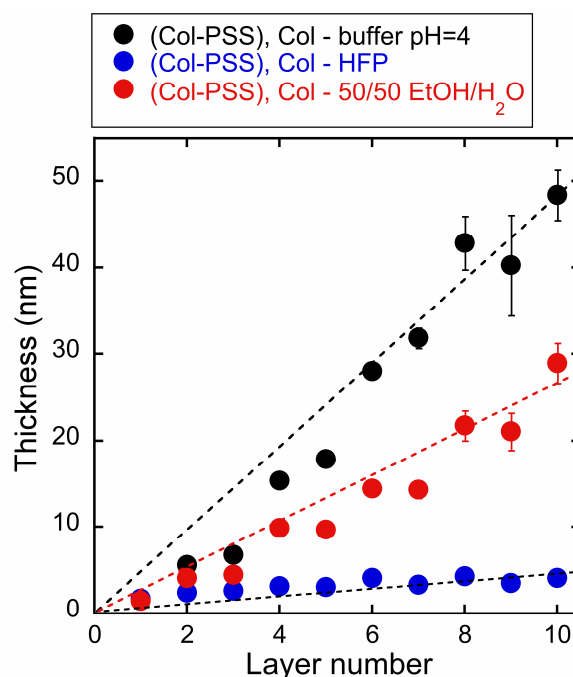


Figure 71. Ellipsometric thickness of the (Col-PSS) film prepared by the LbL technique. The dipping time per layer is 20 min, the rinsing time is 2 min (2 baths). The table below presents the Collagen solvent and its rinsing solution, and the PSS solvent and the rinsing solvent after its deposition. The EtOH/H<sub>2</sub>O ratio is 50/50 %vol.

Sample	Collagen solvent	Rinsing solvent for Collagen adsorption	PSS solvent	Rinsing solvent for PSS adsorption
1	Buffer pH=4	Water	Water	Water
2	EtOH/H <sub>2</sub> O	EtOH/H <sub>2</sub> O	EtOH/H <sub>2</sub> O	EtOH/H <sub>2</sub> O
3	HFP	HFP	Water	Water

Table 16. Solvents used for the dipped LbL (Col-PSS) film deposition

Since the charge density and the concentration solution of the Collagen (0.2 mg/ml) is lower compared to PSS (1 mg/ml), the Collagen adsorption (thickness) per layer is lower than the PSS adsorption per layer (Figure 71).

Among the Collagen films previously prepared, the EtOH/H<sub>2</sub>O (50/50 %vol) Collagen and the pH=4 buffer Collagen films were characterized by AFM, in order to obtain the topography film information (Figure 72). We already measured the film thickness for the

AFM analyzed samples by ellipsometry. The LbL (Col-PSS)<sub>3</sub> film thickness is  $13.6 \text{ nm} \pm 0.1 \text{ nm}$  for the Collagen buffer pH=4 solution and  $5.7 \text{ nm} \pm 0.3 \text{ nm}$  for the Collagen in EtOH/H<sub>2</sub>O (50/50 %vol). The roughness is greater for the ethanol-water mixture films than for usual Collagen films (buffer pH=4). In order to validate this result we compared it with the AFM measurement.

The solubilization of Collagen and the fibrillar structure of the Collagen films depend among the factors on the solvent nature. For the poor solvent (ethanol-water mixture), the fibril Collagen structure is better defined and the Collagen fiber diameter increases (Figure 72 – a, b). Single Collagen fibrils or multiple fibrils “agglomerated” together or twisted are observed for the Collagen films prepared in the ethanol-water mixture. Their presence increases the film roughness (validation of the ellipsometric result). Compared to them, the films prepared from buffer pH=4 Collagen solution are smoother and more homogeneous.

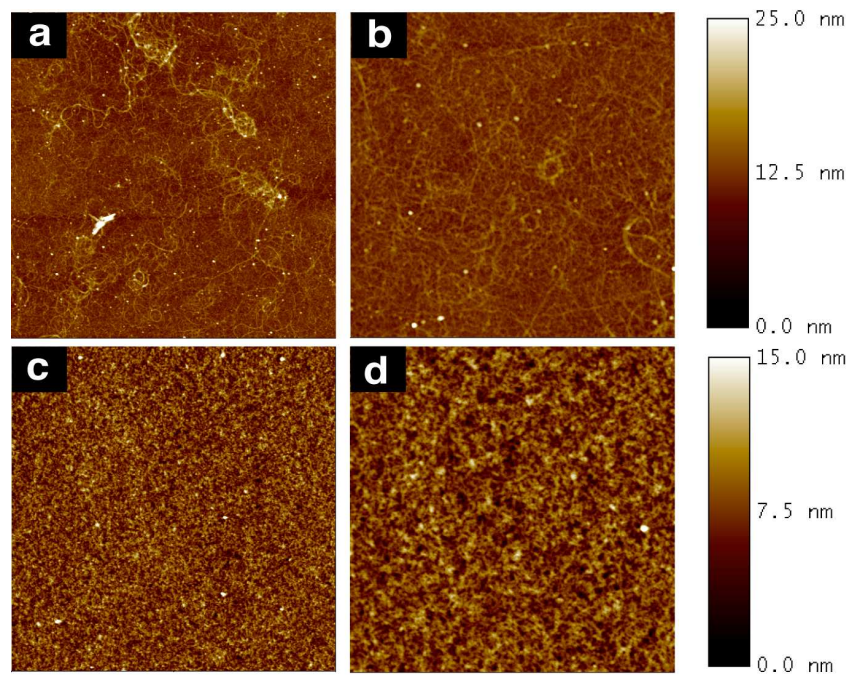


**Figure 72.** Morphology study of the dipped (Col-PSS)<sub>3</sub> films. The solvent used for the Collagen solubilization is the pH=4 buffer (a, b) and the EtOH/H<sub>2</sub>O (50/50 %vol) (c, d). The Collagen concentration is 0.2 mg/ml for all the solutions. The scale image is 5x5 μm (a, c) and 2x2 μm (b, d).

## ***4.2 Consecutive spraying method***

Inorganic coatings were deposited by consecutive and simultaneous spraying of aqueous solutions that get supersaturated after mixing on the surface. Generally, two aqueous solutions were used for spraying onto various substrates (glass, silica, quartz, thermanox). Studies using thin LbL precursor films as substrate or for hybrid film fabrication were also realized by spraying methods.

Collagen thin films are generally prepared in combination with calcium phosphate inorganic coatings for the fabrication of engineered biomaterials.

### **4.2.1 Calcium phosphate (CaP) coatings**

CaP coatings were prepared by consecutive spraying of highly concentrated aqueous solutions. However, due to polycrystallinity the inorganic films become turbid and cannot be characterized as well as classical LbL films. The CaP deposition is monitored, as far as possible, using various techniques: UV-Vis spectroscopy (substrate: quartz slide), ellipsometry (substrate: silicon oxide wafer), FTIR spectroscopy (substrate: ZnSe crystal), electron microscopy (Cu grids/ glass slides/ thermanox), AFM microscopy (various substrates).

Spraying is a deposition technique with numerous parameters that can be varied to control the deposition process. An obvious control parameter is the spraying time for each spraying step. The spraying time is in the range of seconds; it was typically varied from one-second to ten seconds. The spraying is expected to control mainly two effects:

1. The quantity of salt delivered to the surface
2. The quantity of the material removed away from the surface after exchange with the liquid in the interstitial space.

Interestingly, a maximum value of the film thickness is observed for a continuous spraying time of 2 seconds or spraying 2 times 1 second (plot included in article 1). UV-Vis measurements (Figure 73) are in agreement with ellipsometric thickness measurements (Figure 74).

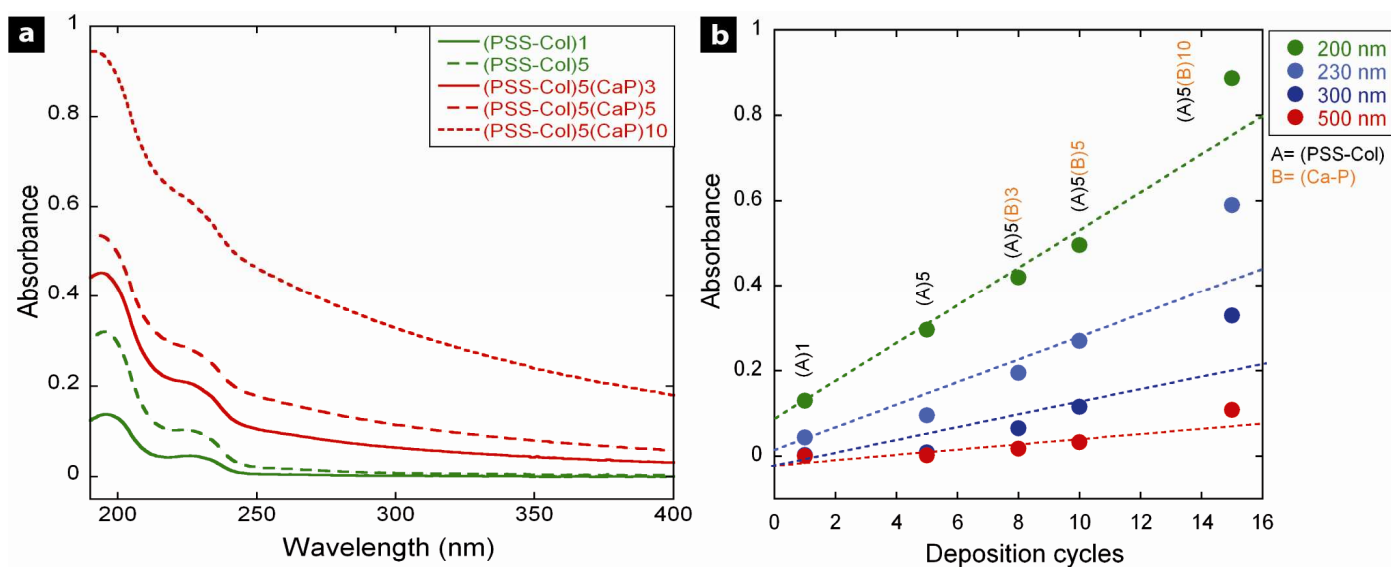


**Figure 73.** CaP deposition on a PEM (PSS-Col)<sub>5</sub> monitored by UV-Vis spectroscopy, using Ca (0.32 M) and P (0.19 M) solutions, spraying time per cycle is 2 x 1sec. a) UV-Vis spectrophotometer (raw data), b) UV-Vis absorbance of coating at 200, 230, 300 and 500 nm versus number of deposition cycles (processed data).

Ellipsometry measurements of samples prepared with different spraying times are presented in the Figure 74. For longer spraying time per cycle deposition (10 seconds, red dots), the deposition rate is practically zero. At long spray intervals it is likely that the supersaturated mixed solution that is present directly after the spraying step is more and more exchanged against the presently sprayed solution in which the inorganic compound on the surface is more soluble (than in the supersaturated solution) and thus dissolved. Another parameter that controls the film thickness is the rinsing step realized before each acquisition measurement. This is observed for the two samples (see Figure 74, blue and green dots) that are fabricated by same spraying time per deposited layer (3 seconds), but with a different number of rinsing steps. For the first experiment (see Figure 74, green dots), more rinsing steps are performed in the first stage of deposition. The coating thickness is decreased compared with the second experiment with less rinsing steps (Figure 74, blue dots).

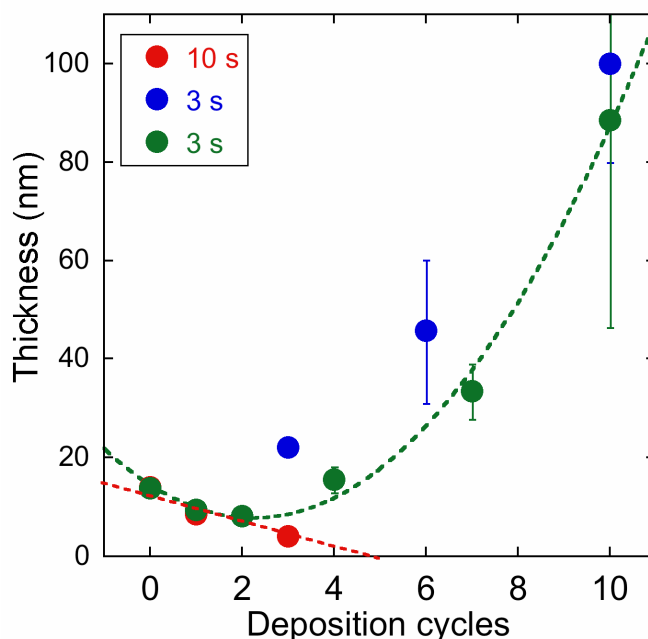


**Figure 74.** Ellipsometric thickness of CaP coatings prepared by consecutive spraying for 10 seconds per layer (red dots), or 3 seconds (green and blue dots). Ca (0.32 M) and P (0.19 M) solutions were sprayed on a LbL film of (PSS-Col)<sub>5</sub> surface.

An FTIR-ATR spectrum was recorded for CaP coating in the dry state using a ZnSe crystal. For the case of a polycrystalline film without orientation the peak intensity is proportional to the amount of crystals deposited. The IR peaks of the sprayed sample are very similar to the calcium phosphate reference peaks (22, 23) (see Table 17) which are characteristics to brushite form (DCPD, CaHPO<sub>4</sub>·2H<sub>2</sub>O). Complementary characterization measurements realized using XRD indicate the brushite form for CaP sprayed coating and then the FTIR result was validated.

Compound	Peak positions (cm <sup>-1</sup> )
Sprayed CaP coating	782, 872, 986, 1050, 1122, 1204, 1354, 1404, 1472, 1647, 3048, 3155, 3472, 3530
DCPD	530, 562, 890, 994, 1052, 1134

**Table 17.** Main FTIR peaks of CaP crystal forms

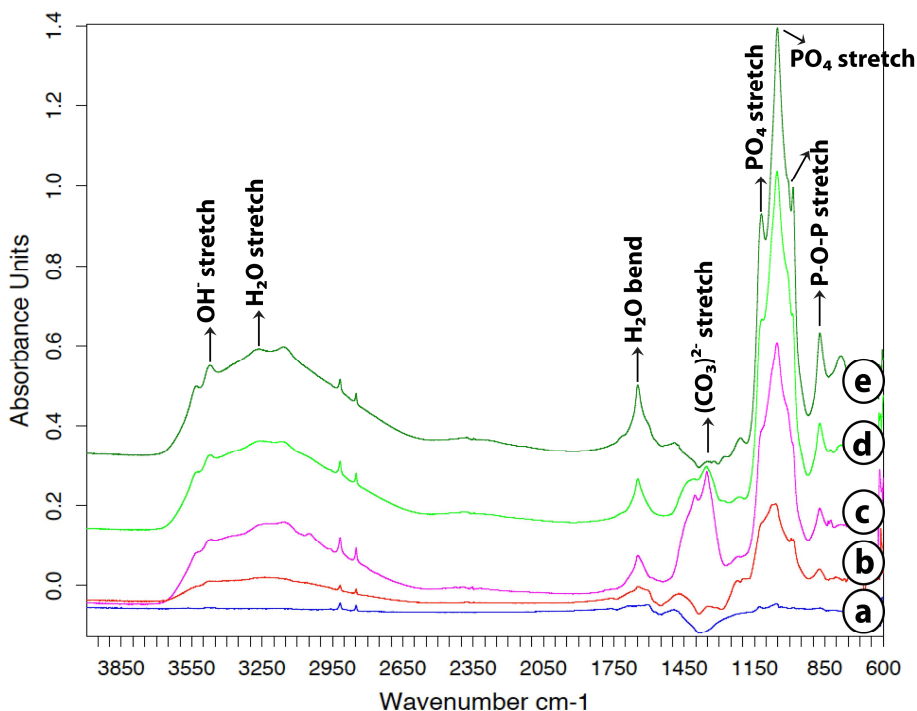


**Figure 75.** FTIR spectra recorded from CaP coatings that were prepared by consecutive spraying of Ca (0.32 M) and P (0.19 M) solutions at pH=10. Spraying time is 2x1s for aqueous solutions. Rinsing time is 5 s with Milliq water. Number of layer pairs deposited is increased from (CaP)<sub>3</sub> (a), (CaP)<sub>5</sub> (b), (CaP)<sub>10</sub> (c), (CaP)<sub>15</sub> (d) to (CaP)<sub>20</sub> (e).

For CaP coatings experiments done on different substrates showed the important influence of substrate properties at the first stage of deposition. For LbL thin films used as substrate, we observed an increase of inorganic coating deposition when the silica wafer is coated by a polyelectrolyte film (Col-Alg)<sub>10</sub> instead of (Col-Alg)<sub>10</sub>(PSS-PAH)<sub>10</sub>. FTIR spectra and UV-Vis data point out that the deposition rate is affected just for the first deposition step (visible phenomenon for first cycle deposition of (CaP)<sub>5</sub>). The substrate influence is “lost” after a certain thickness of sprayed coating. This is to be expected for a film growth mechanism in which the chemical nature of the surface influences the initial nucleation rate of crystals.

Figure 75 reports the film response in IR spectroscopy at 1050 cm<sup>-1</sup> wavelength that corresponds to strong intensity of CaP peak. A correlation between the IR absorbance of inorganic film and the quantity of deposited crystals, as well as with film thickness is observed (Figure 76). One possible explanation could be the (Col-Alg) film roughness

that is decreased by the deposition of (PSS-PAH) film on top of it. Therefore, a rougher coating may favor the deposition of more inorganic crystals compared to smooth film (see Figure 76 b).

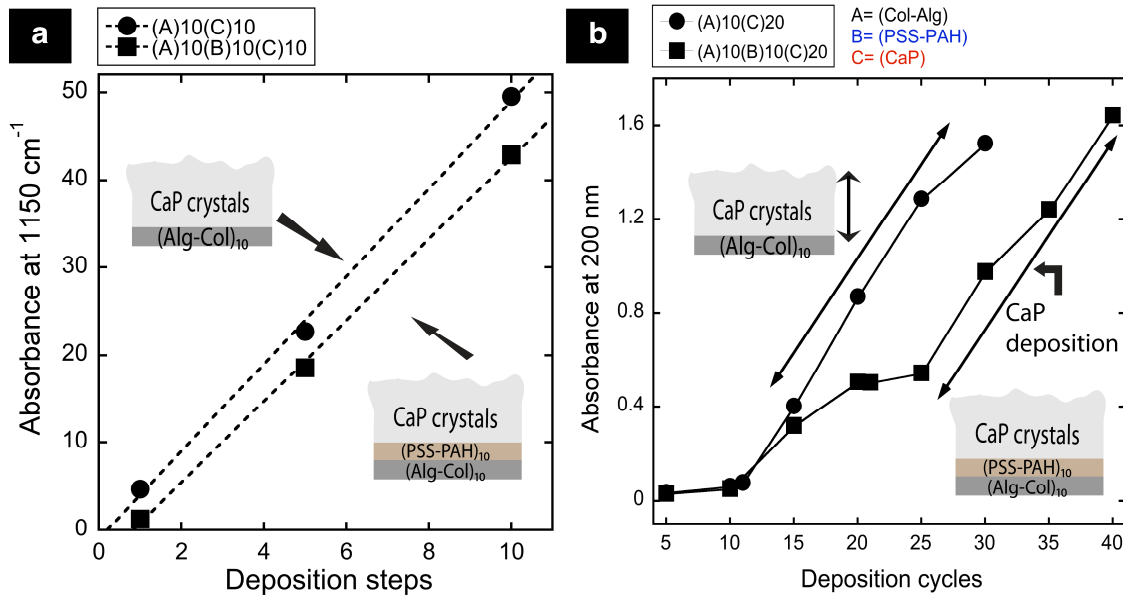


**Figure 76. Substrate influence on the CaP coating preparation. a) IR absorbance evolution with increasing number of (CaP) layer pairs. b) UV-Vis absorbance evolution with increasing number of (LbL)(CaP) layer pairs.**

(LbL) film is a (Col-Alg)<sub>10</sub> film ((A)10) or (Col-Alg)<sub>10</sub>(PSS-PAH)<sub>10</sub> film ((A)10(B)10). Multilayer films ((Col-Alg)<sub>10</sub> and (Col-Alg)<sub>10</sub>(PSS-PAH)<sub>10</sub>) were prepared by classical method of PEM thin film construction (5s spraying, 15s waiting, 5s rinsing with MilliQ water). Ca concentration is 0.32M and P concentration is 0.19M. Both solutions are prepared using buffer pH=10. For FTIR peak calculations, the baseline was manually corrected. The lines are added to guide the eye.

Inorganic coating topography was investigated by AFM microscopy at different deposition stages. AFM images show an increased roughness with the increasing number of deposition cycles and the coating thickness (see Figure 77).



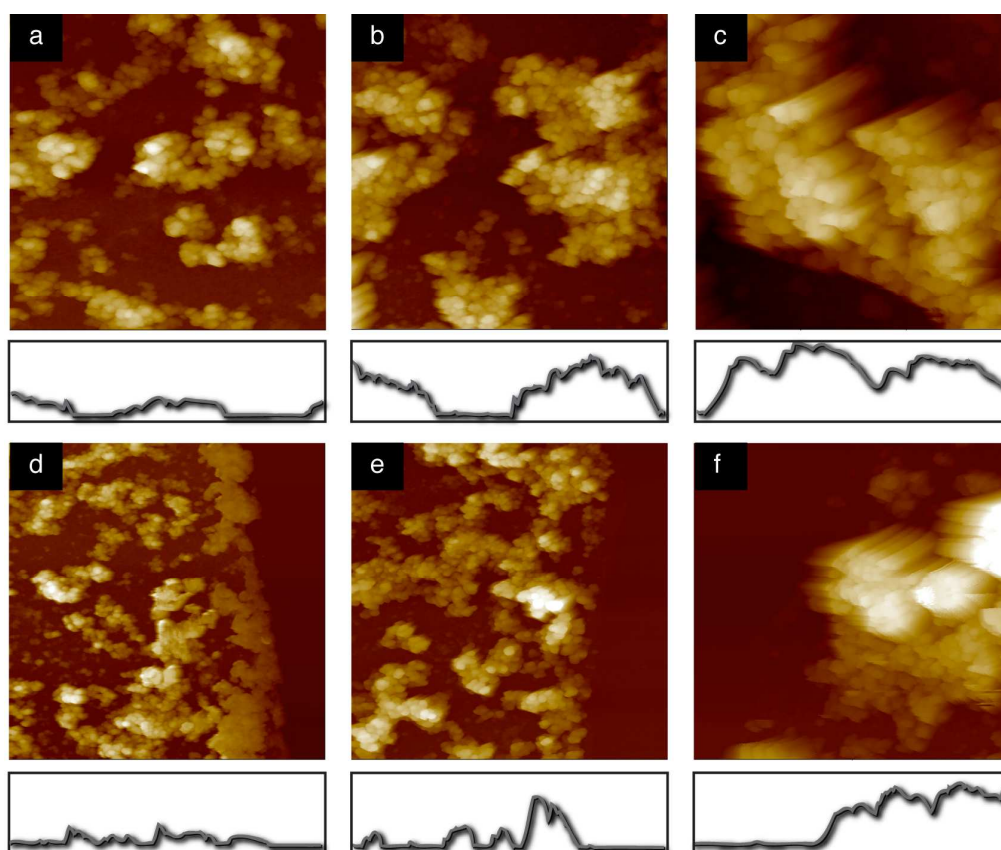


**Figure 77.** AFM images for CaP coating prepared by consecutive spraying on a  $(\text{Col-PSS})_5$  polyelectrolyte film. Top images: AFM images for inorganic crystal deposition of: a)  $(\text{CaP})_3$  coating, b)  $(\text{CaP})_5$  coating, c)  $(\text{CaP})_{10}$  coating. Bottom Z-section images corresponding to center sample-scanned line. Thickness measurements calculated from AFM images for coating scratch of: d)  $(\text{CaP})_3$  deposition, e)  $(\text{CaP})_5$  deposition, f)  $(\text{CaP})_{10}$  deposition. Each AFM image has attached a Z-section image. AFM scan area is  $5 \times 5 \mu\text{m}$  for a-c images and  $10 \times 10 \mu\text{m}$  for d-f images. The y axis scale is constant for all Z-section images ( $1.2 \mu\text{m}$ ). The visible lines from (c, d) images are artifacts due to AFM tip difficulty to scan the high coating roughness. Ca concentration is  $0.32\text{M}$  and P concentration is  $0.19\text{M}$ . Both solutions are prepared using buffer  $\text{pH}=10$ .

CaP coating structure indicates CaP nanoparticles agglomeration on the substrate during the deposition process (see Figure 77). With the increase in the number of deposition steps, an increase of agglomerates size and number is observed. For  $(\text{Col-PSS})_5(\text{CaP})_{10}$  coating, the AFM image reveals not only an increase in size of CaP agglomerates but also an increase of CaP nanoparticle size that forms the inorganic CaP coating. The inorganic film covers more non-deposited area with the increasing number of deposition steps.

After a certain time of spraying (respectively number of deposition cycles), the number of agglomerates is so significant that they cover homogeneously the entire substrate. This set of experiments is obtained for fixed concentration solution and set-up of spraying system.

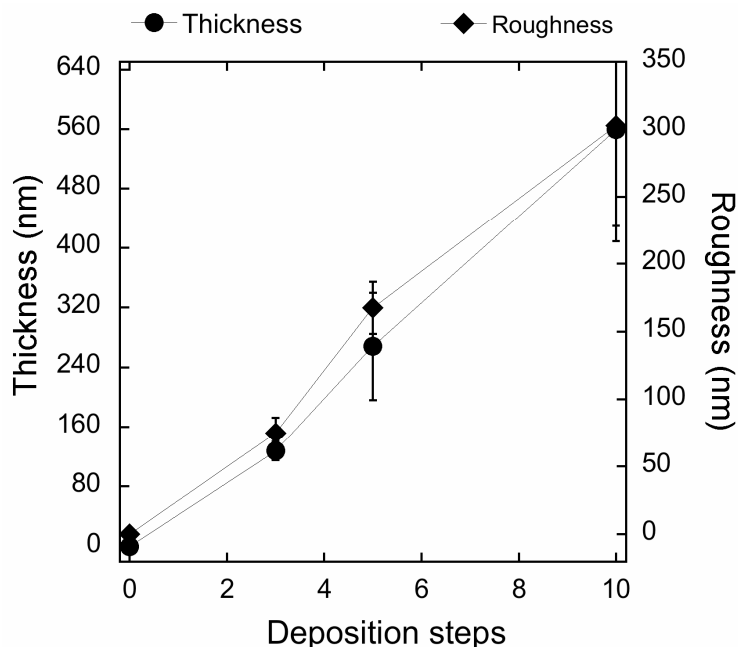


**Figure 78.** Thickness and roughness calculated from  $(\text{Col-PSS})_5(\text{Ca-P})_n$  AFM images versus number of deposition steps ( $n$ ) (see Figure 77).

Thickness and roughness increase linearly with number of deposition cycles (Figure 78). It is observed that the coating thickness is more important than the Root Mean Square roughness (RMS, as determined from AFM). Sprayed coating thickness (Figure 78) is the sum of 30 nm  $(\text{Col-PSS})_5$  precursor film thickness and the respective (CaP) film thickness.

A preliminary test for stability and dissolution of inorganic coatings was realized by measuring the crystal dissolution rate versus spraying time of rinsing water (Figure 79). Linear decrease of UV-Vis absorbance (respectively thickness) coating is observed for a  $(\text{CaP})_{10}$  coating deposited (Figure 79). It also suggests that we can use the film turbidity to estimate the film thickness.

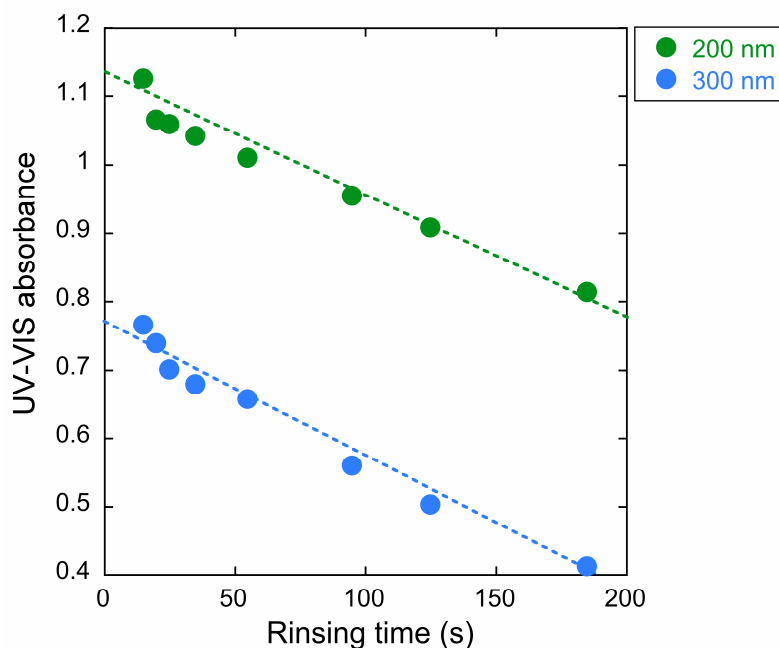


**Figure 79. Dissolution kinetics from rinsing experiments for inorganic coating. Initial film structure is (Col-PSS)<sub>5</sub>(Ca-P)<sub>10</sub>. Ca concentration is 0.32 M and P concentration is 0.1 M. Both solutions are prepared using buffer pH=10.**

#### 4.2.2 Biomaterial fabrication based on Collagen-CaP coatings

The combination of CaP crystals and Collagen in hybrid films is not trivial. Collagen can only be dispersed at low pH while CaP can only be formed at high pH. In consequence, collagen cannot be deposited at high pH (insoluble) and its deposition at low pH causes previously formed CaP crystals to dissolve.

Thus “sandwich” films containing Collagen and CaP are an interesting challenge for LbL assembly. The sandwich is formed from alternating stacks containing CaP crystals and Collagen fibers.

Various experiments confirmed the difficulty of fabrication of such mixed material. The construction of LbL film containing Collagen followed by CaP crystal formation was presented in the precedent chapter. The Figure 80 presents the difficulty to deposit a Collagen PEM film on the CaP inorganic coating without the dissolution of pre-deposited crystals.

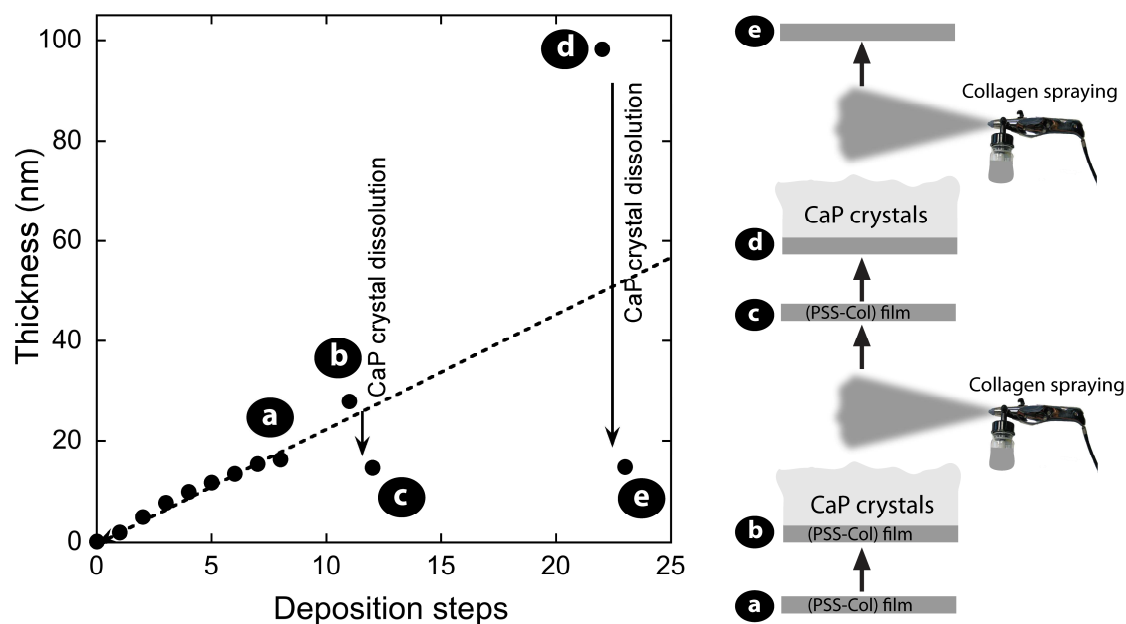


**Figure 80.** Hybrid film thickness measured by ellipsometry. CaP crystal formation on top of (Col-PSS)<sub>8</sub> precursor film and CaP dissolution by spraying one deposition step of (Col-PSS). Ca concentration is 0.32M and P concentration is 0.19 M. Both solutions are prepared using buffer pH=10.

A thick (CaP) inorganic coating is easily dissolved by spraying only one layer of (Col-PSS) film (see the arrows indicating the CaP dissolution/thickness decrease, Figure 80). The (CaP)<sub>10</sub> inorganic coating is so thick that is impossible to measure by ellipsometry. An arbitrary value of 100 nm was chosen for graphic representation (see Figure 80). Unfortunately, a short spray time (5 seconds) of Collagen is enough for dissolving previously deposited CaP crystals. The film thickness has the value of (Col-PSS) precursor film as before the CaP deposition.

In order to verify the CaP coating dissolution by the acidic Collagen solution, an UV-Vis spectrophotometer was used to measure the sprayed mixed coating absorbance increase or decrease. Figure 81 presents the dissolution kinetics of (CaP)<sub>10</sub> coating by spraying only one layer pair (Col-PSS).

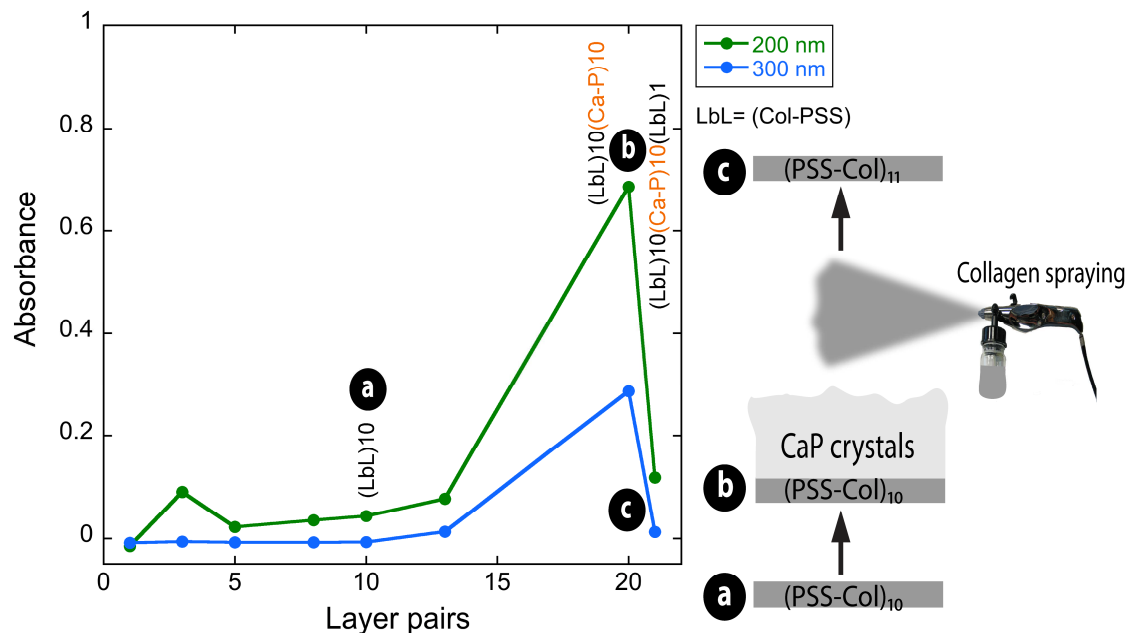


**Figure 81.** UV-Vis measurements for  $(\text{PSS-Col})_{10}(\text{Ca-P})_{10}(\text{PSS-Col})_1$  “sandwich” material. Ca concentration is 0.32M and P concentration is 0.19 M. Both solutions are prepared using buffer pH=10.

Initially the film absorbance increases as usual when the inorganic strata  $(\text{CaP})_{10}$  is added to PEM precursor film. The  $(\text{Col-PSS})_{10}(\text{CaP})_{10}$  hybrid film absorbance rapidly decreases when  $(\text{CaP})$  crystals are dissolved by re-spraying the Collagen layer. We proved by ellipsometry data and UV-Vis spectra results that the fabrication of hybrid material based on Collagen and CaP crystals cannot be achieved by consecutive spraying of Collagen film and CaP coating.

In order to determine both the hybrid film structure and CaP dissolution by Collagen layers, an FTIR-ATR spectrophotometer was used to measure hybrid film construction on the ZnSe crystal. Two main process are observed:

1. The peaks absorbance increasing as the CaP coating is deposited (as the CaP deposition cycles increase from 5 cycles to 20 cycles (see Figure 82)).
2. The immediate disappearing of CaP characteristic peaks (the most visible peak is  $1061 \text{ cm}^{-1}$  peak) characterizes the dissolution process.

The dissolution process consists in the deposition of thin film  $(\text{Col-PSS})_2$  on the pre-coated  $(\text{CaP})_{10}$  surface (transition between 4<sup>th</sup> and 5<sup>th</sup> spectra of Figure 82).

Unfortunately, only  $(\text{Col-PSS})_2$  peaks ( $1008, 1036, 1127 \text{ cm}^{-1}$ ) are visible after the  $(\text{CaP})$  dissolution (see 5<sup>th</sup> IR spectra, Figure 82 ). Interestingly, the  $(\text{CaP})_5$  coating deposited (after the  $(\text{CaP})_{10}$  coating was dissolved) is apparently not dissolved by spraying the PSS solution (7<sup>th</sup> IR spectra, Figure 82). The coating is dissolved after the Collagen adsorption to hybrid material fabrication (8<sup>th</sup> IR spectra, Figure 82). This FTIR-ATR measurement showed the same difficulties for hybrid Collagen-CaP film construction as previous results (ellipsometry, UV-Vis).

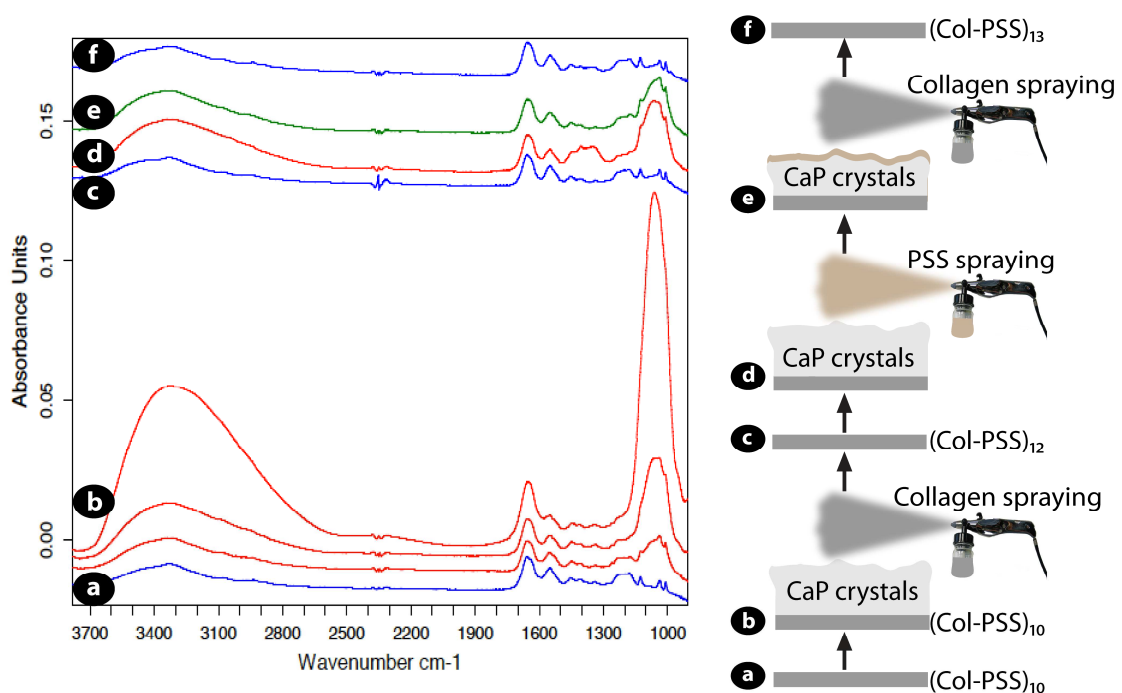


**Figure 82. FTIR-ATR spectrum for Collagen-CaP consecutive stacks hybrid material. The exact structure of construction is  $(\text{Col-PSS})_{10}(\text{Ca-P})_{20}(\text{Col-PSS})_2(\text{Ca-P})_5(\text{PSS-Col})_1$ . The hybrid material construction is presented from the bottom to the top of the spectra. Each layer strata is represented by FTIR-ATR spectra in the figure. Ca (0.32 M) and P (0.19 M) solutions are prepared using buffer pH=10.**

### **4.2.3 Use of (PAH-PSS)<sub>n</sub> films as barrier for preventing dissolution of CaP crystals**

In order to prepare the Collagen-CaP hybrid films we need to solve the “problem” of instantaneous dissolution of CaP crystals when the Collagen and CaP are mixed together for “sandwich” construction.

The “problem” preparation of hybrid “sandwich” film is resolved by the use of classic (PAH-PSS) LbL films as diffusion barrier for preventing the CaP dissolution. The PAH and PSS solutions are prepared in MilliQ water without pH adjustment (as Collagen case) and they shouldn't dissolve the CaP crystals. First, we should be able to validate the “sandwich” material fabrication strategy for (PAH-PSS) barrier films and CaP coatings. The “sandwich” structure is obtained by the consecutive junction of the CaP strata and the (PAH-PSS)<sub>n</sub> strata. For the validation concept of alternating deposition coatings of the hybrid “sandwich”, various techniques are used for characterization such as ellipsometry, UV-Vis spectroscopy, and FTIR-ATR spectroscopy.

We realized some preliminary ellipsometry measurements for the hybrid films preparation of consecutive sprayed (PSS-PAH)<sub>5</sub> films and (CaP)<sub>5</sub> coatings (see figure Figure 83). With the aim to simplify the “sandwich” structure, we will use the notion of elementary brick (strata) that its repetition composes the “sandwich” hybrid film. The strata repetition allows the preparation of hybrid films with a certain thickness and coating properties. In this case (Figure 83), the elementary brick is the (PSS-PAH)<sub>5</sub>(CaP)<sub>5</sub> film that it is repeated 3 times.

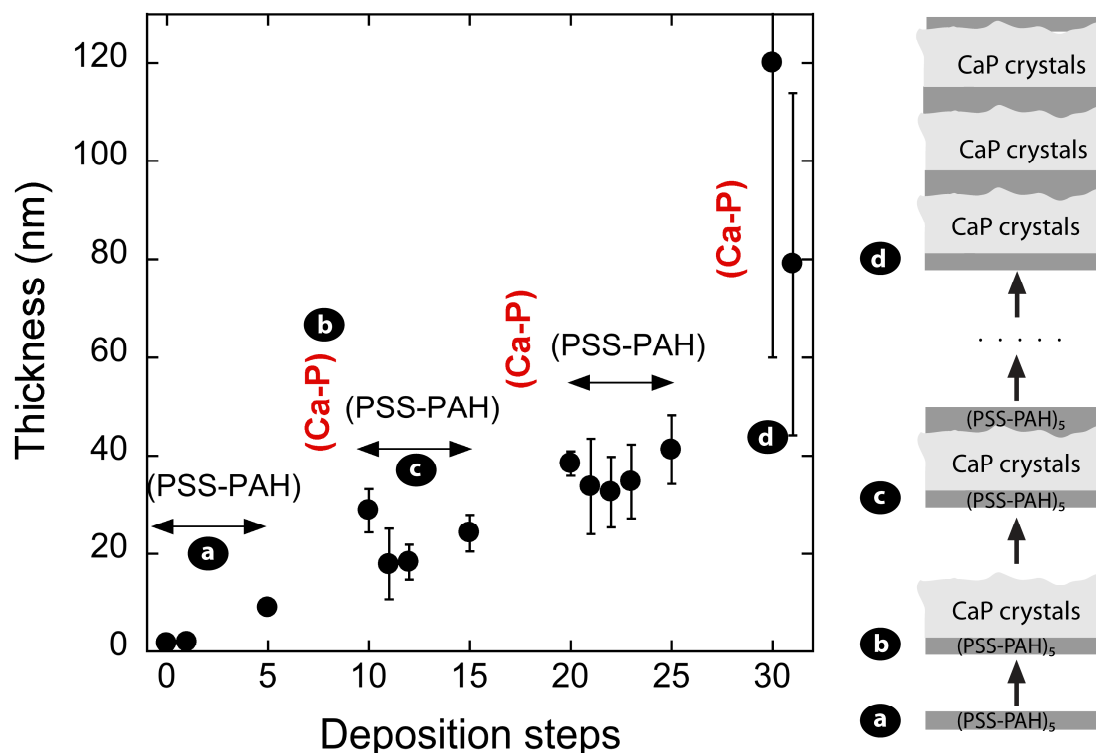


Figure 83. “Sandwich” construction using as elementary stack the  $((PSS-PAH)_5(Ca-P)_5)$  repeated 3 times and finished with  $(PSS-PAH)_1$  where Ca (0.32 M) and P (0.19 M) solutions are at pH=10.

The hybrid film thickness increase is observed in the Figure 83. Only a slight decrease of film thickness is detected at the (PSS-PAH) deposition onto (CaP) coating. The (CaP) coating deposition rate is greater than that of the polyelectrolyte multilayer (PAH-PSS) film construction rate. As always for the ellipsometry measurements, the limit for the detection of the film thickness is reached after about 10 (CaP) deposition steps.

In order to validate the (PAH-PSS) barrier film, we used UV-Vis spectroscopy for “sandwich” hybrid film construction. The consecutive strata depositions were monitored for the hybrid film construction (Figure 84). The (CaP) film absorbance increase is greater than that of the (PAH-PSS) barrier film. It suggests that the (CaP) deposited amount is superior to the deposited polyelectrolytes amount.



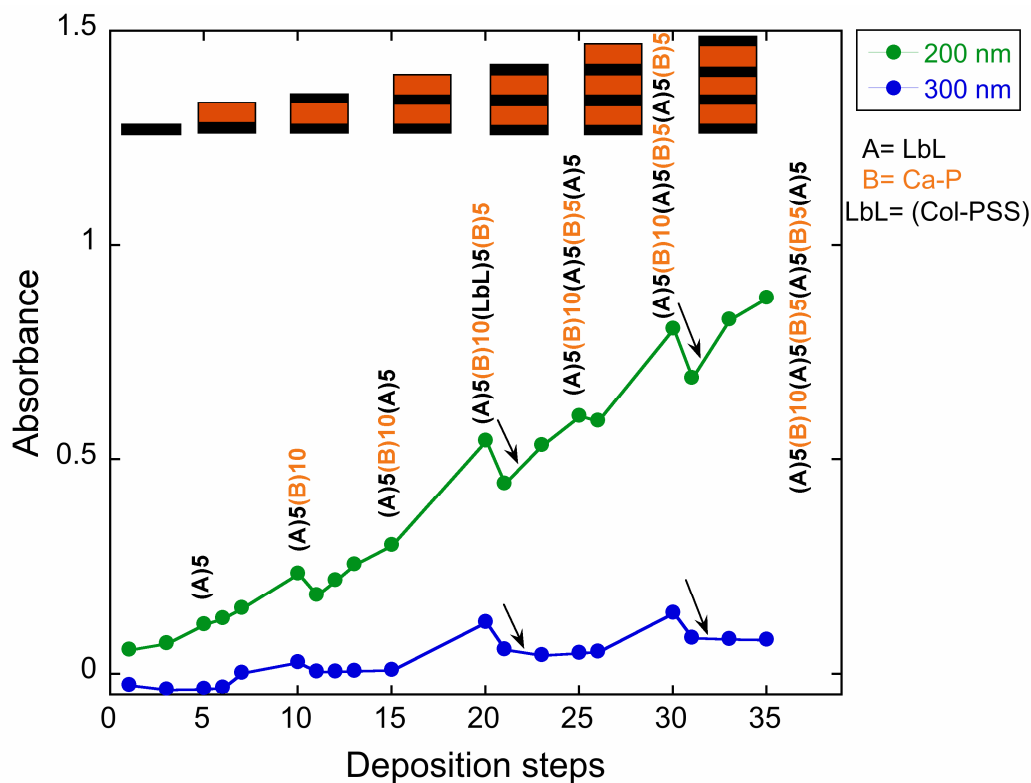


Figure 84. UV-Vis absorbance of hybrid film ((PSS-PAH)<sub>5</sub>(Ca-P)<sub>5</sub>)<sub>3</sub>(PSS-PAH)<sub>5</sub> versus increasing number of layer pairs deposited. Ca (0.32 M) and P (0.19 M) solutions prepared with buffer at pH=10.

It is observed that the (PAH-PSS) barrier film is efficient (the increase of absorbance of the hybrid thin film) and it allows the “sandwich” film formation. Only a slight decrease of film absorbance is observed when the (PSS-PAH) barrier film is deposited on top of the CaP coating (indicated by arrow in Figure 84).

In addition, the adsorbed amounts for hybrid film formation were also analyzed by FTIR-ATR spectroscopy on the ZnSe crystal. In order to obtain additional information on the “sandwich” structure, we use this technique to observe the film formation at each deposition step. The FTIR-ATR spectrum of the hybrid polyelectrolyte-CaP film contains the details about the “sandwich” structure (the characteristic peaks for each coating) and the amount deposited (the peak intensity). We compared the previous results obtained from UV-Vis and ellipsometry measurements with the “sandwich” architecture prepared

on ZnSe crystal and they we obtained the same deposition of hybrid films. Some changes in FTIR-ATR spectrum are observed for the CaP strata deposition (Figure 85):

- The peaks appear at 872, 1033.6, 1058.8, 1348.4  $\text{cm}^{-1}$
- The increase of the peak intensity characteristic for (PSS-PAH) barrier film (1008.1, 1035.1, 1126.3, 1174.5, 1205.6  $\text{cm}^{-1}$ )
- The peaks shift:
  - From 1631.3  $\text{cm}^{-1}$  when the last deposition is the (PAH-PSS) film to 1640  $\text{cm}^{-1}$  for the (CaP) coating as the last deposition cycle,
  - From 1528.7  $\text{cm}^{-1}$  for the (PAH-PSS) barrier film to 1535.5  $\text{cm}^{-1}$  for the (CaP) deposition as last strata.

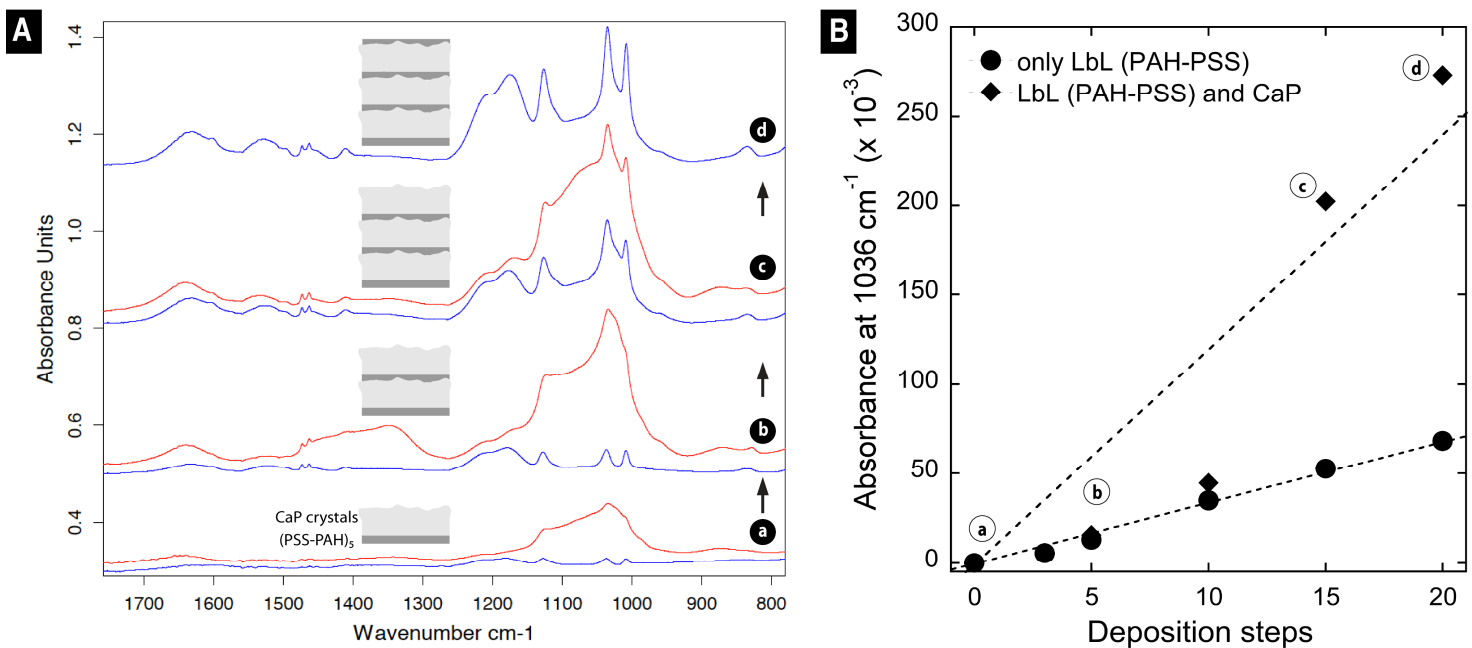


**Figure 85. (A):** FTIR-ATR spectrum for hybrid film versus the increase of the deposition steps. The blue spectra corresponds to (PSS-PAH) barrier film deposition and the red one to the crystal deposition. The spectra are taken after each deposition step and the final structure of hybrid film is  $((\text{PSS-PAH})_5(\text{Ca-P})_5)\times 3(\text{PSS-PAH})_5$ . **(B):** The FTIR absorbance increase at 1036  $\text{cm}^{-1}$  for (PSS-PAH) barrier film with increasing number of deposition steps. The 1036  $\text{cm}^{-1}$  peak is characteristic to (CaP) crystals.

There is an absorbance film difference between classic LbL film and hybrid LbL-CaP film that is observed only after the second (CaP) deposition cycle (see Figure 85B). In

conclusion, the hybrid film containing (CaP) crystals absorbs more IR radiation than the (PAH-PSS) classic LbL film (e.g. hybrid/classic films absorbance at 20 deposition cycles, Figure 85B).

We therefore validate the efficiency of (PAH-PSS) barrier film for hybrid film construction as a result of various experiments (UV-Vis, ellipsometry, FTIR). The “sandwich” architecture of hybrid films can vary the number of layer pairs for (PAH-PSS) barrier film and/or the number of deposition steps for (CaP) film (data not shown in this thesis).

#### **4.2.4 Combination of barrier layers with Collagen and CaP coatings**

The fabrication of hybrid (PAH-PSS) film and CaP inorganic coating was already realized by the consecutive spraying method. The next step for the biomaterial fabrication is the incorporation of Collagen in this hybrid films without the dissolution of the crystals. Our strategy is to use (PSS-PAH) films as a barrier between the CaP and the Collagen films to stop/decrease the CaP dissolution.

First, the thickness measurements (Figure 86) are similar for the two different architectures based on the combination of the Collagen and the CaP films. The first example is one inorganic stack (or strata) of (CaP)<sub>5</sub> film and the second architecture has two (CaP)<sub>3</sub> stacks in the film structure.

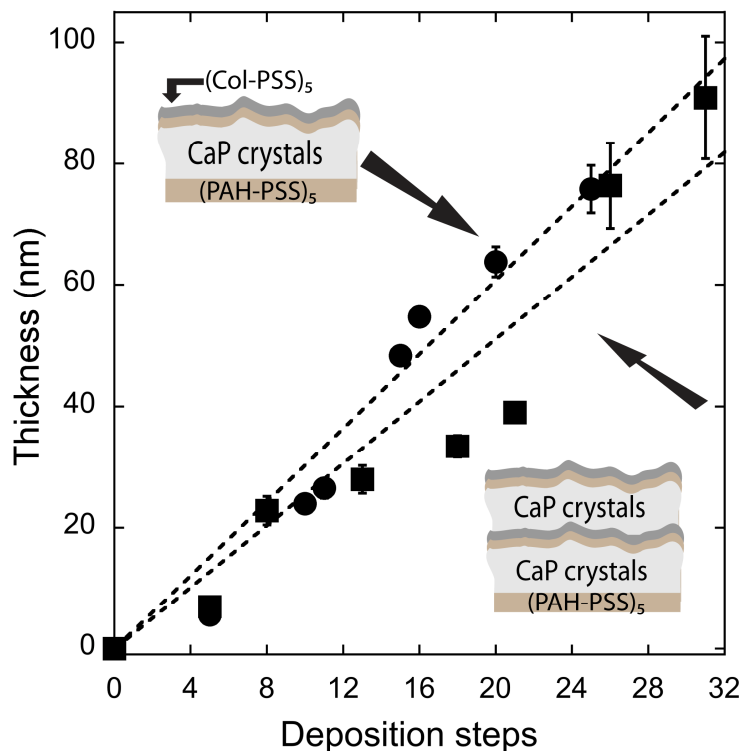


**Figure 86. Ellipsometric thickness of two different architectures containing Collagen and CaP in the hybrid film composition. First architecture is a one stack “sandwich” structure  $(\text{PAH-PSS})_5(\text{Ca-P})_5(\text{PAH-PSS})_5(\text{PSS-Col})_{10}$ . Second architecture contains two  $(\text{CaP})$  stacks and the final hybrid film is  $(\text{PAH-PSS})_5((\text{Ca-P})_3(\text{PAH-PSS})_5(\text{PSS-Col})_5) \times 2$ . Ca (0.32 M) and P (0.19 M) solutions prepared with buffer at pH=10.**

The  $(\text{PAH-PSS})$  barrier film validation was also confirmed from the UV-Vis experiments. The Collagen film is deposited on the  $(\text{PAH-PSS})$  barrier film and not directly on the inorganic crystals (Figure 87). The polymer barrier decreases the proton transport rate from the acidic region containing Collagen films to the alkaline medium of inorganic films. A  $(\text{Col-PSS})$  film was used as precursor film for “sandwich” construction of repeated strata (inorganic coating  $(\text{CaP})$  followed by barrier  $(\text{PSS-PAH})$  and end up with  $(\text{Col-PSS})$  film).

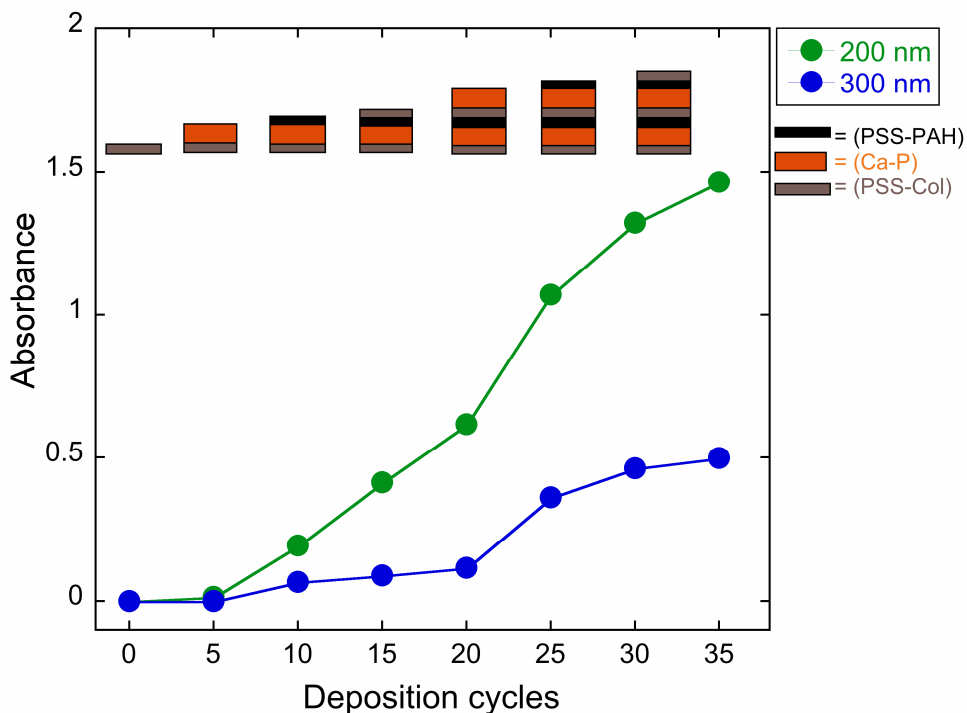


**Figure 87.** UV-Vis measurements for “sandwich” like hybrid film containing Collagen and inorganic CaP. The structure of architecture is  $(\text{Col-PSS})_5((\text{Ca-P})_5(\text{PAH-PSS})_5(\text{PSS-Col})_5)_2$ . Where Ca and P sol at pH=10.

From the Figure 87, it is observed that CaP deposition creates a considerable UV-Vis absorbance increase compared to the lower polyelectrolyte film absorbance. This result is in agreement with ellipsometry results (Figure 86) which shows that the CaP coating thickness (respectively absorbance) is superior to the polyelectrolyte multilayer film thickness.

In addition, FTIR-ATR experiments were realized to provide more structural information for hybrid prepared material. Figure 88 presents the IR spectra for each step of deposition, each sprayed strata. The peak positions are linked to the “sandwich” composition structure comprising the previous and the last sprayed films. As the CaP coating as last deposited coating, the IR spectrum is slightly different from the PEM film spectra. The strong peak around  $1066\text{-}1077\text{ cm}^{-1}$  and the peaks in the  $1350\text{-}1405\text{ cm}^{-1}$  region are the signature of the inorganic last layer (Figure 88). The intensity of IR peaks (absorbance) increases with the number of strata deposited (see Figure 88).

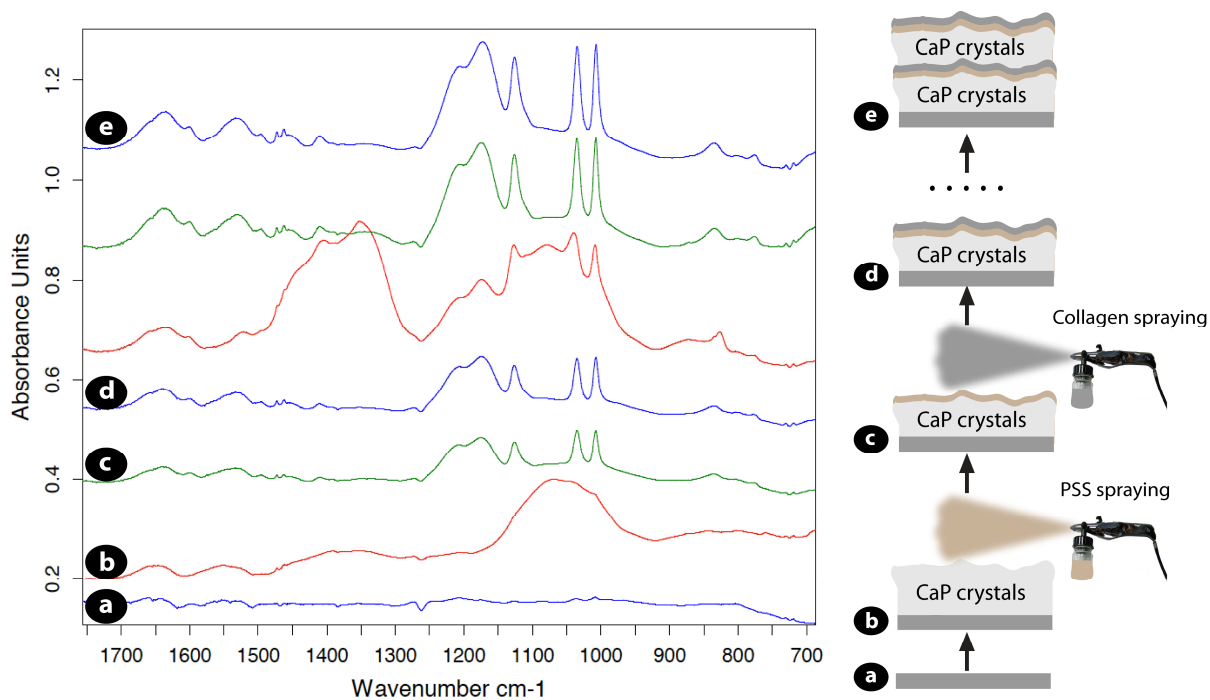


**Figure 88.** FTIR-ATR spectra of hybrid films containing Collagen and CaP inorganic crystals. Final structure of “sandwich” structure is  $(\text{Col-PSS})_5((\text{Ca-P})_5(\text{PAH-PSS})_5(\text{PSS-Col})_5)_2$ . Ca (0.32 M) and P (0.19 M) solutions prepared with buffer at pH=10.

An increase in absorbance of (PSS-Col) film peaks ( $1365, 1406, 1520, 1553, 1653 \text{ cm}^{-1}$ ) is produced when the (CaP) film was deposited on top of the Collagen film. The main peaks of the (PSS-PAH) film IR spectra are similar to the main peaks of the (PSS-Col) IR spectra, but a slight difference is observed for the intensity peak (change in the  $1050\text{-}1100 \text{ cm}^{-1}$  region and  $1353 \text{ cm}^{-1}$  peak), and the peaks shift ( $1530\text{-}1550 \text{ cm}^{-1}$  and  $1637\text{-}1658 \text{ cm}^{-1}$ ).

Other PEM films were investigated for potential application as barrier for hybrid Collagen-CaP films:

- (PAH-PSP) barrier
- (PAH-Dex) barrier
- (PLL-PLGA) barrier

The “sandwich” fabrication was already validated for (PSS-PAH) barrier LbL film. The (PAH-PSP) PEM film is another potential polyelectrolyte barrier that was explored for the preparation of hybrid Collagen- CaP films. The same deposition technique (the consecutive spraying) was used for the PEM film and the inorganic coating fabrication. The Figure 89 shows the efficiency of the (PAH-PSP) barrier film compared with the film where the barrier film is absent from the hybrid film structure.

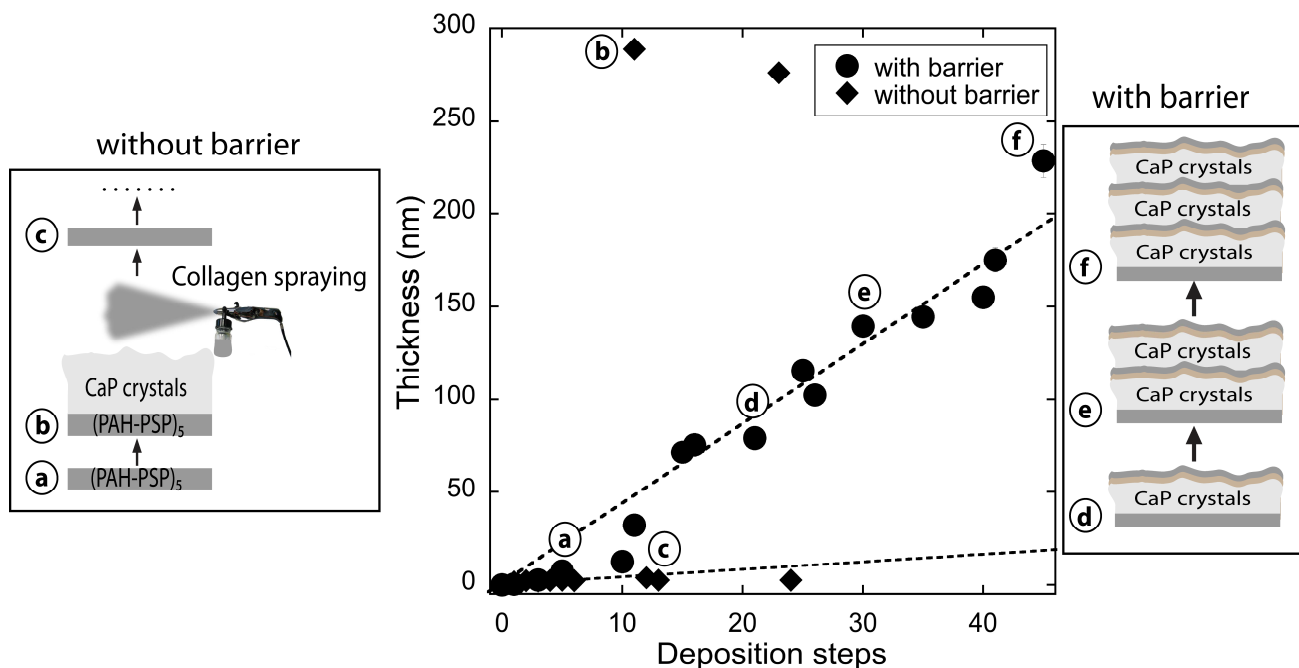


**Figure 89. Thickness measurements by ellipsometry for two architectures: with (PAH-PSP) barrier and without barrier. The film structure for barrier architecture is (PAH-PSP)<sub>5</sub> ((Ca-P)<sub>5</sub>(PAH-PSP)<sub>5</sub>(PSP-Col)<sub>5</sub>)<sub>x3</sub> ( Elli 9-04-08). (PAH-PSP)<sub>5</sub> (Ca-P)<sub>5</sub> (PSP-Col)<sub>2</sub>(Ca-P)<sub>10</sub>(PSP-Col)<sub>1</sub> is the system without barrier. Ca (0.32 M) and P (0.19 M) solutions prepared with buffer at pH=10.**

Two effects are observed for the (PAH-PSP) barrier film presence or not in the hybrid film construction:

1. The linear growth for the hybrid film containing the barrier films.
2. The dissolution of (CaP) coating for films without barrier.

The minimum barrier thickness is 5 layer pairs of (PAH-PSP) in order to avoid (CaP) crystal dissolution. In the absence of the (PAH-PSP)<sub>5</sub> barrier film, the hybrid film thickness is low compared to that with the barrier film included in the structure. However, the (CaP) film thickness highly increases (around 300 nm for the (CaP)<sub>5</sub> film

and 280 nm for the (CaP)<sub>10</sub>, see data series “without barrier”, Figure 89) and it immediately decreases in contact with the (PSP-Col) film.

The “sandwich” hybrid film construction containing two (inorganic coating/ barrier film/ Collagen film) stacks was prepared for tracing the construction UV-Vis spectroscopy (data not shown). In conclusion, the (PSP-PAH) barrier film for Collagen-CaP hybrid films was validated.

The (PAH-PSS) and (PAH-PSP) films are robustly enough to allow the Collagen-CaP hybrid “sandwich” film fabrication. They are characterized by a strong polyelectrolyte interaction that plays an important role for the barrier-film efficiency. There are two barrier systems: the (PAH-Dex) and the (PLL-PLGA) films that cannot be used as barrier for the hybrid film fabrication. The electrostatic interactions between PAH and Dex are less strong and less numerous than the (PAH-PSS) interactions. The (PAH-Dex) films without additional treatments (thermal treatment, chemical crosslinking) cannot be used as barrier films. The (PLL-PLGA) barrier film efficiency is low because of its weakness; the diffusion of polyelectrolytes (PLL, PLGA) chains is more probable than for the robust film (PAH-PSS).

#### **4.2.5 Consecutive spraying method applied to other inorganic coatings**

It was extremely interesting to extend the formation of inorganic crystalline films by alternating spray deposition to other systems. At this point, when the enlargement of our method was realized to other crystals, we discovered the SILAR method. The SILAR (successive ionic layer adsorption and reaction) method is also known as modified version of chemical bath deposition. In this method, thin films are obtained by immersing substrate into separately placed cationic and anionic precursors and rinsing between every immersion with ion-exchanged water. The rinsing time in ion exchange water is critical for ionic layer formation. The consecutive spraying method has some advantages compared to SILAR method such as the homogeneity of the prepared coating, the applicability to bigger substrates, and the reduced deposition time.



A simple rule describes the film formation by the consecutive spraying method. “The film formation on substrate takes place when ionic product exceeds solubility product (the solution is supersaturated).” Generally, the low solubility product of the crystal may favor its precipitation on the surface at lower solution concentration. Particularly promising systems seem to be any complementary solution whose mixing in bulk leads to supersaturation and precipitation. The consecutive spraying deposition method was mainly applied for the CaP layers preparation. The list of other inorganic crystal prepared by the same method is long. It contains crystals as calcium fluoride, calcium oxalate, iron phosphate, silver chloride, Prussian Blue.

#### **4.2.5.1 Calcium oxalate (CaOx)**

Beside the experiments reported for the CaOx deposition in our articles, we complete the characterization list of studies with the substrate influence study, the coating topography (AFM) versus the number of deposition cycles experiments or the study of inorganic coatings structure (FTIR).

We studied the order of spraying solution for the CaOx deposition (the Calcium solution firstly or secondly sprayed on the surface). It is observed that is not a fundamental parameter for the film thickness control. Another deposition parameter that was studied is the nature of the substrate: PEM film as (Col-PSS)<sub>5</sub>, PEI layer, hydrophilic silica wafer.

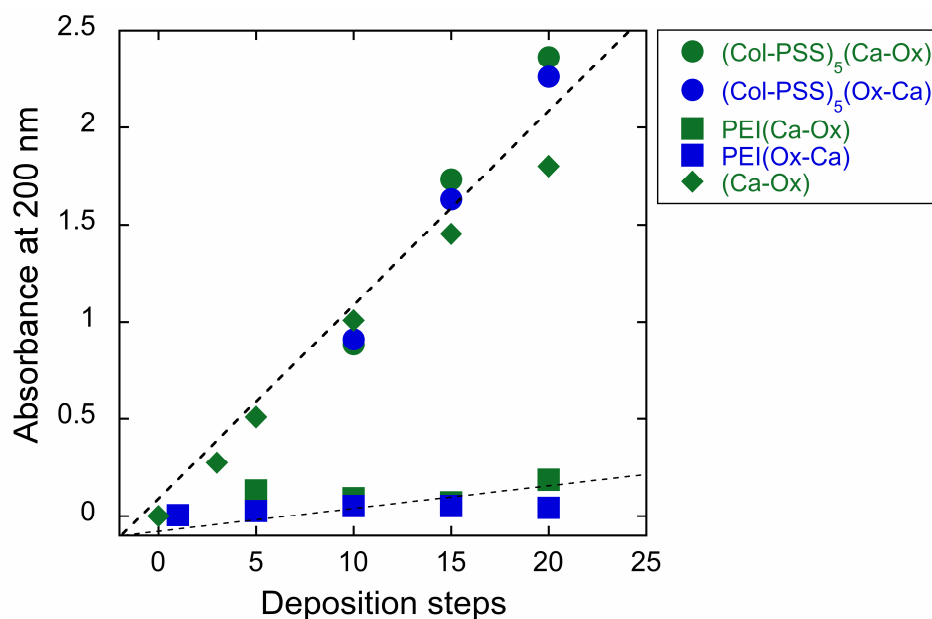


**Figure 90. UV-Vis absorbance of calcium oxalate deposited coating on various coated substrates. Calcium (Ca) and oxalate (Ox) solution are consecutive sprayed for 2x1s.**

Again the nucleation of the first crystals is influenced by the nature of the surface. PEI as first layer inhibits the calcium oxalate crystallization and increasing the number of layer pairs doesn't improve the deposition rate of inorganic CaOx. Similar thickness deposition rates are obtained for a clean silica wafer and for (Col-PSS)<sub>5</sub> multilayer film (both are negatively charged surfaces). FTIR-ATR spectra presents the CaOx characteristic peaks at 783.5, 1331.7, 1617.2, 1643.1  $\text{cm}^{-1}$  (see Figure 91). The IR peak intensity is proportional to the number of layer pairs.

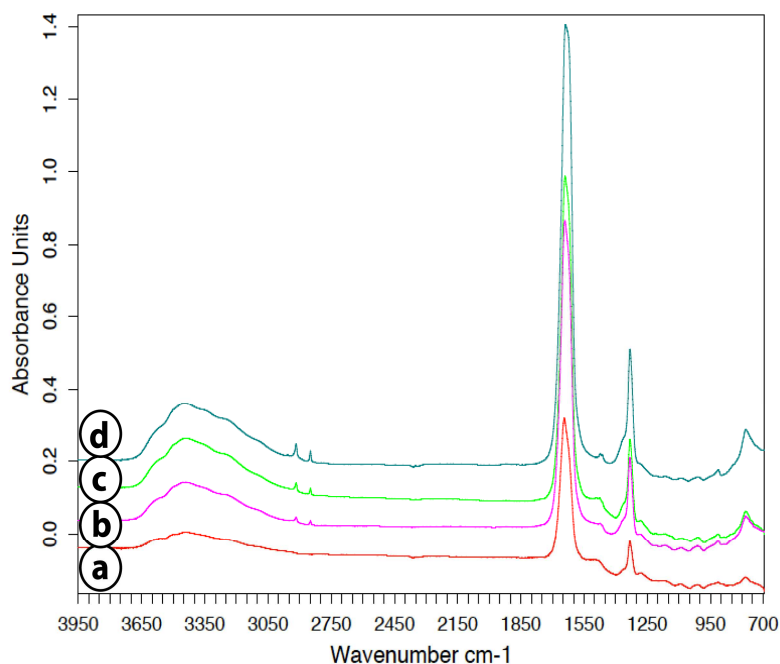


**Figure 91. FTIR spectra of CaOx inorganic deposition versus number of deposition steps. The deposition steps increases from 5 cycles (CaP)<sub>5</sub> (a) to 10 cycles (CaP)<sub>10</sub> (b), to 15 steps (CaP)<sub>15</sub> (c) and to (CaP)<sub>20</sub> (d).**

Topography of inorganic CaOx coatings was investigated by AFM. Coating roughness is increased with the number of deposition steps by consecutive spraying technique. The roughness becomes so high (e.g. (Col-PSS)<sub>5</sub>(CaOx)<sub>15</sub>) that it is difficult to obtain an accurate image by AFM. It is observed that sprayed coatings are not homogeneous from early stages of fabrication. After 5 deposition cycles, the substrate is completely covered by CaOx inorganic crystal deposited by alternating spraying.

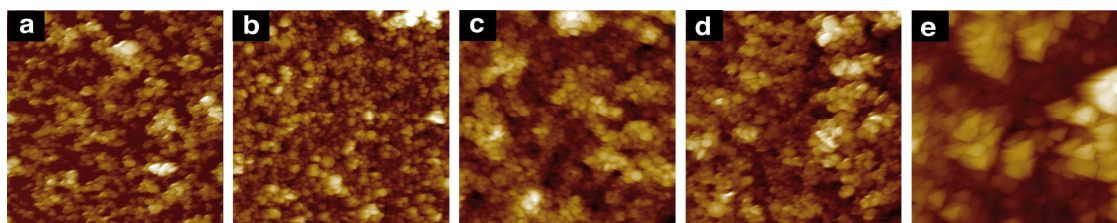


**Figure 92. Morphology characterization of inorganic (CaOx) coatings for different deposition steps by AFM tapping mode. Inorganic coatings are deposited on top of a PEM film of (Col-PSS)<sub>5</sub>. The number of deposition steps characteristic for each image is 3 (a), 5 (b), 10 (c), 15 (d), 25 (e). (e) AFM image contains artifacts. Scan image size is 5x5  $\mu\text{m}$ .**

#### 4.2.5.2 Silver chloride (AgCl)

Silver chloride coatings have been prepared by consecutive spraying method of silver nitrate solution ( $\text{AgNO}_3$ ) and sodium chloride ( $\text{NaCl}$ ). Several experiments (ellipsometry and UV-Vis) have been realized for AgCl coating deposition by this technique. We studied the AgCl deposition on a PEI treated quartz slide (AgCl characteristic peak around 260 nm). Linear growth of peak absorbance at 260 nm is observed for AgCl deposition.

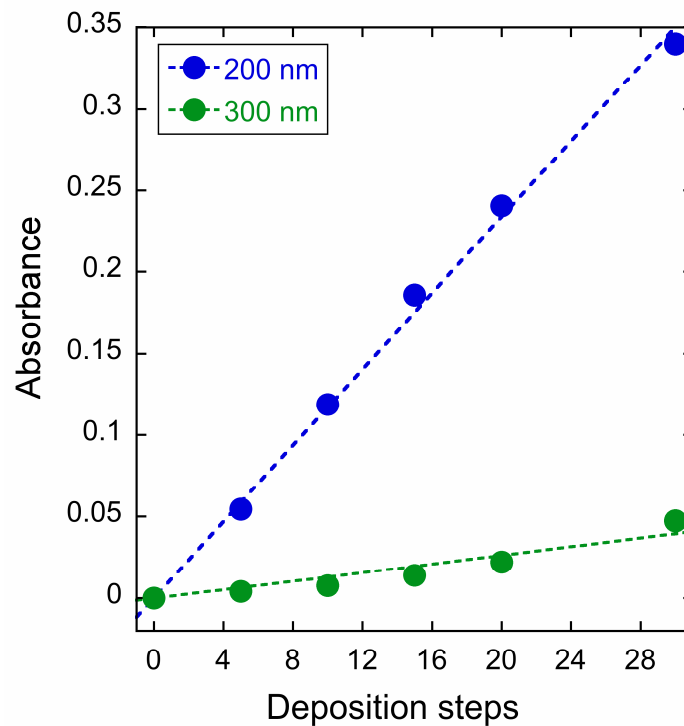


Figure 93. Inorganic coating of AgCl deposition followed in UV-Vis spectroscopy. A first PEI layer is adsorbed on quartz then the coating is prepared by 1-second spray of each reactive solution.

#### 4.2.6 Inorganic “sandwich” structure fabrication by alternating spraying

Extension to new mixed films (hybrid or “sandwich” or mixture of both) is realized for potential applications. The inorganic film architecture is slightly different compared to

the polymer-crystals architecture. The newly arriving material can crystallize on top of the previous film or in the voids between previous crystals or both.

Beside Collagen-inorganic coating “sandwich” construction, the spraying deposition method can be applicable for the fabrication of purely inorganic “sandwich” materials containing different inorganic coatings. Preliminary experiments were done using FTIR-ATR spectroscopy for the structural characterization of each inorganic strata sprayed. In order to study the layer organization and interpenetration (e.g. CaOx first deposited layer, CaP second deposited layer), we used the confocal RAMAN spectroscopy (article 1 figure). The “sandwich” structure containing two inorganic strata (calcium oxalate and calcium phosphate) is characterized at each step of the deposition process by FTIR-ATR spectroscopy (Figure 94).

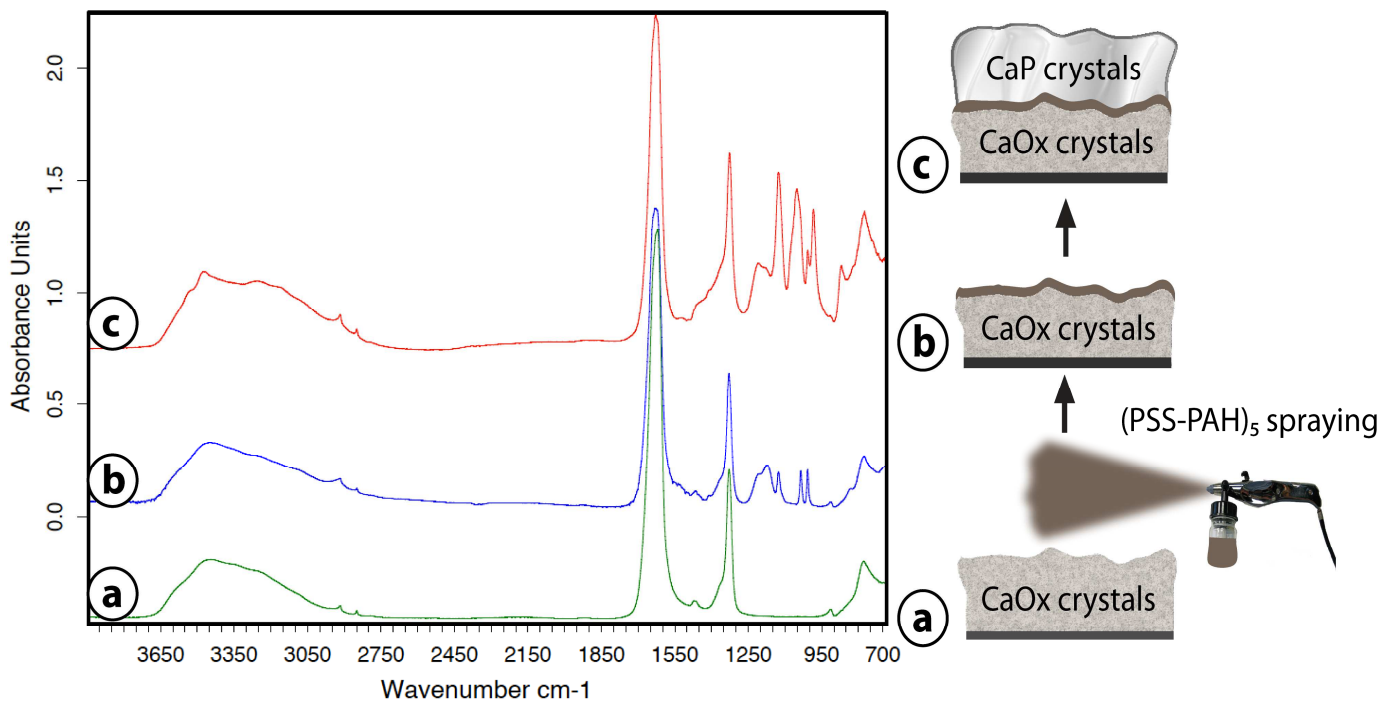


**Figure 94.** FTIR spectra of inorganic “sandwich” coating where first coating is CaOx and then the CaP layers by consecutive spray method are deposited. The structure of sprayed composite is  $(\text{CaOx})_{60}(\text{PAH-PSS})_{10}(\text{CaP})_{100}$ . First IR spectrum (a) corresponds to  $(\text{CaOx})_{60}$ , followed by (PAH-PSS) film (b) and finishing with  $(\text{CaP})_{100}$  deposition IR spectrum (c).

The additional (PAH-PSS) LbL film was inserted in the strata structure for a clear separation of different inorganic coatings. The CaOx peaks are clearly visible in the

1300-1650  $\text{cm}^{-1}$  regions; a second deposition cycle is produced for (PSS-PAH) LbL film. In this case, the IR spectrum indicates CaOx peaks previously sprayed and PEM film peaks at 1007, 1035.1, 1126, 1175, 1204  $\text{cm}^{-1}$ . Last sprayed inorganic coating is the well-studied (CaP) coating characterized by the 872, 982, 1053, 1213  $\text{cm}^{-1}$  IR peaks.

### ***4.3 Simultaneous spraying: deposition method for thin films***

#### **4.3.1 Manually simultaneous spraying deposition**

All inorganic crystals formed by consecutive spraying method have been tested using the simultaneously spraying coating technique. (SSC) In case of consecutive spraying, the variable is the number of spraying cycles (layer pairs) and for SSC, the variable is the spraying time.

Calcium fluoride is an inorganic crystal that was intensively prepared by consecutive spraying method for coating fabrication (see more details article 1). Fabrication of  $\text{CaF}_2$  homogenous coatings by SSC method was investigated by various techniques (ellipsometry, UV-Vis, FTIR, AFM, TEM). Thickness measurements indicate the linearly deposition rate of  $\text{CaF}_2$  coating directly on clean silica wafers. Independently of spraying time step, the deposition rate is constant for inorganic  $\text{CaF}_2$  deposition (see Figure 95).

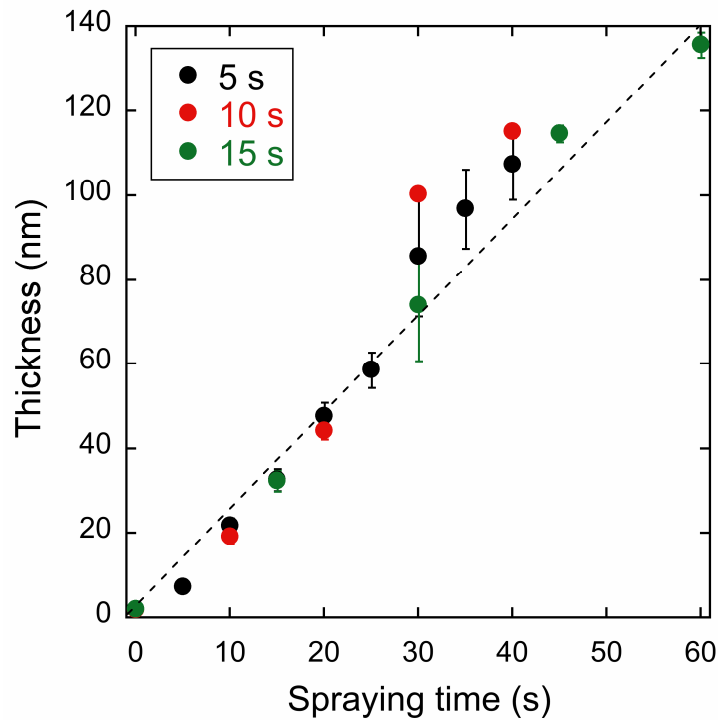


**Figure 95. Ellipsometric thickness measurements of calcium fluoride coatings prepared by SSC technique. Collection data measurement step (spraying time) between acquisitions of thickness is variable from 5, 10 and 15 seconds.**

Spraying time is only one of the multiple deposition parameters that allows controlling the deposition process. Increasing the spraying time for SSC deposition is translated into an increase of coating homogeneity. The number of crystallization grains is increased with spraying time of solutions on the impact surface.  $\text{CaF}_2$  layer morphology characterized by AFM shows different size agglomerates that form the inorganic coating. The size of agglomerates doesn't change with increasing deposition time spraying; it is just the number of these agglomerates that increases.

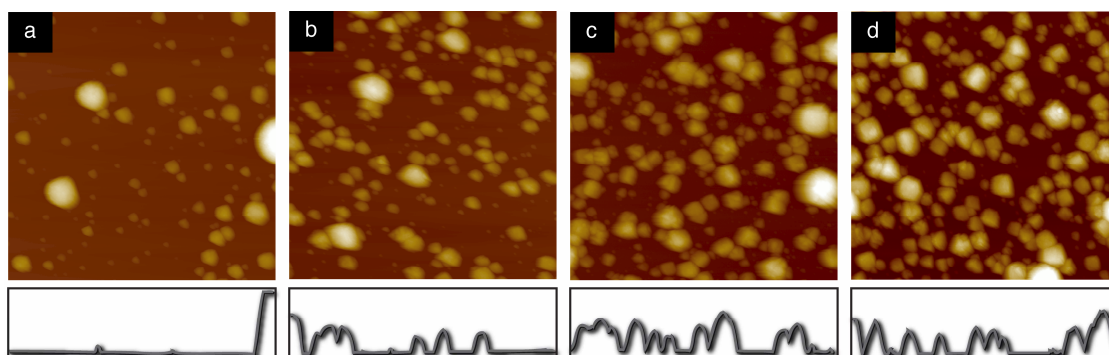


**Figure 96.** AFM images of CaF<sub>2</sub> coatings obtained by SSC method for various time spraying. a) 10 s, b) 20 s, c) 30 s, d) 40 s. Airflow pressure was constantly equal to 2 bars. Scan size image is 5x5  $\mu\text{m}$  for all samples. Bottom images: Z-section obtained from center scanning line.

Complementary investigation experiments by AFM allowed the study of the airflow pressure influence on deposition properties. Two different airflow pressures were tested keeping the others parameters fixed. An increasing of inorganic crystals number with spraying time and with airflow pressure rising from 2 bar to 4 bar is observed.

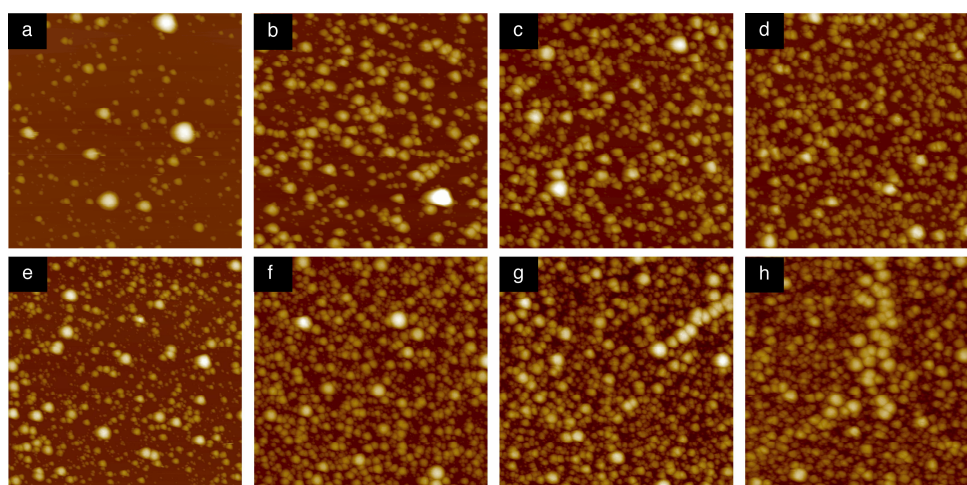


**Figure 97.** Airflow pressure influence on CaF<sub>2</sub> coating properties fabricated by SSC technique. AFM images for CaF<sub>2</sub> coating obtained at an airflow pressure of 2 bars (a-d) and 4 bars (e-h). Spraying time for CaF<sub>2</sub> coatings is 10 s (a, e), 20 s (b, f), 30 s (c, g), 40 s (d, h). Scan size image is 10x10  $\mu\text{m}$  for all presented images.

Silver chloride coating was already fabricated by alternating spraying deposition technique. SSC method concept of inorganic deposition was also validated for AgCl.



Thickness measurements for AgCl are in agreement with UV-Vis absorbance data obtained for AgCl deposition by alternating spraying technique. Linear deposition rate is observed for various samples prepared by SSC process.

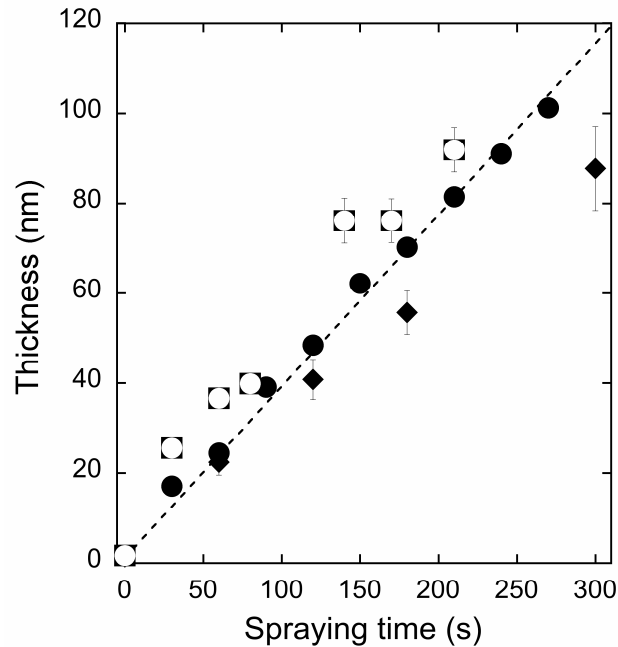


**Figure 98. Thickness data obtained by ellipsometry for AgCl coatings prepared by simultaneous spraying method. The initial solution concentration (Ag salt and Cl salt) is 0.01 M.**

Topography of AgCl coating observed by AFM shows a nanoparticle structure like of inorganic deposition. AgCl nanoparticle formed by SSC technology has a maximum diameter of 100 nm. Nanoparticles are homogeneously deposited on silica substrate. It is observed that AgCl forms preferentially single nanoparticles and fewer aggregates. Ellipsometry thickness of inorganic coating imaged by AFM is  $15.5 \pm 0.7$  nm (see Figure 99).

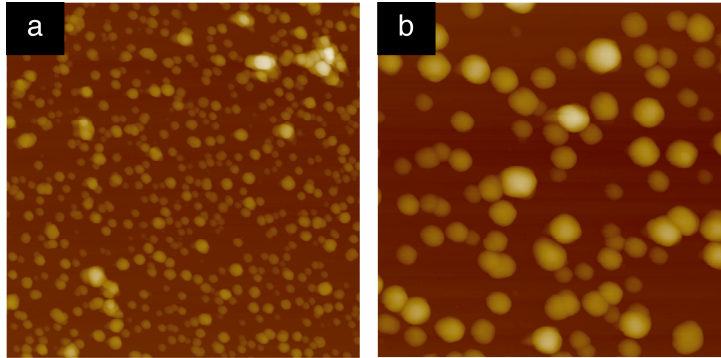


**Figure 99.** AgCl coating prepared by SSC technique for 40 sec spraying time. Coating morphology is analyzed by AFM for a 5x5  $\mu\text{m}$  (a) and 2.5x2.5  $\mu\text{m}$  scan area (b).

### **4.3.2 Calcium phosphate coatings prepared by the method automatic simultaneous spray (ASS) method**

#### **4.3.2.1 Introduction**

At present, the spray-deposition of polyelectrolyte LbL-films is performed manually by using very simple pulverization cans which do not permit sufficient control over the spray process, especially with respect to pressure and delivered liquid volumes. A more precise control of the spray parameters is obtained with automated spray-deposition equipment with high quality nozzles (24).

The simultaneous spray deposition offers a great deal of flexibility because the coating material can be easily changed (calcium phosphate, calcium fluoride, calcium oxalate, iron phosphate, silver chloride, Prussian Blue coatings or functionalized polymeric films). It is an interesting method because it can coat every substrate, regardless of its size or complexity.

Spraying is a tedious task. For example it can take about several hours to coat an object (25). Spraying also requires operator skill to achieve good results (26). For example, it is important to maintain constant the distance between spray nozzles and substrate and the same spraying angle. It is difficult when the simultaneous sprayed coatings are prepared using more than two nozzle spray (e.g. calcium solution, phosphate solution, poly (ethylene oxide) (PEO), see Figure 106).

The use of robots for automated coating operations is a powerful alternative for:

1. **Application Quality** - Spray Robots are generally equipped with six axes, three for the base motions and three for applicator orientation. The spray automation improves application appearance, consistency and throughput. Automation creates more uniform coverage of products, especially those with hard-to-reach portions (27).
2. **Material Savings** - A spray robot improves material savings through greater application efficiency. A savings of 20% to 30% in paint or other coatings can be achieved with the precision of a robotic system.

3. Worker Safety - Automated spraying saves workers from the dangerous, painstaking work of manual spraying.

#### 4.3.2.2 Controlled calcium phosphate coating deposition

Numerous experiments have been done mainly for calcium phosphate coatings, but other inorganic coatings such as calcium fluoride, calcium oxalate or iron phosphate coatings can be prepared by the same simultaneous spraying technique (see Figure 100).

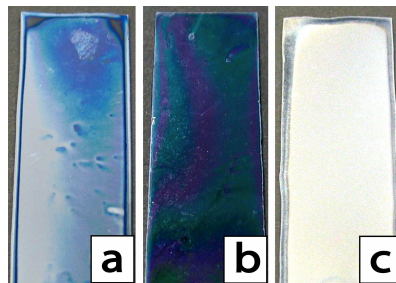


**Figure 100.** a) Calcium oxalate coating prepared by ASS using calcium chloride ( $\text{CaCl}_2$ ), sodium oxalate ( $\text{Na}_2\text{C}_2\text{O}_4$ ) and the water co-pulverization. b) Calcium fluoride coating (interference colors are visible) prepared by ASS using calcium chloride ( $\text{CaCl}_2$ ) and sodium fluoride ( $\text{NaF}$ ). c) Calcium phosphate coating prepared by ASS using calcium nitrate ( $\text{CaNO}_3$ ), ammonium hydrogen phosphate ( $(\text{NH}_4)_2(\text{HPO}_4)$ ) and the water co-pulverization. The solution concentrations and the spraying parameters are presented in the Table 18.

Sample	Number of spray nozzles	Spraying time (min)	Spraying (reactive) solution, Concentration (M)		Flow rates (ml/min)		Air flow rates (l/min)	
					Spraying solutions	Water co-pulverization	Spraying solutions	Water co-pulverization
(a)	3	6	$\text{CaCl}_2$ , 0.1	$\text{Na}_2\text{C}_2\text{O}_4$ , 0.1	1.5	5	40	60
(b)	2	6	$\text{CaCl}_2$ , 0.02	$\text{NaF}$ , 0.02	0.5	0	50	0
(c)	3	5	$\text{CaNO}_3$ , 0.16	$(\text{NH}_4)_2(\text{HPO}_4)$ , 0.095	1	2.5	25	40

**Table 18.** Recapitulative table containing the spraying parameters (solution concentration, flow rate, spraying time)

We generally use three spray nozzles when the water co-pulverization is activated and two without the water spraying.

For the calcium phosphate coatings, the ASS method uses the same solutions (solution concentrations also) as for the consecutive spraying technique. A visible gel-like material forms at the substrate surface, (see Figure 101a) mainly in the drainage zone and less in the direct impact zone of the liquid jets. An inhomogeneous coating is obtained after the extra-rinsing of the substrate. The extra-rinsing step removes the unattached (or weakly attached) material of the coating. The sample is dried with compressed air. The resulting film is thicker in the regions where less gel was obtained.

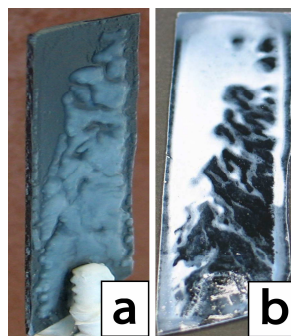


**Figure 101. a) Calcium phosphate coating obtained by the ASS method of calcium solution (0.32M), phosphate solution (0.19M) and H<sub>2</sub>O co-pulverization. b) Dry state of the high non-homogeneous calcium phosphate coating. The ASS spraying parameters: Ca,P flows: 2.5 ml/min, H<sub>2</sub>O flow: 5 ml/min, airflow rate: 40 l/min (Ca, P, H<sub>2</sub>O) for 5 minutes of spraying. The number of spray nozzles is three.**

These preliminary results pointed out the huge importance of the water co-pulverization flow rate (similar to water-rinsing step in the classic LbL method). If the co-pulverization step is efficient enough, a homogenous coating is obtained and the gel phase is reduced or absent. One way to increase the co-pulverization (rinsing) efficiency is increasing the water co-pulverization flow rate or the water airflow rate without changing the concentrations of the initial solutions.

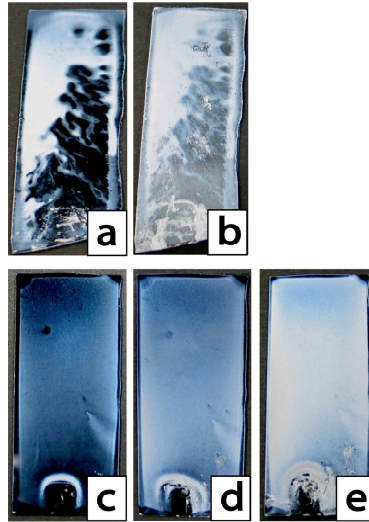


**Figure 102.** Top images (a,b): Inhomogeneous calcium phosphate coatings prepared with a poor water co-pulverization step (spraying conditions: see Table 19, H<sub>2</sub>O airflow rate: 40 l/min) after ASS spraying for 5 min (a) and 10 min (b). Bottom images (c-e): homogeneous calcium phosphate coatings prepared using the same ASS technique but with an improved water co-pulverization step (see Table 19, H<sub>2</sub>O airflow rate is increased to 60 l/min).

Sample (Images Figure 102)	Number of spray nozzles	Spraying time (min), (corresponding image)	Spraying (reactive) solution, Concentration (M)		Flow rates (ml/min)		Air flow rates (l/min)	
					Spraying solutions	Water co- pulverization	Spraying solutions	Water co- pulverization
1 (a-b)	3	5 (a), 10 (b)	CaNO <sub>3</sub> , 0.32	(NH <sub>4</sub> ) <sub>2</sub> (HPO <sub>4</sub> ), 0.19	2.5	5	40	40
2 (c-e)	3	1 (c), 2 (d), 3 (e)	CaNO <sub>3</sub> , 0.32	(NH <sub>4</sub> ) <sub>2</sub> (HPO <sub>4</sub> ), 0.19	2.5	5	40	60

**Table 19.** Solution concentrations and spraying parameters used for the CaP coating preparation

The control of deposition is an important key to control homogeneity and thickness. For the ASS technique, numerous deposition parameters can be changed such as spraying parameters (liquid flow rate, airflow rate, substrate-nozzle spraying distance, spraying set-up, nozzles alignment) and spraying solution (concentration, solvent, incorporation of various agents for controlling properties of sprayed solution: viscosity, surface tension, etc.).

The main parameter that influences on the coating properties and thickness is the initial solution concentration. Initially we worked with the same spraying solutions as for the consecutive spraying system. The concentration was too high and we were able to prepare thicker coatings easily just in a few minutes of ASS spraying. The Figure 103 represents the concentrations change of initial solutions. A lower rinsing airflow rate (sample a, Figure 103) allows measuring the sample ellipsometric thickness for the initially concentrated solution sample.

The concentration variation is a crucial factor; it is a factor of 5 times difference between samples. Higher concentrations produce very thick coatings that are difficult to measure by ellipsometry or UV-Vis spectroscopy.

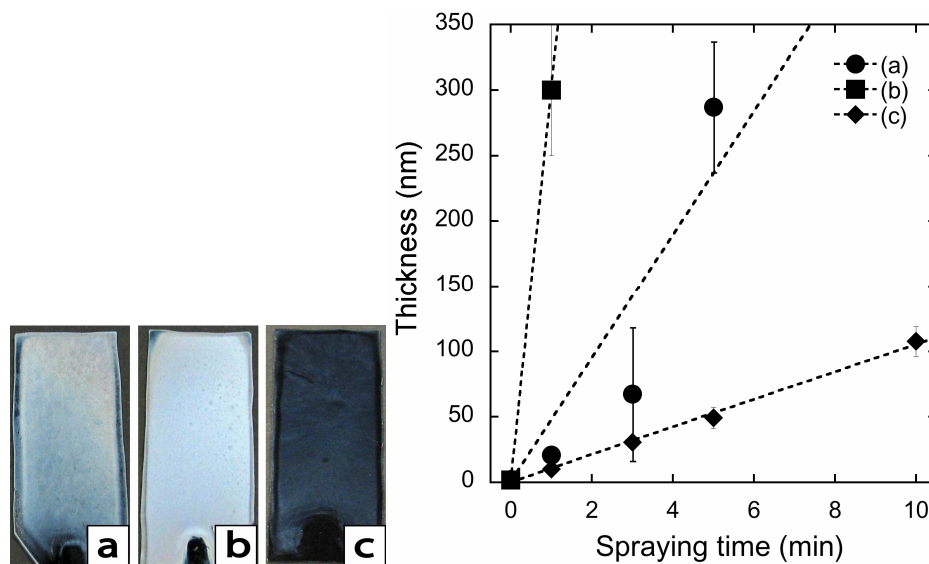


**Figure 103. Left: Photographic images of CaP coatings obtained after 5 minutes of spraying. Right: Thickness variation versus spraying concentration variation. Calcium phosphate coatings prepared by ASS technique using spraying parameters (see Table 20). Solution concentrations are presented in the same table as the spraying parameters. The number of spray nozzles is 3 for all experiments.**

Sample	Concentration (M)		Flow rates (ml/min)			Air flow rates (l/min)		
	Ca	P	Ca	P	H <sub>2</sub> O	Ca	P	H <sub>2</sub> O
(a)	0.16	0.095	1	1	2	20	20	20
(b)	0.16	0.095	1	1	2	20	20	40
(c)	0.032	0.019	1	1	2	20	20	40

**Table 20. Solution concentrations and spraying parameters used for the CaP coating preparation**

A big difference is observed between the samples prepared from the high concentrated solution and the low concentrated solution (samples b and c, Figure 103). Highly concentrated solutions have high deposition rates. The corresponding samples thickness cannot be measured by ellipsometry after 1 min of spraying. The color intensity of coating (optical images), the coating UV-Vis absorbance and the coating thickness measured by ellipsometry are well correlated (Figure 104).

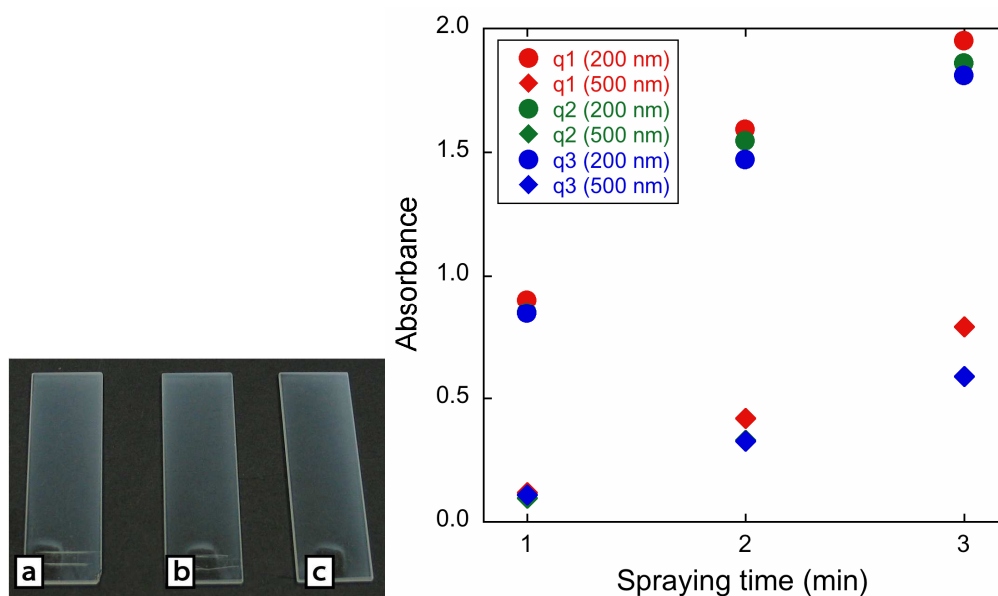


**Figure 104.** Left: Images of calcium phosphate coatings on UV-Vis quartz slides. The spraying parameters are the Ca,P flow rates: 0.1 (q1), 0.5 (q2), 1 (q3) ml/min, H<sub>2</sub>O flow rate: 2 ml/min, airflow rate: 50 l/min (Ca, P, H<sub>2</sub>O), 3 spray nozzles. Right: UV-Vis spectra.

Comparing the coating's thickness from nanoscale range to micrometric scale can be difficult using only one measuring technique (ellipsometry, UV-Vis spectroscopy, nano-indentations, TEM/SEM microscopy, etc.). Thicker coatings ((a-c) Figure 105) cannot be measured by ellipsometry, which is a fast method for the measuring thickness. They should be measured by an appropriate method for rough and non-transparent coatings.



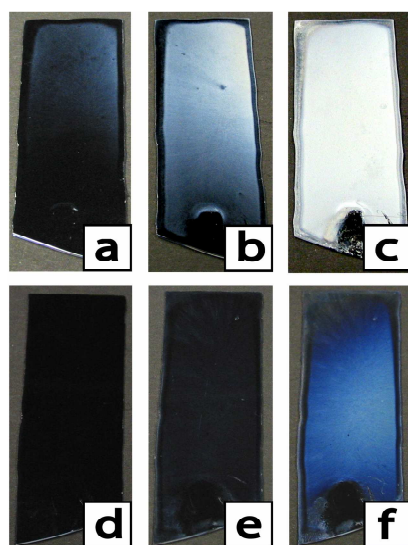


**Figure 105. Calcium phosphate coatings. Increasing thickness with increasing spraying time. Photographic images are taken after 1 min (a and d), 3 min (b and e) and 10 min (c and f) of spraying. See Table 21 for spray parameters (less concentrated solution: sample 2, more concentrated solution: sample 1)**

Sample (corresponding images)	Number of spray nozzles	Spraying time (min)	Concentration (M)		Flow rates (ml/min)			Air flow rates (l/min)		
			Ca	P	Ca	P	H <sub>2</sub> O	Ca	P	H <sub>2</sub> O
1 (a-c)	3	1, 3, 5	0.16	0.095	1	1	2.5	25	25	40
2 (d-f)	3	1, 3, 5	0.032	0.019	1	1	2.5	25	25	40

**Table 21. Solution concentrations and spraying parameters used for the CaP coating preparation**

The coating prepared by 10 min spraying (sample f, Figure 105) of the less concentrated solutions is thinner than the coating obtained after 3 min of a five times more concentrated initial solution (sample b, Figure 105).

### 4.3.2.3 The influence of central polymers on the sprayed inorganic films

Incorporation of polymers into the spraying solution is one of the approaches explored for a better control of calcium phosphate deposition. Poly (ethylene oxide) (PEO) is added in both sprayed solution (calcium and phosphate solution). PEO concentration plays a main role for the amount of material deposited onto the substrate. For constant spraying conditions, PEO concentration seems to allow the control the thickness of calcium phosphate coating (see Figure 106).

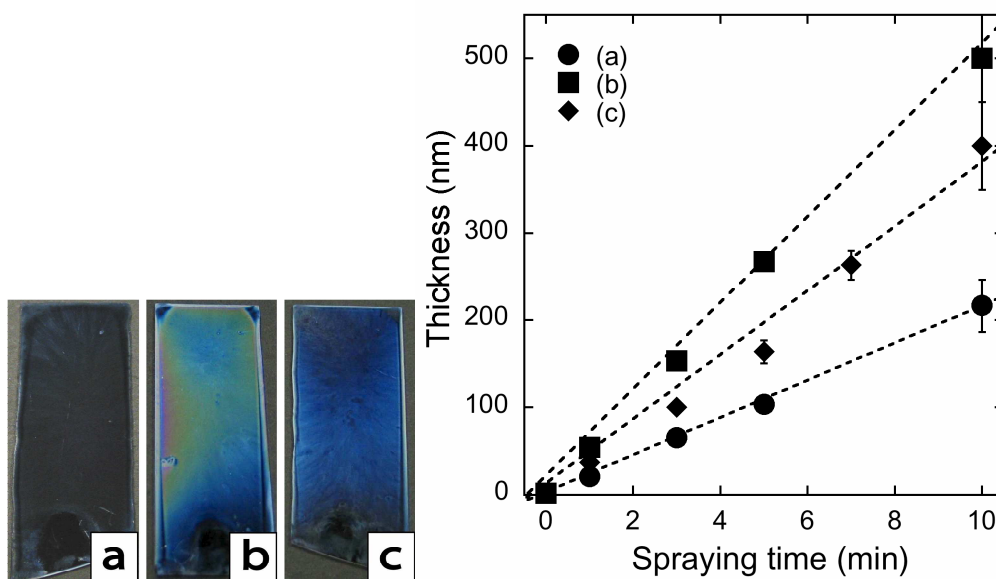


**Figure 106.** Calcium phosphate coatings fabricated by ASS method. Left: PEO influence on homogeneity, coating thickness after 5 min of ASS spraying (optical images). a) Calcium phosphate coating without incorporating PEO, b) Calcium phosphate coating prepared with low PEO concentration (1 mg/ml, Mw = 8000 g/mol) added to spraying solutions, c) Calcium phosphate coating prepared with higher amounts of PEO (10 mg/ml, Mw = 8000 g/mol) added into spraying solutions. Right: Coating thickness versus spraying time for all cases (a-c). Spraying conditions are: 3 spray nozzles, Ca-PEO, P-PEO flow rates: 1 ml/min, H<sub>2</sub>O flow rate: 2.5 ml/min, airflow rate: 25 l/min (Ca-PEO, P-PEO) and 40 l/min for H<sub>2</sub>O. Calcium and phosphate concentrations are 0.032M and 0.019M respectively.

For a low PEO concentration (Figure 106b), the deposition rate is increased by almost a factor of three. For an important amount of PEO in the sprayed solution (10 mg/ml, see Figure 106 c), the deposition rate is two times higher than without the addition of PEO.

There is a strong correlation between the color intensity of coating (optical images) and the coating thickness measured by ellipsometry. The impossibility of ellipsometric data acquisition after a certain spraying time should be noted. This is due to high thickness and roughness of the coating. Inorganic crystals produce a high diffraction of the ellipsometric laser, which makes it impossible to detect the low intensity of the reflected laser beam by the detector of the ellipsometer.

Interference colors visible to the naked eye give an idea of the coating thickness prepared by ASS technique. Figure 107 shows the variation of substrate color and thickness from thin coatings prepared after a few minutes of spraying (white “milky” coating) to thicker coatings obtained after 5 minutes of spraying (various colors: blue, pin, yellow coatings). Thicker coatings (samples a-d, Figure 107) are deposited by spraying more concentrated calcium and phosphate solutions (concentration values same as the example presented above).

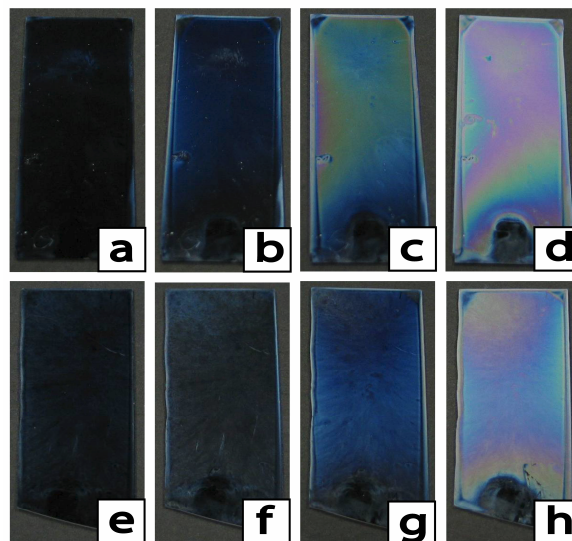


**Figure 107. Calcium phosphate coatings prepared by the ASS method. The spraying time varies from 1 min (a, e), 3 min (b, f), 5 min (c, g) to 8 min (d, h). The spraying solutions have with low PEO content ( $M_w = 8000$  g/mol). Calcium and phosphate concentrations are 0.032M and 0.019M respectively. The deposition parameters are presented in Table 22. The number of spray nozzles is 3 for all experiments.**

Sample	Images (Figure 107)	PEO concentration (mg/ml)	Flow rates (ml/min)			Air flow rates (l/min)		
			Ca-PEO	P-PEO	H <sub>2</sub> O	Ca-PEO	P-PEO	H <sub>2</sub> O
1	a, b, c, d	1	1	1	2.5	25	25	40
2	e, f, g, h	10	1	1	2.5	25	25	40

**Table 22. Deposition parameters for CaP coatings containing low amount of PEO**

To begin, the PEO concentration was varied from 1 to 10 mg/ml (see Figure 108) for PEO with Mw of 8000. We then investigated the influence of the molecular weight of PEO added to initial solutions on the coating deposition. Higher molecular weight PEO (20000 g/mol) was used in the same proportions as before (1 and 10 mg/ml). Keeping the spray conditions constant (liquid flow rate, airflow rate), it is observed that coating thickness is obviously dependent on time, but also on Mw of PEO. The Figure 108 reports the slight difference between low and high Mw of PEO at low polymer concentration and the important thickness difference at higher polymer concentrations. In the case of higher concentrations, longer polymer chains decrease the adherence of the inorganic crystals formed by spraying. They are harder to attach to the substrate.

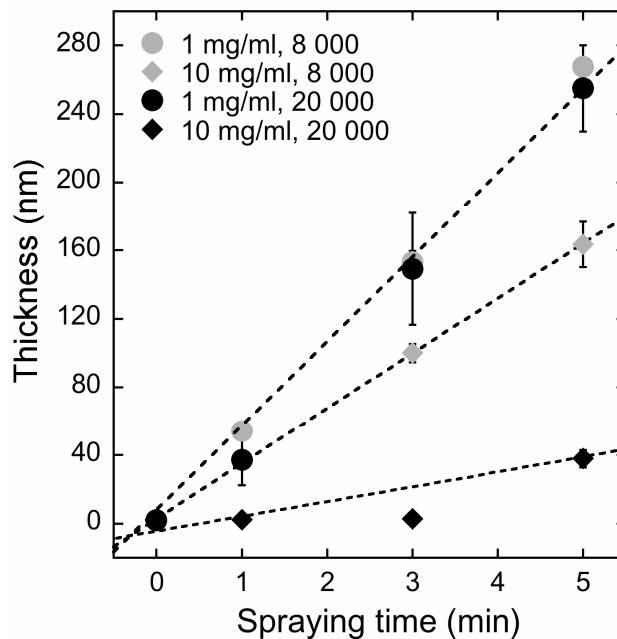


**Figure 108.** Calcium phosphate coatings containing PEO. A large range of deposition parameters can be varied: PEO concentration, PEO Mw. Spraying conditions: 3 nozzles spray, Ca-PEO, P-PEO flow rates: 1 ml/min, H<sub>2</sub>O flow rate: 2.5 ml/min, airflow rate: 25 l/min (Ca-PEO, P-PEO) and 40 l/min for H<sub>2</sub>O. Calcium and phosphate concentrations are 0.032M and 0.019M respectively.

Playing with two deposition parameters at the same time (PEO concentration and spraying parameters as liquid flow rate) allows large control over the thickness of sprayed coatings.

It is possible to have an elevated deposition rate at high liquid flow rates and high airflow rates (see Figure 109, liquid flow rates F3 are higher than flow rates F2 or F1 for Ca-PEO and P-PEO solutions). Independently of liquid flow rate, the quantity of polymer added has the same influence on the coating deposition. It is possible to decrease the thickness coating by increasing the amount of polymer.

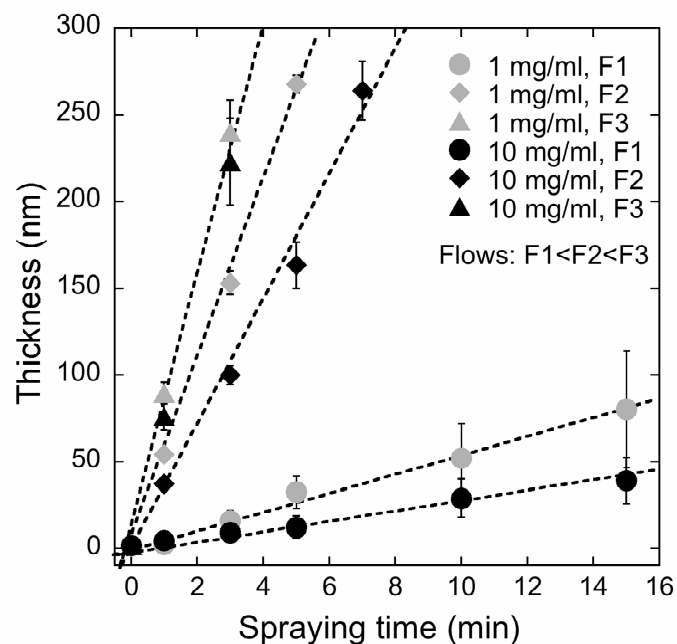
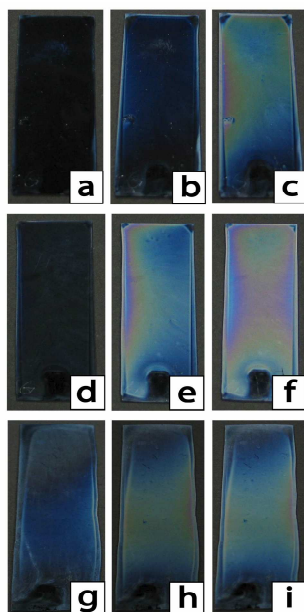


Figure 109. Calcium phosphate coatings containing PEO. Calcium and phosphate concentrations are 0.032M and 0.019M respectively. PEO Mw is 8000 g/mol. Calcium phosphate coatings prepared by ASS technique using spraying parameters (see Table 23).

Flow rate	Number of spray nozzles	Flow rates (ml/min)			Air flow rates (l/min)		
		Ca	P	H <sub>2</sub> O	Ca	P	H <sub>2</sub> O
F1	3	1	1	2.5	8	8	20
F2	3	1	1	2.5	25	25	40
F3	3	5	5	2.5	25	25	40

Table 23. Spray parameters



**Figure 110. Calcium phosphate coatings containing PEO. Mw of PEO is 8000 g/mol (images (a-f)) and 20000 (images g-i). The spraying time is varied form 1 min (a, d, g) to 3 min (b, e, h) to 5 min (c, f, i). Spraying conditions (a-c and g-i): flow rate F2 (see Table 23 above). Spraying conditions (d-f): flow rate F3 (see table above). Calcium and phosphate concentrations are 0.032M and 0.019M respectively.**

#### 4.3.2.4 Hybrid film preparation containing calcium phosphate

The ASS allows the preparation of the hybrid films containing calcium phosphate and Collagen. Generally, for the inorganic coatings (including calcium phosphate) preparation, the water is used as the main solvent for the rinsing step. In the case of collagen-calcium phosphate films, the water is replaced by the Collagen solution. A homogenous coating is obtained for low liquid flow rates (see Figure 111) and for long periods of spraying.

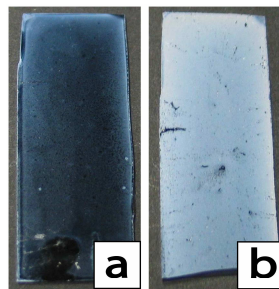


**Figure 111. a) Collagen-calcium phosphate coating sprayed for 1 min, b) Collagen-calcium phosphate coating sprayed for 6 min. Spraying parameters are: Ca,P flow rates: 0.5 ml/min, Collagen flow rate: 1 ml/min, airflow rate: 50 l/min (Ca, P, Col), 3 nozzles. Collagen concentration is 0.1 mg/ml, calcium and phosphate concentrations (0.32 M and 0.19M respectively) are the same as in the previous experiments.**

We explored the preparation of composites based on alginate and calcium phosphate by ASS technique. Alginate is used as the rinsing solution. The thickness of these composites is lower than the classical calcium phosphate coating thickness. It is reported that alginate forms a gel when is in contact with a bivalent cation solution as our initial calcium solution. This gel formation can explain the thin film and high roughness presented for these composites. If the alginate flow rate is too high, the composite thickness decreases. Figure 112 reports the difficulty of alginate- calcium phosphate gel-like biomaterials by ASS technique.



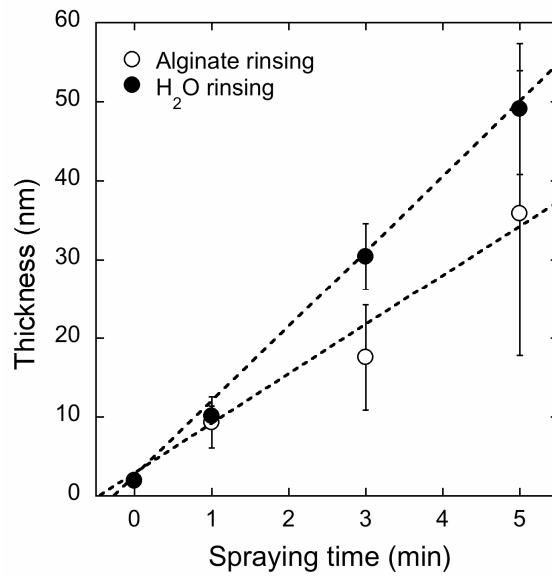


**Figure 112. Importance of the rinsing solution for coating preparation. Alginat (1mg/ml) rinsing solution don't increase the deposition rate as high as the water rinsing step. Spraying conditions: 3 nozzles spray, Ca, P flow rates: 1 ml/min, H<sub>2</sub>O flow rate: 2 ml/min, airflow rate: 20 l/min (Ca, P) and 40 l/min for H<sub>2</sub>O/ Alginat. Calcium and phosphate concentrations are 0.032M and 0.019M respectively.**

#### ***4.4 Prussian Blue film preparation by AS/SSC method***

Prussian Blue (PB) is an inorganic crystal and the oldest coordination compound reported in the scientific literature. PB (iron (III) hexacyanoferrate(II)) has numerous applications because of its interesting electrochemical, electrochromic, photophysical and magnetic properties and also potential analytic applications (e.g. biosensors for glucose) (28, 29). However, common techniques of film preparation are reported in literature such as electrochemical deposition, casting from colloidal solution, dip-coating, Langmuir-Blodgett, multiple sequential adsorptions (MSA) of ferric cations and hexacyanoferrate anions (30-32). As already described in previous articles, two different routes can be applied for the preparation of PB films. According to the first route, the PB synthesis is prepared from an aqueous solution of potassium hexacyanoferrate (II),  $K_4[Fe(CN)_6]$  (K4) and an aqueous ferric chloride (III),  $(FeCl_3)$  solution. The second route to PB film fabrication is based on the reaction between aqueous solutions of potassium hexacyanoferrate (III),  $K_3[Fe(CN)_6]$  (K3) and ferrous cations (II),  $(FeCl_2)$  or  $(NH_4)_2Fe(SO_4)_2$ .

Initially the PB films have been prepared by our AS method from freshly prepared aqueous solutions of potassium hexacyanoferrate (III),  $K_3[Fe(CN)_6]$  and ferrous chloride (II),  $(FeCl_2)$  solution.

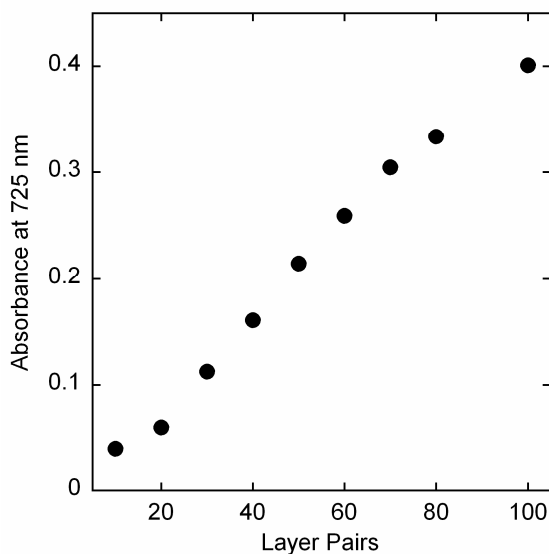


**Figure 113.** UV-Vis absorbance of PB films prepared by AS technique (such as inorganic coating deposition) increases with number of layer pairs. PB synthesis is obtained from an aqueous solution of potassium hexacyanoferrate (III) (9mM) and a ferrous chloride solution (3mM). Quartz slide is pre-coated with one PAH layer.

Thick PB films prepared by the AS method (see Figure 113) have been characterized by various analytical techniques (UV-Vis spectroscopy, AFM). A change of PB film color intensity (from clear blue to intense blue color) is observed by naked eye as the number of layer pairs increases. This is translated by a linear increase of the absorbance peak around 725 nm (attributed to PB). The PB coating morphology shows small NPs size that form the homogeneous PB film prepared by the AS method (Figure 114).

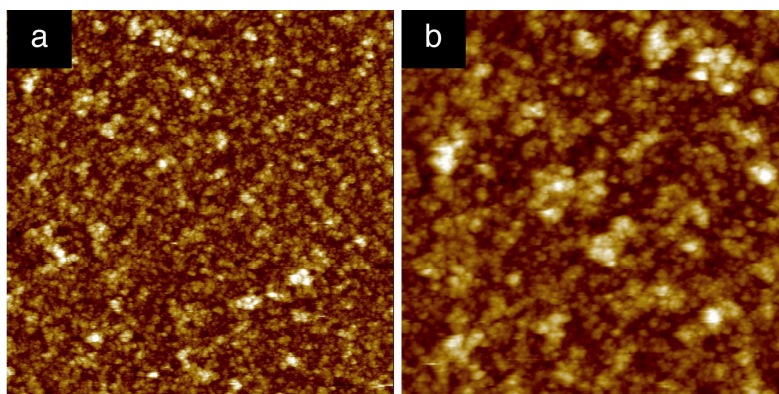


**Figure 114.** AFM image of PB film ( $(\text{K}_3\text{-Fe})_{50}$ ) prepared by the AS method. Solution concentrations are: K3 (9 mM) and Fe (3mM). A PAH pre-coated silica wafer is used. Scans size are: 5x5  $\mu\text{m}$  (a) and 2.5x2.5  $\mu\text{m}$  (b).

The PB NP size is around 10 nm (DLS measurement) and the PB film roughness is around 16 nm (calculated from AFM images, see Figure 114). PB films prepared by the AS technique are smooth and homogenous.

A second route for PB deposition is the SSC method that uses the same aqueous solution concentrations as the AS technique. First, we investigate the substrate influence on PB film deposition. Because of the choice of different substrate coatings, the PB deposition rate can be widely tailored. The preference of PB nucleation and growth is observed on positive substrates as PAH and PEI (Figure 115). Clean silica substrate (untreated, see Figure 115) that is highly negatively charged cannot be used as substrate for PB film deposition. The NP zeta potential charge is measured by DLS and it shows negative values (around  $-35$  mV) for PB NP.

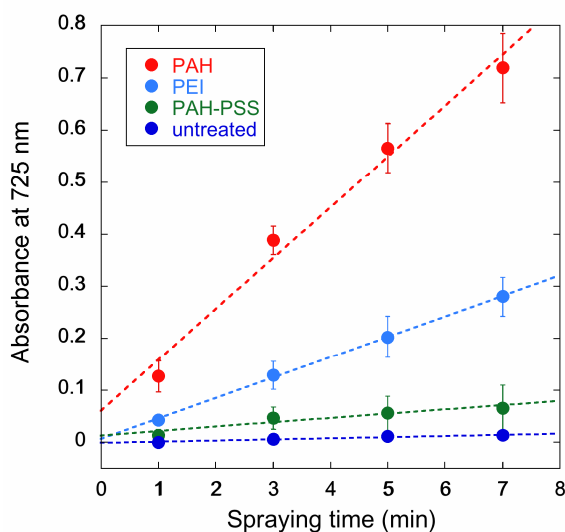


**Figure 115.** UV-Vis absorbance increase with increasing spraying time for PB films prepared by SSC deposition. Study of the substrate influence on PB film deposition rate. The liquid flow rates are constant (around 6.5-7 ml/min) and the solution concentration is 3mM for all experiments.

We investigated the significance of changing the liquid flow rate on the PB deposition rate (see Figure 116). Three situations have been investigated for PB film formation: Fe flow rate < K3 flow rate, Fe flow rate > K3 flow rate and K3 flow rate = Fe flow rate (see Figure 116).

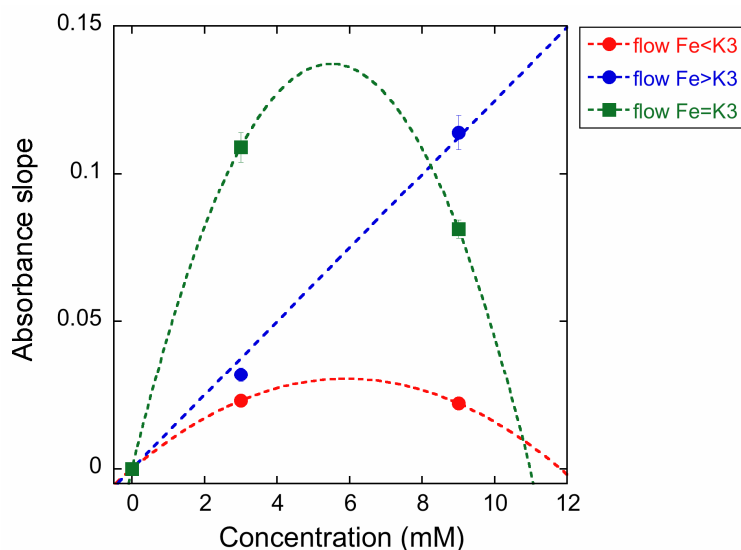


**Figure 116. Liquid flow rate influence on the PB film UV-Vis absorbance at 725nm (or thickness). Quartz slides are pre-coated with a PAH layer. For the first case (Fe flow rate < K3 flow rate), the Fe flow rate is roughly 3-3.5 ml/min and the K3 flow rate is around 6.5-7 ml/min. For the second experiment (Fe flow rate > K3 flow rate), the Fe flow rate is roughly 6.5-7 ml/min and the K3 flow rate is around 3-3.5 ml/min. The last case is with equal liquid flow rates (6.5-7 ml/min).**

Three different liquid flow rate situations are explored for different initial solutions concentrations: 3mM solutions and 9mM solutions. For the experiments where K3 flow rate is roughly twice the Fe flow rate (see red curve, Figure 116), the PB film thickness has a maximum value but is lower than other presented examples. Linear increase of PB thickness is observed for the case where Fe is flow rate higher than K3 flow rate (see blue curve, Figure 116). The same maximum thickness (absorbance) curve is observed for equal liquid flow rates (see green curve, Figure 116).

Supplementary experiments are realized to understand the influence of solution concentration on PB film preparation for the case of equal liquid flow rates. We prepared PB films with various initial solution concentrations: 1mM, 2mM, 3mM, 6mM and 9mM (Figure 117). A maximum absorbance value is observed for 3mM and a minimum around 7mM. During PB film deposition, an equilibrium exists between the formation and the dissolution rates of PB crystals. Homogeneous PB films are obtained for concentrations lower than 3mM characterized by a crystallization rate greater than a dissolution rate of PB crystals. The PB films are less homogeneous at concentrations higher than 3mM

because there is a competition between crystallization/dissolution rates for PB deposition. Even though the same film absorbance is observed for films prepared from 3mM and 9mM concentrations, the 3mM coatings are much more homogeneous than the 9mM coatings (much lower homogeneity).

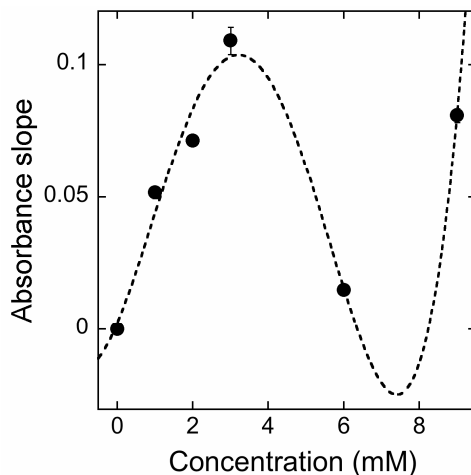


**Figure 117. The solution concentration influence on UV-Vis film absorbance at 725 nm for PB film deposition by SSC technique. For the presented experiments, the liquid flow rates are more or less equal to 6.5-7 ml/min and PAH pre-coated quartz slides are used.**

We followed the deposition process by UV-Vis spectroscopy (PB absorbs in 700-750 nm region) in order to avoid the non-accurate values obtained by ellipsometry for thick films. The same effect of the solution concentration variation is studied for PB films deposited on PAH treated silica wafers (Figure 118). Increasing the concentrations for Fe and K3 solutions increases the PB deposition rate. A 50 nm thick PB film is obtained after 4 min of simultaneous spraying 3mM solutions.

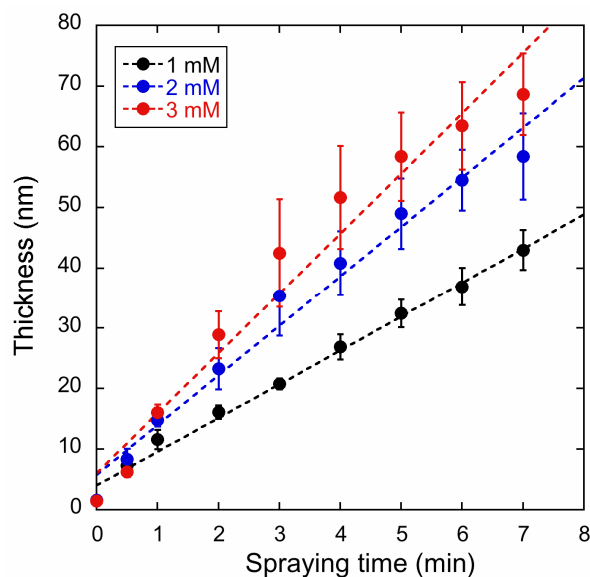
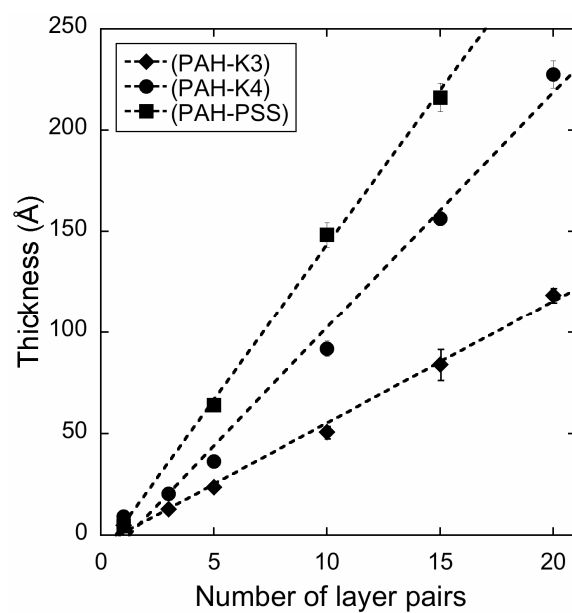


Figure 118. PB film thickness variation for different solution concentrations (1mM, 2mM and 3mM) by increasing spraying time. The liquid flow rates are similar (around 6.5-7 ml/min). The silica wafers are pre-coated with one PAH layer.

#### 4.5 Thin film preparation based on polyelectrolyte-small molecule interaction

The main polyelectrolyte used in film formation based on polymer-small molecule interactions is the well known PAH. Positive charged polyelectrolyte (PAH) interacts with negatively charged small molecules as oxalate, citrate, ferrocyanide or ferricyanide ions. For the PAH-ferri/ferrocyanide molecule interaction, various experiments are realized by consecutive and simultaneous spraying deposition techniques. For consecutive/alternatingly spraying method (AS), two strategies are followed for the polyelectrolyte-small molecule thin film preparation. The first method is the classical technique for PEM film preparation that consists in 5 sec spraying of the first component, waiting for 15 sec, and then 5 sec MilliQ water rinsing. This cycle is repeated for the second component so that a layer pair is formed. The second deposition method is usually applied for inorganic coating deposition that is achieved by spraying 2x1s the first component, and then spraying 2x1s the second component without waiting. The rinsing step is exclusively realized before the characterization measurement of the prepared film.



**Figure 119.** Thickness measurement by ellipsometry for polyelectrolyte-small molecule films prepared by consecutive spraying methods similar to PEM films.

Linear growth of films is observed for all studied systems. Independent of the deposition method, the (PAH-K4) film is thicker than the (PAH-K3) film (data not shown for films prepared by AS inorganic deposition method). The classical PEM (PAH-PSS) film thickness is however clearly greater than polyelectrolyte-small molecule film thickness.



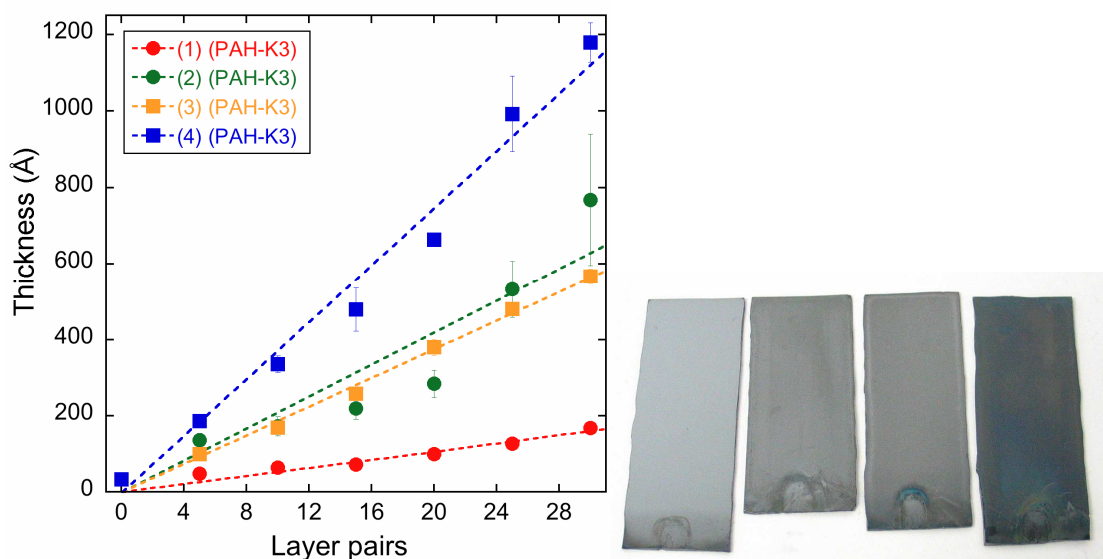


**Figure 120.** Left: Ellipsometric thickness increase of (PAH-K3) films prepared by consecutive spraying method versus the number of layer pairs. Various spraying methods/solution concentrations are used for samples preparation: (1) 5s spraying, 15s wait, 5s rinsing like for PEM preparation, K3 (30mM); (2) 5s spraying, 15s wait, K3 (30mM); (3) 2s spraying as in the inorganic AS method, K3 (30mM); (4) 5s spraying, 15s wait like for PEM fabrication, K3 (9mM). PAH concentration is constant (1mg/ml). Right: Image of the samples after 30 deposited layer pairs. The sample presentation order is from left to right (from sample (1) to (4)).

The importance of the deposition method (spraying time, rinsing step) on film thickness is presented in Figure 120. A controlled deposition process based on controlling important parameters such as solution concentration, rinsing time, deposition time and spraying experiment set-up (liquid flow rate, airflow rate, spraying distance...) is observed for PEM film preparation and inorganic coating deposition.

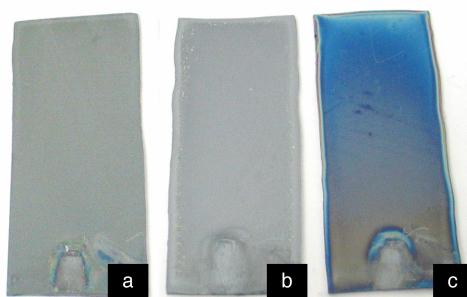


**Figure 121. Polyelectrolyte-small molecule thin films prepared by the SSC method after spraying for 5 min. (a) (PAH-K3) film, (b) (PAH-K3) film, (c) (PAH-Oxalate) film. Solutions concentration: PAH (1mg/ml, 0.15M NaCl, K3 (30mM), K4 (30mM), Ox (0.1M). Spraying parameters: Aztek spraying system, airflow rate P=3 bars, liquid flow rates: 6.5 ml/min.**

PAH-small molecule films can also be prepared by the SSC deposition (Figure 121). (PAH-K3) and (PAH-K4) films prepared by the SSC method have a “milky” color. The thickness of these films is difficult to evaluate since the ellipsometry measurements are imprecise immediately after 30 sec of spraying. On the other hand, the (PAH-Ox) film possesses interference colors (blue in our sample, Figure 121) with lower film roughness. The ellipsometry measurements are therefore accurate. If we compared consecutive spraying method (where it is obvious that (PAH-K3) film thickness is higher than (PAH-K4) coating thickness) to the SSC process, we observe an increased thickness and roughness for the SSC prepared films (Figure 122).

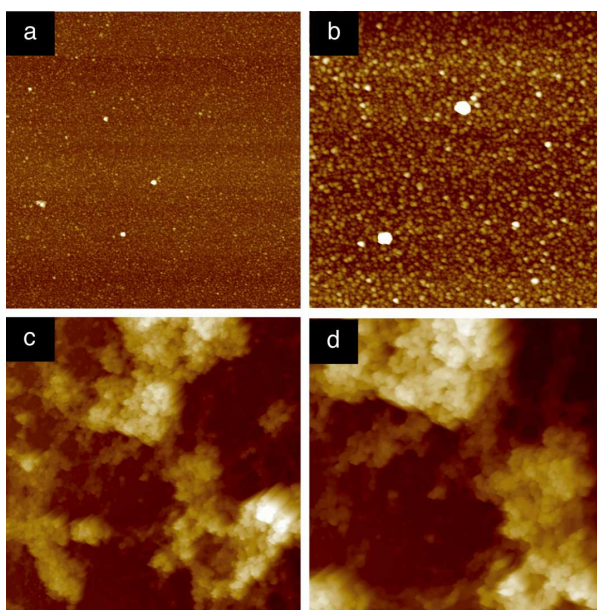


**Figure 122.** (PAH-K4) film morphology studied by AFM. (a, b) AFM images are acquired for a sample prepared by the AS method. Scan image size is 5x5 um (a) and 2x2 um (b). The second sample (c, d) is fabricated by the SSC process. Image size is: 10x10 um (c) and 5x5 um (d).

For samples obtained by the consecutive spraying method (low film roughness) and by the SSC method (high film roughness and “milky” aspect), the topography studies are presented in Figure 122. For rough films (c, d, Figure 122), the agglomerates size (forming the coating) exceeds approximately 700 nm. The presence of big agglomerates for the SSC samples confirms the difficulties of measuring the thickness by ellipsometry. After spraying for 5 min, the SSC film thickness measured by ellipsometry is approximately 50 nm. A huge difference is observed between ellipsometry and AFM measurements for (PAH-K4) SSC films. However, it is not the case for smooth AS film where the ellipsometric thickness is  $24.6 \pm 0.5$  nm and the roughness calculated by AFM is 25 nm.

## 4.6 Bibliography

1. J. T. Lu, C. J. Lee, S. F. Bent, H. A. Fishman, E. E. Sabelman, *Biomaterials* **28**, 1486 (2007).
2. E. Bianchi, G. Conio, A. Ciferri, D. Puett, L. Rajagh, *Journal of Biological Chemistry* **242**, 1361 (1967).
3. S. Leikin, V. A. Parsegian, W. H. Yang, G. E. Walrafen, *Proceedings of the National Academy of Sciences of the United States of America* **94**, 11312 (1997).
4. S. Leikin, D. C. Rau, V. A. Parsegian, *Nature Structural Biology* **2**, 205 (1995).
5. J. A. Johansson *et al.*, *Biomacromolecules* **6**, 1353 (May-Jun, 2005).
6. W. Friess, *European Journal of Pharmaceutics and Biopharmaceutics* **45**, 113 (1998).
7. N. Barbani *et al.*, *Journal of Applied Polymer Science* **72**, 971 (1999).
8. Q. B. Chen, S. T. Xu, R. Li, X. D. Liang, H. L. Liu, *Journal of Colloid and Interface Science* **316**, 1 (2007).
9. C. C. Dupont-Gillain, I. Jacquemart, P. G. Rouxhet, *Colloids and Surfaces B-Biointerfaces* **43**, 179 (2005).
10. Q. K. Lin *et al.*, *Biomaterials* **31**, 4017 (2010).
11. J. Zhang *et al.*, *Biomaterials* **26**, 3353 (2005).
12. J. B. Schlenoff, S. T. Dubas, T. Farhat, *Langmuir* **16**, 9968 (2000).
13. A. Izquierdo, S. S. Ono, J. C. Voegel, P. Schaaf, G. Decher, *Langmuir* **21**, 7558 (2005).
14. L. F. Sukhodub *et al.*, *Journal of Molecular Structure* **704**, 53 (2004).
15. K. Potter, L. H. Kidder, I. W. Levin, E. N. Lewis, R. G. S. Spencer, *Arthritis and Rheumatism* **44**, 846 (2001).
16. C. C. Dupont-Gillain *et al.*, *Journal of Materials Science-Materials in Medicine* **15**, 347 (2004).
17. C. C. Dupont-Gillain, P. G. Rouxhet, *Langmuir* **17**, 7261 (2001).
18. I. Jacquemart, E. Pamula, V. M. De Cupere, P. Rouxhet, C. C. Dupont-Gillain, *Journal of Colloid and Interface Science* **278**, 63 (2004).
19. E. Poptoshev, B. Schoeler, F. Caruso, *Langmuir* **20**, 829 (2004).
20. S. T. Dubas, J. B. Schlenoff, *Macromolecules* **32**, 8153 (1999).
21. B. Dong, O. Arnoult, M. E. Smith, G. E. Wnek, *Macromolecular Rapid Communications* **30**, 539 (2009).
22. V. Ball *et al.*, *Crystal Growth & Design* **6**, 327 (2006).
23. J. Xie, C. Riley, M. Kumar, K. Chittur, *Biomaterials* **23**, 3609 (2002).
24. O. Felix, Z. Q. Zheng, F. Cousin, G. Decher, *C. R. Chim.* **12**, 225 (Jan-Feb, 2009).
25. K. Hartmann, R. Krishnan, R. Merz, C. Neplotnik, L. S. F.B. Prinz, M. Terk and L.E. Weiss, *IEEE*, (1994).
26. H. P. Chen, T. Fuhlbrigge, X. Z. Li, *Ieee, 2008 Ieee International Conference on Automation Science and Engineering, Vols 1 and 2*, 522 (2008).
27. S. H. Suh, I. K. Woo, S. K. Noh, *Journal of Manufacturing Systems* **10**, 396 (1991).

28. D. M. DeLongchamp, P. T. Hammond, *Chemistry of Materials* **16**, 4799 (2004).
29. A. A. Karyakin, E. E. Karyakina, *Russian Chemical Bulletin* **50**, 1811 (2001).
30. D. M. DeLongchamp, P. T. Hammond, *Advanced Functional Materials* **14**, 224 (2004).
31. R. C. Millward *et al.*, *Chemical Communications*, 1994 (2001).
32. W. Zhao, J. J. Xu, C. G. Shi, H. Y. Chen, *Langmuir* **21**, 9630 (2005).

# Article 1

# Nanoscale Precipitation Coating: The Deposition of Inorganic Films through Step-by-Step Spray-Assembly

Gabriela Popa,<sup>†</sup> Fouzia Boulmedais,<sup>†</sup> Peng Zhao,<sup>†,¶</sup> Joseph Hemmerlé,<sup>\*,§</sup> Loïc Vidal,<sup>‡</sup> Eric Mathieu,<sup>\*,§</sup> Olivier Félix,<sup>†</sup> Pierre Schaaf,<sup>†,||</sup> Gero Decher,<sup>†,\*,||,∇,\*</sup> and Jean-Claude Voegel<sup>\*,§,\*</sup>

<sup>†</sup>Centre National de la Recherche Scientifique, Institut Charles Sadron (ICS), UPR 22, 23 rue Loess 67083 Strasbourg, France, <sup>‡</sup>Institut National de la Santé et de la Recherche Médicale, UMR 977, 11 rue Humann, 67085 Strasbourg, France, <sup>§</sup>Faculté de Chirurgie Dentaire, Université de Strasbourg, 1 place de l'Hôpital 67000 Strasbourg, France, <sup>‡</sup>Institut de Science des Matériaux de Mulhouse (IS2M) - CNRS LRC 7228, 15 rue Jean Starcky, BP 2488, 68057 Mulhouse Cedex, France, <sup>¶</sup>Faculté de Chimie, Université de Strasbourg, 1 rue Blaise Pascal 67008, Strasbourg, France, <sup>||</sup>International Center for Frontier Research in Chemistry, 8 allée Gaspard Monge, 67083 Strasbourg, France, and <sup>∇</sup>Institut Universitaire de France, 103 Boulevard Saint-Michel, 75005 Paris, France. <sup>\*</sup>Present address: The Institute for Advanced Materials and Nano Biomedicine, Tongji University, 1239 Siping Road, Shanghai, 200092, China.

**ABSTRACT** Thin films and surface coatings play an important role in basic and applied research. Here we report on a new, versatile, and simple method (“precipitation coating”) for the preparation of inorganic films, based on the alternate spraying of complementary inorganic salt solutions against a receiving surface on which the inorganic deposit forms. The method applies whenever the solubility of the deposited material is smaller than that of the salts in the solutions of the reactants. The film thickness is controlled from nanometers to hundreds of micrometers simply by varying the number of spraying steps; 200 spray cycles, corresponding to less than 15 min deposition time, yield films with thicknesses exceeding one micrometer and reaching tens of micrometers in some cases. The new solution-based process is also compatible with conventional layer-by-layer assembly and permits the fabrication of multimaterial sandwich-like coatings.

**KEYWORDS:** inorganic coatings · spray assembly · aqueous solutions · nucleation and growth · thin films

Thin films and functional surfaces constitute an important field in materials science<sup>1–10</sup> with applications in areas such as device engineering, corrosion protection, antistatic coatings, photovoltaics, or biosensing, to name a few. The last decades have brought the evolution of film deposition methods involving transfer through the gas phase such as physical vapor deposition (PVD), chemical vapor deposition (CVD), sputtering, and some variants. However, vacuum-based techniques are somewhat hampered because conformal coatings are often limited to small surface areas on smooth objects, because they are more difficult to integrate in production processes than solution based techniques, because they are often time-consuming and costly, or because it is highly desirable to improve the sustainability benchmarks of the corresponding products. Consequently, solvent based methods such as surface<sup>11,12</sup>

or more recently nanometric<sup>13</sup> or spray pyrolysis<sup>14</sup> have increasingly been investigated for the fabrication of inorganic coatings. A particularly interesting technique for producing a large variety of different inorganic films is the step-by-step dipping method or SILAR (successive ionic layer adsorption and reaction) first reported by Nicolau in 1984.<sup>15–17</sup> A major advantage of the SILAR method over surface sol–gel technology is that inorganic films composed of a much wider range of inorganic components can be prepared using a single process.

One aspect of the SILAR method, the consecutive immersion of surfaces in different liquids, is somewhat similar to the well-known layer-by-layer (LbL)<sup>4,18,19</sup> deposition of organic, polymeric, or hybrid thin films that has become attractive because of a wealth of different functionalities available for incorporation in such nanometric coatings.<sup>20–27</sup> Both SILAR and LbL methods allow the construction of nanometer-sized coatings with precise thickness, but they both suffer from the same drawback, namely that the immersion of an object in a liquid and its subsequent withdrawal, especially if carried out hundreds of times in different solutions, is a time-consuming process and therefore limited to the coating of small and simply shaped objects from which the adhering liquid easily drains. Not surprisingly, multistep dipping-based methods are difficult to implement in industrial production with the possible exception of roll-to-roll processes. Inevitably, the LbL-assembly of thin multimaterial films has

\*Address correspondence to Jean-Claude.Voegel@medecine.u-strasbg.fr, decher@ics.u-strasbg.fr.

Received for review March 18, 2010 and accepted July 2, 2010.

Published online July 16, 2010. 10.1021/nn1005667

© 2010 American Chemical Society

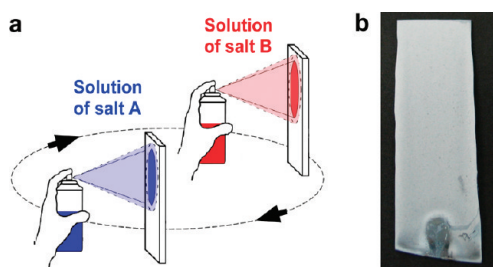


**Figure 1.** (a) Schematic depiction of the deposition of purely inorganic films AB from aqueous solutions by consecutively spraying solutions of the complementary salts A and B onto a receiving solid surface. (b) Optical micrograph of a film of calcium phosphate after 75 spray cycles deposited on a silicon wafer of a size of  $1.5 \times 5.0$  cm. Due to its polycrystallinity and nanoporous morphology the film appears white in reflected light. Besides a mark at the bottom that originates from mounting the wafer, the film is macroscopically very homogeneous.

gained enormously from the introduction of spray-assisted deposition as reported by, for example, Schlenoff,<sup>28</sup> Winterton,<sup>29</sup> Izquierdo,<sup>30</sup> Kotov,<sup>31</sup> or Hammond.<sup>32</sup> LbL-films assembled by spray deposition can often be prepared in a fraction of the time as compared to deposition by dipping and often possess a superior homogeneity sometimes in combination with improved materials properties.

The nanoscale “precipitation coating” technique that we introduce here is based on the step-by-step spraying of solutions of complementary salts (Figure 1a) that possess a non-negligible difference of the solubility products compared to that of the solid inorganic product that forms a film on the receiving surface by precipitation due to a local supersaturation.

It is as versatile for the preparation of inorganic coatings as the SILAR method, but it is very fast and has the additional advantage that spray technology is widely accepted in industrial production. In contrast to spray-LbL which is mostly used for the assembly of polyelectrolyte and related multilayer films, it is more difficult to prevent small salt ions (such as  $\text{Ca}^{2+}$ ,  $\text{F}^-$ ,  $\text{Cl}^-$ ,  $\text{H}_2\text{PO}_4^-$  /  $\text{HPO}_4^{2-}$ ) adsorbed on a surface in the previous deposition step or even nanocrystals from being washed off under the shear of the sprayed solution in the next adsorption step. It actually turns out that the subsequent removal or dissolution of previously adsorbed material is a critical factor that must, in some cases, be controlled for growing high quality films. The very short contact times of the complementary liquids attainable only by spraying against a receiving surface can clearly be shown, for example, in the case of  $\text{CaHPO}_4$ , to be essential for precisely controlling the film growth over hundreds of spray cycles.

The consecutive spray application of solution A and solution B can be repeated hundreds of times in a few minutes to increase the thickness of the inorganic coating until a film with the desired thickness (from a few nanometers up to several micrometers or more) is obtained. It should be clear that these inorganic coatings

do not possess a multilayer structure as in the case of classic polyelectrolyte multilayer films; however, they are fabricated in the same way by employing the step-by-step assembly method as adapted to spray deposition. The following complementary salt pairs (for solubility data see Table S1 in Supporting Information) were chosen as model cases for demonstrating the fabrication of inorganic films by step-by-step spraying: (i)  $\text{CaCl}_2$  and  $\text{NaF}$  which yields calcium fluoride ( $\text{CaF}_2$ ) possessing a high UV transparency which makes it interesting for applications in optical components such as lenses, prisms or windows and because it forms very dense and rather smooth inorganic films. (ii)  $\text{CaCl}_2$  and  $(\text{NH}_4)_2\text{HPO}_4$  which yields calcium phosphate ( $\text{CaHPO}_4$ ), a material that has wide ranging applications in the biomedical field, for example for bone reconstruction. (iii)  $\text{Ca}(\text{NO}_3)_2$  and  $\text{Na}_2\text{C}_2\text{O}_4$  which yields calcium oxalate ( $\text{CaC}_2\text{O}_4$ ) serving as an example for the use of a carbon-based anion.

## RESULTS AND DISCUSSION

**Preparation of Inorganic Films by Spray Deposition.** The spray-assembly of inorganic films—a typical sample is shown in Figure 1b—was carried out by using conventional air pump spray cans equipped with single-component nozzles. We refer to a spraying cycle (A/B)<sub>1</sub> as a process consisting of the spraying of a component A for about 2 s followed by spraying of a component B for about 2 s. The desired spray cycles can be repeated  $n$  times to form (A/B) <sub>$n$</sub>  films. Prior to the deposition of the inorganic films the receiving surface was coated with at least one polyelectrolyte layer to promote its adhesion, in some cases the receiving surface was coated with a LbL-film of collagen and poly(styrene sulfonate) (COL/PSS)<sub>8</sub> with a thickness of about 10 nm because the combination of calcium phosphate with collagen has a certain interest for the reconstruction of bone or cartilage. However, the deposition of inorganic films does not require the presence of collagen in the layer underneath, and similar films can be prepared on many other types of surfaces.

While the first spraying step only leads to the formation of a thin liquid film of solution A, the subsequent spraying step of solution B “into” the draining film of solution A leads to a reaction between both complementary salt solutions. If the solutions of the two complementary starting materials (e.g.,  $\text{CaCl}_2$  and  $\text{NaF}$ ) are chosen such that the resulting reaction product (in this case  $\text{CaF}_2$ ) becomes supersaturated in the liquid film close to the surface of the solid, nucleation will start and germs close to the surface will, depending on the chemical nature of the surface, attach to it. However, since solution B was sprayed last it will, depending on the sprayed volume, now be in excess and the subsequent spray application of solution A will again produce a supersaturated solution of the reaction product (in this case  $\text{CaF}_2$ ). Starting with the third spray application, nucleation is either starting as before or induced

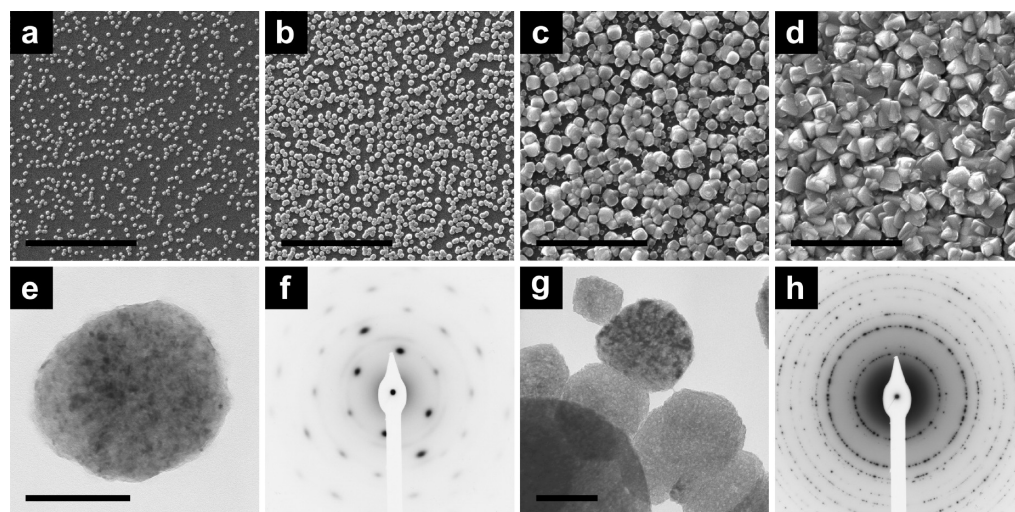


**Figure 2.** Top view scanning electron micrographs of films composed of  $\text{CaF}_2$  (a–d) at various stages of film growth. The numbers of spray cycles for each sample are as follows: 3 (a), 10 (b), 50 (c) and 200 (d). The scale bar represents  $10\ \mu\text{m}$ . Electron micrographs and diffraction patterns were obtained by transmission electron microscopy from  $\text{CaF}_2$  crystals after one cycle (e, f) and three cycles (g, h). Scale bars represent 100 nm for image e and 200 nm for image g.

by crystals already attached to the surface thus accelerating the growth of the inorganic film.

Films of all different materials were spray-assembled up to a given thickness by adjusting the number of deposition cycles, dried in a stream of air or nitrogen, and then characterized. The chemical composition and crystalline phase of the components were determined by electron and X-ray diffraction by comparison with known data (see Tables S2–S4 and Figure S1 in Supporting Information). The alternate spraying of  $\text{CaCl}_2$  and  $\text{NaF}$  yields fluorine films ( $\text{CaF}_2$ ), the spraying of  $\text{Ca}(\text{NO}_3)_2$  and  $(\text{NH}_4)_2\text{HPO}_4$  yields calcium phosphate films (brushite,  $\text{CaHPO}_4$ ), and the spraying of  $\text{CaCl}_2$  and  $\text{Na}_2\text{C}_2\text{O}_4$  yields calcium oxalate films ( $\text{CaC}_2\text{O}_4$ ).

**Dense Polycrystalline Films: Spray Deposition of Calcium Fluoride Films.** For  $\text{CaF}_2$ , scanning electron microscopy (SEM) revealed that the film growth starts by the forma-

tion of nanocrystals with a very small lateral density (Figure 2a). By increasing the number of spray cycles, the size and density of crystals increases until most voids are filled and layer growth proceeds predominantly along the layer normal (Figure 2a–d). Transmission electron microscopy (TEM) and electron diffraction show that in the case of  $\text{CaF}_2$  the smallest observable crystals (about 70 nm) are monocrystalline (Figure 2e,f) which further increase in size (Figure 2b–d) and become polycrystalline (Figure 2g,h).

**Porous Polycrystalline Films: Spray Deposition of Calcium Phosphate and Oxalate Films.** In the case of  $\text{CaHPO}_4$ , the film growth proceeds by nucleation of additional small crystals rather than by crystal growth (Figure 3a–d) which also leads to more porous film morphology. In contrast to  $\text{CaF}_2$ , even the smallest crystals are polycrystalline (Figure 3e,f) as evidenced by the circular diffrac-

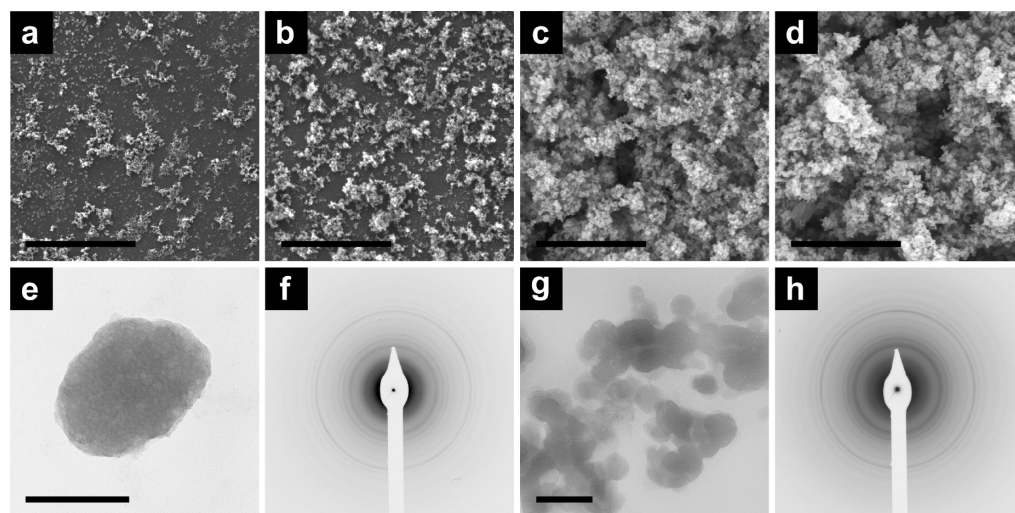


**Figure 3.** Top view scanning electron micrographs of films composed of  $\text{CaHPO}_4$  (a–d) at various stages of film growth. The numbers of spray cycles for each sample are as follows: 3 (a), 10 (b), 50 (c) and 200 (d). The scale bar represents  $10\ \mu\text{m}$ . Electron micrographs and diffraction patterns were obtained by transmission electron microscopy from  $\text{CaHPO}_4$  crystals after one cycle (e, f) and three cycles (g, h). Scale bars represent 100 nm for image e and 200 nm for images g.



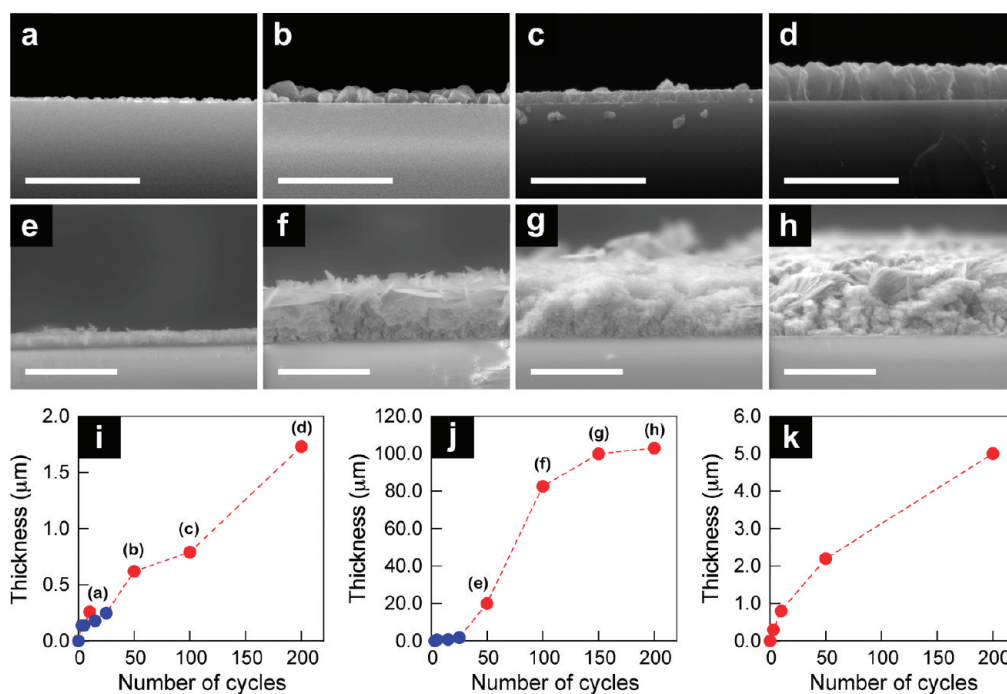


**Figure 4.** Side-view scanning electron micrographs of films composed of CaF<sub>2</sub> (a–d) and CaHPO<sub>4</sub> (e–h) at various stages of film growth. Evolution of the thickness of (i) CaF<sub>2</sub>, (j) CaHPO<sub>4</sub>, and (k) CaC<sub>2</sub>O<sub>4</sub> films versus the number of spraying cycles. Thicknesses were determined either by AFM (scratch of the coating: blue circles) and SEM side-view (red circles). The numbers of spray cycles for each sample are as follows: 10 (a), 50 (b, e), 100 (c, f), 150 (g), and 200 (d, g). The scale bars represent 5 μm for (a–d) and 100 μm for (e–h). Dotted lines are guides.

tion pattern. Please note that the high magnification in Figure 3d leaves the impression of a rather irregular film morphology. However, Figure 1b and Figure S2 clearly underlines the good film homogeneity at a larger scale. The same porous morphology of CaC<sub>2</sub>O<sub>4</sub> films was observed (see Figure S3 in Supporting Information).

**Analysis of Film Growth.** Because of the large range of attainable film thicknesses to the solution-based deposition and to the polycrystalline and porous nature of the films, it was impossible to characterize the film thickness by some of the usual methods such as ellipsometry or quartz crystal microbalance. Film thicknesses were therefore determined by AFM (below 200 nm) and SEM (up to the 100 μm range) (Figure 4) and also estimated by UV–vis spectrophotometry (Figure 5).

From left to right in the case of CaF<sub>2</sub> (Figure 4a–d) and CaHPO<sub>4</sub> (Figure 4e–h), one clearly observes the increasing film thickness with an increasing number of

spray cycles. In all cases presently investigated, films reached a thickness above 1 μm after 200 spray cycles (Figure 4i–k). In the case of CaHPO<sub>4</sub> a thickness of about 1 μm is reached after a few spray cycles and film growth leveled off at a thickness of about 100 μm. All three cases show that the thickness of the inorganic films is controlled by the number of spray cycles.

**Factors Controlling Film Growth.** Depending on the exact chemical composition of each pair of complementary salts, a second control mechanism becomes important: the control of contact times and thus the speed by which one solution can be replaced by the following complementary one. As we show in Figure 5 the spraying time has a strong influence on the buildup of inorganic films. While in the case of CaF<sub>2</sub> (Figure 5a) a spraying time of 2 s leads to films with twice the absorbance (corresponding approximately to twice the thickness) as compared to films sprayed for 1 s, the thickness of films of CaC<sub>2</sub>O<sub>4</sub> are almost independent of spraying

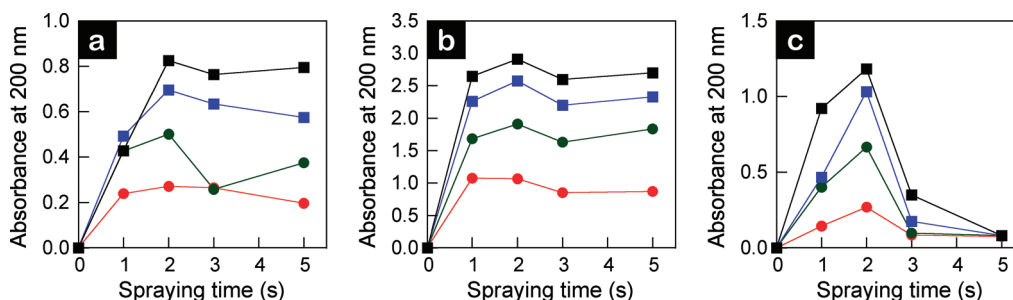


**Figure 5.** Evolution of the absorbance measured by UV at 200 nm versus spraying time of (a) CaF<sub>2</sub>, (b) CaC<sub>2</sub>O<sub>4</sub>, and (c) CaHPO<sub>4</sub> coatings after 5 (red), 10 (green), 15 (blue), and 20 (black) cycles. Solid lines are guides.

times above 1 s (Figure 5b).  $\text{CaHPO}_4$  films even start to redissolve at spraying times longer than 2 s (Figure 5c).

It is evident that in cases in which a fast switching between complementary solutions is required to prevent the redissolution of the film, spraying is the sole method applicable to create such coatings, since the whole surface of a substrate can almost simultaneously be exposed to the spray cone from the third dimension. In contrast, the immersion of a substrate into a liquid always leads to a distribution of contact times along the dipping direction except for a roll-to-roll process, which can only be used with foils and similar soft substrates. The observed redissolution of some inorganic films at longer contact times (Figure 5c) may be due to two different phenomena, the effects of each of which can equally and effectively be reduced at short spraying times. For films of inorganic salts composed of weakly adhering crystals, the draining liquid exercises a sufficient drag for removing poorly sticking crystals mechanically. For films in which the final inorganic product is partially soluble in one of the two solutions of the complementary starting materials, previously formed crystals can also partly or completely be redissolved.

**Toward Multimaterial and Sandwich Films.** The “precipitation coating” technique described above is also compatible with the classic LbL-assembly of polyelectrolytes and can be used for the fabrication of multimaterial sandwich films. Figure 6 shows profiling information obtained by confocal Raman microspectroscopy along the layer normal of a film prepared by 100 spray cycles of calcium oxalate followed by 100 spray cycles of calcium fluoride.

Despite of the limited spatial resolution it is evident that the film is rich in calcium oxalate at the bottom

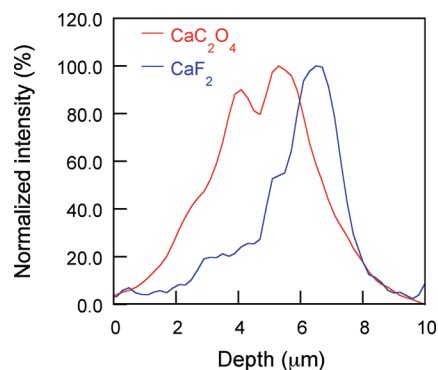


**Figure 6.** Depth profile for a  $\text{PEI}-(\text{CaC}_2\text{O}_4)_{100}-(\text{PSS}/\text{PAH})_5-(\text{CaF}_2)_{100}$  hybrid film visualized as the intensities of the Raman bands of calcium oxalate (red line) at  $1478\text{ cm}^{-1}$  and calcium fluoride (blue line) at  $312\text{ cm}^{-1}$  as obtained by confocal Raman microspectroscopy. For each band, the intensity was normalized by attributing the value 100% to the maximum intensity.

and rich in calcium fluoride at the top. Because of its versatility and simplicity, we anticipate the “precipitation coating” technique to become a method of wide use for the preparation of inorganic nanoscale coatings. At the present time we have not yet optimized the materials properties of our new films with respect to evaluating their potential for application in devices. However, we do believe that our step-by-step spray process could become relevant for some applications because it does not seem to depend much on the shape and size of the receiving surface. Further, our method opens the possibility to fabricate films of hybrid precipitates by spraying more than one complementary component in each spraying step.

## METHODS

**Materials.** Collagen (COL, batch: 07CBPE2040) was purchased from SYMATESE (Grenoble, France). Poly(ethylene imine) (PEI,  $M_w = 700\,000\text{ g/mol}$ ), poly(styrene sulfonate) (PSS,  $M_w = 70\,000\text{ g/mol}$ ), calcium nitrate ( $\text{Ca}(\text{NO}_3)_2 \cdot 4\text{H}_2\text{O}$ ) and Trizma hydrochloride (T32253) were purchased from Sigma Aldrich. Sodium acetate ( $\text{CH}_3\text{COONa}$ , aqueous 3 M solution), diammonium hydrogen phosphate ( $(\text{NH}_4)_2\text{HPO}_4$ ), sodium fluoride (NaF), and sodium oxalate ( $\text{Na}_2\text{C}_2\text{O}_4$ ) were purchased from Fluka. Calcium chloride ( $\text{CaCl}_2 \cdot 2\text{H}_2\text{O}$ ) and acetic acid ( $\text{CH}_3\text{COOH}$ ) were respectively purchased from Carlo Erba Reagents and VWR Prolabo. All the products were used without further purification. The salt solutions were prepared in ultrapure water (Milli-Q Gradient System, Millipore) with a resistivity of  $18.2\text{ M}\Omega \cdot \text{cm}$ . PEI solutions were prepared at a concentration of  $2.5\text{ mg/mL}$  in Milli-Q water. One liter of acetate buffer (pH = 4) was prepared from acetic acid ( $8.1\text{ mM}$ ), sodium acetate ( $1.8\text{ mM}$ ), and NaCl ( $154\text{ mM}$ ). COL solutions were prepared at a concentration of  $0.2\text{ mg/mL}$  in acetate buffer at pH 4 where it is positively charged. PSS solutions were prepared at a concentration of  $1\text{ mg/mL}$  in  $0.15\text{ M}$  NaCl at pH 6.5. For calcium phosphate ( $\text{CaHPO}_4$ ) synthesis, a calcium solution of  $\text{Ca}(\text{NO}_3)_2 \cdot 4\text{H}_2\text{O}$  ( $0.32\text{ M}$ ) and a phosphate solution of  $(\text{NH}_4)_2\text{HPO}_4$  ( $0.19\text{ M}$ ) were prepared in Tris buffer ( $10\text{ mM}$  Trizma, pH = 10). Calcium fluoride ( $\text{CaF}_2$ ) was synthesized from a solution of  $\text{CaCl}_2$  ( $2 \times 10^{-2}\text{ M}$ ) and NaF ( $2 \times 10^{-2}\text{ M}$ ) prepared in Milli-Q water. Calcium oxalate ( $\text{CaC}_2\text{O}_4$ ) was prepared using

$\text{Na}_2\text{C}_2\text{O}_4$  ( $10^{-1}\text{ M}$ ) and  $\text{CaCl}_2$  ( $2 \times 10^{-1}\text{ M}$ ) prepared in Milli-Q water.

**Inorganic Spray Assembly.** The spray deposition was carried out by using air pump spray cans (“Air Boy”) made of polypropylene and polyethylene purchased from Roth (reference number: 0110.1) with a height of 217 mm and a diameter of 55 mm; equipped with a nozzle of 0.40 mm). Each can was filled with the respective salt solution and then pressurized by pumping cycles in such a way that the spray rate remained approximately constant over the entire film deposition process. The spray rate was determined to be about  $0.6\text{ mL/s}$  with pump flasks as they were received from the manufacturer. Spraying was carried out perpendicularly to the receiving surface which was fixed in a vertical orientation. Inorganic salt solutions were alternately sprayed for 2 s unless otherwise stated until the desired number of cycles. After a rest time of 60 s, a rinsing step with Milli-Q-water of  $5 \times 1\text{ s}$  using the spraying bottles was applied to the inorganic film.

**LbL-Multilayer Films.** All the films were built on glass slides of 12 mm diameter (VWR, Fontenay sous Bois, France), silicon wafers (100) (Wafernet, Inc., San Jose, CA), or quartz plates (665.000-QS, HELMA, Paris, France) of the same size, previously cleaned for 1 h in a 1:1 mixture of  $\text{CH}_3\text{OH}$  and HCl, then cleaned with a  $\text{H}_2\text{SO}_4$  solution ( $>1\text{ h}$ ), and rinsed extensively with ultrapure water. The buildup of multilayer films by the spray technology consisted in the sequential spraying of the polycation (COL) and of the polyanion (PSS) solutions perpendicularly to the substrate in vertical position to allow the drainage of the solution, using com-

mercial paintbrushes (Airbrush 134) from SEDIP (Poncarré, France) equipped with two-component nozzles with a diameter of 0.3 mm and operated at an air pressure of 1 bar. Each polyelectrolyte solution (COL or PSS) was sprayed onto the substrate surface for 5 s. After a rest time of 15 s, we rinsed with Milli-Q-water for 5 s. Finally, after a further rest time of 15 s, the deposition of the next polyelectrolyte layer followed the same sequence. Thereby, the deposition of a layer pair was achieved in 60 s. The obtained film is denoted (COL/PSS)<sub>n</sub>, after the deposition of *n* COL/PSS pairs of layers.

**Transmission Electron Microscopy.** The particle size of the inorganic crystals in films at various stages of growth was determined by transmission electron microscopy (TEM, Philips CM200) while their crystalline structure was studied by electron diffraction (ED) operating the instrument in the low-dose mode at 200 kV accelerating voltage. Images were taken with a numerical camera (Gatan, Orius 1000). The resolution of this setup is about of 0.2 nm.

**Environmental Scanning Electron Microscopy.** Side-views of the cross sections of the inorganic coatings were obtained by environmental scanning electron microscopy (ESEM, FEI Quanta 400) after appropriately cutting the corresponding coated glass substrate.

**UV–Visible Spectroscopy. (UV–vis).** UV–vis absorption spectra of inorganic layers were recorded on a Varian Cary 500 scan spectrometer on a quartz slides. The quartz slides were first cleaned with a 2% Hellmanex solution and then thoroughly rinsed with water. The polycrystallinity and sometimes the porosity of the films caused non-negligible light scattering and only allowed the monitoring of the absorbance up to a limited thickness of the coatings.

**Acknowledgment.** This work was supported by the project ANR06-BLAN-0197-01, “CartilSpray” from the Agence Nationale de la Recherche and the Fondation Avenir. G. Popa was supported by a doctoral fellowship of the Ministère de l’Enseignement Supérieur et de la Recherche. P. Zhao was supported by Sino-French Ph.D Institute Cooperation Program (2007). G. Decher is indebted to Institut Universitaire de France (IUF) for financial support. We thank E. Lancelot from Horiba Scientific (Villeneuve d’Ascq, France) for technical help concerning confocal Raman microspectroscopy.

**Supporting Information Available:** Table of solubility of investigated inorganic compounds, tables of observed and expected *d* spacings of CaF<sub>2</sub>, α-C<sub>2</sub>CaOα and Ca<sub>5</sub>(PO<sub>4</sub>)<sub>3</sub>(OH) crystals, X-ray diffraction pattern of CaHPO<sub>4</sub> obtained by spraying, top view scanning electron micrographs of films composed of CaHPO<sub>4</sub> after 100 spray cycles and top view and side view scanning electron micrographs of films composed of CaC<sub>2</sub>O<sub>4</sub> at various stages of film growth. This material is available free of charge via the Internet at <http://pubs.acs.org>.

## REFERENCES AND NOTES

- Venables, J. A.; Spiller, G. D. T.; Hanbucken, M. Nucleation and Growth of Thin-Films. *Rep. Prog. Phys.* **1984**, *47*, 399–459.
- Zhang, Z. Y.; Lagally, M. G. Atomistic Processes in the Early Stages of Thin-Film Growth. *Science* **1997**, *276*, 377–383.
- Barth, J. V.; Costantini, G.; Kern, K. Engineering Atomic and Molecular Nanostructures at Surfaces. *Nature* **2005**, *437*, 671–679.
- Decher, G. Fuzzy Nanoassemblies: Toward Layered Polymeric Multicomposites. *Science* **1997**, *277*, 1232–1237.
- Forrest, S. R. The Path to Ubiquitous and Low-Cost Organic Electronic Appliances on Plastic. *Nature* **2004**, *428*, 911–918.
- Ozgur, U.; Alivov, Y. I.; Liu, C.; Teke, A.; Reshchikov, M. A.; Dogan, S.; Avrutin, V.; Cho, S. J.; Morkoc, H. A Comprehensive Review of ZnO Materials and Devices. *J. Appl. Phys.* **2005**, *98*, 041301.
- Dawber, M.; Rabe, K. M.; Scott, J. F. Physics of Thin-Film Ferroelectric Oxides. *Rev. Mod. Phys.* **2005**, *77*, 1083–1130.
- Chaneliere, C.; Autran, J. L.; Devine, R. A. B.; Baland, B. Tantalum Pentoxide (Ta<sub>2</sub>O<sub>5</sub>) Thin Films for Advanced Dielectric Applications. *Mater. Sci. Eng., R* **1998**, *22*, 269–322.
- Polman, A. Erbium Implanted Thin Film Photonic Materials. *J. Appl. Phys.* **1997**, *82*, 1–39.
- Li, X. M.; Reinhoudt, D.; Crego-Calama, M. What Do We Need for a Superhydrophobic Surface? A Review on the Recent Progress in the Preparation of Superhydrophobic Surfaces. *Chem. Soc. Rev.* **2007**, *36*, 1529.
- Klein, L. C. *Sol-Gel Technology for Thin Films, Fibers, Preforms, Electronics, and Specialty Shapes*; Noyes Publication: Park Ridge, NJ, 1988.
- Attia, S. M.; Wang, J.; Wu, G. M.; Shen, J.; Ma, J. H. Review on Sol-Gel Derived Coatings: Process, Techniques and Optical Applications. *J. Mater. Sci. Technol.* **2002**, *18*, 211–218.
- Ichinose, I.; Senzu, H.; Kunitake, T. A Surface Sol–Gel Process of TiO<sub>2</sub> and other Metal Oxide Films with Molecular Precision. *Chem. Mater.* **1997**, *9*, 1296–1298.
- Patil, P. S. Versatility of Chemical Spray Pyrolysis Technique. *Mater. Chem. Phys.* **1999**, *59*, 185–198.
- Nicolau, Y. F.; Menard, J. C. Solution Growth of ZnS, CdS, and Zn<sub>1-x</sub>Cd<sub>x</sub>S Thin-Films by the Successive Ionic-Layer Adsorption and Reaction Process—Growth-Mechanism. *J. Cryst. Growth.* **1988**, *92*, 128–142.
- Nicolau, Y. F. Solution Deposition of Thin Solid Compound Films by a Successive Ionic-Layer Adsorption and Reaction Process. *Appl. Surf. Sci.* **1985**, *22–3*, 1061–1074.
- Nicolau, Y. F. Process and apparatus for the deposition on a substrate of a thin film of a compound containing at least one cationic constituent and at least one anionic constituent. Patent 4675207, 1987.
- Decher, G.; Hong, J. D. Buildup of Ultrathin Multilayer Films by a Self-Assembly Process. 1. Consecutive Adsorption of Anionic and Cationic Bipolar Amphiphiles on Charged Surfaces. *Makromol. Chem. Macromol. Symp.* **1991**, *46*, 321–327.
- Decher, G.; Schlenoff, J. B. *Multilayer Thin Films: Sequential Assembly of Nanocomposite Materials*; Wiley-VCH: Weinheim, Germany, 2003.
- Ariga, K.; Hill, J. P.; Ji, Q. M. Layer-by-layer Assembly as a Versatile Bottom-up Nanofabrication Technique for Exploratory Research and Realistic Application. *Phys. Chem. Chem. Phys.* **2007**, *9*, 2319–2340.
- Bertrand, P.; Jonas, A.; Laschewsky, A.; Legras, R. Ultrathin Polymer Coatings by Complexation of Polyelectrolytes at Interfaces: Suitable Materials, Structure and Properties. *Macromol. Rapid Commun.* **2000**, *21*, 319–348.
- Decher, G. Layered Nanoarchitectures via Directed Assembly of Anionic and Cationic Molecules. In *Comprehensive Supramolecular Chemistry*; Sauvage, J.-P., Hosseini, M. W., Eds.; Templating, Self-Assembly and Self-Organization, Vol. 9; Pergamon Press: Oxford, 1996; pp 507–528.
- Decher, G.; Ecker, M.; Schmitt, J.; Struth, B. Layer-by-layer Assembled Multicomposite Films. *Curr. Opin. Colloid Interface Sci.* **1998**, *3*, 32–39.
- Hammond, P. T. Recent Explorations in Electrostatic Multilayer Thin Film Assembly. *Curr. Opin. Colloid Interface Sci.* **2000**, *4*, 430–442.
- Jessel, N.; Lavallo, P.; Ball, V.; Ogier, J.; Senger, B.; Picart, C.; Schaaf, P.; Voegel, J.-C.; Decher, G. Polyelectrolyte Multilayer Films—A General Approach to (Bio)-Functional Coatings. In *Macromolecular Engineering*; Gnanou, Y., Leibler, L., Matyjaszewski, K., Eds.; Elements of Macromolecular Structural Control, Vol. 2; Wiley-VCH: Weinheim, Germany, 2007; pp 1249–1306.
- Johnston, A. P. R.; Cortez, C.; Angelatos, A. S.; Caruso, F. Layer-by-Layer Engineered Capsules and Their Applications. *Curr. Opin. Colloid Interface Sci.* **2006**, *11*, 203–209.
- Tang, Z. Y.; Wang, Y.; Podsiadlo, P.; Kotov, N. A. Biomedical Applications of Layer-by-Layer Assembly: From

- Biomimetics to Tissue Engineering. *Adv. Mater.* **2006**, *18*, 3203–3224.
28. Schlenoff, J. B.; Dubas, S. T.; Farhat, T. Sprayed Polyelectrolyte Multilayers. *Langmuir* **2000**, *16*, 9968–9969.
29. Winterton, L.; Vogt, J.; Lally, J.; Stockinger, F. *Coating of Polymers*. Patent 9935520, 1999.
30. Izquierdo, A.; Ono, S. S.; Voegel, J.-C.; Schaaf, P.; Decher, G. Dipping versus Spraying: Exploring the Deposition Conditions for Speeding up Layer-by-Layer Assembly. *Langmuir* **2005**, *21*, 7558–7567.
31. Ostrander, J. W.; Mamedov, A. A.; Kotov, N. A. Two Modes of Linear Layer-by-Layer Growth of Nanoparticle–Polyelectrolyte Multilayers and Different Interactions in the Layer-by-Layer Deposition. *J. Am. Chem. Soc.* **2001**, *123*, 1101–1110.
32. Krogman, K. C.; Lowery, J. L.; Zacharia, N. S.; Rutledge, G. C.; Hammond, P. T. Spraying Asymmetry into Functional Membranes Layer-by-Layer. *Nat. Mater.* **2009**, *8*, 512–518.

# Article 2

# Spray-On Organic/Inorganic Films: A General Method for the Formation of Functional Nano- to Microscale Coatings

Mathias Lefort, Gabriela Popa, Emek Seyrek, Rafael Szamocki, Olivier Felix, Joseph Hemmerlé, Loïc Vidal, Jean-Claude Voegel, Fouzia Boulmedais, Gero Decher,\* and Pierre Schaaf\*

Surface coatings are important in science and technology with applications that span domains as diverse as biomaterials, optical coatings, photovoltaic cells, or corrosion protection.<sup>[1–4]</sup> Such applications were enabled by the development of methods for the preparation of organic and inorganic thin films that either involve transfer through the gas phase (e.g., physical vapor deposition (PVD), chemical vapor deposition (CVD), sputtering)<sup>[5,6]</sup> or deposition from solution (e.g., sol-gel methods, spin-coating, electrospraying, spray pyrolysis, electroplating).<sup>[7–9]</sup> Many methods are also specific for a given application and only a few are applicable to a wide range of materials and surfaces. A potent and simple solution-based method for the preparation of multicomposite nanoscale films on surfaces of almost any kind and any shape is the well-known layer-by-layer (LbL) method.<sup>[10]</sup> The introduction of spray-assisted deposition was an important improvement of the LbL technique with respect to accelerating and scaling up of the process.<sup>[11–14]</sup>

Herein we show that spray-assisted LbL deposition can be further advanced to lead to a general method, the so-called “simultaneous spray coating of interacting species” (SSCIS). Instead of bringing two spontaneously interacting species into contact step-by-step at an interface to form LbL films, SSCIS is based on the simultaneous spraying of two or more interacting components against a receiving surface. This process results in a fast reaction between the complementary components on a macroscopic surface, hence leading to a continuous and gradual buildup of a coating, the thickness of which is controlled by the spraying time, while the solvent and excess material are removed by drainage. This one-step deposition process is extremely user-friendly and allows the preparation of very homogeneous films, which show optical interference colors over large areas (Figure 1). This property is a prerequisite for the fabrication of, for example, optical devices. The uniform color of the films when exposed to white light indicates a homogeneous refractive index and thickness, which is of the order of a hundred nanometers with a variation of a few nanometers over the entire surface (excluding some edge effects). The film thickness can easily be tuned from a few tens up to hundreds of nanometers and even micrometers simply by varying the spraying time. The results and

[\*] M. Lefort,<sup>[†]</sup> G. Popa,<sup>[†]</sup> Dr. E. Seyrek, Dr. R. Szamocki, Dr. O. Felix, Dr. F. Boulmedais, Prof. G. Decher, Prof. P. Schaaf  
Institut Charles Sadron (UPR 22)  
Centre National de la Recherche Scientifique  
23 rue du Loess, 67034 Strasbourg (France)  
Fax: (+33) 3-9041-4000  
E-mail: gero.decher@ics-cnrs.unistra.fr  
pierre.schaaf@ics-cnrs.unistra.fr  
Homepage: <http://www-ics.u-strasbg.fr>  
Dr. J. Hemmerlé, Dr. J.-C. Voegel  
Biomaterials and Tissue Engineering (UMR 977), Institut National de la Santé et de la Recherche Médicale Strasbourg (France)  
and  
Faculté de Chirurgie Dentaire, Université de Strasbourg (France)  
Dr. L. Vidal  
Institut de Science des Matériaux de Mulhouse (LRC 7228)  
Centre National de la Recherche Scientifique, Mulhouse (France)  
Prof. G. Decher  
Faculté de Chimie, Université de Strasbourg  
1 rue Blaise Pascal, 67008 Strasbourg (France)  
and  
International Center for Frontier Research in Chemistry  
8 allée Gaspard Monge, 67083 Strasbourg (France)  
and  
Institut Universitaire de France  
103 Boulevard Saint-Michel, 75005 Paris (France)  
Prof. P. Schaaf  
Ecole Européenne de Chimie, Polymères et Matériaux, Université de Strasbourg, 25 rue Becquerel, 67087 Strasbourg (France)

[†] These authors contributed equally to this work.

Supporting information for this article is available on the WWW under <http://dx.doi.org/10.1002/anie.201002729>.

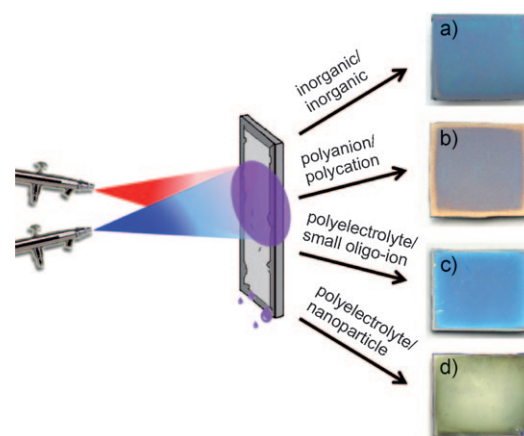
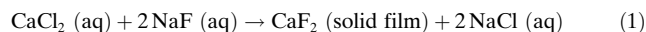


**Figure 1.** Left: Representation of the simultaneous spray coating (SSCIS) setup. Right: Images of films deposited on silicon wafers (40 mm × 40 mm); the colors arise from optical interference. The sprayed solutions are: a) NaF ( $2 \times 10^{-2} \text{ mol L}^{-1}$ ) and  $\text{CaCl}_2 \cdot 2 \text{ H}_2\text{O}$  ( $10^{-2} \text{ mol L}^{-1}$ ), b) PAH ( $1 \text{ mg mL}^{-1}$ ,  $M_n = 15\,000 \text{ g mol}^{-1}$ , in  $0.6 \text{ mol L}^{-1}$  aq NaCl) and PSS ( $1 \text{ mg mL}^{-1}$ ,  $M_n = 15\,000 \text{ g mol}^{-1}$ , in  $0.6 \text{ mol L}^{-1}$  aq NaCl), c) PAH ( $1 \text{ mg mL}^{-1}$ ,  $M_n = 56\,000 \text{ g mol}^{-1}$ ) and sodium citrate ( $0.02 \text{ mol L}^{-1}$ ), d) PAH ( $1 \text{ mg mL}^{-1}$ ,  $M_n = 15\,000 \text{ g mol}^{-1}$ ) and gold nanoparticles. The silicon wafers were slowly rotated to improve film homogeneity. Note that some samples show slight edge effects.

experimental details for all examples described below are given in the Supporting Information.

For inorganic coatings, the general requirement is that the solubility limit of the sprayed compounds (i.e., of the complementary salts) is much larger than that of the resulting solid deposit. We present herein calcium fluoride ( $\text{CaF}_2$ ) as a model case [Eq. (1)], but other inorganic deposits have also



successfully been prepared: calcium hydrogen phosphate ( $\text{CaHPO}_4$ ), calcium oxalate ( $\text{CaC}_2\text{O}_4$ ), Prussian blue ( $\text{Fe}_4[\text{Fe}(\text{CN})_6]_3$ ), and silver chloride ( $\text{AgCl}$ ; see the Supporting Information). The preparation of some noble metal films (Au and Ag) and films of CdS and ZnS by similar methods was previously reported.<sup>[15–18]</sup>

For  $\text{CaF}_2$  layers, aqueous solutions of calcium chloride ( $10^{-2}\text{M}$ ) and sodium fluoride ( $2 \times 10^{-2}\text{M}$ ) were sprayed simultaneously in a 1:1 v/v ratio against a vertically oriented receiving surface. This procedure leads to solution concentrations higher than the solubility limit of  $\text{CaF}_2$  ( $2 \times 10^{-4}\text{M}$ ).<sup>[19]</sup> After drying, the film thickness and morphology were determined by AFM and scanning electron microscopy (SEM) at different stages of growth, and the images show a good correlation between the thickness and the spraying time (Figure 2). We observed ongoing nucleation and growth of isolated monocrystalline particles, which eventually leads to the formation of a dense layer of  $\text{CaF}_2$ . The polycrystalline nature of the resulting deposit was confirmed by transmission electron diffraction (Figure 2a). The growth then continues perpendicularly to the substrate and the film thickness increases steadily with spraying time.

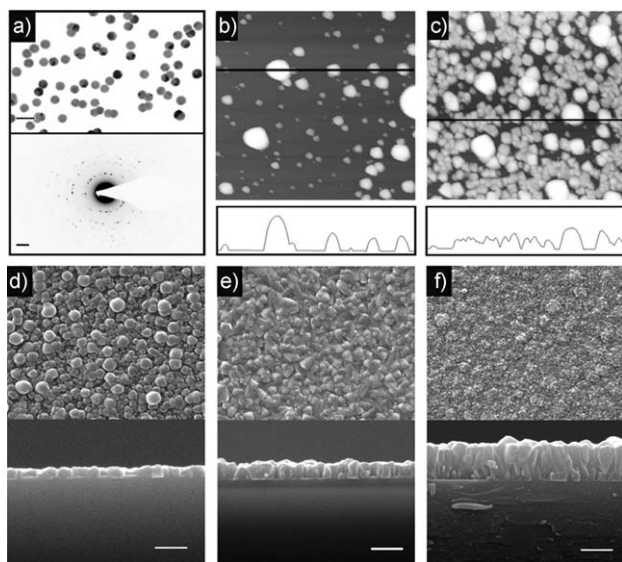
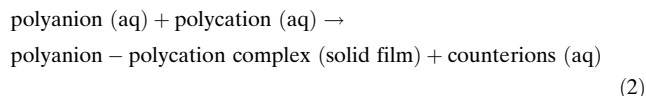


**Figure 2.** Micrographs of  $\text{CaF}_2$  coatings obtained by spraying for: a) 1 s on a Formvar support, analyzed by TEM, scale bar  $0.5 \mu\text{m}$  (top) and electron diffraction, scale bar  $0.2 \text{nm}^{-1}$  (bottom); b) 10 s and c) 40 s on a silicon wafer, analyzed by AFM topography (top) and line profiles (bottom). The scan areas for both b) and c) are  $5 \mu\text{m} \times 5 \mu\text{m}$ , the z-axis scale is  $400 \text{nm}$ ; d) 1 min, e) 5 min, and f) 10 min on a glass substrate, analyzed by SEM, top views (top) and cross-section images (bottom). The scale bars in (d) and (f) are  $2 \mu\text{m}$ .

As in the case of inorganic layers, the general requirement for polymer-based SSCIS films is a rapid reaction between the components, which leads to complex formation. The strength and versatility of electrostatic complex formation [Eq. (2)]



renders it particularly well suited for SSCIS. In addition, as in the case of electrostatic LbL deposition, the polyanionic and polycationic nature of the compounds leads to a wide choice of different materials.<sup>[20,21]</sup>

Several pairs of strong and weak polyelectrolytes, for which classic LbL assembly has already been reported, were investigated for SSCIS film formation. Such film formation by simultaneous spraying has only been reported once for a pair of weak polyelectrolytes, namely poly(glutamic acid) (PGA) and poly(allylamine hydrochloride) (PAH).<sup>[22]</sup> All investigated systems, that is, dextran sulfate/poly(L-lysine) (PLL), poly(styrene sulfonate) (PSS)/poly(allylamine hydrochloride) (PAH), poly(dimethyl diallyl ammonium chloride) (PDADMAC)/poly(acrylic acid) (PAA), poly(ethylene imine) (PEI)/PAA, and PAH/PAA, show a linear film growth as a function of spraying time (Figure 3; the term spraying time represents the cumulated spraying time). An interruption of the deposition does not influence the growth rate of the films (to within experimental error). The same film thicknesses are obtained, regardless of whether the film is grown in a single step or in multiple steps while the overall spraying time is kept constant, and even if the film is dried after each step. This behavior is observed for both polymer-based and inorganic coatings and demonstrates that the SSCIS process is very robust.

Another interaction that is sufficiently strong for the preparation of SSCIS films is hydrogen bonding, as illustrated

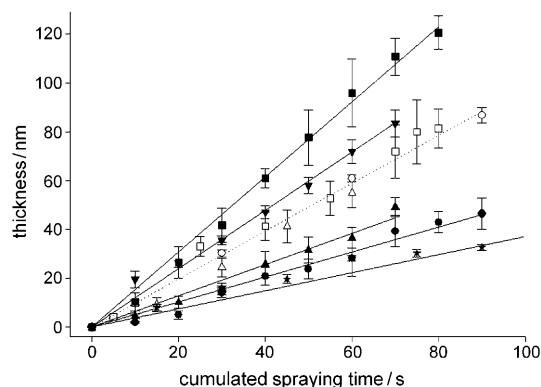


**Figure 3.** Ellipsometric film thickness as a function of the spraying time for different polymeric systems; ■: dextran sulfate ( $0.5 \text{mg mL}^{-1}$ ) and PLL ( $0.5 \text{mg mL}^{-1}$ ) at pH 7.5; ▼: PEO ( $0.5 \text{mg mL}^{-1}$ ) and PAA ( $0.5 \text{mg mL}^{-1}$ ) at pH 2; ○, □, △: PSS ( $0.5 \text{mg mL}^{-1}$ ) and PAH ( $0.5 \text{mg mL}^{-1}$ ) at pH 7.5 with 5 s, 15 s, and 30 s spraying intervals respectively; ▲: PDADMAC ( $0.5 \text{mg mL}^{-1}$ ) and PAA ( $0.5 \text{mg mL}^{-1}$ ) at pH 7.5; ●: PEI ( $0.5 \text{mg mL}^{-1}$ ) and PAA ( $0.5 \text{mg mL}^{-1}$ ) at pH 7.5; \*: PAH ( $0.5 \text{mg mL}^{-1}$ ) and PAA ( $0.5 \text{mg mL}^{-1}$ ) at pH 7.5. The error bars represent the standard deviation.

by the regular growth of the PAA/poly(ethylene oxide) (PEO) system (Figure 3). In solution, this system shows strong complexation below a pH value of approximately 3.5. SSCIS films are built up by simultaneous spraying at pH 2, and can easily be dissolved at pH values above 5, similar to PAA/PEO LbL films.<sup>[23]</sup>

One interesting aspect of polyanion/polycation complex formation is its dependence on the relative degrees of polymerization of both polyelectrolytes; these values are typically highest when the lengths of both compounds match.<sup>[21]</sup> However, simultaneous spraying of a polyelectrolyte with an oppositely multicharged small oligoion can unexpectedly lead to film formation. For such systems, we present PAH and sodium citrate as a model case, as these compounds do not allow conventional LbL deposition. Films of other components (PAH/K<sub>3</sub>[Fe(CN)<sub>6</sub>], PAH/sodium oxalate, PAH/phytic acid sodium salt, PAA/spermine, and PAH/sulfated  $\alpha$ -cyclodextrin sodium salt) were also successfully prepared by SSCIS (see the Supporting Information). In all these cases, the film growth is regular with respect to the spraying time. In the case of PAH and sodium citrate, the film deposition could be followed by AFM, and the mechanism for film formation was derived. At the initial stages of the buildup, the layer is rather inhomogeneous and is constituted of isolated droplet-like objects (Figure 4a), which grow in size and also increase in number. With further spraying, these structures coalesce upon lateral contact, thus forming a film with holes (Figure 4b) and finally a continuous and very smooth coating (Figure 4c and Figure 1c). A similar development of morphologies as a function of spraying time was also

observed for polyanion/polycation systems such as PDADMAC/PAA (Figure 4d–f).

SSCIS films of PAH and sodium citrate rapidly dissolve when immersed in aqueous solutions of NaCl at ionic strengths above 0.15 M, thus offering possibilities for use as bioresponsive materials or triggered release applications. The rapid degradation of such films can easily be prevented and controlled by cross-linking, for example by heating at 130 °C for 18 hours in an oven or by heating with a heat gun for 2–3 minutes. This process leads to partial thermal cross-linking by formation of amide bonds through reaction of the carboxylic acid groups of citrate with the amino groups of PAH; this behavior is similar to a case described for LbL films.<sup>[24]</sup>

The SSCIS method also allows for in situ chemical cross-linking of films by adding reactive components to the spraying solutions. In the case of PAH/citrate films, the addition of glutaraldehyde to the citrate solution leads to the formation of a covalent network through Schiff base formation.<sup>[25]</sup> Such coatings do not dissolve in brine over a long period of time. Interestingly, the simultaneous spraying of PAH and glutaraldehyde in the absence of citrate ions did not lead to the formation of any films. Different functionalities in addition to chemical reactivity can also be incorporated into SSCIS films by spraying multicomponent solutions simultaneously. For example, gold nanoparticles (1st component) stabilized with citrate (2nd component), which are sprayed simultaneously with PAH (3rd component) result in very smooth films (Figure 1d) that display regular growth like all other systems presented above. In addition, the presence of gold nanoparticles offers the advantage of monitoring film growth by changes in the plasmon band (see the Supporting Information).

The simplicity and broad applicability of the SSCIS method is proved by the different systems described here, even without detailed studies of the parameters and variables involved in spraying technologies. The growth rates and coating morphologies not only depend on spraying time, but are expected to also be a function of solution concentration, nozzle type, spraying rate, spraying distance, and other factors. SSCIS is very flexible, yet robust, and the method can be quickly adapted to different requirements through further optimization of such parameters.

While LbL deposition methods have received considerable attention because of their widespread potential applications (e.g., biomaterial coatings,<sup>[26]</sup> fuel cells,<sup>[27,28]</sup> and anti-corrosion protection<sup>[29]</sup>), not all of them require a stratified structure of the film at the nanometer scale. In such cases, simultaneous spray coating offers a much faster option, which is also applicable to larger surfaces. The SSCIS spray technology with two nozzles described here can be extended to multinozzle systems for the preparation of coatings with gradients along the layer normal, including sandwich-like films made from different materials through multisequence spraying.

Received: May 5, 2010

Published online: ■■■■■, 2010

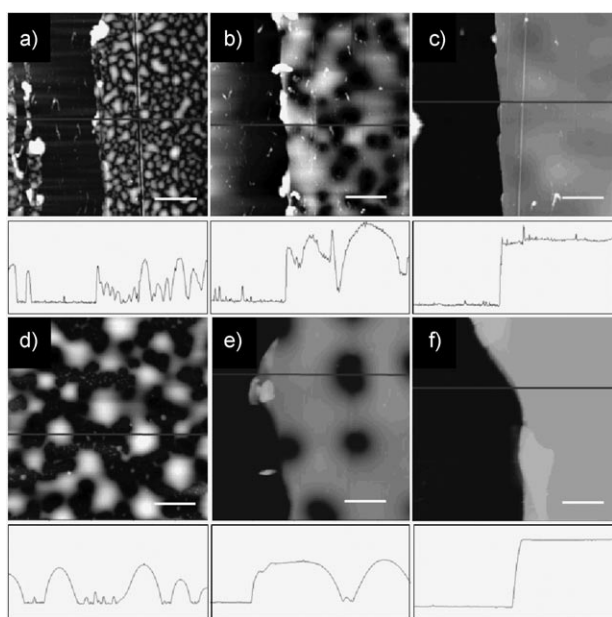


**Figure 4.** AFM topography (top) and line profiles (bottom) of SSCIS films on silicon wafers of: a–c) PAH/citrate after spraying times of 30 s, 75 s, and 120 s of spraying time, respectively; d–f) PDADMAC/PAA after spraying times of 70 s, 120 s, and 180 s, respectively. Scan areas are  $12\ \mu\text{m} \times 12\ \mu\text{m}$  and the scale bars are  $2.5\ \mu\text{m}$ . For a proper determination of height profiles, that is, the film thickness, the films were scratched. For line profiles, the y-axis scales from 0 to 120 nm (a–c) and from 0 to 400 nm (d–f).



**Keywords:** coatings · functional materials · nanotechnology · surface chemistry · thin films

- 
- [1] B. D. Ratner, A. S. Hoffman, *Biomaterials Science: An Introduction to Materials in Medicine*, 2nd ed., Elsevier Academic, San Diego, CA, **2004**.
- [2] P. W. Baumeister, *Optical Coating Technology*, SPIE, Bellingham, WA, **2004**.
- [3] F. C. Krebs, *Sol. Energy Mater. Sol. Cells* **2009**, 93, 394.
- [4] Z. Ahmad, *Principles of Corrosion Engineering and Corrosion Control*, Elsevier, Oxford, UK, **2006**.
- [5] K. L. Choy, *Prog. Mater. Sci.* **2003**, 48, 57.
- [6] J. E. Mahan, *Physical Vapor Deposition of Thin Films*, Wiley, New York, **2000**.
- [7] L. C. Klein, *Sol-Gel Technology for Thin Films, Fibers, Preforms, Electronics, and Specialty Shapes*, Noyes Publications, Park Ridge, NJ, **1988**.
- [8] I. Ichinose, H. Senzu, T. Kunitake, *Chem. Mater.* **1997**, 9, 1296.
- [9] P. S. Patil, *Mater. Chem. Phys.* **1999**, 59, 185.
- [10] G. Decher, *Science* **1997**, 277, 1232.
- [11] L. Winterton, J. Vogt, J. Lally, F. Stockinger (Novartis AG), World Patent WO 9935520, **1999**.
- [12] J. B. Schlenoff, S. T. Dubas, T. Farhat, *Langmuir* **2000**, 16, 9968.
- [13] A. Izquierdo, S. S. Ono, J.-C. Voegel, P. Schaaf, G. Decher, *Langmuir* **2005**, 21, 7558.
- [14] K. C. Krogman, J. L. Lowery, N. S. Zacharia, G. C. Rutledge, P. T. Hammond, *Nat. Mater.* **2009**, 8, 512.
- [15] D. J. Levy (Lockheed Aircraft Corporation), US Patent No. US 3 515 571, **1970**.
- [16] D. O'Brian, J. Vogler, J. M. Landry, G. S. Jakubowski, US Patent No. US 6 168 825, **2001**.
- [17] A. Sakurai, J. Togasaki (Advance Company Ltd, Ohra Sangyo Co. Ltd), European Patent No. EP 1 557 483, **2005**.
- [18] K. Kalberlah, Z. Mollah, German Patent No. DE 10 2004 020 879, **2005**.
- [19] E. C. Weast, *Handbook of Chemistry and Physics*, 57th ed., CRC Press, Cleveland, OH, **1976–1977**.
- [20] B. Philipp, H. Dautzenberg, K. J. Linow, J. Koetz, W. Dawydoff, *Prog. Polym. Sci.* **1989**, 14, 91.
- [21] A. F. Thünemann, M. Müller, H. Dautzenberg, J. F. O. Joanny, H. Löwen, *Adv. Polym. Sci.* **2004**, 166, 113.
- [22] C. Porcel, A. Izquierdo, V. Ball, G. Decher, J.-C. Voegel, P. Schaaf, *Langmuir* **2005**, 21, 800.
- [23] S. A. Sukhishvili, S. Granick, *Macromolecules* **2002**, 35, 301.
- [24] S. Y. Yang, M. F. Rubner, *J. Am. Chem. Soc.* **2002**, 124, 2100.
- [25] G. T. Hermanson, *Bioconjugate techniques*, Academic Press, San Diego, CA, **1996**.
- [26] Z. Y. Tang, Y. Wang, P. Podsiadlo, N. A. Kotov, *Adv. Mater.* **2006**, 18, 3203.
- [27] J. L. Lutkenhaus, P. T. Hammond, *Soft Matter* **2007**, 3, 804.
- [28] A. D. Taylor, M. Michel, R. C. Sekol, J. M. Kizuka, N. A. Kotov, L. T. Thompson, *Adv. Funct. Mater.* **2008**, 18, 3003.
- [29] D. Fix, D. V. Andreeva, Y. M. Lvov, D. G. Shchukin, H. Möhwald, *Adv. Funct. Mater.* **2009**, 19, 1720.
-

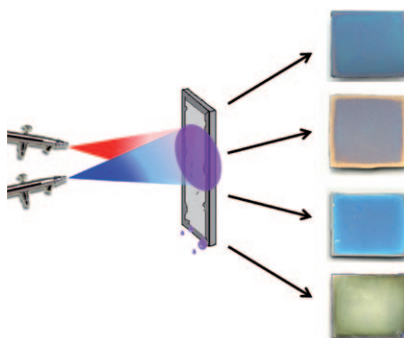
## Communications



### Thin Films

M. Lefort, G. Popa, E. Seyrek, R. Szamocki,  
O. Felix, J. Hemmerlé, L. Vidal,  
J.-C. Voegel, F. Boulmedais, G. Decher,\*  
P. Schaaf\* ————— ■■■■-■■■■

Spray-On Organic/Inorganic Films: A  
General Method for the Formation of  
Functional Nano- to Microscale Coatings



**Technicolor dreamcoat:** Spray-on nano-scale coatings are formed by simultaneous spraying of complementary species (e.g., polyanion/polycation, polyelectrolyte/small oligomeric ion, two inorganic salt solutions) against a receiving surface (see picture). The process leads to the formation of ultrathin films, the thicknesses of which are controlled by the spraying time. This general one-step coating method results in optically homogeneous films from a broad choice of functional compounds.

# Conclusions and Perspectives



## 5 Conclusions and perspectives

Important steps were undertaken toward the fabrication of collagen and calcium phosphate coatings for the use as artificial cartilage. Our strategy to mimic some aspects of natural articular cartilage was realized by the fabrication of “sandwich” like structures based on alternating collagen Layer-by-Layer films and inorganic coatings (calcium phosphate). The first step was the calcium phosphate coating deposition using the new consecutive spraying method. The Layer-by-Layer deposition technique, mostly used for the polyelectrolyte deposition, was extended for the deposition of inorganic coatings by the consecutive spray method. The spraying time of aqueous salt solutions, required for the inorganic coating deposition, is in the seconds range (from one to five seconds) and the adsorption time of ions on the surface is very short (less than one second). The consecutive deposition of the second component solution is immediately sprayed after the first component adsorption. The rinsing step (generally water rinsing or buffer) doesn't exist in the inorganic deposition process. It turned out that a large variety of inorganic films can be prepared by either alternating or simultaneous spraying.

Collagen cannot be dispersed at  $\text{pH} > 4$  and the phosphate coating dissolves at  $\text{pH} < 6$ . The use of the (PAH-PSS) barrier films was necessary in order to prepare the collagen and calcium phosphate coatings in the same hybrid film. The dissolution of the calcium phosphate crystals is observed after the collagen adsorption on the freshly prepared inorganic coating. In order to decrease or to stop the destruction of the inorganic film prepared by consecutive spraying of alkaline solutions, we need to deposit the (PAH-PSS) film barrier. By using the Layer-by-Layer assembly, we were able to prepare the “sandwich” hybrid films, which contain three “strata” containing organic coating- barrier film- Collagen film.

Another strategy used in the cartilage engineered scaffold fabrication is linked to the Collagen solubilization possibility in different solvents. In order to obtain the scaffold, we used non-aqueous solvents for the collagen dispersion and not anymore the acidic

buffer solution. The non-aqueous collagen multilayer film on top of the inorganic coatings growth was successfully observed by AFM.

The Collagen/ calcium phosphate matrix materials obtained and characterized can open the perspectives for the fabrication of biocompatible cartilage scaffolds by the incorporation of biological materials (e.g. growth factors, chondrocyte cells).

We chose the liquid spray coating method because it is probably the most versatile coating technique and the consecutive spray method is particularly well suited for industrial production. In order to improve further extend the above, we studied other materials to be deposited, the applicability for different substrates as well the optimization of other deposition factors, such as spraying time, solution concentration.

We tested the deposition of calcium oxalate, calcium fluoride, silver chloride, Prussian Blue coatings by spraying. With the extension to new materials it was interesting to test the deposition of different materials on top of each other. This also led to purely organic “sandwich” films by the same consecutive spray method.

An important part of this thesis work was focused especially on sprayed inorganic coatings and their deposition. The simultaneous spray method can be applied for different films formation such as purely polymeric materials, polymer – nano-object hybrid film formation, polymer – small molecule, purely inorganic coatings. The polymer – small molecule and purely inorganic films formation showed generally linear growth and a good thickness control of films. Numerous other studies as deposition time versus film rate deposition, solution concentration, surface nature of substrate, the co-pulverization of water as well as spray parameters variation were realized for the validation of the simultaneous spray method.

Of course it would be interesting to study the mechanical characterization and stability of coatings, coating thickness versus spray parameters (e.g. spraying system configuration, spray nozzle diameter, distance spray nozzle - substrate) or the applicability to other materials in the future work. The film formation mechanism is not fully understood until this moment. Liquid exchange, nucleation and crystal growth are likely very complex

processes in nano to micro porous films and should be studied in the future as well, such phenomena exceed by far the scope of the present thesis work. A broader study on the droplets coalescence (before and/or after the substrate contact), the droplet size influence on the coating properties, the thin liquid film thickness produced at the substrate surface could be also of interest.

**Summary: Spray-on hybrid thin films**

Hybrid thin films were prepared by a modified variant of the classical Layer-by-Layer (LbL) deposition method. Inorganic coatings are deposited using the consecutive spray method, in which aqueous solutions are alternately sprayed for short times (less than 5 seconds). Numerous inorganic coatings were prepared this way such as calcium phosphate, calcium fluoride, calcium oxalate, silver chloride, Prussian Blue.

The main target of the hybrid films comprised of calcium phosphate and Collagen is for application in the cartilage repair. “Sandwich”-like structures of these components mimic the natural articular cartilage structure. In order to obtain the hybrid film containing Collagen and calcium phosphate, we used a (PAH-PSS) barrier film.

The deposition of inorganic coating can also be realized using the simultaneous spraying method where both solutions (cationic and anionic solution) are sprayed simultaneously. Homogeneous on several cm<sup>2</sup> of surface thin films are obtained in which the film thickness is controlled by spray parameters such as spraying time, solution concentration, nature of substrate to be coated.

**Keywords:** consecutive spray, simultaneous spray, Collagen multilayer film, inorganic coating, calcium phosphate deposition, cartilage repair, biocompatible scaffold, thin film deposition, hybrid films



### **Résumé: Fabrication de couches minces hybrides par pulvérisation**

Des couches minces hybrides ont été préparé par une version modifiée de la méthode classique de déposition « couches-par-couches ». Les couches inorganiques de ces films hybrides sont déposés en utilisant la méthode de pulvérisation consécutive (qui est la méthode modifiée) pour laquelle la pulvérisation de solutions aqueuses se fait de manière alterné avec des temps de pulvérisation très courts (moins de 5 secondes).

Nombreuses couches inorganique sont obtenues par cette technique telles que des couches de phosphate de calcium, oxalate de calcium, fluorure de calcium, Blue de Prusse, chlorure d'argent, etc. L'application principale des couches hybrides contenant de phosphate de calcium et Collagène est la fabrication de nouveaux biomatériaux pour la régénération/réparation du cartilage articulaire (le domaine d'ingénierie tissulaire). La structure de type « sandwich » de ces composants permet la mimique du cartilage articulaire naturel. Pour la préparation de ces couches hybrides on a utilisé un film mince de polyélectrolytes de (PAH-PSS).

Le dépôt de couche mince inorganique peut se faire aussi en utilisant la méthode de pulvérisation simultanée des deux solutions contenant les cations et les anions. Des couches minces homogènes sur des surfaces d'ordre des  $\text{cm}^2$  ont été obtenues et pour lesquelles l'épaisseur peut être contrôlée par la variation de paramètres de pulvérisation tels que le temps de pulvérisation, la concentration de la solution, la nature du substrat.

**Mots clés:** pulvérisation alterné ou consécutive, pulvérisation simultanée, multicouche de polyélectrolytes, Collagène, dépôt inorganique, couches minces de phosphate de calcium, ingénierie tissulaire, réparation de cartilage articulaire, technique de dépôt par pulvérisation, couches minces hybrides.